IMPACTS OF ATMOSPHERIC MOISTURE TRANSPORT ON THE GREENLAND ICE SHEET

by

KYLE S. MATTINGLY

(Under the Direction of Thomas Mote)

ABSTRACT

Among the most pressing consequences of recent climate warming is the acceleration of mass loss from the Greenland Ice Sheet (GrIS) since the late 1990s. GrIS mass loss contributes directly to global mean sea level rise and affects many other components of the global ocean-atmosphere-cryosphere system, including oceanic and atmospheric circulation and oceanic primary productivity. Several episodes of widespread GrIS surface melt in recent years have coincided with intense poleward water vapor transport in narrow plumes called “atmospheric rivers” (ARs), suggesting that these events play an important role in high-latitude warming. Climate model projections indicate that poleward moisture transport will intensify as a consequence of anthropogenic climate change.

In this dissertation, the impact of poleward moisture transport by ARs on the GrIS is comprehensively assessed from a local- to planetary-scale energy and mass balance perspective. Impacts of ARs on GrIS surface mass balance (SMB) on daily, seasonal, and annual time scales are first examined. Strong summer ARs are found to cause intense melt events in western Greenland, and an increasing trend in AR-related moisture transport is found to correspond with the recent increase in GrIS mass loss. The physical mechanisms by which ARs force GrIS melt

are analyzed in the second part of this work through examination of changes to the surface energy balance and cloud properties induced by AR events. ARs are found to provide melt energy through multi-scale, spatially variable surface-atmosphere interactions, with ice sheet surface melt produced in cloudy, windy conditions in the area of AR "landfall" and in clear-sky downsloping flow in areas separated from the AR landfall by the topographic barrier of the ice sheet. The third part investigates the dynamical processes by which ARs link distant regions within the global hydrological cycle, through identification of the evaporative water vapor source regions and moisture transport processes that produce AR events in western Greenland. Moisture fluxes during ARs originate from lower-latitude evaporative sources compared to typical conditions, with enhanced moisture uptake occurring over a broad swath of the Atlantic Ocean during summer and winter, as well as northeastern North America during summer.

INDEX WORDS: Climatology, Synoptic Meteorology, Greenland Ice Sheet, Cryosphere, Self-organizing Maps

IMPACTS OF ATMOSPHERIC MOISTURE TRANSPORT ON THE GREENLAND ICE SHEET

by

KYLE S. MATTINGLY

B.S., Western Kentucky University, 2012

M.S., University of Georgia, 2014

A Dissertation Submitted to the Graduate Faculty of The University of Georgia in Partial Fulfillment of the Requirements for the Degree

DOCTOR OF PHILOSOPHY

ATHENS, GEORGIA

2019

IMPACTS OF ATMOSPHERIC MOISTURE TRANSPORT ON THE GREENLAND ICE SHEET

by

KYLE S. MATTINGLY

Major Professor:	Thomas Mote
Committee:	J. Marshall Shepherd
	Andrew Grundstein
	Patricia L. Yager

Electronic Version Approved:

Suzanne Barbour
Dean of the Graduate School
The University of Georgia
August 2019

ACKNOWLEDGEMENTS

I would first like to thank Tom Mote, my major professor during the seven years I have spent at UGA completing my M.S. and PhD. It's hard to adequately express my gratitude for the positive influence Tom has had on my scholarly and personal development during that time. Perhaps the best compliment I can give is that without exception, he has always made time for me anytime I have needed his guidance, and again without exception, I have left the conversation feeling better than I did before. In my own academic career, I hope to be able to help students become scholars as effectively as he has done for me.

Thank you to my doctoral advising committee — Andy Grundstein, Marshall Shepherd, and Tish Yager — for their support and flexibility throughout the process of completing this dissertation, and for providing helpful advice and critiques that have challenged me to think about my work in a different way.

During the final three years of my PhD, I have received financial support from a NASA Earth and Space Science Fellowship (NASA grant number NNX16A022H). This support has been invaluable in allowing me the time to dig deeply into the topics addressed in this dissertation, and has opened the door for many opportunities to interact with researchers from around the world. I also have benefited from funding provided by NASA Interdisciplinary Research in Earth Science grant number NNH12ZDA001N-IDS.

UGA, and the Geography department in particular, has been a welcoming and inspiring place to spend the past seven years. The number of faculty and staff who have helped me along the way is too large to try and list here and I want to extend my thanks to all of them. In

particular, thanks to Lynne Seymour for helping myself and other geographers understand statistics, and for being an awesome person to hang out with in general. And thanks to John Knox for also being a great person to chat with and learn from, and for being an outstanding teacher whose example I plan to follow throughout my career.

I will leave UGA with lots of fond memories of times spent with fellow graduate students in the classroom, in the lab, and many other places near and far. Again the amount of peers to thank is too long to list here. Thanks to Neil Debbage for being a great friend and roommate for many years. Thanks also to all the fantastic people who I've had the privilege of sharing the Climate Research Lab penthouse with — Alan Black, Jordan McLeod, Craig Ramseyer, Jared Rackley, Paul Miller, Josh Rosen, Nick Morgan, Lori Wachowicz, Flávia Moraes, Haylie Mikulak, and Jonathan Preece. And shout out to Taylor Hafley for helping me bring a little bit of Kentucky to Athens.

Thank you to my family and friends for their support during all the ups and downs that come along with getting a PhD. Kait, thank you for being a wonderful companion, patient listener, and source of many good ideas. And finally, thanks to Beamer for being such a good boy through it all.

TABLE OF CONTENTS

Page

LIST OF TABLES

Page

LIST OF FIGURES

Page

CHAPTER 1

INTRODUCTION AND LITERATURE REVIEW

1.1 Introduction

Nearly 10% of Earth's fresh water is stored as solid ice atop the land mass of Greenland, forming the Greenland Ice Sheet (GrIS; see Figure 1.1). As a grounded ice sheet, any loss of ice mass from the GrIS — either through discharge of solid ice from marine-terminating glaciers or runoff of surface meltwater into the ocean — contributes to global mean sea level rise if not replaced by an equivalent amount of accumulation. The GrIS contains enough ice to raise sea levels by ~7.4 m and has been losing mass at an enhanced rate since the late 1990s, becoming the single largest contributor to global mean sea level rise after 2002 [*Bamber et al*., 2018] (Figure 1.2). Meltwater runoff from the GrIS may influence the Atlantic Meridional Overturning Circulation through its effects on Labrador Sea convection [*Hu et al*., 2011; *Luo et al*., 2016; *Castelao et al*., 2019] and may modulate oceanic carbon storage through its impacts on primary production in the Labrador Sea [*Oliver et al*., 2018]. These changes at the base of the marine food chain are critical to the local economy — 90% of Greenland's export sector relies on fishing, and changes to the marine ecosystem including decreases in northern shrimp and the appearance of fish species native to warmer waters have taken place in recent years [*Rosen*, 2016; *Koeller et al*., 2009; *MacKenzie et al*., 2014]. Ice sheet retreat and warming temperatures raise the prospect of new mining and agricultural development, as the nation seeks new sources of revenue in the face of decreased subsidies from Denmark after Greenland obtained self-government in 2009 [*Bendixen et al*., 2017; *Hansen and Johnstone*, 2019]. GrIS mass loss also

affects atmospheric circulation, as the "ice mountain" of Greenland shifts the Northern Hemisphere storm track southward, and a reduction in its size would alter global atmospheric circulation through the removal of this dynamical effect as well as decreased high-latitude albedo [*Peterson et al*., 2004; *Van Angelen et al*., 2011; *Clark et al*., 1999].

In July 2012, nearly the entire ice sheet briefly experienced surface melt, a phenomenon that last occurred in 1889 and likely had not happened for seven centuries prior to that, during the Medieval Warm Period [*Nghiem et al*., 2012]. This extreme melt occurred at the same as an intense corridor of poleward water vapor transport, known as an "atmospheric river" (AR), was present over western Greenland [*Neff et al*., 2014] (see Figure 2.1). Several other instances of anomalous GrIS melt in recent years also occurred during AR events, which suggests that ARs act as substantial poleward energy fluxes and play an important role in recent Arctic warming. To date, no studies have examined the effects of ARs on the mass and energy balance of the GrIS or determined whether increased moisture transport from lower latitudes contributed to the recent uptick in GrIS mass loss. This research provides the first such investigation, organized into the following objectives and motivated by the accompanying research questions:

1. Temporal trends in ARs affecting Greenland and their impacts on surface mass balance (SMB): Has the amount of water vapor transported to Greenland by ARs increased alongside the recent decreasing GrIS mass trend? How do ARs impact GrIS melt and surface mass balance (SMB) on daily, seasonal, and annual time scales?

2. Physical processes driving GrIS surface melt during strong summer AR events: How do strong summer AR events alter the terms of the surface energy balance to provide anomalous energy flux into the GrIS surface? How do cloud cover and cloud phase change during these events relative to times with no AR, and how do clouds affect the GrIS surface energy balance?

How do synoptic- to local-scale atmospheric circulation features and surface-atmosphere interactions control the observed surface energy balance and cloud changes?

3. Evaporative sources of water vapor transported to western Greenland: What are the characteristics of large-scale evaporative conditions preceding strong ARs in western Greenland, and how do these conditions differ from periods with no AR? Are AR events in western Greenland associated with enhanced moisture export toward the GrIS from lower latitudes?

Each of these research objectives comprises a separate chapter of this dissertation, with each chapter forming a self-contained manuscript suitable for publication as a scholarly journal article. The results of research objective 1 are described in Chapter 2 and have been published in the *Journal of Geophysical Research: Atmospheres*. Research objective 2 forms Chapter 3 of the dissertation and will be submitted to *Journal of Climate*. The third research objective is detailed in Chapter 4 and will be submitted to *Journal of Geophysical Research: Atmospheres*.

1.2 Literature Review

1.2.1 Arctic Amplification

GrIS surface melt is driven by energy exchanges at the interface between the ice / snow surface and the near-surface layer of the atmosphere. Thus, the immediate cause of the recent decreasing trend in GrIS SMB is increased near-surface temperatures that provide anomalous energy to the ice sheet surface. Observed changes in a number of atmospheric and coupled ocean-atmospheric phenomena have been invoked to explain the rising temperatures over Greenland. The most readily observed change in atmospheric processes operating on daily to weekly time scales is an increase in slow-moving anticyclones known as “Greenland blocks” over the ice sheet [*Hanna et al*., 2014, 2018a], which are typically strongest when accompanied by a precursor cyclone [*McLeod and Mote*, 2015]. This increase in blocking events has been

linked to the state of longer-term (seasonal to decadal) climate oscillations including the North Atlantic Oscillation (NAO) [*Fettweis et al*., 2013b] and Atlantic Multidecadal Oscillation (AMO) [*Rimbu et al*., 2017; *Hahn et al*., 2018].

These regional climatic trends are occurring within the broader context of "Arctic Amplification" — the enhanced warming of the Northern Hemisphere high latitudes relative to the rest of the world [*Serreze and Barry*, 2011]. Near-surface temperatures in the Arctic are increasing at roughly double the rate of lower latitudes, with warming especially enhanced during autumn and winter [*Serreze et al.*, 2009; *Cohen et al.*, 2014] (Figure 1.3). These temperature changes are both a cause and a consequence of the rapid decline in Arctic sea ice, which has decreased in volume by 75% since the 1980s [*Overland et al.*, 2014]. September minimum sea ice extent decreased to record lows during 2007 and 2012 [*Wernli and Papritz*, 2018], and record or near-record low ice extent at the end of the freeze-up season in early spring was observed in 2016 [*Hegyi and Taylor*, 2018] (Figure 1.4). A number of studies suggest that Arctic sea ice loss is connected to atmospheric circulation anomalies and extreme weather events in the Northern Hemisphere mid- and high-latitudes [e.g., *Francis and Vavrus*, 2012; *Liu et al.*, 2012; *Overland et al.*, 2015; *Tachibana et al*., 2019], although this relationship has been called into questioned by other researchers [*Barnes*, 2013; *Wallace et al.*, 2014; *Screen and Simmonds*, 2014] and is likely dependent on subtleties such as the location and magnitude of sea ice loss as well as the background climate state [*Screen et al*., 2018].

Several interrelated mechanisms have been hypothesized as responsible for the disproportionate warming of the Arctic. The most commonly cited cause is the ice-albedo feedback — reduced sea ice coverage in the Arctic Ocean, along with the melting or disappearance of snow cover on the GrIS and high-latitude land surfaces, causes a greater

fraction of incoming solar radiation to be absorbed [*Budyko*, 1969; *Cess et al.*, 1991; *Box et al.*, 2012]. Enhanced absorption in turn lowers the albedo of an increasing fraction of the ocean and land surface and thus further accelerates warming. This effect may be compounded by increases in absorptive aerosols such as black carbon on snow and ice surfaces [*Quinn et al.*, 2008; *Bond et al.*, 2013; *Dumont et al.*, 2014]. Although the ice-albedo feedback is clearly important, modeling experiments have found that Arctic Amplification occurs in response to increases in greenhouse gases even in the absence of changes in high-latitude albedo [*Winton*, 2006; *Graversen and Wang*, 2009]. Other local factors invoked to explain this result include the concentration of warming near the surface due to the stable atmosphere of the high latitudes and the "Planck feedback" whereby a larger temperature increase is needed to emit a given amount of longwave radiation at lower temperatures [*Pithan and Mauritsen*, 2014]. However, in recent years researchers have increasingly recognized that the preferential warming of the Arctic cannot be purely local in its causes, but rather must be understood within the context of the global-scale fluxes of energy and mass (including moisture) that comprise the Earth's climate system [*Solomon*, 2006; *Graversen et al.*, 2008; *Yang et al.*, 2010; *Alexeev and Jackson*, 2013; *Laliberté and Kushner*, 2014; *Gimeno et al.*, 2015; *Yang et al.*, 2015; *Graversen and Burtu*, 2016; *Messori et al*., 2018; *Wernli and Papritz*, 2018]. Accordingly, the role played by heat and moisture transport from lower latitudes in the changing energy budget of the GrIS and the wider Arctic region has emerged as a pressing topic of inquiry in Earth system science.

1.2.2 The global energy balance and poleward moisture transport

On the global scale, the Earth's climate system is characterized by a surplus in net radiation (the balance of incoming and outgoing shortwave and longwave radiation) in the tropics and a net radiative deficit in the polar regions (Figure 1.5). Meridional transport of energy

by the atmosphere and oceans partially offsets the global radiative imbalance and prevents runaway tropical warming and polar cooling [*Trenberth and Solomon*, 1994; *Overland et al.*, 1996]. This poleward energy transport is particularly important to the climate of the Arctic, as meridional energy transport at the Arctic boundary (~70°N) is similar in magnitude to the absorbed solar radiation integrated across the entire Arctic [*Oort and Peixóto*, 1983]. Calculations based on satellite observations and atmospheric reanalyses suggest that the majority (~78%) of poleward energy transport occurs within the atmosphere in the mid- and high-latitudes of both the Northern and Southern hemispheres [*Trenberth and Caron*, 2001; *Wunsch*, 2005] (Figure 1.6), although a number of authors have noted that the atmospheric and oceanic components of meridional energy transport cannot be cleanly separated and the two should instead be conceptualized as a "joint" energy transport mode [*Ruixin*, 2005; *Rhines et al.*, 2008; *Yang et al.*, 2015]. The oceans store an immense amount of energy in comparison to the atmosphere, and the oceanic circulation can transfer this energy through the climate system on timescales much longer than those typically considered in planetary energy budget calculations [*Murphy et al.*, 2009; *Stouffer*, 2004; *Knutti et al.*, 2008].

The atmospheric component of poleward energy transport occurs through both "dry" dynamics (fluxes of sensible heat and potential energy) and through atmospheric moisture flux, which results in latent heat release when water vapor condenses to form liquid water [*Trenberth and Stepaniak*, 2004; *Frierson et al*., 2007]. Atmospheric moisture transport, in particular, plays a pivotal role in global climate variability because of the tremendous heat capacity of water — water vapor is 100 times more efficient at transporting heat than dry air — and the frequent occurrence of transient eddies in the atmospheric circulation that redistribute this "fluid sunshine" [*Pierrehumbert*, 2002] across large distances on short timescales. This poleward

transport of latent heat is stronger over the Atlantic Ocean relative to the Pacific, as the Atlantic provides more water vapor to the tropical atmosphere despite its smaller size [*Yang et al.*, 2015].

A number of theoretical and model-based studies [e.g., *Manabe and Wetherald*, 1975; *Held and Soden*, 2006; *Skific et al.*, 2009; *Wu et al.*, 2011; *Zelinka and Hartmann*, 2012; *Bengtsson et al.*, 2013; *S. J. Koenig et al.*, 2014; *Lavers et al.*, 2015] have concluded that poleward moisture transport to the Arctic will increase in a warming climate. This is predicted because a warmer atmosphere has a higher water vapor capacity, and because greater anomalous radiative energy gain in the tropics relative to higher latitudes under greenhouse warming will require increased poleward atmospheric energy transport to maintain energy conservation within the climate system [*Zelinka and Hartmann*, 2012; *Baggett and Lee*, 2015]. Most models project increasing latent energy flux to the Arctic with corresponding decreases in dry static energy transport, and even simulations with an overall weakening of poleward atmospheric energy transport feature an increase in poleward moisture flux [*Hwang and Frierson*, 2010; *Skific and Francis*, 2013; *Graversen and Burtu*, 2016]. These predictions are supported by observations of an increasing trend in Arctic atmospheric water vapor content in recent decades [*Francis and Hunter*, 2007; *Rinke et al.*, 2009; *Serreze et al.*, 2012; *Boisvert and Stroeve*, 2015; *Gimeno et al*., 2019].

1.2.3 Cryospheric effects of poleward moisture transport by "atmospheric rivers"

A major fraction — up to 65–70% according to *Liu and Barnes* [2015] — of annual moisture transport into the Northern Hemisphere high latitudes occurs during a small number of intense moisture transport events [*Zhu and Newell*, 1998; *Woods et al.*, 2013; *Liu and Barnes*, 2015]. These events, often termed "atmospheric rivers" (ARs), are driven by transient eddies in the synoptic atmospheric circulation that deviate from the climatological mean flow [*Newman et*

al., 2012]. A dramatic example of the interaction of these moisture transport events with the cryosphere occurred during July 2012 when an intense AR transported extremely anomalous quantities of water vapor from lower latitudes to Greenland just prior to the most spatially extensive GrIS surface melt in over a century on 12 July 2012 [*Nghiem et al.*, 2012; *Tedesco et al.*, 2013; *Neff et al.*, 2014; *Bonne et al.*, 2015].

The effects of this AR on the GrIS are consistent with findings [*Lee et al.*, 2011; *Yoo et al.*, 2012; *H.-S. Park et al.*, 2015b; *Hegyi and Taylor*, 2018; *Zhong et al*., 2018] of decreased sea ice concentration in the Arctic following periods of anomalous moisture flux from lower latitudes. During periods of anomalous moisture flux into the Arctic, additional longwave radiation is retained locally due to water vapor's strong greenhouse gas properties and the air mass is warmed by condensational latent heat release (both locally and upstream within poleward-moving air streams). No comparable efforts have been made to comprehensively investigate the effects of ARs on the GrIS surface energy budget, but recent case studies of exceptional melt events [*Fausto et al.*, 2016a,b; *Hermann et al*., 2018] suggest that non-radiative energy fluxes (primarily turbulent fluxes of sensible and latent heat) may be more important than radiative energy in driving GrIS melt during anomalous moisture transport events.

In addition to their direct radiative and turbulent energetic effects, poleward moisture transport events over the GrIS may enhance the well-documented [*Shupe and Intrieri*, 2004; *Francis and Hunter*, 2007; *Chen et al.*, 2011; *Cox et al.*, 2015; *Miller et al.*, 2015; *Gallagher et al*., 2018] warming effects of polar clouds. *Bennartz et al.* [2013] observed that low liquid clouds over the highest elevations of the GrIS during the July 2012 melt event trapped an anomalous amount of outgoing longwave radiation that outweighed their slight dimming effect on incoming solar radiation, while *Van Tricht et al.* [2016] showed that both liquid and ice clouds contribute

to increased meltwater runoff from the GrIS by reducing meltwater refreezing at night. However, *Hofer et al*. [2017] found a decreasing trend in summer cloud cover over Greenland from 1995–2009 using regional climate model and satellite data, suggesting that the impact of clouds on GrIS melt should be investigated more thoroughly.

The body of research described in the previous section provides growing evidence of links between episodes of poleward water vapor transport — predicted to increase in a warming climate — and increased energy available for sea and land ice melt in the Northern Hemisphere high latitudes. However, this work has either consisted of case studies of a few moisture transport events affecting the GrIS or has examined the effects of poleward moisture flux on Arctic sea ice, rather than on the grounded GrIS. Extreme transient moisture transport events (i.e. ARs) provide much of the annual water vapor input to the Northern Hemisphere high latitudes, but previous to this dissertation there has been no effort to study long-term trends in Greenland-bound ARs, which may substantially differ from trends for the Arctic as a whole. There has previously been no comprehensive analysis of moisture flux effects on the GrIS energy budget and cloud properties across a large sample of events, and the links between lower-latitude moisture source regions and water vapor transported to the GrIS by ARs are not well understood. To address this gap in scientific understanding, the overarching objective of this dissertation is to comprehensively assess the impact of poleward moisture transport by ARs on the GrIS from a local- to planetary-scale energy and mass balance perspective, following the specific research objectives outlined in Section 1.1.

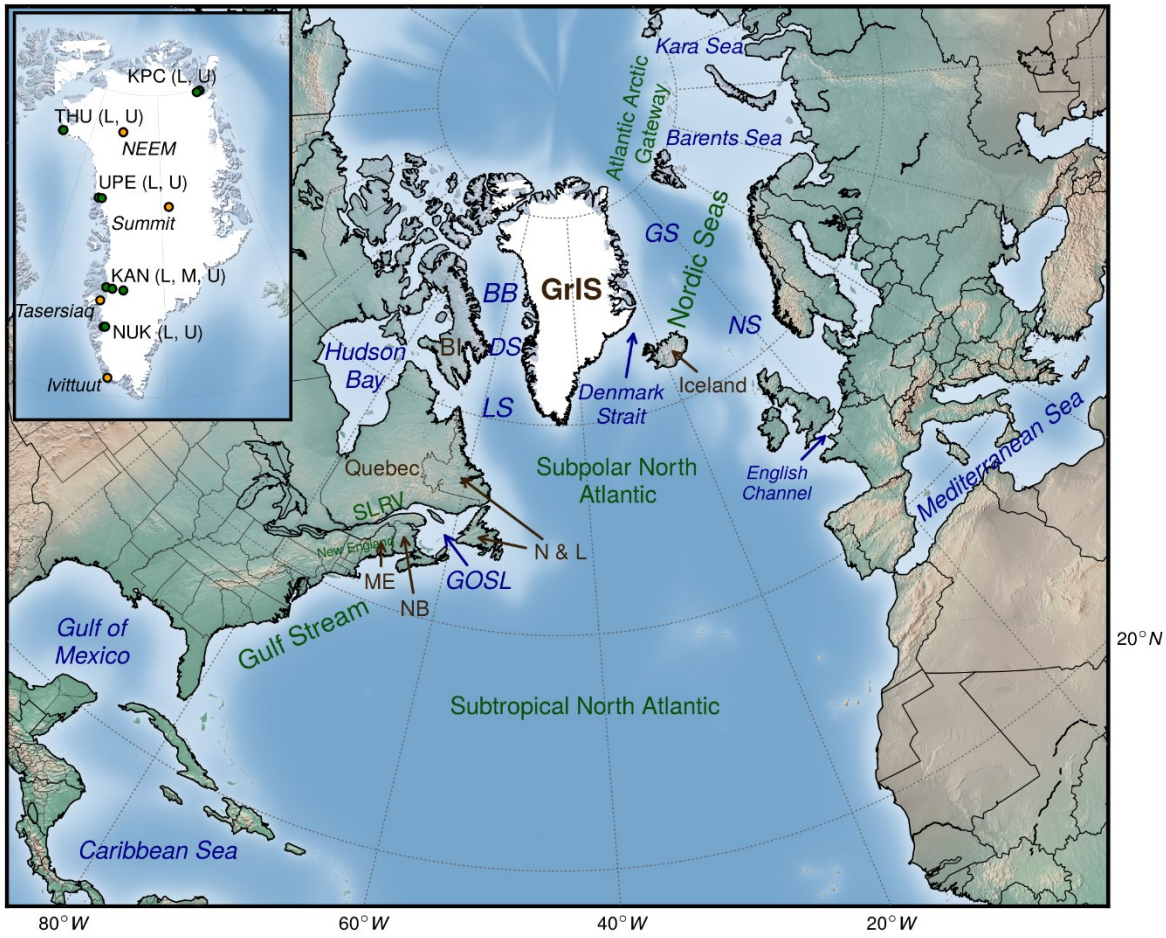

Inset map:
KAN: Kangerlussuaq
KPC: Kronprins Christian Land
NUK: Nuuk
THU: Thule
UPE: Upernavik

Large map:
BB: Baffin Bay
DS: Davis Strait
GOSL: Gulf of St. Lawrence
GS: Greenland Sea
LS: Labrador Sea
NS: Norwegian Sea

Large map:
BI: Baffin Island
GrIS: Greenland Ice Sheet
ME: Maine
N & L: Newfoundland and Labrador
NB: New Brunswick
SLRV: St. Lawrence River Valley

Figure 1.1. Overview map of geographic features mentioned throughout this dissertation (large map), and map of PROMICE stations (green dots) and other locations in Greenland (orange dots) discussed in this dissertation (inset map). On the large map, bodies of water are labeled in blue, bounded land features (i.e. countries, states, provinces, the GrIS) are labeled in brown, and terms that refer to a general feature or region without definite boundaries are labeled in green. Terms that are abbreviated to save space on the map are given in the legend at bottom.

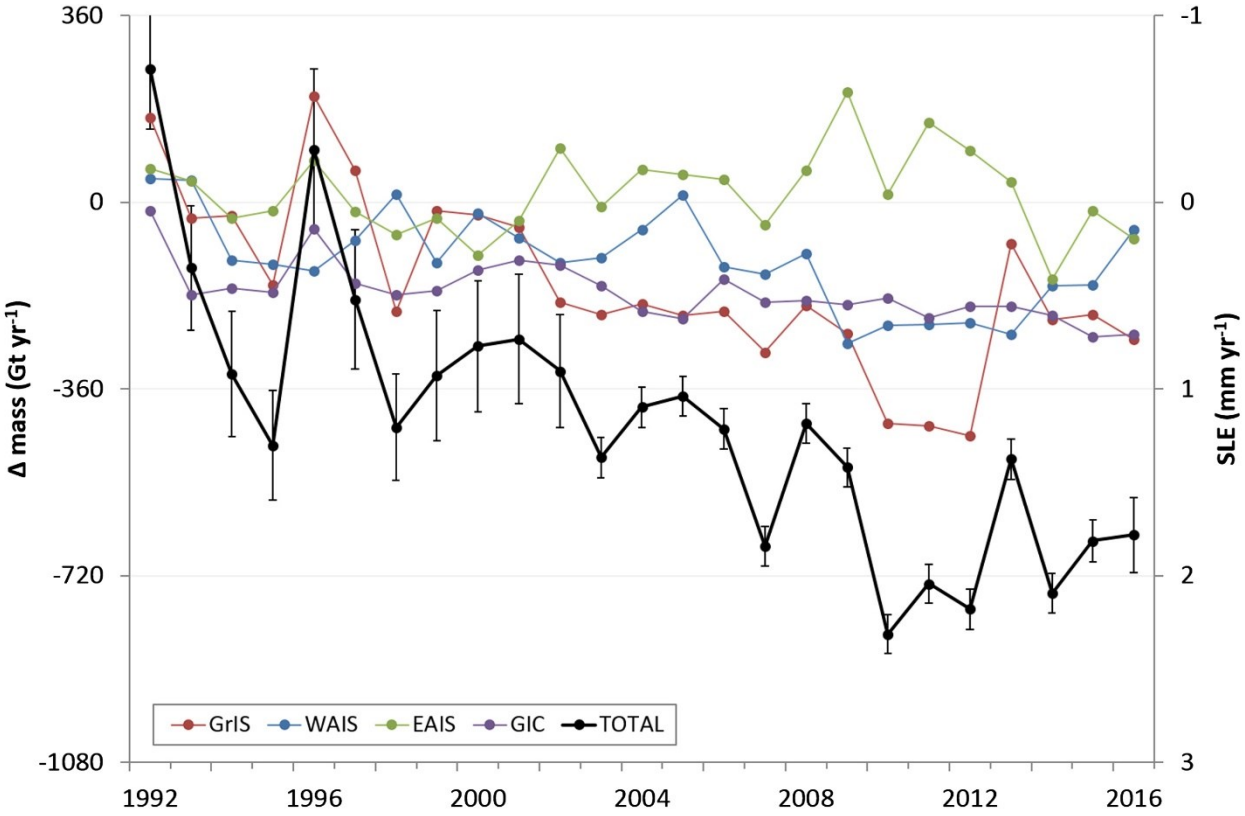

Figure 1.2. Time series of annual mass loss from the GrIS, West Antarctic Ice Sheet (WAIS), East Antarctic Ice Sheet (EAIS), and other global glaciers and ice caps (GIC). Figure reproduced from *Bamber et al*. [2018], with permission granted by the Creative Commons Attribution 3.0 License: https://creativecommons.org/licenses/by/3.0/.

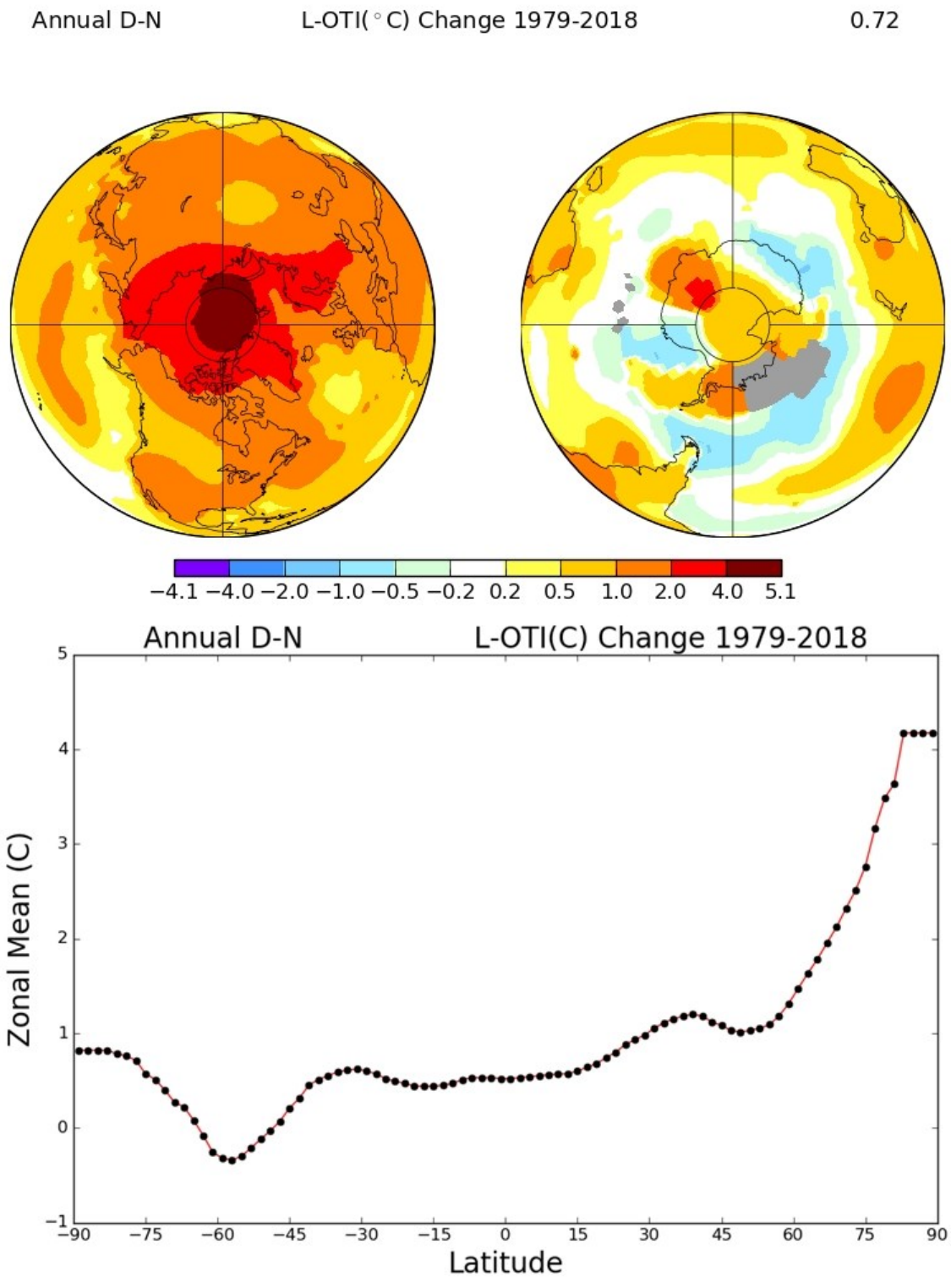

Figure 1.3. Top: maps of annual global temperature change (°C) during 1979–2018. Bottom: Plot of 1979–2018 annual temperature change averaged over 2° latitude bands. Temperature data are from the NASA Goddard Institute for Space Studies (GISS) Surface Temperature Analysis version 4 [*GISTEMP Team*, 2019; *Lenssen et al*., 2019].

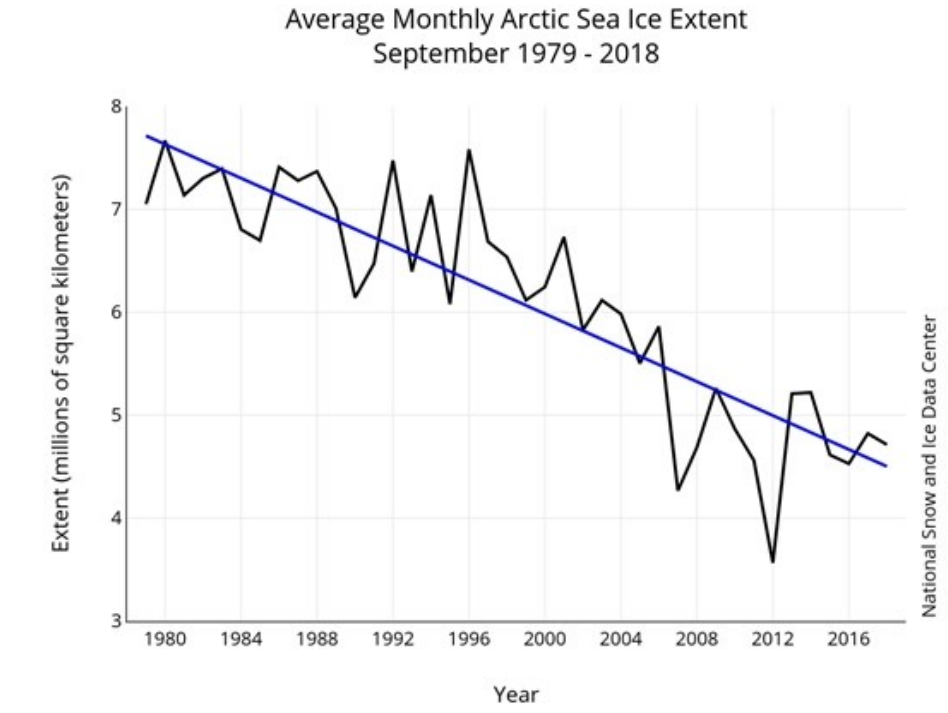

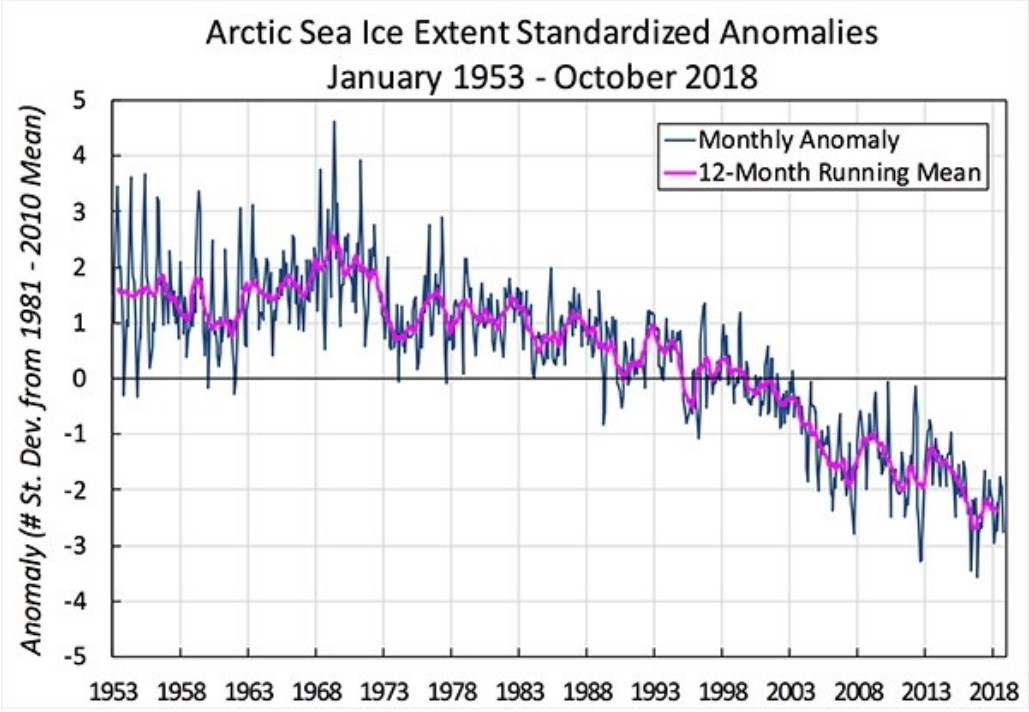

Figure 1.4. Top: time series of average September sea ice extent during 1979–2018. Bottom: Time series of monthly Arctic sea extent standardized anomalies from January 1953 through October 2018. Images reproduced from *Gautier* [2018] and *NSIDC* [2019], with permission granted by the NSIDC Use and Copyright policy: https://nsidc.org/about/use_copyright.html.

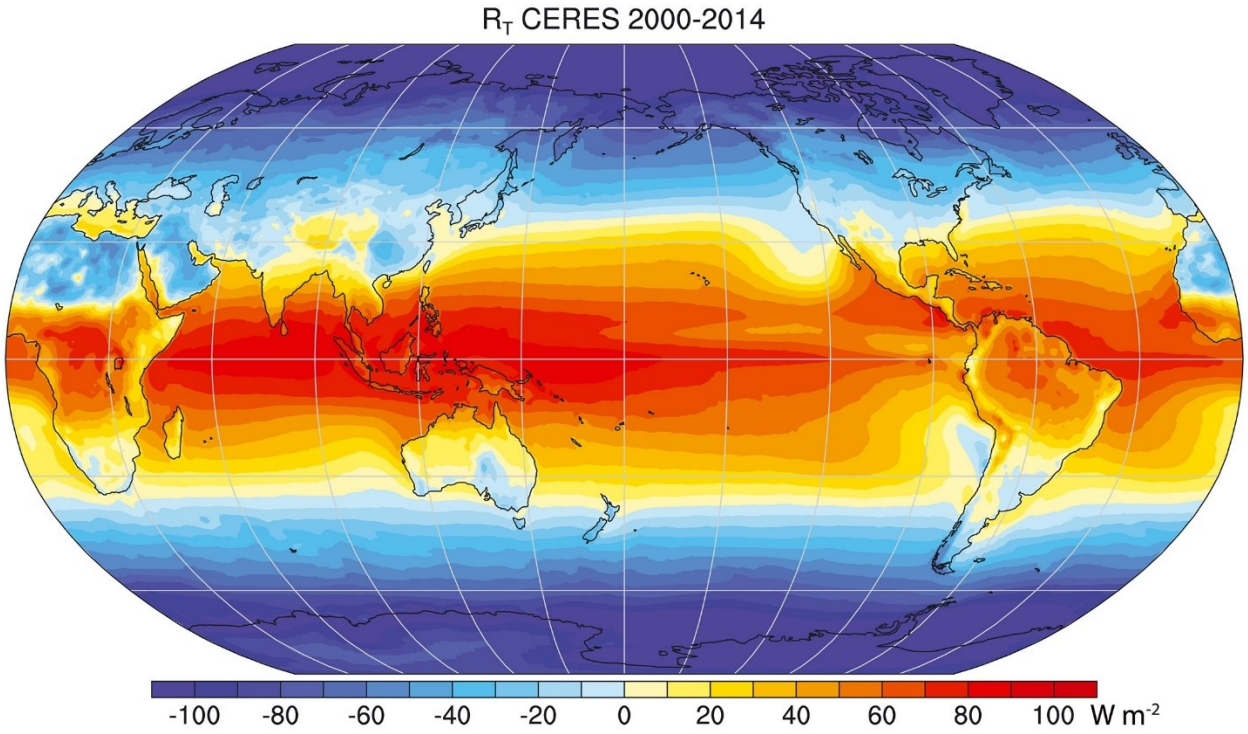

Figure 1.5. Annual mean net top of atmosphere (TOA) radiation downwards during 2000–2014 from the Clouds and the Earth's Radiant Energy System (CERES) satellite dataset. Figure reproduced from *Trenberth and Fasullo* [2017], with permission granted by the American Geophysical Union usage permissions policy: https://publications.agu.org/author-resource-center/usage-permissions/.

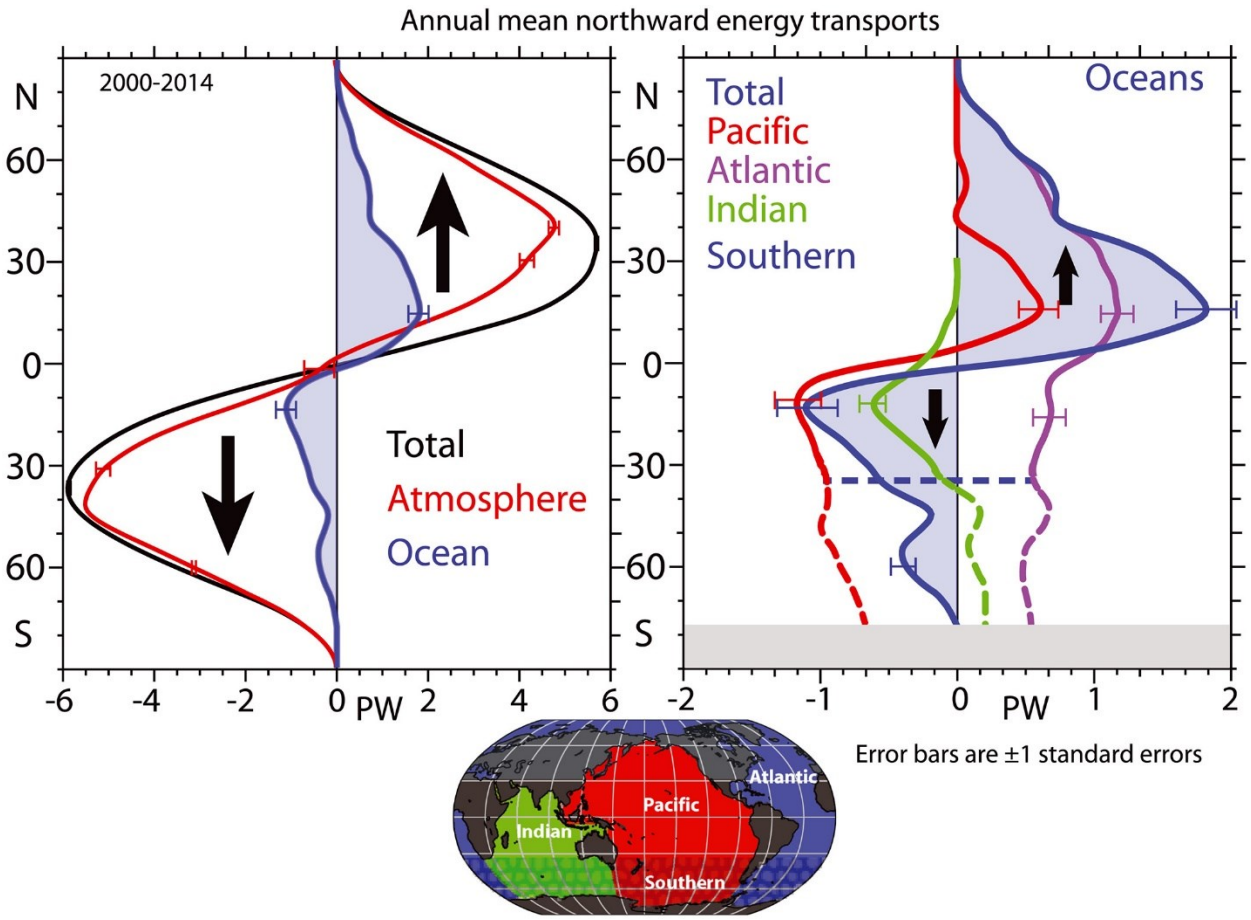

Figure 1.6. Left: the annual and zonal means of the northward energy transports for 2000–2014 in petawatts (PW) for the total Earth system (black), the atmosphere (red), and the ocean (blue). Right: The ocean component broken down into the contributions from the Atlantic (violet), Pacific (red), and Indian (green) Oceans which combine south of 35°S to give the southern ocean value, as given in the small map at bottom. The error bars are ±1 standard deviation. Figure reproduced from *Trenberth and Fasullo* [2017], with permission granted by the American Geophysical Union usage permissions policy: https://publications.agu.org/author-resource-center/usage-permissions/.

CHAPTER 2

ATMOSPHERIC RIVER IMPACTS ON GREENLAND ICE SHEET SURFACE MASS BALANCE[1]

[1] Mattingly, K. S., T. L. Mote, and X. Fettweis (2018), Atmospheric river impacts on Greenland Ice Sheet surface mass balance, *Journal of Geophysical Research: Atmospheres*, *123*(16), 8538–8560, doi:10.1029/2018JD028714. Reprinted here with permission of the publisher.

Abstract

Greenland Ice Sheet (GrIS) mass loss has accelerated since the turn of the 21st Century. Several recent episodes of rapid GrIS ablation coincided with intense moisture transport over Greenland by atmospheric rivers (ARs), suggesting that these events influence the evolution of GrIS surface mass balance (SMB). ARs likely provide melt energy through several physical mechanisms, and conversely, may increase SMB through enhanced snow accumulation. In this study, we compile a long-term (1980–2016) record of moisture transport events using a conventional AR identification algorithm as well as a self-organizing map (SOM) classification applied to MERRA-2 data. We then analyze AR effects on the GrIS using melt data from passive microwave satellite observations and regional climate model output. Results show that anomalously strong moisture transport by ARs clearly contributed to increased GrIS mass loss in recent years. AR activity over Greenland was above normal throughout the 2000s and early 2010s, and recent melting seasons with above-average GrIS melt feature positive moisture transport anomalies over Greenland. Analysis of individual AR impacts shows a pronounced increase in GrIS surface melt after strong AR events. AR effects on SMB are more complex, as strong summer ARs cause sharp SMB losses in the ablation zone that exceed moderate SMB gains induced by ARs in the accumulation zone during summer and in all areas during other seasons. Our results demonstrate the influence of the strongest ARs in controlling GrIS SMB, and we conclude that projections of future GrIS SMB should accurately capture these rare ephemeral events.

2.1 Introduction

The Greenland Ice Sheet (GrIS) contains nearly 10% of the world's fresh water in a ~1.7 million km^2 grounded ice mass that is up to 3 km thick [*Noël et al*., 2014; *Thomas*, 2001; *Alley et al*., 2010]. It has been losing mass at an accelerating rate since the late 1990s [*Hanna et al*., 2013a; *Khan et al*., 2015; *Wilton et al*., 2017]. Consequently, the estimated GrIS contribution to the rate of global mean sea level rise has increased from around 5% in 1993 to over 25% in 2014, and this contemporary figure may be as high as 43% when mass losses from glaciers and ice caps along the ice sheet periphery are taken into account [*Chen et al*., 2017; *Noël et al*., 2017].

GrIS mass loss occurs when snow accumulation is exceeded by the combined losses from ablation (melting, sublimation, and wind-induced erosion of snow and ice) and solid ice discharge from marine-terminating glaciers. Mass losses from ice discharge and negative surface mass balance (SMB – the difference between surface accumulation and ablation) were roughly equivalent prior to 2005. Since 2005 the SMB component of GrIS mass loss has exceeded the ice discharge component, and SMB is projected to dominate the GrIS contribution to global sea level rise during the 21st Century [*Enderlin et al*., 2014; *van den Broeke et al*., 2017]. The primary cause of the decreasing SMB trend is increasing melt during summer, as there has been no significant trend in precipitation over the GrIS during this time [*van As et al*., 2014; *Fettweis et al*., 2017; *Noël et al*., 2017].

Spatiotemporal variability of GrIS melt and SMB has been highly significant in recent years. Total annual GrIS SMB steadily decreased from the late 1990s through the extraordinary melt season of 2012, when GrIS melt extent and duration reached the highest levels in the modern record [*Tedesco et al.,* 2013]. Subsequently, SMB recovered to typical pre-2000 levels in

2013, then positive but not extreme melt anomalies during 2014–2016 preceded abnormally high accumulation during fall 2016 and a below average 2017 melt season [*van den Broeke et al*., 2016; *Lindsey*, 2017; *Polar Portal*, 2017; *Tedesco et al*., 2017a]. Surface melt anomalies were concentrated across the western and southern GrIS during most of the high-melt seasons from the mid-2000s through the early 2010s, after which the highest anomalies shifted poleward to the northern GrIS during the 2014–2016 melt seasons [*Hall et al*., 2013; *NSIDC*, 2015, 2016; *Tedesco et al*., 2016b]. The net result of these recent variations has been continued year-on-year net GrIS mass loss but at a lesser rate than that observed from the mid-2000s through 2012, and the GrIS may have actually gained mass during the 2016–17 mass balance year for the first time in the 21st Century [*van den Broeke et al*., 2016; *Lindsey*, 2017].

Atmospheric conditions tightly control both the ablation and accumulation constituents of SMB. The temporal evolution of overall GrIS SMB and the spatial patterns of SMB across the ice sheet therefore vary widely in response to short-term weather events as well as lower-frequency climate variability [*Auger et al*., 2017]. Previous studies have shown that anomalous GrIS melt episodes during the warm season often occur under slow-moving high-pressure regimes known as “Greenland blocks”, with these blocking anticyclones favored during negative NAO conditions and often preceded by extratropical cyclones tracking to the west of Greenland [*Hanna et al*., 2013b; *McLeod and Mote*, 2015; *Lim et al*., 2016; *Ahlstrøm et al*., 2017]. Greenland blocking has significantly increased in summer over the past few decades, and is an important contributor to recently enhanced GrIS melt rates [*Hanna et al*., 2016, 2018b]. Another, possibly related, type of synoptic atmospheric circulation feature that may exert an important influence on GrIS SMB is the transport of water vapor by atmospheric rivers (ARs). ARs are narrow corridors of strong horizontal water vapor transport that accomplish most of the annual

moisture transport into the high latitudes of the Northern Hemisphere during a relatively small number of transient events [*Zhu and Newell*, 1998; *Woods et al*., 2013; *Liu and Barnes*, 2015].

Several recent instances of exceptional GrIS melting have occurred at the same time as strong ARs affected the GrIS. These episodes include the extreme July 2012 event (Figure 2.1) – when virtually the entire GrIS experienced surface melt for the first time in over a century – and less extensive but highly unusual out-of-season melt during early April 2016 [*Nghiem et al*., 2012; *Neff et al*., 2014; *Bonne et al*., 2015; *Tedstone et al*., 2017]. The physical mechanisms by which ARs may influence ice sheet melt include enhancement of the water vapor greenhouse effect, formation of clouds that retain additional longwave radiation, condensational latent heat release in the advected air mass [*Binder et al*., 2017], and surface melt energy provided by liquid precipitation [*Doyle et al*., 2015].

A growing body of recent work [e.g. *H.-S. Park et al*., 2015a, 2015b; *Yang and Magnusdottir*, 2017; *S. Lee et al*, 2017; *Johansson et al*., 2017] has shown that atmospheric moisture intrusions into the Arctic strongly influence sea ice conditions by increasing downwelling longwave radiation, but research into any similar AR impacts on the GrIS has been limited to a few case studies of individual moisture transport events. These studies suggest that clouds generated by influxes of water vapor help to initiate surface melt and inhibit meltwater refreezing [*Bennartz et al*., 2013; *van Tricht et al*., 2016; *Solomon et al*., 2017], and that turbulent fluxes of heat into the ice also contributed an abnormal amount of melt energy during two AR-coincident melt events in July 2012 [*Fausto et al*., 2016a, 2016b]. Although these studies point toward the probable role of warm season ARs in enhancing GrIS melt, AR events can also provide positive inputs to SMB through snow accumulation and decrease of solar radiation over the low albedo ablation zone [*Hofer et al*., 2017]. Net AR impacts on SMB likely

vary according to factors including season, elevation, latitude, and moisture transport intensity [*Fettweis et al*., 2013a; *Le clec'h et al*., 2019].

Recent studies have found evidence of an increasing trend in poleward moisture transport toward the GrIS [*Mattingly et al*., 2016 – hereafter M16] and the Arctic basin [*Boisvert and Stroeve*, 2015; *D.-S. Park et al*., 2015; *Woods and Caballero*, 2016; *Alexeev et al*., 2017; *Cao et al*., 2017; *Gong et al*., 2017; *H. J. Lee et al*., 2017], in accordance with predictions of enhanced moisture transport to the Arctic in a warming climate [*Gimeno et al*., 2015; *Lavers et al*., 2015; *Graversen and Burtu*, 2016; *Yoshimori et al*., 2017]. In light of these observed and projected trends, and recent case studies suggesting that ARs may play a significant role in determining the evolution of GrIS SMB, an examination of AR trends and impacts on GrIS SMB across a much larger sample of moisture transport events is needed. Therefore, in this study, we first investigate whether AR-related moisture transport to the GrIS has increased alongside the recent downturn in GrIS SMB. We then consider the implications of these moisture transport trends by analyzing the daily, seasonal, and annual scale impacts of AR events on GrIS melt and SMB. In order to examine the GrIS response to a broad range of moisture transport conditions and ensure that any trends we find are not artifacts of a single analysis method, we use both a self-organizing map (SOM) classification as well as a conventional object-based AR identification algorithm to identify moisture transport events. We hypothesize that the cryospheric effects of AR events vary seasonally and are also sensitive to the location and intensity of AR moisture transport, and thus we present detailed analyses of AR impacts partitioned by season, area of intersection with the GrIS, and strength of moisture transport within this AR-GrIS intersection zone.

2.2 Data and Methods

2.2.1 Data

The SOM classification and AR identification algorithm were initially applied to integrated water vapor transport (IVT – see Section 2.2.2a) data over the Northern Hemisphere from four atmospheric reanalysis datasets: MERRA-2 [*Gelaro et al*., 2017], MERRA [*Rienecker et al*., 2011], ERA-Interim [*Dee et al*., 2011], and CFSR [*Saha et al*., 2010]. We found close agreement between all four reanalyses regarding moisture transport trends and impacts on the GrIS (Figure 2.2), and the main conclusions of this study are not dependent on the choice of reanalysis. Previous studies [e.g. *Jakobson et al*., 2012; *Lindsay et al*., 2014; *Liu and Key*, 2016; *Huang et al*., 2017; *Reeves Eyre and Zeng*, 2017] have found that ERA-Interim and MERRA-2 are among the best-performing reanalyses in the Arctic region, and we further note that a specific purpose of MERRA-2 is improved reanalysis of the global hydrological cycle [*Bosilovich et al*., 2017]. For these reasons, we describe only the MERRA-2 results in the following sections, meaning that the study period for the moisture transport trend analysis is 1980–2016.

To examine impacts of moisture transport on modeled GrIS meltwater production and SMB, we utilize daily output from the Modèle Atmosphérique Régionale (MAR) regional climate model [*Gallée and Schayes*, 1994]. MAR is a coupled atmosphere-land surface model that employs the 1-D Surface Vegetation Atmosphere Transfer scheme (SISVAT) to calculate surface properties and exchange of mass and energy with the atmosphere. SISVAT incorporates a detailed 1-D snowpack model (CROCUS) that simulates energy and mass fluxes within the snowpack and is also capable of modelling changes in snow grain properties and their effects on surface albedo. MAR has been extensively validated against *in situ* and satellite observations over Greenland [e.g. *Lefebre et al*., 2005; *Alexander et al*., 2014; *Fettweis et al*., 2011; *Fettweis*

et al., 2017] and has been widely employed to simulate historical and future GrIS SMB [e.g. *Tedesco et al*., 2013; *Fettweis et al*., 2017; *Meyssignac et al*., 2017]. Daily total melt, snowfall, SMB, and surface temperature data used in this study are from MAR version 3.8, run at 7.5km resolution and forced by ERA-Interim reanalysis during 1980–2016. All variables are interpolated to a resolution of 5km on the grid of *Box* [2013] and corrected to account for topography differences between the native 7.5km MAR results and the 5km topography based on the Greenland Ice Mapping Project (GIMP) data set. In addition to the usual bug corrections, the main improvement with respect to MAR version 3.5 (used in *Fettweis et al*. [2017]) is the increase of cloud life, which partially corrects the overestimation of snow accumulation inland and the underestimation of infrared radiation highlighted in *Fettweis et al*. [2017] for MAR version 3.5.

In addition to the MAR output, the National Snow and Ice Data Center (NSIDC) MEaSUREs Greenland Surface Melt daily dataset [*Mote*, 2014] is used to obtain the daily extent of surface melt during the nominal melt season (May–September). These data are derived from satellite passive microwave observations (DMSP SSMI and SSMIS, Nimbus-7 SMMR) during 1979–2015.

2.2.2 Methods

In the following sections, we describe the IVT calculations performed on each set of reanalysis data, then detail the SOM classification and object-based AR identification method applied to this IVT data. We employ both these methods with the expectation that their strengths will complement one another and provide a richer level of detail than either method alone. The SOM method categorizes moisture transport patterns across a continuous range of synoptic atmospheric configurations, and by virtue of its unsupervised classification procedure is not

biased by the researchers' conceptions of what constitutes a noteworthy moisture transport event. Object-based AR identification methods have been successfully applied in a number of studies to advance scientific understanding of the role ARs play in the climate system, and are well suited for analyzing the impacts of discrete moisture transport episodes.

2.2.2a Integrated water vapor transport (IVT) calculation

IVT quantifies the instantaneous flux of water vapor through the depth of an atmospheric column and is the preferred variable for AR identification in most studies [e.g., *Rutz et al*., 2014; *Brands et al*., 2016; *Froidevaux and Martius*, 2016]. As in M16, IVT is calculated at 6-hourly time increments over the 1000–200 hPa atmospheric layer as follows:

$$IVT = \frac{1}{g}\int_{1000\ hPa}^{200\ hPa} qV\ dp \qquad (2.1)$$

where g is gravitational acceleration (9.80665 m s^{-2}), q and V are specific humidity (in kg kg^{-1}) and vector wind (in m s^{-1}) at the given pressure level, and dp is the difference between pressure levels. Consecutive pressure levels are incremented by 50 hPa between 1000 hPa and 500 hPa and by 100 hPa between 500 hPa and 200 hPa. IVT units are kg m^{-1} s^{-1}. To facilitate comparison of the AR and SOM results across reanalyses, MERRA-2 IVT data were re-gridded (using bilinear interpolation) to a 0.5° × 0.5° grid before further processing.

As in M16, the climatological percentile rank of IVT (IVT PR) is calculated to account for the seasonal cycle in the magnitude of moisture transport, which is particularly pronounced at high latitudes. IVT PR values are determined by ranking each 6-hourly IVT value at a given grid point relative to all the other 6-hourly values at that point occurring within ± 15 Julian days during the 1980–2016 study period. These 6-hourly IVT PR values form part of the input into the object-based AR identification algorithm (see Section 2.2.2c), while daily mean IVT PR data for

the SOM classification are the mean of the four 6-hourly IVT PR values on each day (see Section 2.2.2b).

2.2.2b Self-organizing map (SOM) classification of IVT patterns

SOMs are an unsupervised, iterative machine learning method used to reduce the dimensionality of large datasets and organize them into a two-dimensional array or "map" of characteristic "nodes" for easier interpretation [*Skific and Francis*, 2012]. The SOM classification method has become increasingly common in the atmospheric sciences due to its usefulness in linking patterns of large-scale atmospheric variability to their finer-scale local and regional effects [*Harman and Winkler*, 1991; *Hewitson and Crane*, 2002]. Several recent studies [e.g., *Cassano et al*., 2007; *Skific et al*., 2009; *Schuenemann et al*., 2009; *Schuenemann and Cassano*, 2009, 2010; *Mioduszewski et al*., 2016] have used SOMs to analyze the impacts of synoptic atmospheric variability across the Arctic and Greenland. While most of these studies characterized the synoptic circulation by applying SOM classifications to atmospheric pressure or geopotential height, a few recent studies [*Radić et al*., 2015; *Swales et al*., 2016; M16] have shown that SOMs can also be used to directly categorize IVT patterns.

We perform the SOM classification on MERRA-2 daily mean IVT PR data across the same Greenland-centered spatial domain (see Figure 2.3) and with the same 20-node configuration that M16 applied to ERA-Interim. We then subjectively place each node into non-overlapping "moist", "neutral", or "dry" groups based on the composite mean IVT PR patterns around Greenland across all days that most closely match the given node according to the SOM algorithm. We also calculate the mean daily NAO index for each node using values obtained from the Climate Prediction Center.

2.2.2c Atmospheric river (AR) identification and impacts

Our AR detection routine generally follows AR identification criteria employed by other researchers – particularly *Guan and Waliser* [2015] and *Mundhenk et al*. [2016] – in that potential ARs are classed as contiguous areas or "objects" where the overlap of absolute or "raw" IVT and IVT PR values above some minimum threshold occurs. Further requirements concerning the potential AR objects' size, location, length, shape, and location-dependent IVT transport direction (Table 2.1) are then applied to distill the dataset into a final catalog of AR events. As in previous studies, these requirements ensure that ARs are relatively long, narrow, filamentary mid- and high-latitude features that transport moisture poleward (with consideration for some high-latitude exceptions in this research – see below) and are distinct from zonally oriented tropical and subtropical moisture plumes. ARs are defined separately at each 6-hourly MERRA-2 timestep with no duration criterion for AR identification.

While we maintain the > 85th IVT PR threshold common to prior studies [e.g. *Guan and Waliser*, 2015; *Payne and Magnusdottir*, 2015; *Gao et al*., 2016; *Nayak et al*., 2016], we alter other criteria to account for potential differences in high-latitude AR characteristics compared to typical mid-latitude AR study regions. Because a few studies [*Gorodetskaya et al*., 2014; *Guan and Waliser*, 2015] have determined a relatively low IVT threshold is needed to reliably detect ARs in polar regions, we fix the minimum raw IVT value for potential AR identification at 150 kg m^{-1} s^{-1} rather than the value of 250 kg m^{-1} s^{-1} common in mid-latitude AR studies [e.g. *Rivera et al*., 2014; *Rutz et al*., 2014]. We also set a relatively short minimum AR length threshold of 1500 km and a lenient length-to-width ratio of 1.5, based on our observation that many moisture transport features affecting Greenland have a shorter length scale than lower-latitude ARs. This is especially true of some ARs that we observe approaching Greenland from the Arctic basin,

which occur almost exclusively during summer (JJA). In order to capture these events, we discard the requirement of mean poleward moisture transport for potential AR objects centered north of 70°N.

ARs were automatically detected using a python script that first ingests the required MERRA-2 data (raw IVT, IVT PR, wind) and identifies grid cells that meet the baseline raw IVT and IVT PR requirements. The algorithm then inspects the size, location, length, shape, and location-dependent IVT transport direction of contiguous grid cells that meet the baseline criteria to determine the final AR outlines (see Table 2.1). After all AR outlines are identified at each 6-hourly timestep, we overlay these AR outlines onto the raw IVT fields and remove raw IVT grid points located outside of AR outlines to quantify total AR-related moisture transport over longer time scales. The resulting metric, which we call "time integrated AR-related IVT" (AR-IVT), is calculated by multiplying the instantaneous IVT value at each grid point by the number of seconds in the 6-hourly time period extending -/+ 3 hours from the timestep (resulting in units of kg m^{-1}). Because we are specifically interested in AR-related impacts, only grid points located within an AR outline at the given 6-hourly timestep are included in the calculation. We then sum or average AR-IVT values over monthly, seasonal, and annual time periods to relate AR-related moisture transport to GrIS impacts over these longer time scales.

The glaciological and climatic characteristics of the GrIS exhibit substantial regional variability [*van As et al*., 2014; *Poinar et al*., 2015; *MacGregor et al*., 2016; *Auger et al*., 2017; *Langen et al*., 2017; *Wilton et al*., 2017], and we reiterate that the recent acceleration in mass loss has been most acute in western Greenland [*McMillan et al*., 2016]. We further hypothesize based on the results of *Liu and Barnes* [2015] and M16 that AR moisture transport is often directed into one of two favored pathways to the west or east of Greenland depending on interactions

between the North Atlantic storm track and the GrIS topography. For these reasons, we separately analyze the character and impacts of moisture transport in western and eastern Greenland regions formed by the merging of GrIS drainage basins delineated by previous studies [e.g. *Luthcke et al*., 2013; *Wilton et al*., 2017]. See Figure 2.16 for the outline of these regions, which we hereafter call WG and EG. We also separately analyze AR impacts in the ablation zone (MAR grid points classified as > 50% permanent ice with annual mean SMB < 0 averaged over the entire 1980–2016 study period) and accumulation zone (> 50% permanent ice, annual mean SMB > 0) for each region. Finally, we partition AR impacts into three intensity categories — $AR_{<85}$, AR_{85+}, and AR_{95+} —— based on the daily maximum IVT value found in the areal overlap between any AR and the given region on each day an AR is present in the region. The $AR_{<85}$ category comprises AR events of "normal" intensity (daily maximum IVT less than the 85th percentile of the region-specific distribution), while the AR_{85+} (IVT between the 85th and 95th percentiles) and AR_{95+} (IVT > 95th percentile) classes contain stronger AR impacts found in the positive tail of the intensity distribution.

To analyze the characteristic time scales of AR impacts on GrIS SMB and investigate any effects extending beyond the day of the AR event, we calculate mean anomalies of MAR snowfall, total surface meltwater production (which can run-off or refreeze afterwards in the model), and SMB for 8 days before and after the beginning of each AR event (day 0). Anomalies are defined relative to the -/+ 15-day centered mean in a similar manner to the IVT PR calculations described above. To isolate the impacts of individual AR events, only days surrounding day 0 with no AR impact of the given intensity are included in the composites. For example, if day 0 is a AR_{85+} impact day and AR_{85+} events also occur on day -6, day -4, day +3, and day +7, *only* days -3 through +2 are included in the calculation of anomalies.

In Section 2.3.3, we present composite seasonal AR-IVT anomalies before and during GrIS melt seasons categorized by mean May–September melt extent quantified by the MEaSUREs Greenland Surface Melt data. To relate seasonal AR-IVT anomalies to their immediate GrIS melt impacts and control for the long-term increasing trend in GrIS melt extent, we detrend the 1979–2015 melt time series using the nonlinear Ensemble Empirical Mode Decomposition (EEMD) method [*Chen et al*., 2016]. "High melt" and "low melt" seasons are then defined relative to this background trend (Figure 2.4).

2.3 Results

2.3.1 Trends in AR moisture transport to Greenland

AR impacts on Greenland can occur at any time during the year but are most common during summer (JJA), with this summer peak in frequency especially pronounced in northern and western Greenland (Figure 2.5). Moisture transport by ARs occurs predominantly in the lowest few km of the troposphere [*Ralph et al*., 2004; *Neiman et al*., 2008; *Backes et al*., 2015], and thus ARs are much more common along the low-elevation coastal regions of Greenland compared with the high interior GrIS (see Figure 2.5). Maps of AR frequency across SOM nodes (Figure 2.6) demonstrate the close agreement between moisture transport patterns identified by the SOM classification and the object-based AR detection algorithm (compare to Figure 2.3). They highlight two primary channels or "pathways" for poleward moisture transport by ARs near Greenland. One pathway is through Baffin Bay along the western coast of Greenland (Nodes 1 and 6 in top left corner of SOM grid), which is favored during negative NAO phases (refer to Figure 1.1 for the location of Baffin Bay and other geographic features mentioned throughout this chapter). The other pathway is through the Nordic Seas / Atlantic Arctic Gateway region to the southeast, east, and northeast of Greenland (Nodes 3, 4, 5). This pathway — along with

patterns characterized by moisture transport well to the south and east of Greenland toward northwest Europe (e.g. Nodes 15, 19, 20) — is favored during positive NAO conditions. Enhanced AR activity in the main North Atlantic storm track shifts equatorward (poleward) when the Baffin Bay / West Greenland (Atlantic Arctic Gateway / East Greenland) pathway is active. ARs impinging on Greenland from the south may also bifurcate around the high topography in the interior of the GrIS (Nodes 2 and 7), while the pattern of AR frequency anomalies for Node 16 suggests ARs occasionally approach northern Greenland from the Arctic basin.

To visualize spatial variability and trends in AR-related moisture transport toward Greenland, Figure 2.7 maps the standardized anomalies in AR-IVT accumulated during each year from 1980–2016. The maps reveal a preponderance of negative AR-IVT anomalies around Greenland prior to the late 1990s, although positive AR-IVT z-scores were present around Greenland in some years (e.g. 1981, 1995). Beginning in 1999 there was a continuous string of years with at least moderately positive anomalies prevailing around Greenland through 2008, with highly anomalous AR-IVT (exceeding +2 standard deviations) over parts of Greenland in several of these years (e.g. 2002, 2003, 2005). Positive AR-IVT anomalies were concentrated over eastern Greenland in 2002 due to exceptional non-summer AR activity in eastern Greenland (Figure 2.8), but positive anomalies were focused on western Greenland in most other years from 1999–2008. Western Greenland experienced positive AR-IVT anomalies in both summer and non-summer months (see Figures 2.8 and 2.9). After below-normal AR-IVT around Greenland in 2009, there were again positive anomalies over western Greenland from 2010–2012, with exceptionally strong (>2.5 standard deviations) and widespread AR-IVT anomalies over western Greenland during the record-breaking melt year of 2012 due to highly anomalous AR activity

during JJA. The study period ended with several years of smaller anomalies from 2013–2016, and the focus of above-normal AR-IVT shifted to northern Greenland in most of these years, particularly 2016.

The above results showing enhanced AR activity over Greenland during the GrIS mass loss acceleration of the 2000s and early 2010s are further confirmed when AR-IVT anomalies are aggregated over longer time periods (Figure 2.10). Mean annual AR-IVT during 1980–1989 was below the 1980–2016 average over virtually all of Greenland, with strong negative anomalies also present over central and northeast Canada, Baffin Bay, and the Greenland and Norwegian Seas. During the 1990s, weak to moderate positive AR-IVT anomalies occurred over southeast Greenland, along with much of the Nordic Seas and Arctic Basin, while negative anomalies prevailed over the western half of Greenland. From 2000–2009 strong positive AR-IVT anomalies dominated much of Greenland, particularly its southern half. These above-normal AR-IVT values were connected to a coherent upstream belt of positive anomalies extending across most of northern North America into Baffin Bay. Positive anomalies were focused on the western half of Greenland in JJA and covered all of Greenland in non-summer months during this period.

From 2010–2012, including the unprecedented GrIS melt seasons of 2010 and 2012, strong positive AR-IVT anomalies were located over Baffin Bay and adjacent areas of western and northern Greenland, particularly during JJA. This activity over Greenland was again contiguous with positive anomalies located upstream across northeast North America. In contrast, mostly negative anomalies occurred over the Nordic Seas, the Atlantic sector of the Arctic, and adjacent areas of the eastern Greenland coast, especially during JJA. The pattern

changed markedly from 2013–2016, as below-normal AR-IVT prevailed over most of southern Greenland and positive anomalies were found over northern and northeastern Greenland.

2.3.2 Daily-scale AR impacts on GrIS SMB

2.3.2a GrIS melt and SMB variability across SOM nodes

During the melt season (May–September), there is a clear connection between daily moisture transport patterns around Greenland and GrIS surface melt extent (Figure 2.11). Positive melt extent anomalies occur over virtually the entire GrIS on days classified into the most common "moist" SOM pattern (Node 1 – see Figure 2.6). Melt extent is also anomalously high for most of the other "moist" nodes, and the location and intensity of these anomalies varies in concert with the location of anomalous moisture transport toward the GrIS. For example, positive melt extent anomalies occur over the northeastern GrIS in association with enhanced AR frequency along the northeast coast of Greenland on days classified into Node 5, and Node 13 features anomalously frequent melt along the western and southeastern fringes of the GrIS. The spatial extent of GrIS melt is much more restricted on days with anomalously low AR frequency around Greenland (bottom and right sides of the SOM grid). Only the low-elevation margins of the GrIS experience melt on an appreciable number of these days, and melt extent is below average throughout the GrIS. An exception, however, is Node 16 where enhanced AR frequency along the northern coast of Greenland corresponds to more frequent surface melt across the northern GrIS (see Figure 2.3). On days classified into "neutral" nodes, melt frequency is generally between the "moist" and "dry" nodes.

Expanding the analysis to the overall impacts of moisture transport events on GrIS SMB, we find that the tendency of ARs to induce surface melt in summer is somewhat counterbalanced by AR-induced increases in snow accumulation as simulated by MAR. There is a well-defined

spatial structure to these positive and negative AR impacts on SMB during JJA (Figure 2.12). "Moist" SOM nodes with anomalous AR activity result simultaneously in decreased SMB in the low-elevation ablation zone (due to increased melt — see Figure 2.13) and gains in SMB in the interior accumulation zone (due to greater snow accumulation — see Figure 2.14). As with melt extent, these SMB effects are dependent on the location and intensity of moisture transport. Nodes 1 and 6 feature above-average AR frequency over Baffin Bay and the western Greenland coast, which causes the greatest low-elevation SMB losses and interior SMB gains to be located over the western GrIS. The scale of these elevation-dependent positive and negative AR impacts on SMB is not balanced, however. For example, mean SMB on JJA Node 1 days is -20.40 mmWE / day in the western Greenland (WG) ablation zone and 1.55 mmWE / day in the WG accumulation zone (Table 2.2). The highest mean SMB value in the WG accumulation zone for any node is only 2.56 mmWE / day (Node 2). In eastern Greenland (EG), JJA SMB losses in the ablation zone are most intense on days with enhanced AR activity in *western* Greenland (e.g. mean EG ablation zone SMB of -15.91 mmWE / day for Node 1). The more modest SMB gains in the EG accumulation zone are highest on days with increased AR frequency across southeast Greenland (e.g. mean EG accumulation zone SMB of 2.17 mmWE / day for Node 4 and 1.88 for Node 8). In localized areas where moisture transport interacts with the abruptly rising topography of southeast Greenland, mean SMB gains on these days exceed 10 mmWE / day. Most "neutral" and "dry" nodes are characterized by lesser but still substantial SMB losses in the ablation zones of both WG and EG (on the order of -9 to -15 mmWE / day), while mean SMB gains in the accumulation zone are generally less than 1 mmWE / day.

During non-summer months, mean SMB is almost universally positive throughout the GrIS (Figure 2.13). The effect of enhanced AR activity is to accentuate these generally modest

SMB gains, with the location of greatest snowfall (see Figure 2.14) again varying in close association with AR activity. As in JJA, there are localized areas of southeast Greenland with mean SMB greater than 10 mmWE / day for nodes with enhanced moisture transport toward this region, but mean SMB is never greater than 3.55 mmWE / day for any node when averaged over the entire ablation or accumulation zone of WG or EG (Table 2.2). There are also small areas of negative mean SMB in southwest Greenland for a few "moist" nodes, which are the imprint of occasional spring and autumn melt events triggered by strong ARs affecting western Greenland.

2.3.2b Impacts of discrete AR events on GrIS SMB

Turning to the effects of discrete AR events over western and eastern Greenland, Figure 2.16 shows that days with AR impacts on WG have higher mean SMB across the interior WG accumulation zone than non-AR days during all seasons. The magnitude of this positive impact on SMB increases with increasing AR intensity. AR_{85+} and AR_{95+} events affecting WG result in higher snowfall than $AR_{<85}$ events, and even though total melt in the WG accumulation zone also increases with increasing AR intensity during JJA, the overall effect remains an increase in SMB with increasing AR intensity during all seasons (see Figures 2.17 and 2.18, and Table 2.3). Over the EG accumulation zone, however, less SMB is gained on both JJA and non-summer days with WG AR impacts than on days with no AR present in WG. In the WG ablation zone, mean SMB again increases with increasing AR intensity during non-summer months. During JJA, however, mean total melt in the WG ablation zone increases sharply from 15.29 mmWE / day on days with no WG AR to 18.46, 25.79, and 31.89 mmWE / day on WG $AR_{<85}$, AR_{85+} and AR_{95+} days. JJA snowfall in the WG ablation zone is slightly higher on WG $AR_{<85}$ and AR_{85+} days than on non-AR days, but mean snowfall on WG AR_{95+} days is actually less than on WG $AR_{<85}$ and AR_{85+} days, likely due to an increased proportion of liquid precipitation. The overall effect is a

pronounced decrease in mean JJA SMB in the WG ablation zone from -13.10 mmWE / day on days without WG AR impacts to -14.28, -16.60, and -18.51 mmWE / day on WG $AR_{<85}$, AR_{85+} and AR_{95+} days.

Compared to WG AR events, GrIS SMB responds somewhat differently to EG ARs. As expected, ARs cause large SMB gains in the southeast GrIS accumulation zone during all seasons. However, one might also expect EG AR events to result in a substantial decrease in WG accumulation given that WG AR days feature negative SMB anomalies in EG, but this is not the case. Rather, EG AR events result in enhanced SMB over nearly the entire southern two-thirds of the GrIS during all seasons, with slight negative SMB impacts over the northern GrIS accumulation zone. Even during JJA, EG AR impacts result in increased SMB in most of the southern GrIS ablation zone, with negative mean SMB values confined to much lower elevations compared to WG AR events. This is because JJA snowfall increases substantially in both the ablation zone and accumulation zone with increasing AR intensity over EG, while increases in total melt in the ablation zone are much less than occurs with WG AR events (see Figures 2.17 and 2.18 and Table 2.3). These findings suggest that ARs affecting western Greenland tend to be more “warm” in the western Greenland ablation zone and induce greater JJA SMB losses than their eastern Greenland counterparts (see Figure 2.19).

The above results establish a clear link between AR activity and GrIS SMB on the day of AR impact. Now we examine whether AR effects on GrIS surface properties extend beyond the day of the event using the lead/lag analysis described in Section 2.2.2c. During non-summer months, the response of SMB and total melt to AR events in both the ablation zone and accumulation zone is broadly similar across western and eastern Greenland (Figure 2.20). Maximum positive SMB anomalies occur on day 0 (the day of the AR impact) and day +1 (the

day after the AR impact), with a rapid decrease to pre-AR levels by day +3 to day +4. AR_{95+} events cause the most positive SMB anomalies and AR_{85+} impacts also result in pronounced increases in SMB, while $AR_{<85}$ impacts are followed by a much more muted increase in SMB that peaks roughly a day later. There is also a notable tendency for positive SMB anomalies to peak and fall more quickly in EG than in WG, with a pronounced SMB spike on day 0 followed by a steep decrease in SMB anomalies over subsequent days. Small to moderate amounts of melt may occur in the ablation zone after non-summer AR_{85+} and AR_{95+} impacts, particularly in WG where total melt anomalies on the order of 2–4 mmWE / day occur. These modest melt anomalies after AR_{85+} and AR_{95+} events are typically outweighed by snowfall anomalies along with meltwater refreezing, resulting in mean positive SMB anomalies after AR events throughout the GrIS during the non-summer months.

The effects of summer (JJA) AR events on SMB and total melt are more complex than in other seasons, with significant differences between WG versus EG and between the ablation and accumulation zone in each region. Summer melt is possible in both the ablation zone and accumulation zone in both regions, particularly after AR_{85+} and AR_{95+} events. In the accumulation zone of both WG and EG, the relatively small anomalies in total melt are typically not enough to offset the increase in snow accumulation and refreezing of meltwater. Thus the SMB response to JJA AR events in the accumulation zone remains positive as in non-summer months, albeit with positive SMB anomalies that are slightly (1–2 mmWE / day) lesser in magnitude.

In the ablation zone of both WG and EG, JJA AR_{85+} and AR_{95+} events induce substantial total melt anomalies that are not counterbalanced by any increase in snowfall, resulting in anomalously negative SMB during the days following AR_{85+} and AR_{95+} impacts. The magnitude

and timing of this effect differs between WG and EG. In the WG ablation zone, a steady decline into negative SMB anomalies begins on day 0 as total melt sharply increases (anomalies exceed 10 mmWE / day on the date of AR_{95+} impacts). Negative SMB anomalies reach their nadir of approximately -5.53 (-3.51) mmWE around days +1–2 after WG AR_{95+} (AR_{85+}) events, and SMB remains below pre-AR levels through the end of the window (day +8) due to lingering melt anomalies. (Note that this lagged effect of ARs on melt refers only to the local production of meltwater and does not account for any delay between melt and runoff.) A qualitatively similar SMB evolution is observed in the EG ablation zone, but negative SMB anomalies are substantially less than in WG. Total melt anomalies reach their greatest magnitude of 2.50 (4.28) mmWE / day on day +1 following EG AR_{85+} (AR_{95+}) impacts and SMB anomalies reach their lowest value of -1.46 (-2.98) mmWE / day on day +2 (day +1) after EG AR_{85+} (AR_{95+}) impacts. This again indicates that ablation zone mass losses after JJA AR_{85+} and AR_{95+} events are greater in WG than in EG. These plots also show that AR_{85+} and AR_{95+} events have a much greater influence than $AR_{<85}$ events on the evolution of SMB in the ablation zone during JJA.

2.3.3 Seasonal and annual relationships between AR moisture transport and GrIS SMB

At the seasonal scale, there is a clear relationship between enhanced AR-IVT over Greenland and above-normal GrIS melt extent. Figure 2.21 shows positive AR-IVT anomalies over all of Greenland during the MAM, JJA, and SON surrounding melt seasons with anomalously high melt extent. In a similar manner to the enhanced AR-IVT values observed over Greenland during the 2000s and early 2010s (Figure 2.10), these positive anomalies during the melt season are connected to an area of above-normal AR-IVT extending across North America and the Baffin Bay / Labrador Sea region of the northwest Atlantic Ocean. Note that the melt time series used to define categories of melt seasons is detrended using the EEMD method

described in Section 2.2.2c (see Figure 2.4), so these positive AR-IVT anomalies are independent of the temporal correspondence between the recent increasing AR-IVT and GrIS melt trends. During the SON and DJF preceding above-normal melt seasons, AR-IVT tends to be below normal over Greenland, which affects the amount of winter snow pack above the low albedo zone. Lower winter accumulation results in an earlier appearance of low albedo zones and greater melt during the following summer. The opposite situation occurs for GrIS melt seasons with anomalously low melt extent, as positive AR-IVT anomalies over Greenland during the preceding SON and (to a lesser extent) DJF are replaced by negative AR-IVT anomalies over most of Greenland during MAM, JJA, and SON. Negative AR-IVT anomalies are particularly intense over southwest Greenland during JJA.

As expected given the nuances in individual AR impacts on GrIS SMB described in the previous section, annual and seasonal relationships between AR-IVT and SMB are complex and spatially variant (Figure 2.22). Note that the sign of total melt has been reversed in this figure so that increased melt represents a negative contribution to SMB.

At the annual scale, the relationship between mean AR-IVT and SMB in the WG ablation zone is negative ($r=-0.30$) but not statistically significant. Although the positive correlation between annual mean AR-IVT and snowfall ($r=0.48$) is similar to the negative correlation between AR-IVT and total melt ($r=-0.47$), the greater magnitude of annual total melt relative to snowfall in the WG ablation zone means that melt plays a greater role in determining annual SMB. The opposite is true in the WG accumulation zone, as the greater magnitude of snowfall means that the significant positive relationship ($r=0.47$) between annual mean AR-IVT and SMB is influenced more strongly by the significant positive AR-IVT – snowfall relationship ($r=0.70$) than the significant negative relationship with total melt ($r=-0.40$). The signs of these annual

mean relationships between AR-IVT and total melt / snowfall / SMB are all the same in EG as in WG, but the correlation values are universally smaller. This suggests that AR activity exerts less influence on annual SMB variability in EG compared to WG, and there is also less year-to-year variability in annual mean melt, snow, and SMB in EG.

Notably, the correlation between annual mean AR-IVT and SMB in the WG accumulation zone is considerably higher (r=0.56) if an obvious high AR-IVT, low SMB outlier is removed from the calculation. That outlier is 2012, a year with record-high amounts of both AR-IVT and total melt in the WG accumulation zone. This result shows that enhanced moisture transport by ARs generally leads to increased SMB throughout the accumulation zone of both EG and WG during all seasons, but during the exceptional melt year of 2012, unusually intense summer melt above the long-term mean equilibrium line in WG led to a negative SMB anomaly.

Similar to the daily-scale influence of ARs on SMB detailed in Figure 2.20, monthly relationships between AR-IVT and SMB in the ablation zone of both WG and EG are of the opposite sign during JJA compared to non-summer months. There is a significant negative correlation (r=-0.26) between JJA monthly mean AR-IVT and SMB in the WG ablation zone, as the negative AR-IVT – total melt relationship (r=-0.28) predominates over the virtually nonexistent variability in snowfall. In the WG accumulation zone, however, the magnitude of JJA snowfall and its positive relationship with AR-IVT (r=0.51) outweighs the significant negative correlation (r=-0.34) between AR-IVT and total melt, resulting in a significant positive monthly mean relationship between AR-IVT and SMB (r=0.31). Robust opposing relationships between AR-IVT versus total melt (r=-0.66) and snowfall (r=0.74) occur in the WG ablation zone during non-summer months, with the greater magnitude of snowfall resulting in a significant positive relationship between AR-IVT and SMB (r=0.31). This is also the case for the

WG accumulation zone, but the much greater magnitude of snowfall relative to melt in this area during non-summer months results in a strong (r=0.85) positive relationship between AR-IVT and SMB.

Like the annual mean relationships described above, monthly correlations between AR-IVT and total melt / snowfall / SMB in EG are generally of the same sign but weaker in magnitude than in WG. In the EG ablation zone during JJA, the greater magnitude of total melt compared to snowfall means that the negative relationship between AR-IVT and total melt prevails over the significant positive AR-IVT – snowfall correlation, resulting in a significant negative relationship (r=-0.25) between AR-IVT and SMB. There is essentially no correlation between AR-IVT and melt in the EG accumulation zone during JJA, leading to a significant positive relationship between AR-IVT and SMB (r=0.41) that is mostly determined by the AR-IVT – snowfall relationship (r=0.62). During non-summer months the scale of total melt and snowfall in the EG ablation zone are similar, resulting in only a moderately positive (r=0.14) relationship between AR-IVT and SMB. In the EG accumulation zone the magnitude of snowfall substantially exceeds total melt during non-summer months, resulting in a significant positive relationship (r=0.52) that is not quite as robust as the corresponding relationship in WG.

It is worth noting that our definition of the ablation and accumulation zones, based on long-term (1980–2016) mean SMB, has the effect of blending positive and negative SMB responses to AR events in areas near the equilibrium line where the sign of mean SMB may vary from year to year. If we restrict our definition of the ablation / accumulation zones to areas where mean SMB was below / above zero during *every year* in the study period, correlations between AR-IVT and SMB generally become more robust while retaining the same sign (Figure 2.23). For example, the correlation between AR-IVT and SMB in the western Greenland ablation zone

decreases from -0.30 to -0.42 for the full year and the annual correlation increases from 0.47 to 0.68 in the western Greenland accumulation zone.

2.4 Summary and Discussion

Synthesizing our analyses of recent trends in AR activity around Greenland (Section 2.3.1) and moisture transport impacts on the GrIS at daily and seasonal to annual time scales Sections 2.3.2 and 2.3.3), this study provides clear evidence of the key role played by enhanced AR activity in the recent GrIS mass loss acceleration. The extended period of above-normal frequency and intensity of AR events affecting Greenland during 2000–2012 coincided with a well-documented uptick in GrIS mass loss, culminating with the extreme melt season of 2012 which also featured highly anomalous moisture transport by ARs to western and northern Greenland. Subsequent years have seen less extreme GrIS mass loss and a shift of the greatest melt anomalies to northern areas of the GrIS [*Tedesco et al*., 2016b], as the focus of more moderately positive AR-IVT anomalies also shifted to northern Greenland. Furthermore, our investigation of the short- and long-term relationships between moisture transport events and modeled GrIS surface properties proves that this correspondence between the years of enhanced AR activity and anomalous GrIS mass loss is not a coincidence. Strong AR impacts cause increased melt in all areas of the GrIS and decreased SMB in the ablation zone during summer, and warm seasons with above-average GrIS melt extent are characterized by anomalously strong moisture transport by ARs over Greenland. ARs typically result in SMB gains in the GrIS ablation zone during non-summer seasons and in the accumulation zone during all seasons. However, the intense summer SMB losses in the ablation zone during years of enhanced moisture transport outweigh the positive AR contributions to SMB in other regions and seasons. The scaling of melt versus snowfall in Figures 2.20 and 2.22 shows that the magnitude of mass

loss from summer melt in the ablation zone has a much greater upper limit than mass gain from snowfall.

A key point to emphasize from our results is the disproportionate impact of the strongest AR events on the evolution of GrIS SMB. ARs in the highest intensity categories (AR_{85+} and AR_{95+}) exert a much greater influence on SMB than "normal" ($AR_{<85}$) ARs, both in terms of highly anomalous summer surface mass loss in the ablation zone and enhanced accumulation accompanied by limited melt increases in other regions and seasons. We find that nearly all of the most intense AR events with IVT > 1000 kg m^{-1} s^{-1} over Greenland during the 1980–2016 study period occurred since 1999. A prominent example of the outsized importance of short-lived intense AR events is provided by the extraordinary conditions observed during July 2012, when two extreme ARs resulted in the most extensive GrIS surface melt in the modern record. The lasting effects of these and other ephemeral events include the development of unusually thick buried ice layers in the GrIS percolation zone [*Nilsson et al*., 2015; *de la Peña et al*., 2015; *Steger et al*., 2017] and a substantial rise in the water table of firn aquifers in southeast Greenland [*L. S. Koenig et al*., 2014; *Miège et al*., 2016].

This study joins an existing body of research describing the synoptic atmospheric conditions associated with GrIS surface mass loss. Previous studies have detailed the roles of blocking high pressure systems [*Hanna et al*., 2013b, 2014; *McLeod and Mote*, 2016; *Mioduszewski et al*., 2016] and warm air advection by extratropical cyclones [*Mote*, 1998; *Schuenemann and Cassano*, 2009; *McLeod and Mote*, 2015] in forcing ice sheet melt. We propose that moisture transport by ARs is a complementary and interrelated mechanism affecting GrIS SMB rather than a distinct phenomenon. In most cases, ARs are understood to form as part of the process of air mass convergence and advection in the warm sector of extratropical

cyclones — according to the American Meteorological Society glossary, ARs are "typically associated with a low-level jet stream ahead of the cold front of an extratropical cyclone" [*AMS*, 2017]. Moreover, previous studies have linked both atmospheric blocking development and instances of extreme moisture transport into the Arctic to Rossby wave breaking events [*Barnes and Hartmann*, 2012; *Liu and Barnes*, 2015; *Kim et al*., 2017], suggesting that blocking and AR events may be instigated by similar atmospheric dynamics. *Liu and Barnes* [2015] showed that extreme moisture transport in the Labrador Sea / Baffin Bay region along the southwest coast of Greenland (resembling the "moist" SOM nodes and western Greenland AR events described in the present work) is favored by cyclonic Rossby wave breaking in the North Atlantic jet stream, while anticyclonic wave breaking more often results in extreme moisture transport off the eastern coast of Greenland toward Iceland and the Nordic Seas. Episodes of extreme moisture transport may actually aid in the development and reinforcement of blocking patterns through diabatic latent heat release [*Pfahl et al*., 2015; *Grams and Archambault*, 2016; *O'Reilly et al*., 2016], and thus there may be mutually reinforcing dynamical linkages between cyclonic Rossby wave breaking, extratropical cyclones, ARs, and Greenland blocking, ultimately modulating GrIS mass loss. Future research should investigate the interrelationships between ARs and these other synoptic-scale atmospheric phenomena affecting the GrIS.

A further avenue for future research is to investigate the regional- and planetary-scale atmospheric and oceanic variability modulating the characteristics of ARs and other atmospheric controls on GrIS SMB. Many recent studies [e.g. *Yoo et al*., 2014; *Baggett et al.*, 2016; *Ding et al*., 2014; *Flournoy et al*., 2016; *Gong et al*., 2017; *Jiang et al*., 2017], focusing primarily on Arctic sea ice rather than the GrIS, have detailed the role of tropical forcing in initiating Rossby wave trains that enhance poleward energy and moisture transport to the Arctic. *Ding et al*. [2014]

found indications of tropical Pacific forcing of recent negative NAO anomalies and associated warming in northeastern Canada and Greenland, but did not discuss how this forcing modulates synoptic atmospheric phenomena such as ARs, blocking, or Rossby wave breaking in the vicinity of Greenland. ARs, as corridors of enhanced moisture transport that often extend from the tropics and subtropics to high latitudes, may provide an especially useful framework for evaluating tropical-extratropical interactions. Understanding any potential connections between tropical forcing, North Atlantic and Arctic ARs, Greenland blocking, and Rossby wave breaking will be crucial in evaluating model simulations of future GrIS evolution. Future projections of blocking and Rossby wave breaking are uncertain due to the inability of models to accurately simulate the climatology of these features in the current climate [*Scaife et al*., 2011; *Davini and D'Andrea*, 2016; *Pithan et al*., 2016]. Likewise, climate models must be able to reproduce the dynamical drivers and spatiotemporal variability of ARs if their representation of future Greenland climate is to be reliable, particularly given the major impacts on the GrIS from relatively rare and short-lived extreme AR events detailed in this study. Increasing poleward moisture transport is a universal feature of theoretical and model projections of a warming climate [e.g. *Held and Soden*, 2006; *Bengtsson*, 2010; *Feldl et al.*, 2017], but the spatial patterns of this enhanced moisture transport will be constrained by (changing) atmospheric dynamics, with the precise details bearing critical implications for GrIS mass balance.

One final set of future research questions involves the physical mechanisms underpinning the AR impacts on GrIS SMB described in this study. Many recent studies [e.g. *D.-S. Park et al*., 2015; *Mortin et al*., 2016; *H. J. Lee et al*., 2017] have found that Arctic moisture intrusion events cause melt or inhibited growth of sea ice due to increased cloud cover and downward longwave radiation, especially during the cold season when there is no shortwave radiation to offset the

positive longwave cloud radiative forcing. No similar long-term study of the impacts of moisture transport events on the GrIS surface energy balance has been conducted to determine if a similar mechanism is at work, although a few case studies have highlighted the increased contribution of turbulent energy fluxes to the GrIS energy balance during AR events [*Fausto et al*., 2016a, 2016b]. Cloud influences on the GrIS are particularly uncertain, as most studies [*Bennartz et al*., 2013; *Miller et al*., 2015, 2017; *Van Tricht et al*., 2016; *Solomon et al*., 2017] have found that clouds increase energy input to the GrIS surface, while another recent analysis [*Hofer et al*., 2017] suggested that the recent GrIS mass loss has been driven by reduced summer cloud cover. Future studies should analyze how ARs affect the GrIS surface energy budget throughout a long-term record of moisture transport events and clarify the role of clouds in the GrIS energy balance during all seasons.

Table 2.1. Summary of AR identification criteria.

	Raw IVT	IVT PR	Minimum size	Location	Length	Length-to-width ratio	Zonal transport component	Meridional transport component
Criterion applied to potential AR objects	> 150 kg m^{-1} s^{-1}	> 85th %-ile	> 150 reanalysis grid points (0.5° × 0.5°)	Some part of object located poleward of 10°N	> 1500 km	> 1.5	u-wind > 2 m s^{-1} (from west) if object centroid is south of 35°N	v-wind > 0 m s^{-1} (from south) if object centroid is south of 70°N
Purpose / other notes	Relatively low threshold accounts for lesser magnitude of moisture transport in higher latitudes		First pass which reduces number of objects processed by algorithm in subsequent tests		Great circle distance between the two most distant perimeter points of object	"Effective Earth surface width" – object length divided by object Earth surface area	Filters out zonal tropical moisture plumes with east-to-west moisture transport	Ensures that ARs transport moisture poleward, but allows for high-latitude ARs approaching Greenland from Arctic

Table 2.2. Mean SMB (mmWE / day) in the ablation (abl.) and accumulation (accum.) zones of western (WG) Greenland and eastern (EG) Greenland during JJA and non-summer seasons across SOM nodes. Rows are color-coded according to node groupings described in the main text.

SOM node	*WG abl. SMB (non-summer)*	*WG accum. SMB (non-summer)*	*EG abl. SMB (non-summer)*	*EG accum. SMB (non-summer)*	*WG abl. SMB (JJA)*	*WG accum. SMB (JJA)*	*EG abl. SMB (JJA)*	*EG accum. SMB (JJA)*
1	1.48	2.45	0.42	1.07	-20.40	1.55	-15.91	-0.19
2	2.03	3.05	1.25	2.07	-16.46	2.56	-15.22	0.68
3	1.02	2.04	3.04	3.55	-14.29	1.99	-14.14	1.42
4	0.96	1.36	2.69	2.76	-11.92	1.11	-11.39	2.17
5	0.64	0.65	2.61	2.06	-12.66	0.66	-11.56	0.97
6	1.51	1.77	0.43	0.80	-16.03	2.08	-13.09	0.04
7	1.65	2.06	0.76	1.36	-14.44	2.13	-11.59	1.00
8	1.53	2.12	2.29	2.42	-13.57	1.80	-11.88	1.88
9	1.21	1.31	1.93	1.93	-11.93	1.02	-10.60	1.47
10	0.63	0.67	1.26	1.24	-11.59	0.79	-10.92	0.99
11	0.67	1.05	0.35	0.66	-15.19	0.89	-12.34	0.18
12	1.31	1.34	0.69	0.92	-15.79	0.85	-12.87	0.46
13	1.39	1.59	1.27	1.43	-14.63	1.11	-11.96	0.80
14	1.25	1.06	1.21	1.22	-13.16	0.71	-11.36	0.87
15	0.56	0.62	1.05	1.10	-10.43	0.72	-9.20	0.85
16	0.32	0.64	0.18	0.53	-14.97	0.33	-11.83	0.22
17	0.69	0.66	0.46	0.58	-12.83	0.61	-10.26	0.27
18	1.25	1.12	0.59	0.76	-12.41	1.05	-10.36	0.49
19	0.80	0.66	0.47	0.56	-14.73	0.59	-11.38	0.29
20	0.53	0.50	0.64	0.73	-9.96	0.48	-8.88	0.46

Table 2.3. Mean JJA snow, melt, and SMB (mmWE / day) across AR impact categories in the ablation (abl.) and accumulation (accum.) zones of western (WG) and eastern (EG) Greenland.

	No AR	***AR$_{<85}$***	***AR$_{85+}$***	***AR$_{95+}$***
WG abl. snowfall	0.88	1.24	1.36	1.19
WG abl. melt	15.29	18.46	25.79	31.89
WG abl. SMB	-13.10	-14.28	-16.60	-18.51
WG accum. snowfall	1.03	1.73	2.95	3.16
WG accum. melt	1.66	2.06	3.26	5.03
WG accum. SMB	0.56	1.29	2.91	3.51
EG abl. snowfall	0.48	0.85	1.02	1.05
EG abl. melt	14.12	15.38	16.09	18.17
EG abl. SMB	-11.63	-12.18	-11.45	-12.60
EG accum. snowfall	0.74	1.38	2.28	3.19
EG accum. melt	1.55	1.57	1.70	2.01
EG accum. SMB	0.31	0.97	2.07	3.08

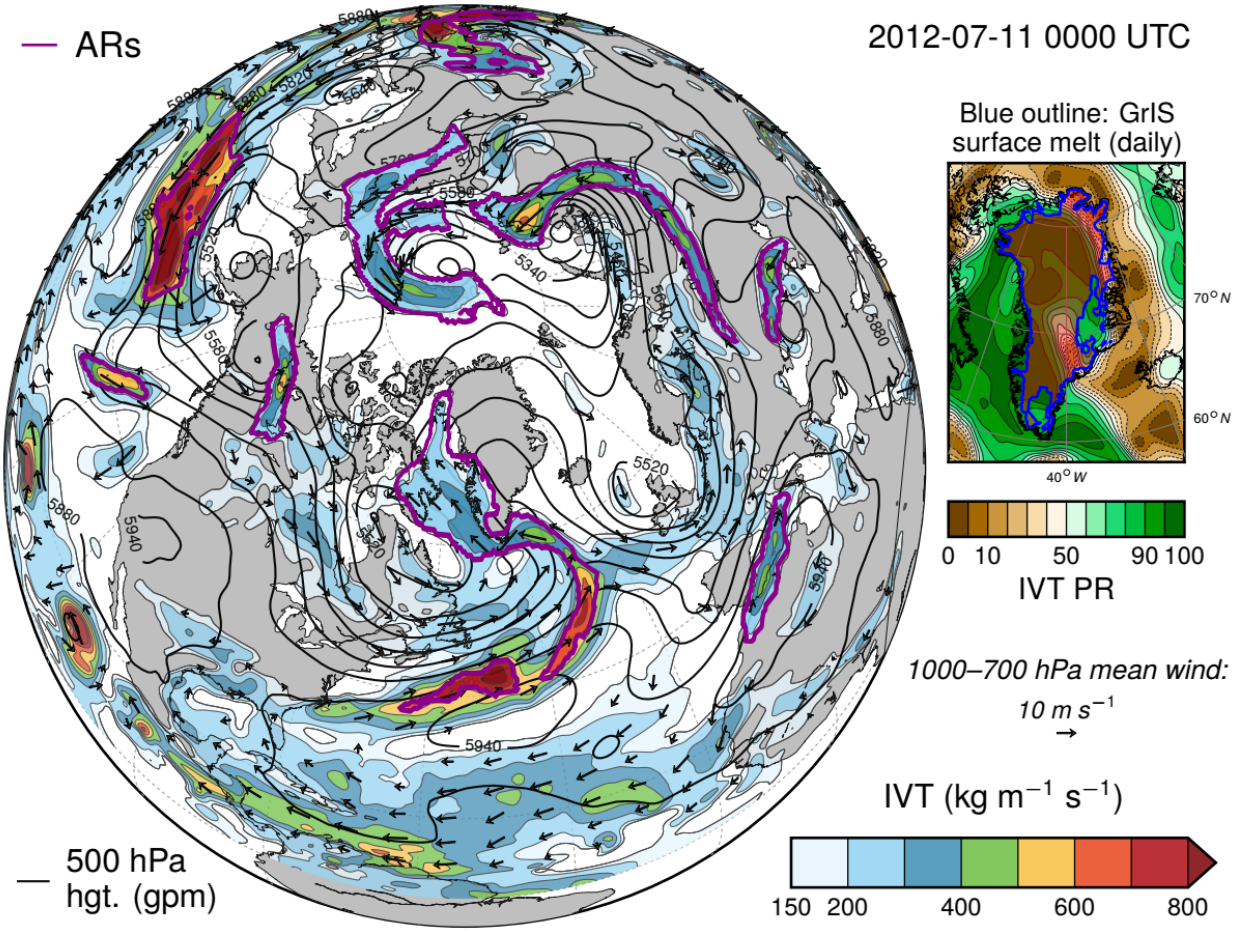

Figure 2.1. Example of ARs detected using MERRA-2 data at 0000 UTC 10 July 2012. Purple outlines identify features classified as ARs based on the criteria outlined in Table 1.

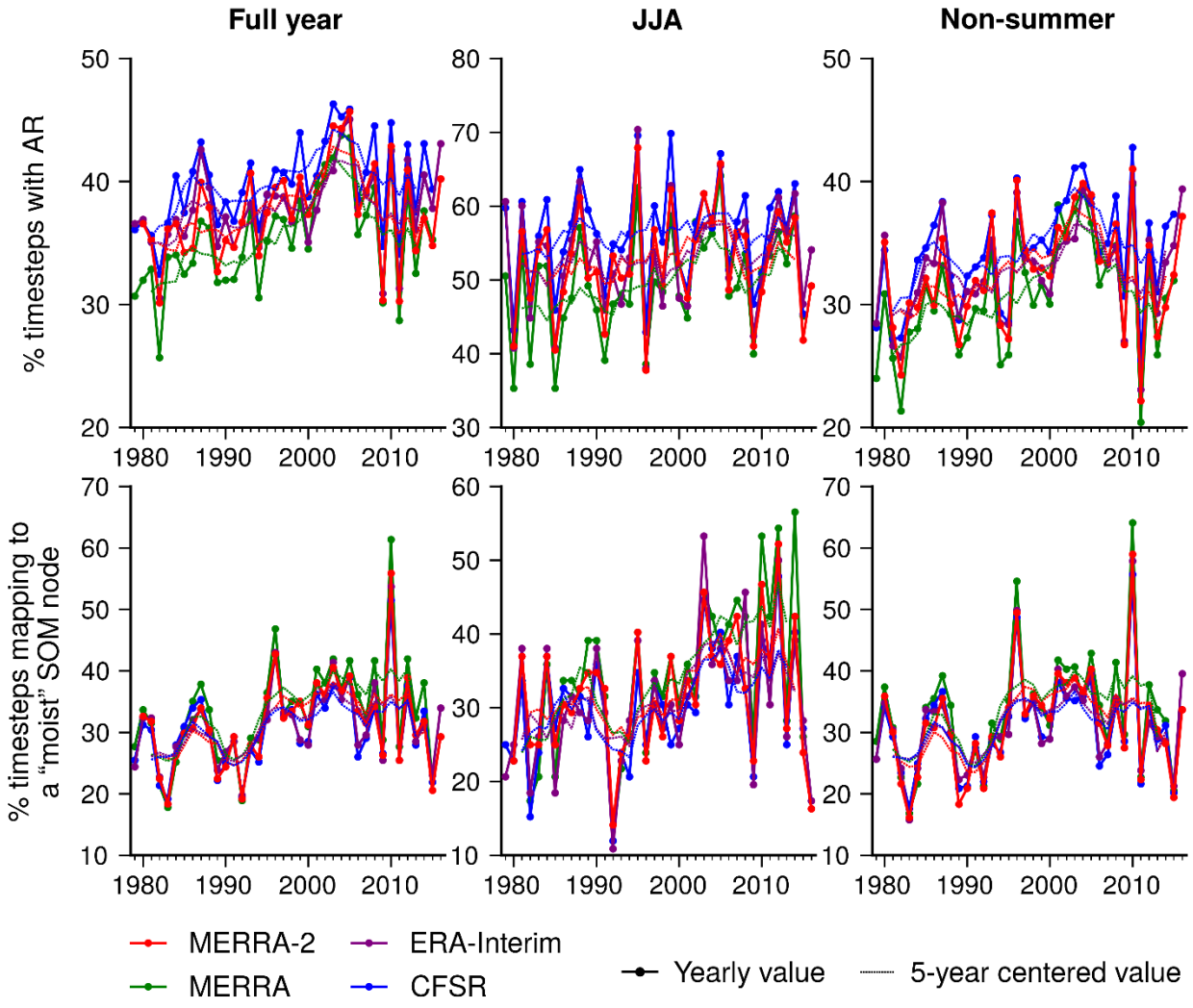

Figure 2.2. Top row: Time series of Greenland AR impact frequency (defined as the percentage of 6-hourly reanalysis timesteps with an AR present over Greenland) during the full year, JJA, and non-summer months for each of the four reanalysis datasets employed in this study (MERRA-2, MERRA, ERA-Interim, CFSR). Bottom row: Time series of the percentage of days during all seasons classified into the "moist" SOM node group by each reanalysis during the full year, JJA, and non-summer months.

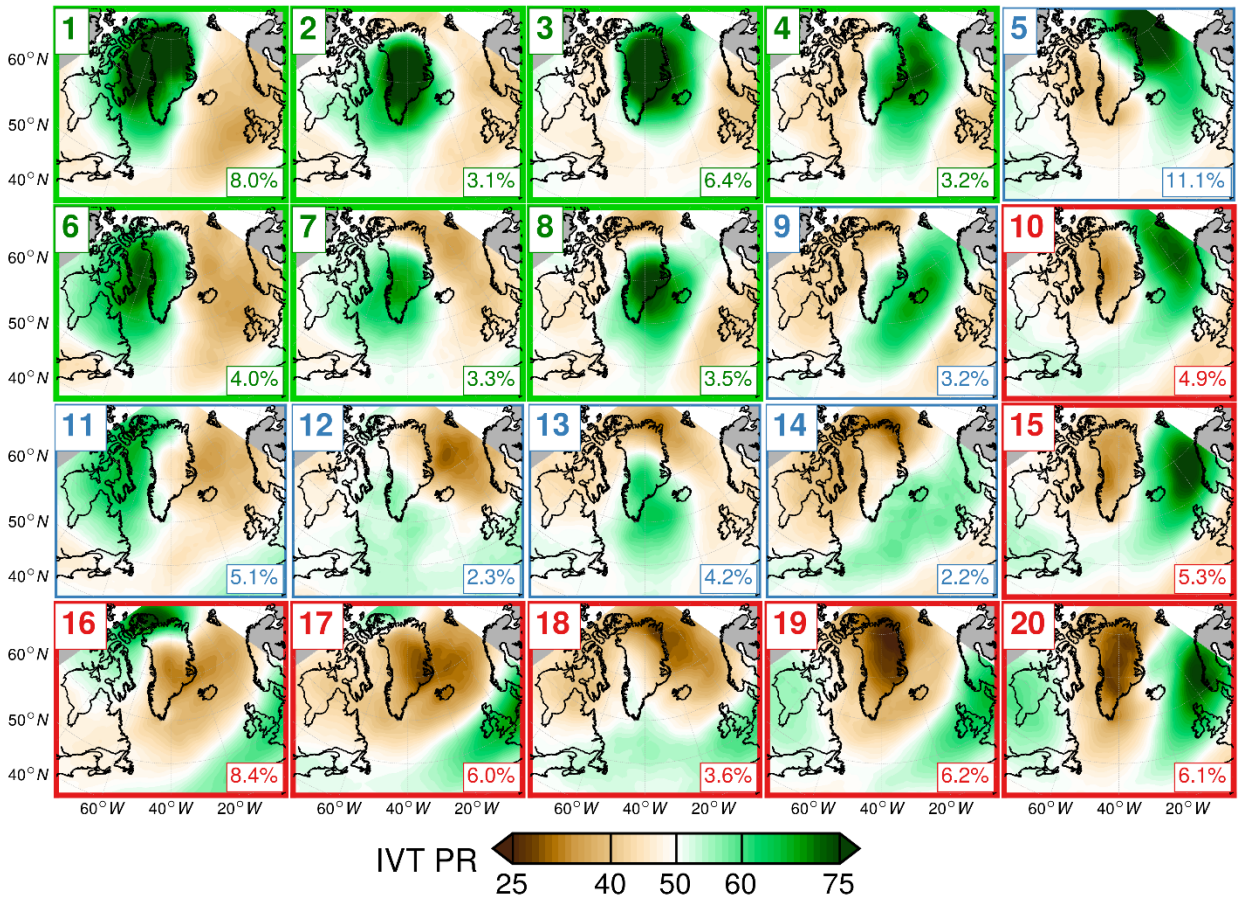

Figure 2.3. Composite daily mean IVT PR across all days (during all seasons) classified as best matching each node by the MERRA-2 SOM. The borders of each map denote the group into which each node was subjectively placed according to the AR frequency pattern near Greenland: "moist" (green border), "neutral" (blue border), or "dry" (red border). Each panel is also annotated with the percentage of the days in the study period with IVT PR patterns that were classified as most closely matching that node.

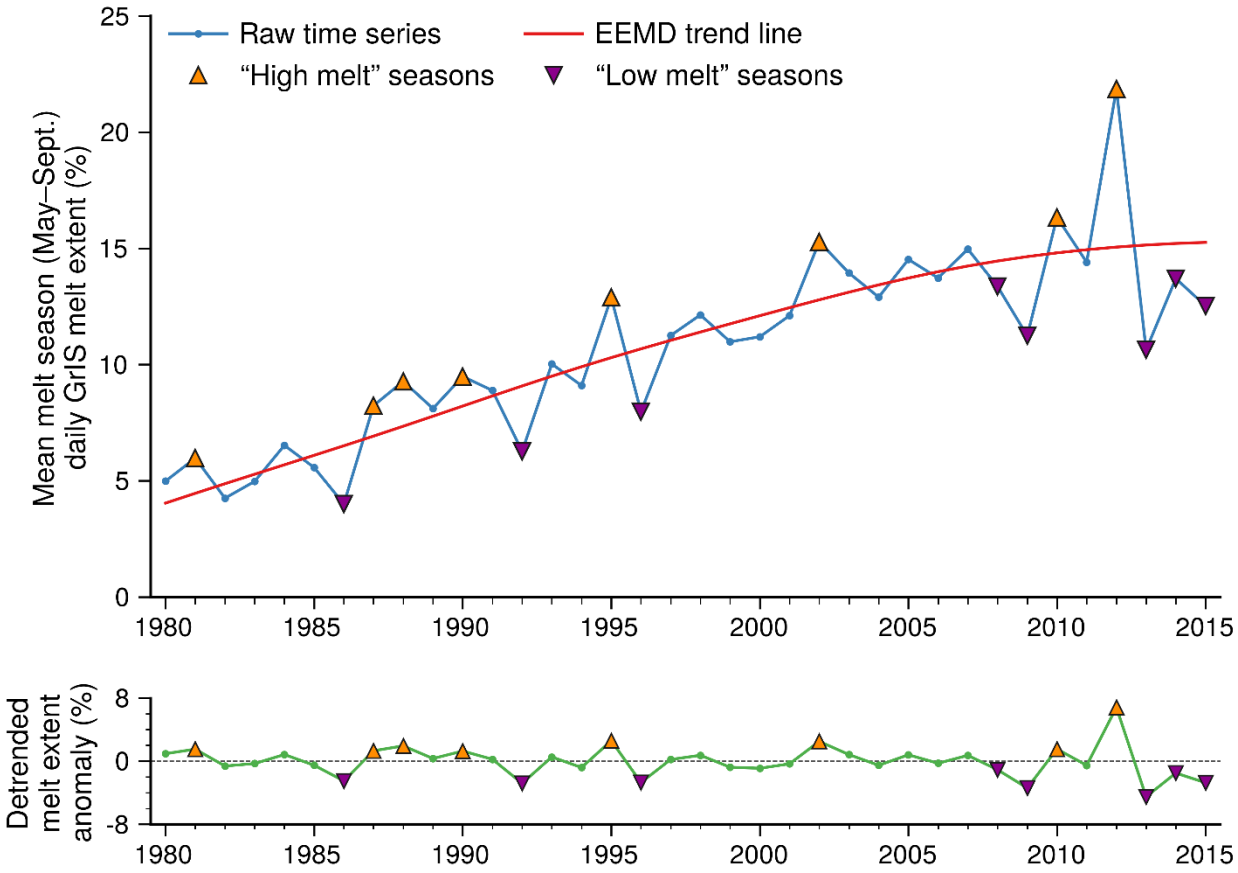

Figure 2.4. Time series of mean GrIS melt extent during the May–September melt season (blue line), along with nonlinear trend line fit using EEMD method (red line) and yearly detrended mean melt extent anomalies (green line).

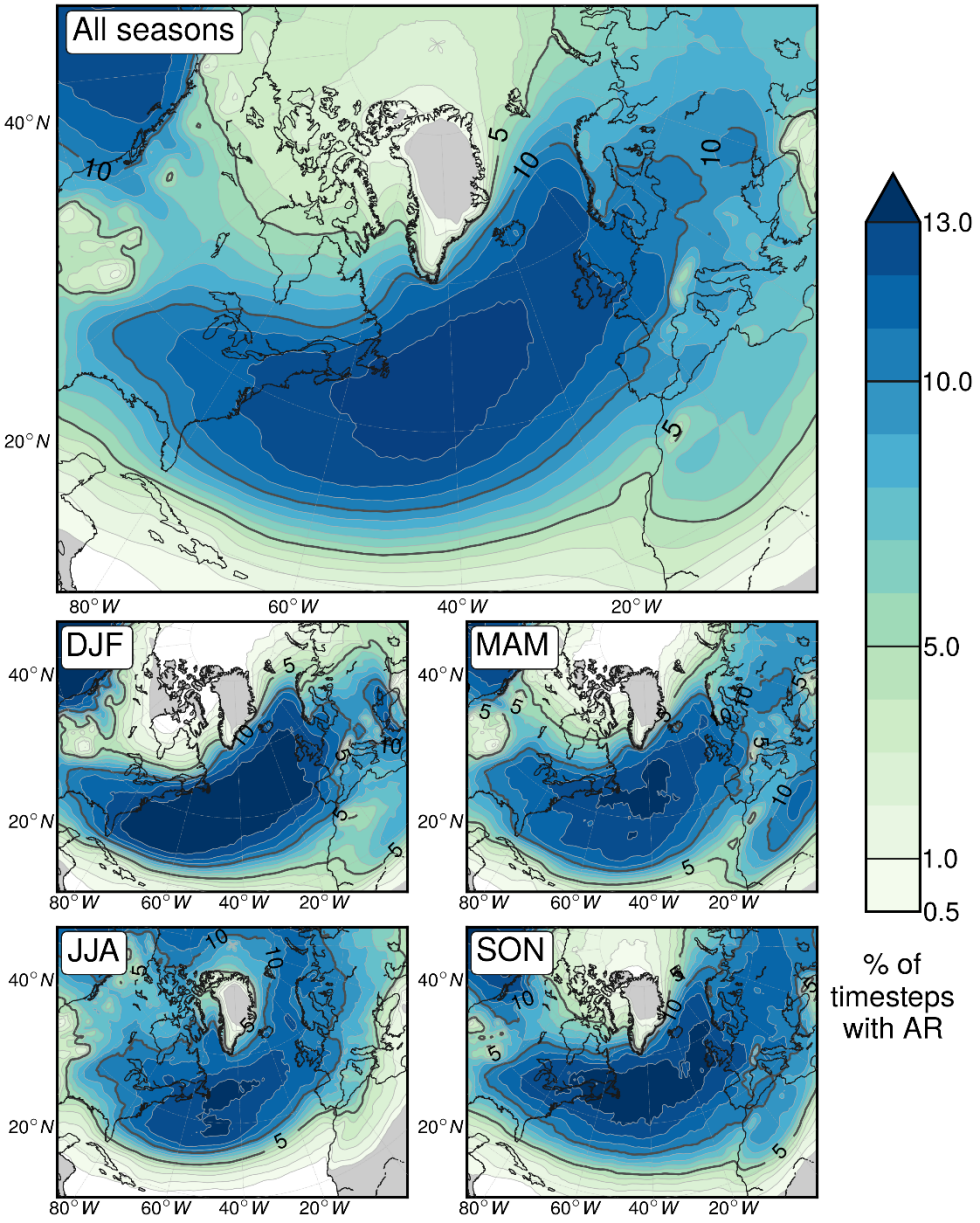

Figure 2.5. Climatological (1980–2016) AR frequency (defined as the percentage of 6-hourly reanalysis timesteps with an AR present over the given reanalysis grid cell) over the North Atlantic / Arctic region during all seasons (top) and each individual season (bottom panels).

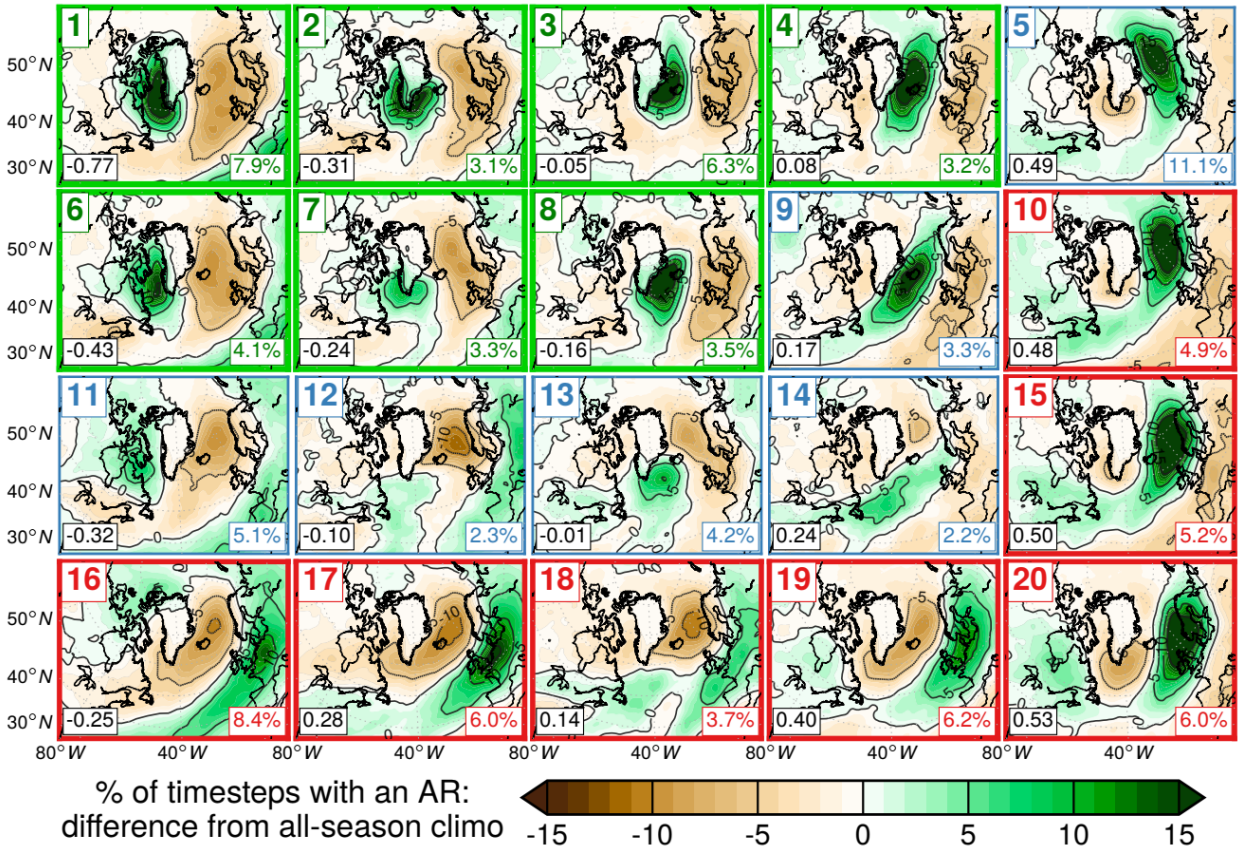

Figure 2.6. All-season AR frequency anomalies mapped across each SOM node. Anomalies are calculated as the percentage of 6-hourly reanalysis timesteps with an AR present on days classified into the given SOM node, minus the climatological percentage. The colored borders of each panel denote node groupings: "moist" (green), "neutral" (blue), or "dry" (red). Each panel is also annotated with the percentage of the days in the study period with IVT PR patterns matching the given node (bottom right) and the mean NAO index for that node (bottom left).

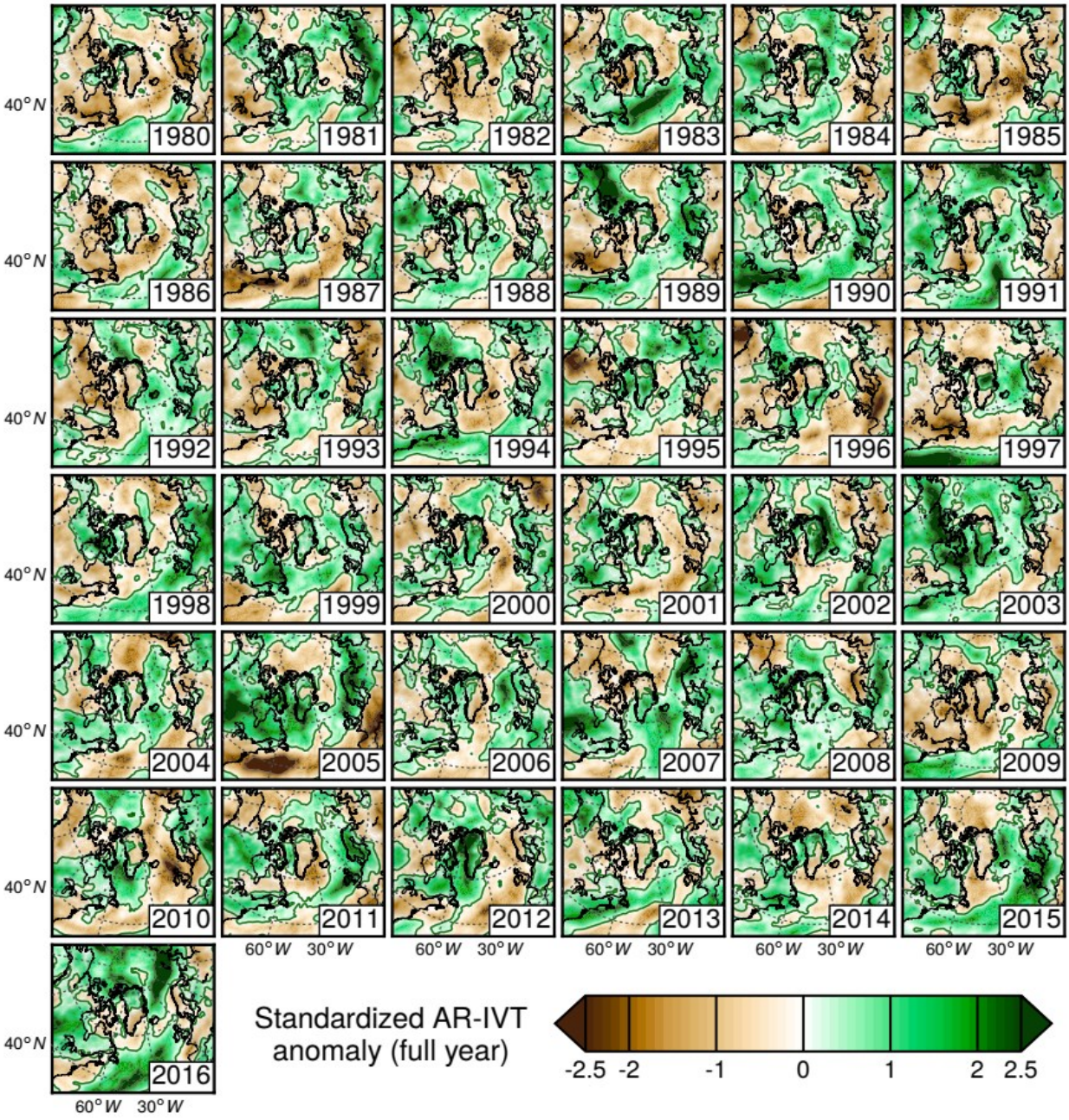

Figure 2.7. Standardized anomaly of time integrated AR-related IVT (AR-IVT; see text) for each full year during the 1980–2016 study period.

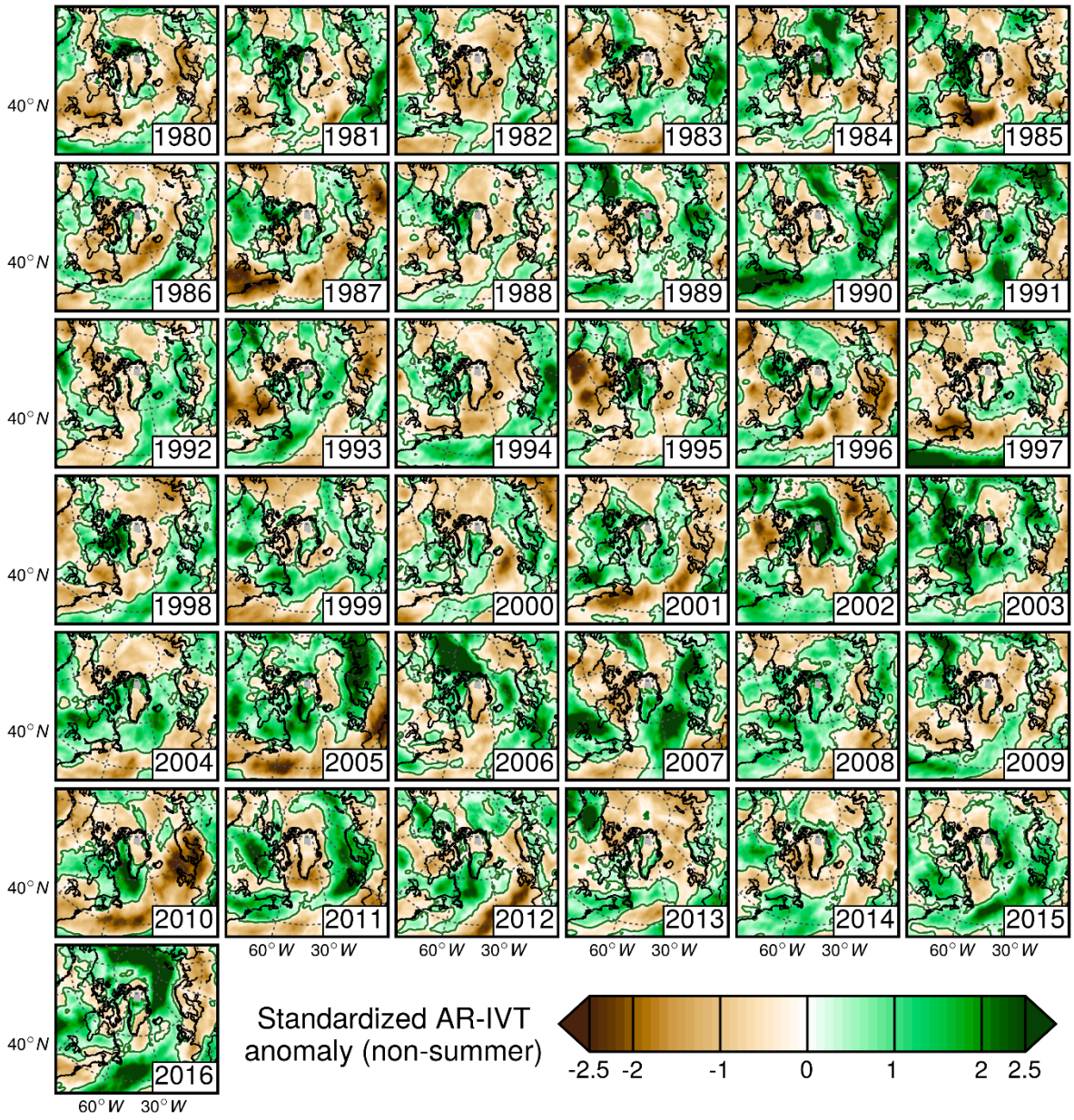

Figure 2.8. Standardized anomaly of time integrated AR-related IVT (AR-IVT; see text) accumulated during the non-summer months of each year of the 1980–2016 study period.

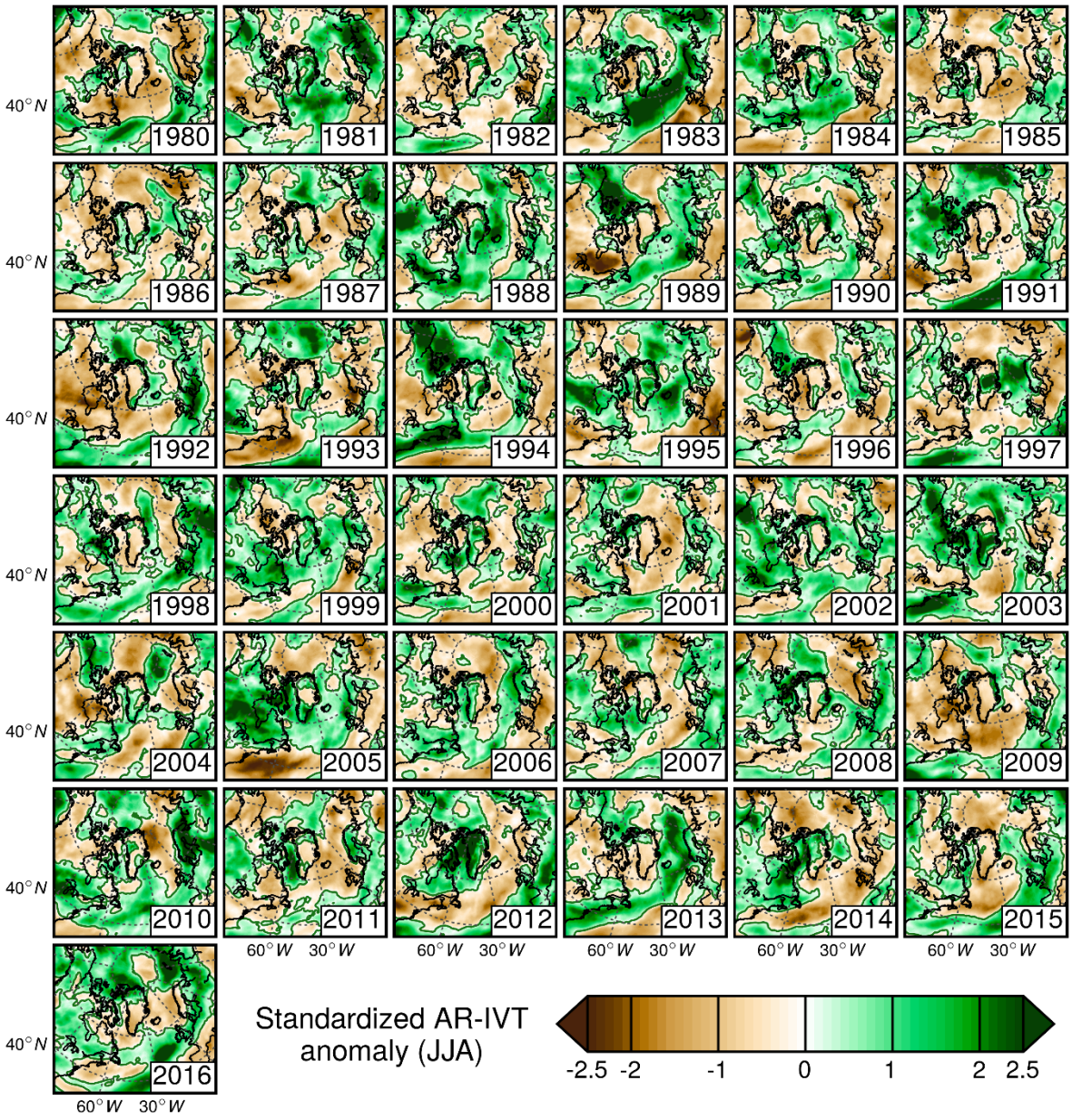

Figure 2.9. Standardized anomaly of time integrated AR-related IVT (AR-IVT; see text) accumulated during each *JJA* of the 1980–2016 study period.

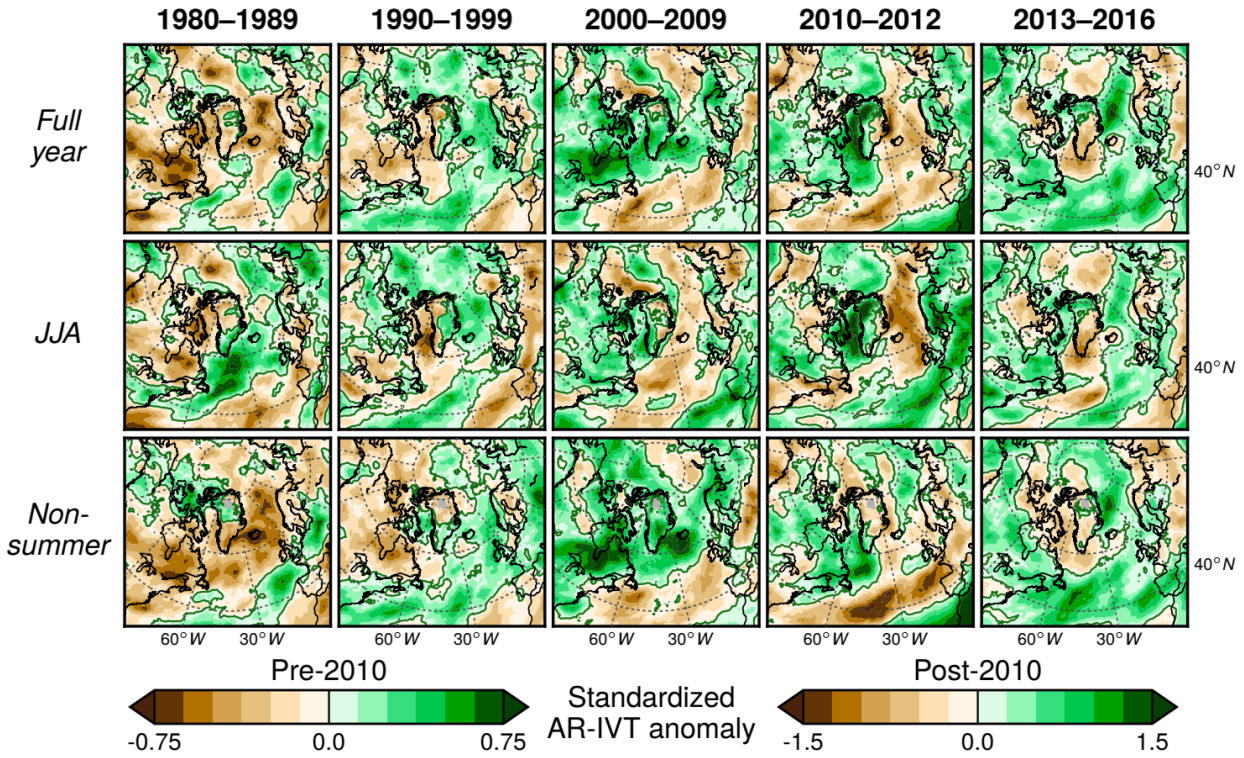

Figure 2.10. Standardized AR-IVT anomalies during full year, JJA, and non-summer months for decadal and other time periods: 1980–89, 1990–99, 2000–09, 2010–12, and 2013–16.

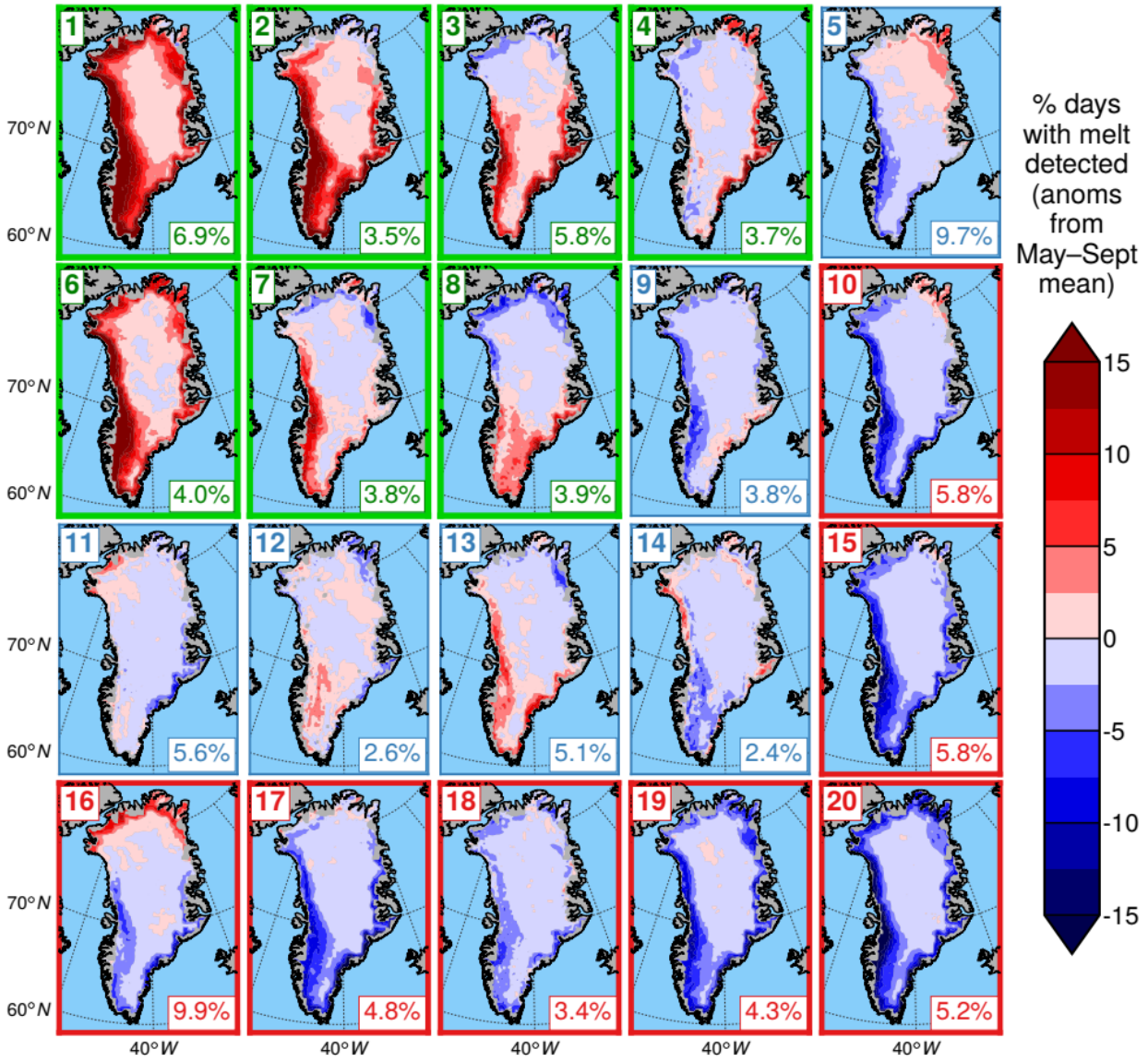

Figure 2.11. Anomalies in the percentage of *melt season* (May – Sept.) days with surface melt detected for each SOM node (relative to mean May – Sept. melt day frequency). Each panel is annotated with the percentage of melt season days classified into each node and colored according to node group.

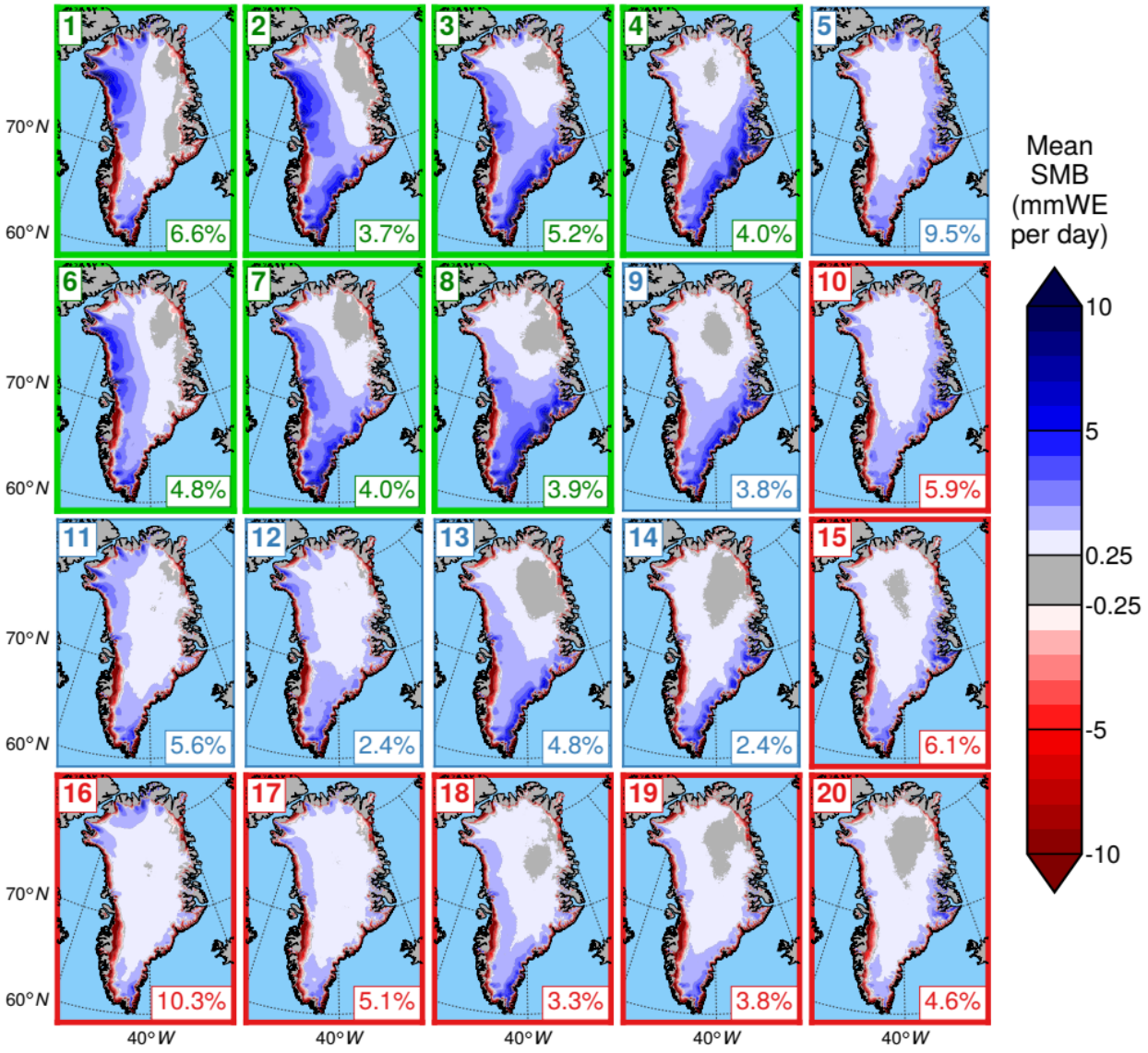

Figure 2.12. Mean daily SMB (mmWE / day) for each SOM node during *JJA*. Note that SMB is only mapped for grid cells with > 50% permanent ice cover.

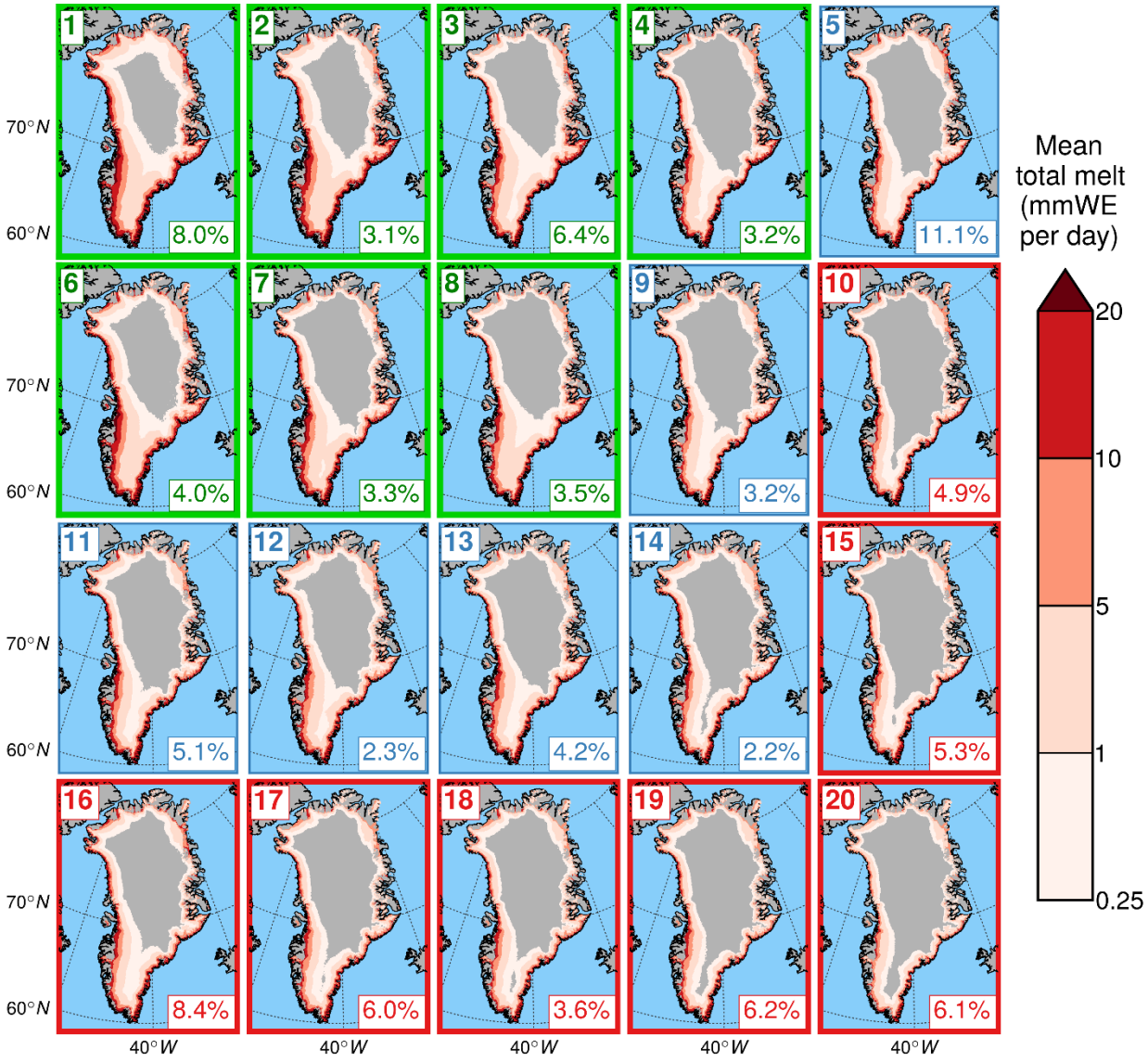

Figure 2.13. Mean daily total melt (mmWE / day) during the *melt season (May – Sept.*) for each SOM node. Note that total melt is only mapped for grid cells classified by MAR as having > 50% permanent ice.

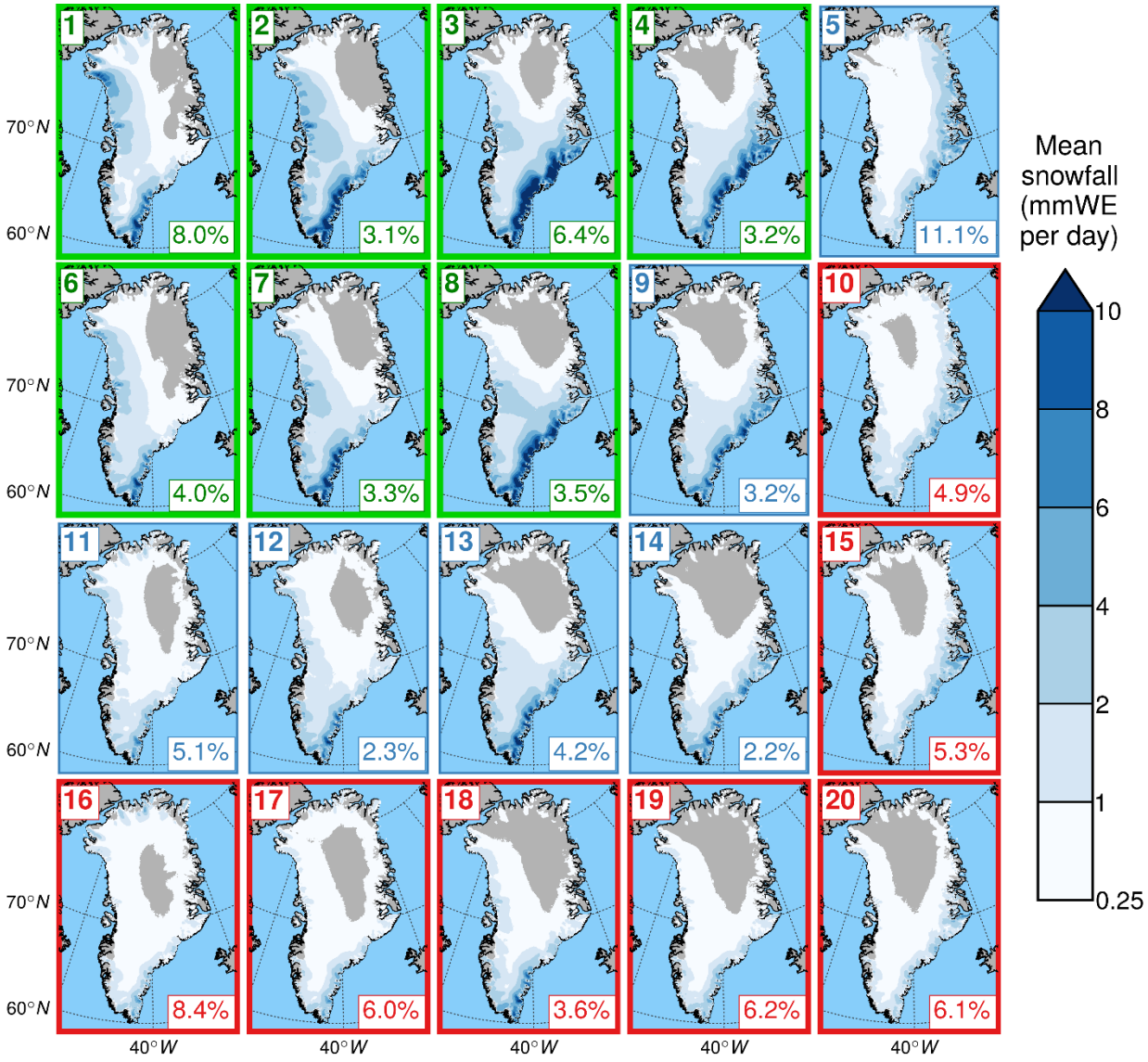

Figure 2.14. Mean daily snowfall (mmWE / day) during *all months* for each SOM node. Note that snowfall is only mapped for grid cells classified by MAR as having > 50% permanent ice.

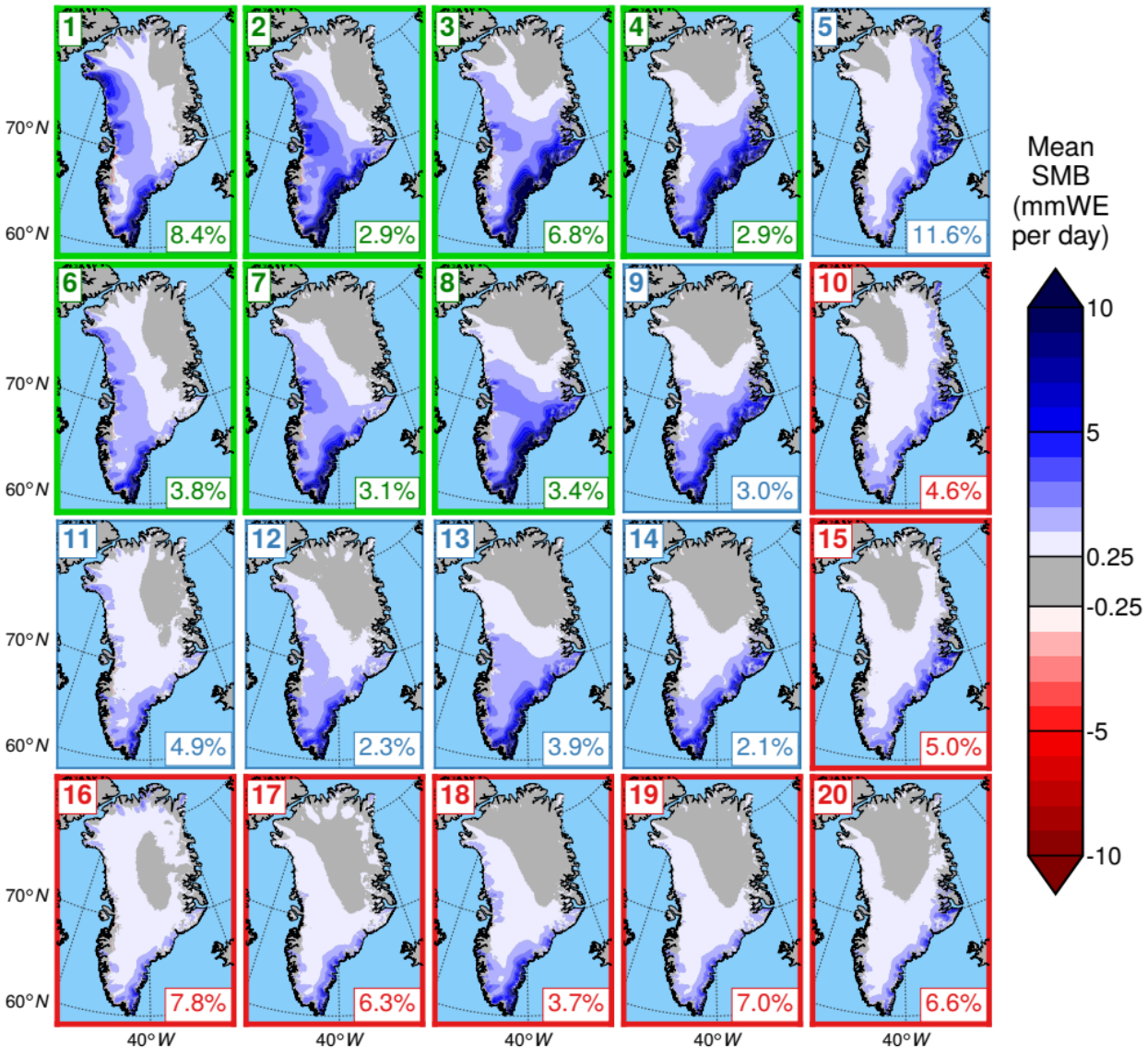

Figure 2.15. As in Figure 2.12 but for *non-summer months*.

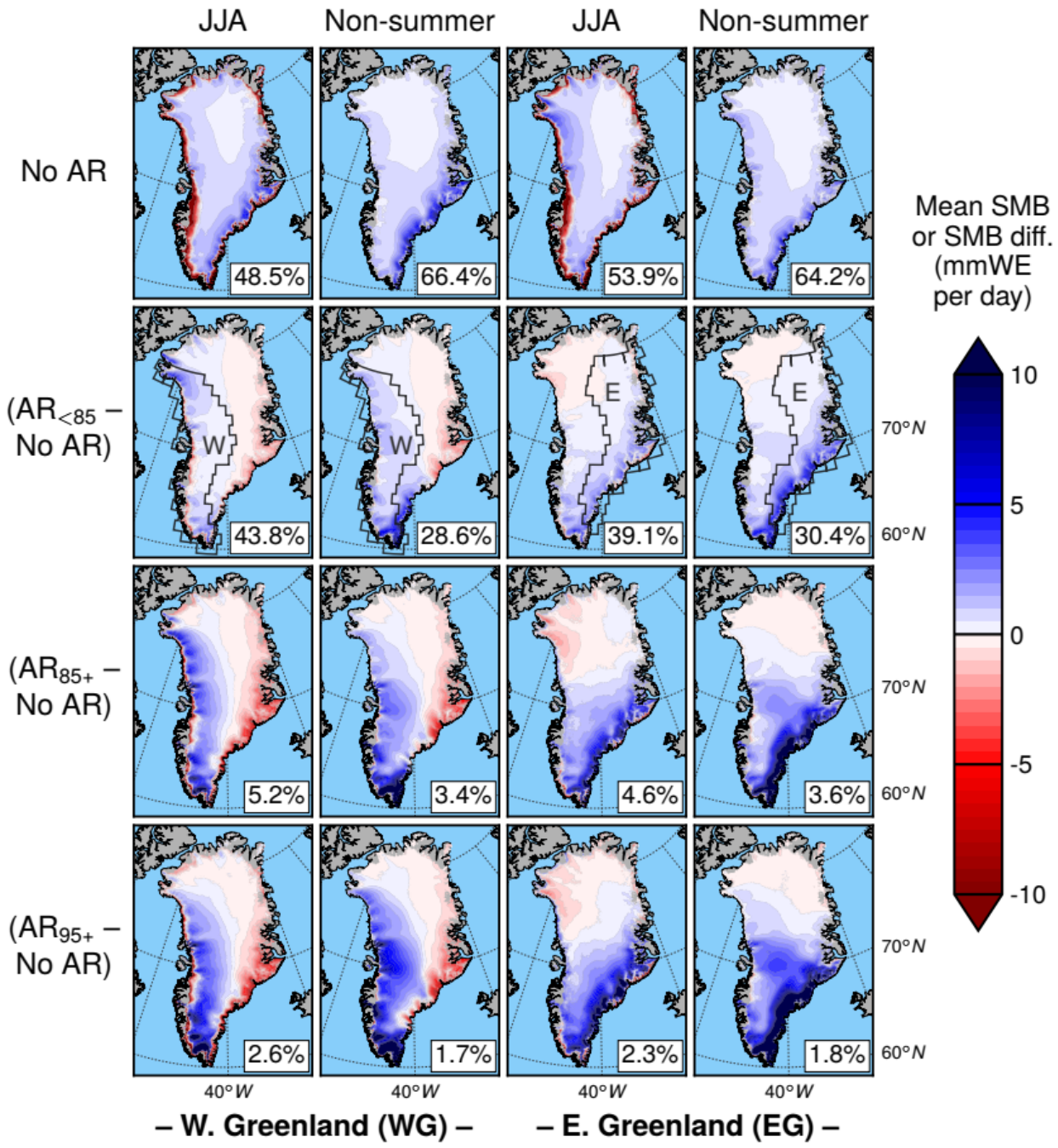

Figure 2.16. Top row: Mean SMB (mmWE / day) on days with no AR impact in western (WG) and eastern (EG) Greenland during JJA compared to non-summer months. Bottom three rows: Mean SMB difference between days with no AR impact and days with AR events of varying intensity: $AR_{<85}$ (second row), AR_{85+} (third row), AR_{95+} (bottom row). Borders of the WG and EG regions are outlined on maps in the second row.

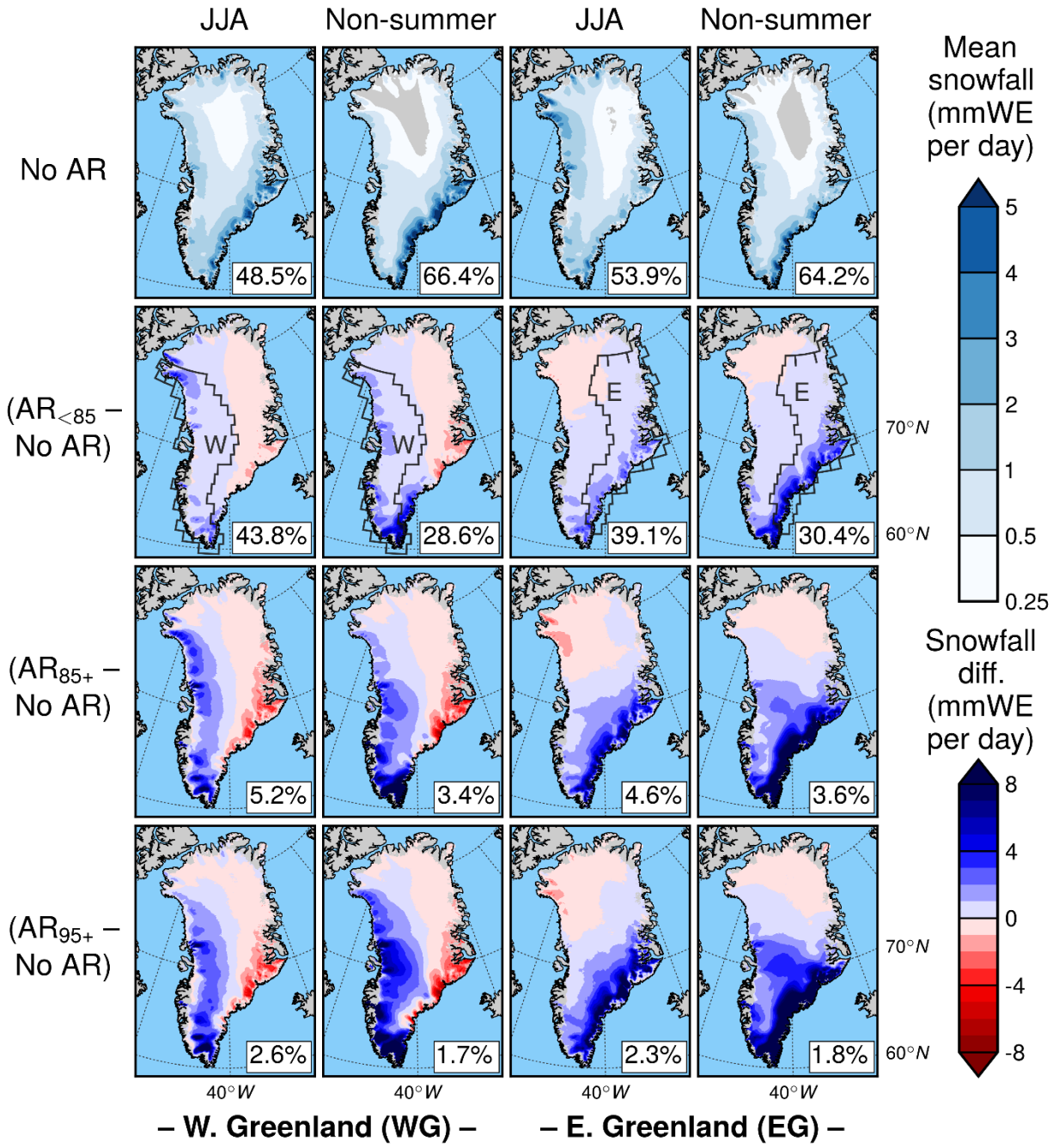

Figure 2.17. Top row: Mean daily snowfall (mmWE / day) on days with no AR impact in WG and EG during JJA compared to non-summer months. Bottom three rows: Mean snowfall difference between days with no AR impact and days with AR events of varying intensity: $AR_{<85}$ (second row), AR_{85+} (third row), AR_{95+} (bottom row). Borders of the WG and EG regions are outlined on maps in the second row.

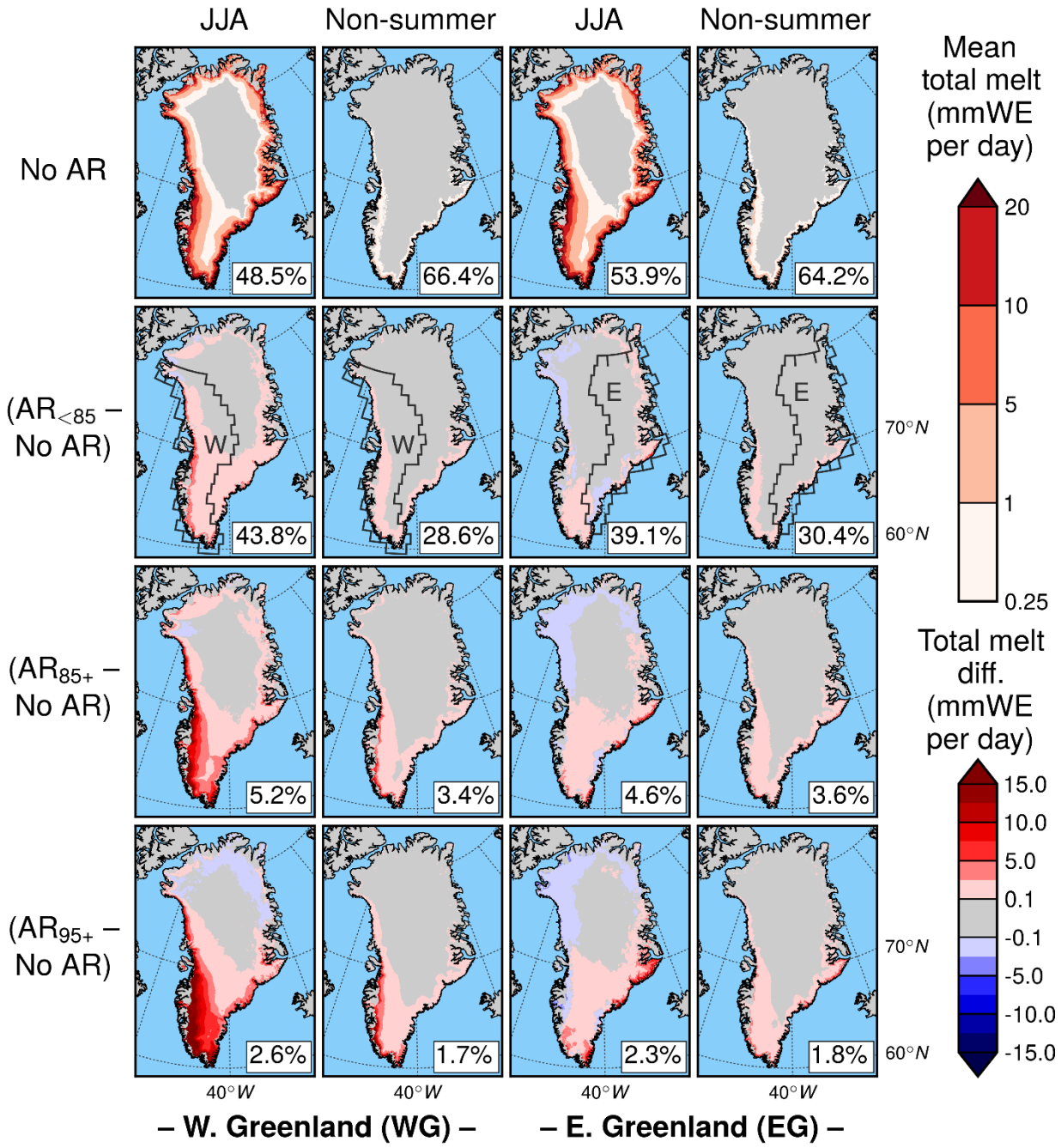

Figure 2.18. Top row: Mean daily total melt (mmWE / day) on days with no AR impact in WG and EG during JJA compared to non-summer months. Bottom three rows: Mean total melt difference between days with no AR impact and days with AR events of varying intensity: $AR_{<85}$ (second row), AR_{85+} (third row), AR_{95+} (bottom row). Borders of the WG and EG regions are outlined on maps in the second row.

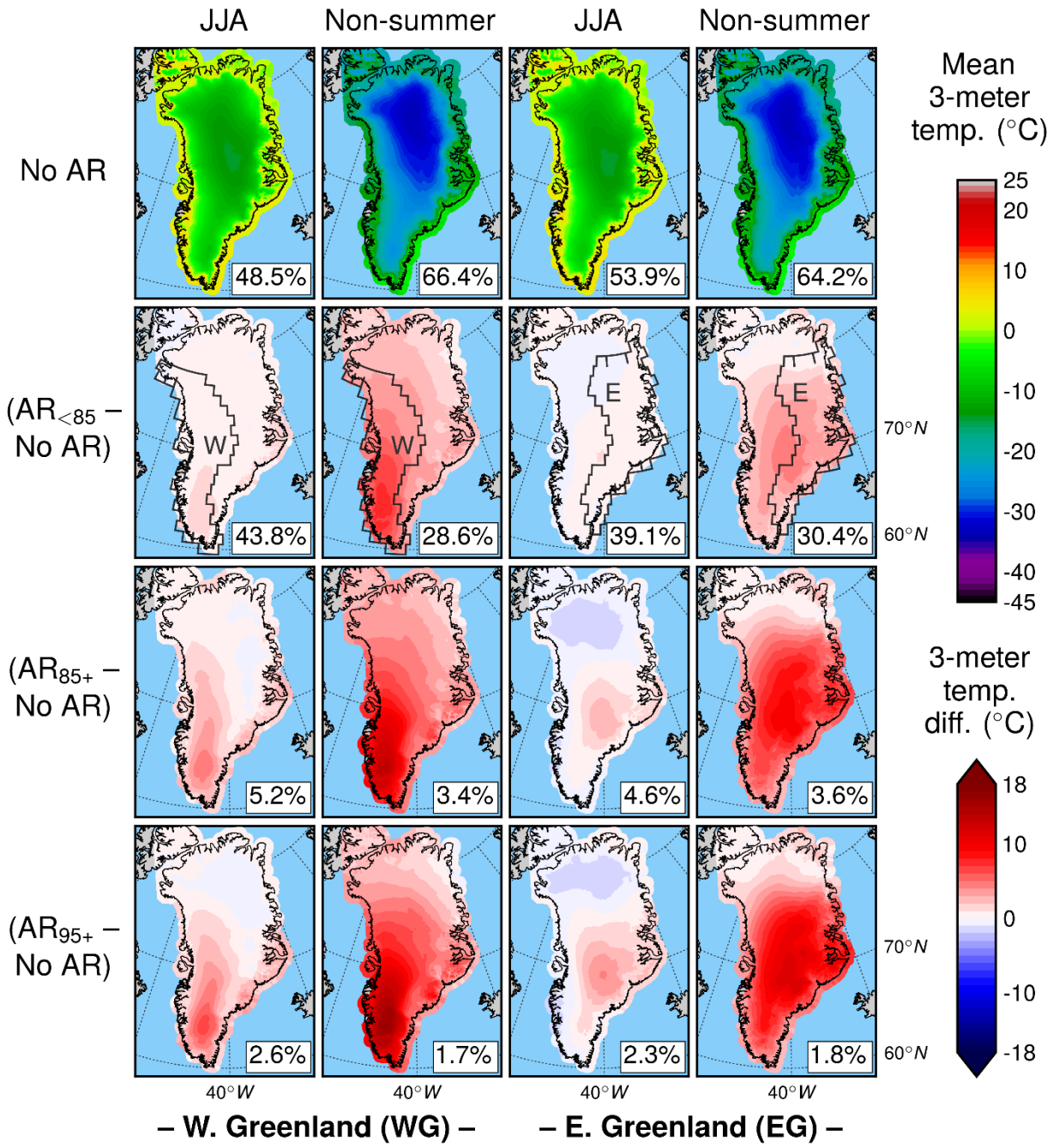

Figure 2.19. Top row: Mean 3-m temperature (°C) on days with no AR impact in WG and EG during JJA compared to non-summer months. Bottom three rows: Mean 3-m temperature difference between days with no AR impact and days with AR events of varying intensity: $AR_{<85}$ (second row), AR_{85+} (third row), AR_{95+} (bottom row). Borders of the WG and EG regions are outlined on maps in the second row.

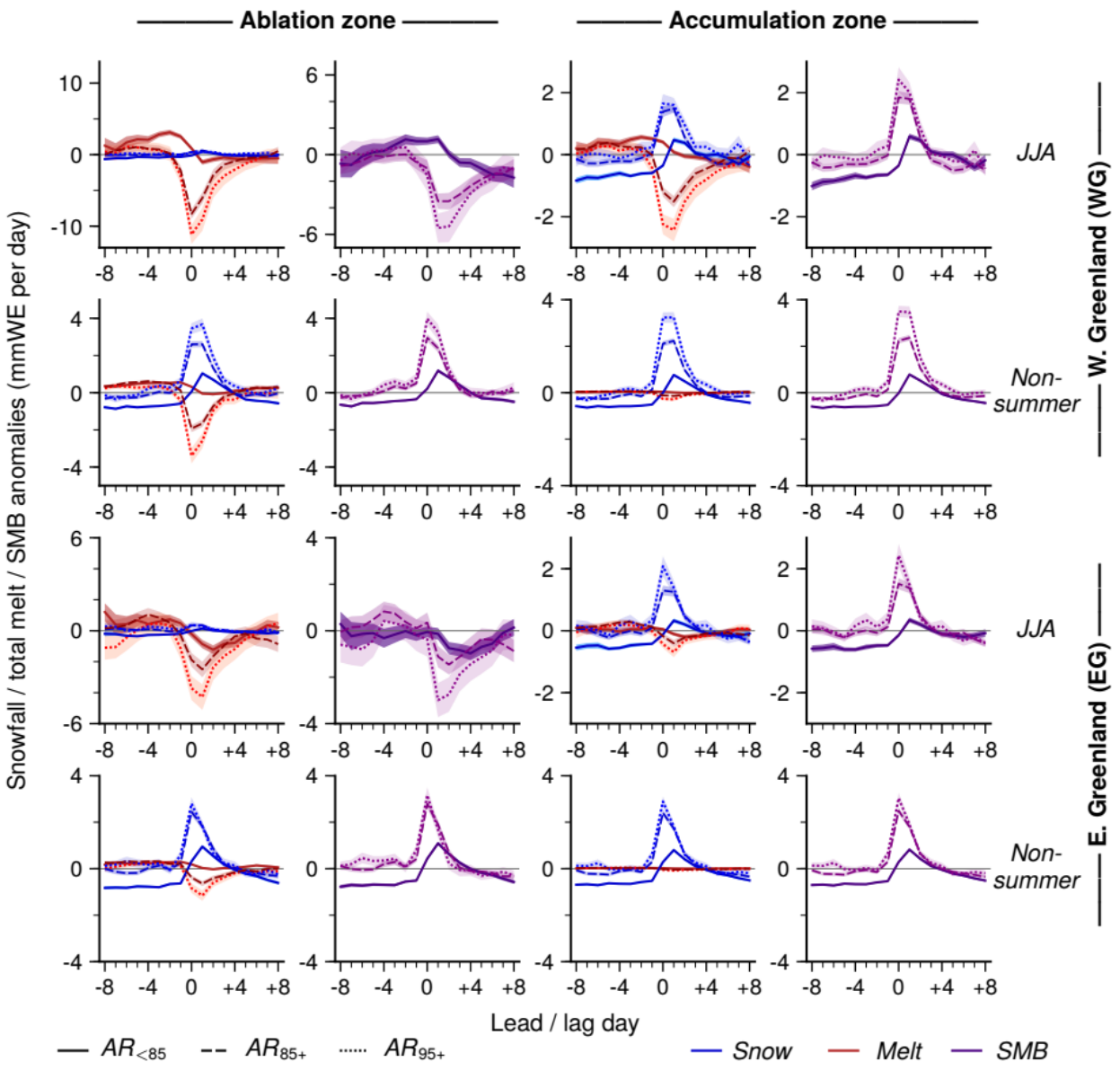

Figure 2.20. Composite anomalies of mean snowfall, total melt, and SMB (mmWE / day) in WG (top two rows) and EG (bottom two rows) for periods of -/+ 8 days surrounding the date of $AR_{<85}$, AR_{85+}, and AR_{95+} events during JJA (top row for each region) and non-summer months (bottom row for each region). For each region, separate plots are shown for the ablation zone (left columns) and the accumulation zone (right columns). Shaded areas around each line indicate the standard error of the mean anomalies.

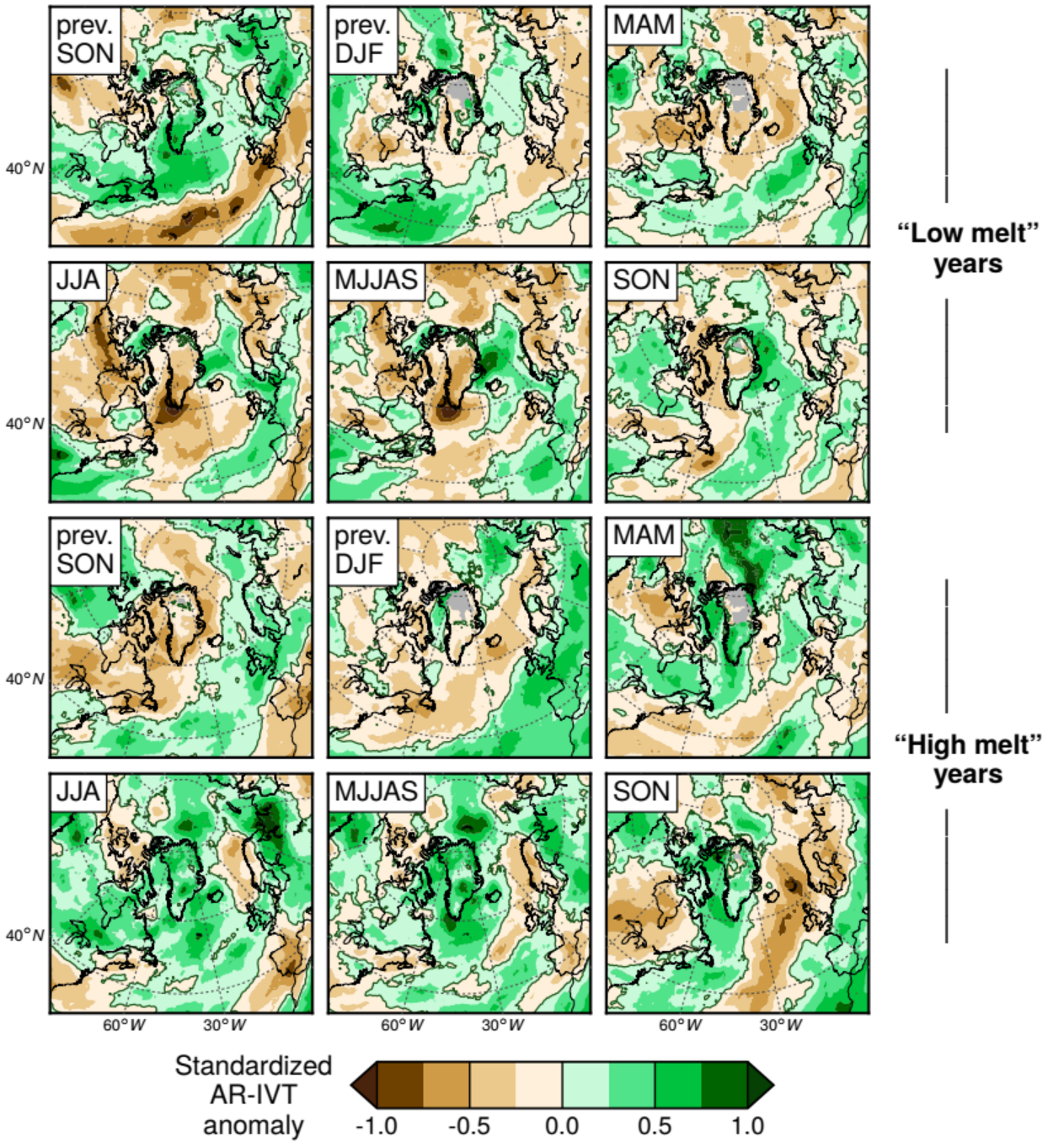

Figure 2.21. Standardized anomalies of seasonally-accumulated AR-IVT for seasons preceding and contemporaneous with below-normal GrIS melt seasons (top) and above-normal GrIS melt seasons (bottom).

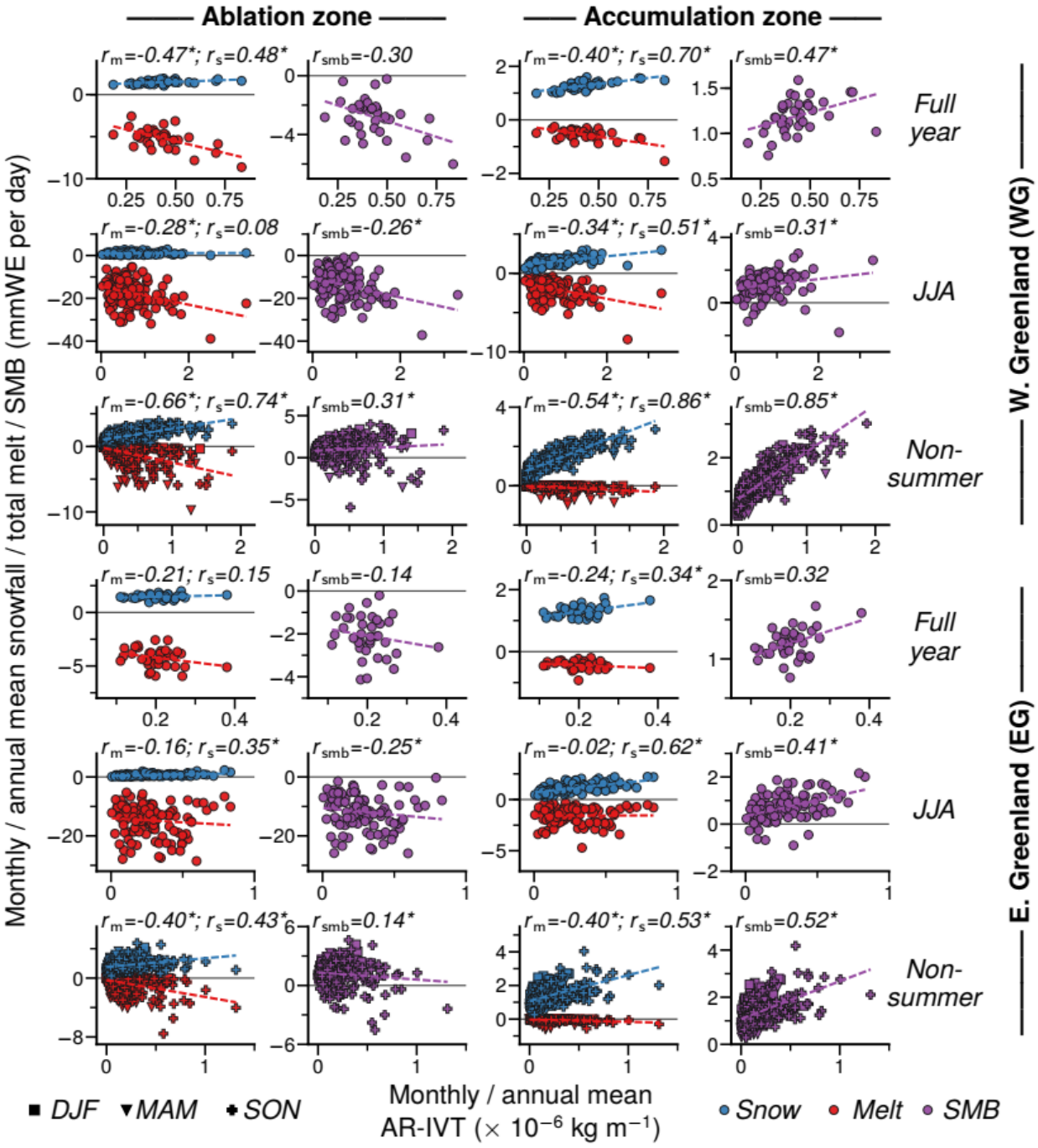

Figure 2.22. Scatter plot of mean snowfall, total melt, and SMB vs mean AR-IVT for WG (top three rows) and EG (bottom three rows) during the full year (top row for each region), JJA (middle row for each region), and non-summer months (bottom row for each region). For each region, separate plots are shown for the ablation zone (left columns) and the accumulation zone (right columns). Variables are averaged at the monthly scale for JJA and non-summer plots and at the annual scale for full year plots. The sign of total melt has been reversed so that increased melt represents a negative contribution to SMB. Correlations labeled with an asterisk are statistically significant at the 95% confidence level.

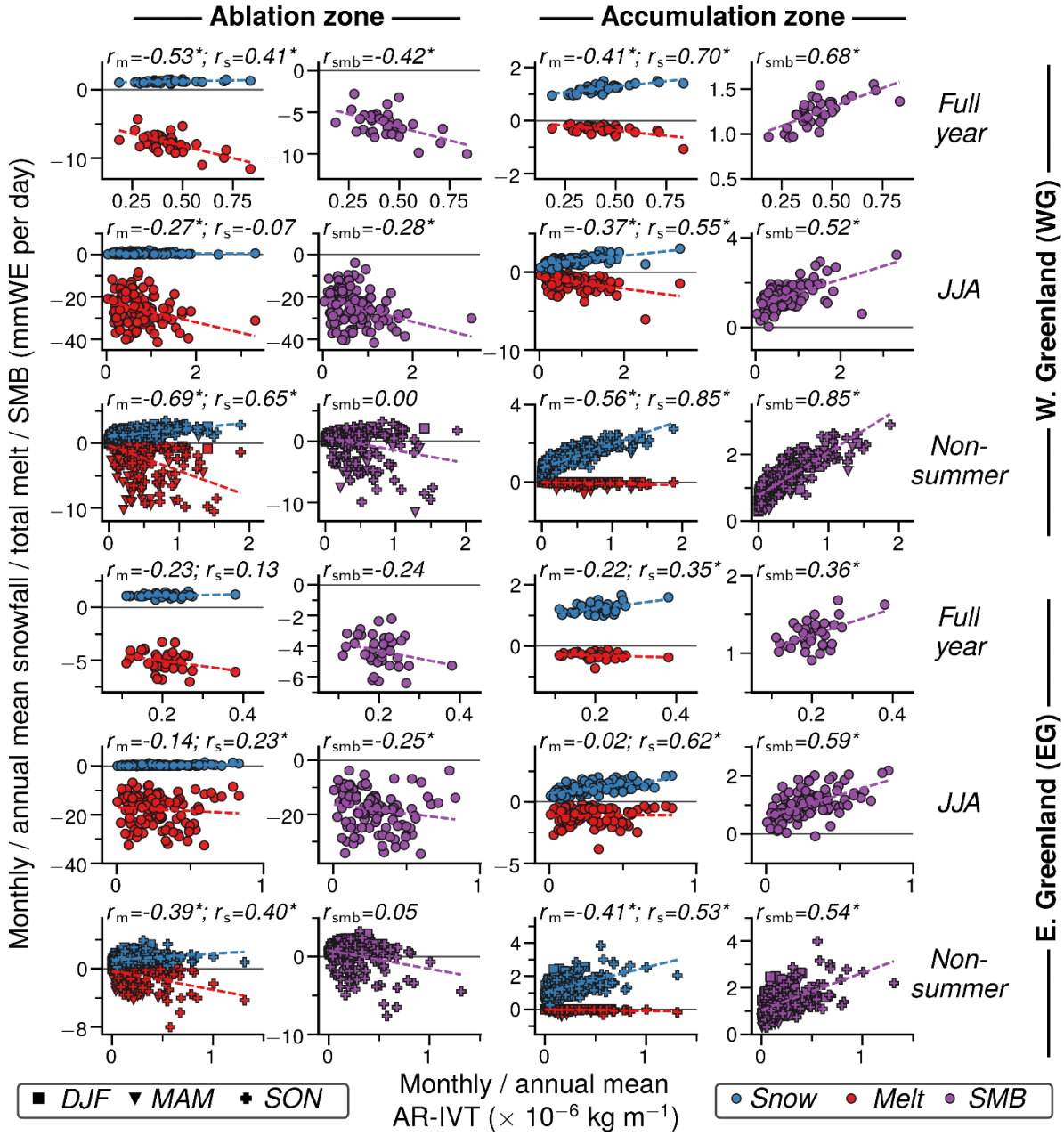

Figure 2.23. Scatter plot of mean snowfall, total melt, and SMB vs mean AR-IVT for WG (top three rows) and EG (bottom three rows) during the full year (top row for each region), JJA (middle row for each region), and non-summer months (bottom row for each region). For each region, separate plots are shown for the ablation zone (left columns) and the accumulation zone (right columns). Note that the ablation zone and accumulation zone are defined as areas with annual mean SMB < 0 and annual mean SMB > 0, respectively, *during every year* in the 1980–2016 study period (unlike in Figure 2.22 where these zones are defined by mean SMB averaged across all years). Variables are averaged at the monthly scale for JJA and non-summer plots and at the annual scale for full year plots. The sign of total melt has been reversed so that increased melt represents a negative contribution to SMB. Correlations labeled with an asterisk are statistically significant at the 95% confidence level.

CHAPTER 3

STRONG SUMMER ATMOSPHERIC RIVERS TRIGGER GREENLAND ICE SHEET MELT THROUGH SPATIALLY VARYING SURFACE ENERGY BALANCE AND CLOUD REGIMES[2]

[2] Mattingly, K. S., T. L. Mote, and X. Fettweis (2019), Strong summer atmospheric rivers trigger Greenland Ice Sheet melt through spatially varying surface energy balance and cloud regimes. To be submitted to *Journal of Climate*.

Abstract

Mass loss from the Greenland Ice Sheet (GrIS) has accelerated over the past two decades, coincident with increasing moisture transport over Greenland by atmospheric rivers (ARs). Summer ARs affecting western Greenland trigger intense GrIS melt events, but the physical mechanisms through which ARs induce melt are not well understood. This study elucidates the coupled surface-atmosphere processes by which ARs force GrIS melt through analysis of the surface energy balance (SEB), cloud properties, and local- to synoptic-scale atmospheric conditions during strong summer AR events affecting western Greenland. ARs are first identified in integrated water vapor transport (IVT) fields from MERRA-2 reanalysis and classified according to IVT intensity. SEB, cloud, and atmospheric data from regional climate model, observational, reanalysis, and satellite-based datasets are then used to analyze the sources of melt energy during strong, > 90th percentile "AR$_{90+}$" events. In the vicinity of AR landfall, AR$_{90+}$ days feature increased cloud cover that reduces net shortwave radiation and increases net longwave radiation. As these oppositely-signed radiative anomalies tend to cancel, melt energy in the ablation zone is primarily provided by turbulent heat fluxes, driven by enhanced barrier winds that are in turn generated by a strong synoptic pressure gradient combined with an enhanced local temperature contrast between cool over-ice air and anomalously warm surrounding atmosphere. During northwest Greenland AR$_{90+}$ events, anomalous melt is forced remotely in eastern Greenland through a physically distinct downsloping regime, with clear skies and enhanced katabatic winds that entrain adiabatically warmed air from above the boundary layer.

3.1 Introduction

The Greenland Ice Sheet has experienced substantial mass loss during the past two decades, resulting in an increased contribution to global mean sea level rise [*Bamber et al*., 2018]. This mass loss exhibits a large degree of interannual variability and was especially pronounced during a period of accelerating mass loss from roughly 2000–2012 [*Van den Broeke et al*., 2016]. In recent years, the GrIS has continued losing ice mass but at a reduced rate [*Bevis et al*., 2019; *Mouginot et al*., 2019]. The GrIS loses mass through solid ice discharge and through negative surface mass balance (SMB), when surface ablation exceeds snow accumulation and meltwater refreezing. SMB losses were responsible for a greater proportion of total mass loss than ice dynamical processes during the recent GrIS mass loss acceleration [*Enderlin et al*., 2014; *Van den Broeke et al*., 2017], and model projections indicate that SMB will play the dominant role in future GrIS mass losses [*Calov et al*., 2018; *Rückamp et al*., 2018].

GrIS surface melt is driven by energy exchanges at the interface between the ice / snow surface and the atmosphere, and is therefore highly sensitive to atmospheric conditions. A number of atmospheric and coupled ocean-atmospheric phenomena, operating across a broad spectrum of spatiotemporal scales, have been found to influence GrIS SMB variability. These include slow-moving anticyclones known as "Greenland blocks" [*McLeod and Mote*, 2016; *Ahlstrøm et al*., 2017; *Hanna et al*., 2018a] and extratropical cyclones [*McLeod and Mote*, 2015; *Berdahl et al*., 2018], whose occurrence has been linked to the state of the North Atlantic Oscillation (NAO) [*Fettweis et al*., 2013b; *Delhasse et al*., 2018] and the Atlantic Multidecadal Oscillation (AMO) [*Rajewicz and Marshall*, 2014; *Auger et al*., 2017].

Another recurring feature of the synoptic-scale atmospheric circulation that has been shown to influence GrIS SMB variability is the organization of intense water vapor transport into

narrow corridors known as atmospheric rivers (ARs). ARs are responsible for a large proportion of total poleward moisture transport, and episodes of extreme moisture transport affecting Greenland are frequently associated with cyclonic Rossby wave breaking over the North Atlantic during the negative phase of the NAO [*Newman et al*., 2012; *Liu and Barnes*, 2015]. A particularly intense AR affected western Greenland during the extreme melt event of mid-July 2012, when nearly the entire ice sheet experienced surface melt for the first time in over a century [*Nghiem et al*., 2012; *Neff et al*., 2014; *Bonne et al*., 2015].

Mattingly et al. [2018] (hereafter M18) analyzed the influence of ARs on GrIS SMB during 1980–2016, finding that strong AR events produce intense melt in the low-elevation ablation zone during summer and that ARs affecting western Greenland are responsible for the largest SMB losses. ARs typically provide positive contributions to SMB outside the summer season through enhanced snow accumulation, but SMB losses during strong summer ARs greatly exceed SMB gains generated by the strongest non-summer ARs. Recent trends in AR-related moisture transport to western Greenland align with GrIS SMB trends, as enhanced AR activity during ~2000–2012 has been followed by more moderate moisture transport by ARs to Greenland in subsequent years [*Oltmanns et al*., 2019; *Mattingly et al*. 2016; M18]. Climate models project increased moisture transport to the high-latitude Northern Hemisphere under future emissions scenarios [*Lavers et al*., 2015; *Singh et al*., 2017], underscoring the importance of understanding interactions between ARs and the ice sheet surface.

Although the influence of ARs on warm season GrIS melt events has been established, the physical mechanisms through which ARs and other features of the synoptic-scale atmospheric circulation induce melt are not well understood. On an annual basis, the absorption of solar radiation is the greatest source of melt energy across the ice sheet [*Box et al*., 2012].

Hofer et al. [2017] found evidence for a decreasing trend in summer cloud cover over Greenland from 1995 to 2009 and deduced that this decrease in cloud cover drove the corresponding negative GrIS mass trend through enhanced absorption of shortwave radiation. However, other studies have found that clouds can enhance GrIS surface melt and prevent meltwater refreezing through enhanced downwelling longwave radiation over at least some areas of the GrIS [*Bennartz et al*., 2013; *Van Tricht et al*., 2016; *Solomon et al*., 2017; *Cullather and Nowicki*, 2018; *Wang et al*., 2018]. Given the large fluxes of water vapor delivered by ARs, it is likely that some parts of the GrIS that M18 showed are prone to intense SMB losses during AR events also experience anomalous cloud cover. Additionally, studies of intense melt events at field sites in the ablation zone of southern and western Greenland have shown that turbulent fluxes of sensible and latent heat — driven by enhanced wind speeds — are a major source of melt energy and exceed the magnitude of radiative fluxes during these anomalous melt episodes [*Braithwaite and Olesen*, 1990; *Fausto et al*., 2016a; *Fausto et al*., 2016b; *Hermann et al*., 2018].

In light of this uncertainty over the physical processes contributing to enhanced GrIS summer melt, in this study we examine the local- to synoptic-scale atmospheric mechanisms and surface-atmosphere interactions that drive GrIS melt during AR events. As M18 found that the negative GrIS SMB response is greatest when strong summer ARs affect western Greenland, we focus on these events in our analysis. We first explore the response of the radiative (shortwave and longwave radiation) and turbulent (sensible and latent heat flux) terms of the surface energy balance (SEB) to strong AR events, including the spatial variability of these energy balance components across the GrIS. We then analyze the atmospheric processes that produce these SEB responses, focusing on the role of clouds in altering radiative fluxes and the local- to synoptic-scale changes in temperature and pressure fields that produce enhanced wind speeds and

turbulent fluxes. Acknowledging that values of SEB terms and cloud properties are uncertain over Greenland, we employ a number of observational, regional climate model, reanalysis, and satellite-derived datasets to represent the spread of plausible results and highlight areas of agreement and disagreement between data sources. Finally, we devote particular attention to a distinct contrast in the processes contributing to melt in the western versus eastern Greenland ablation zone during strong AR events that reach the higher latitudes of northwest Greenland. This contrast is characterized by simultaneous cloudy, moist conditions over western Greenland and clear, dry conditions produced by downsloping in eastern Greenland, with anomalous melt energy present under both these regimes.

3.2 Data and Methodology

3.2.1 Data sources

3.2.1a Modèle Atmosphérique Régionale (MAR) regional climate model

The primary data source employed to examine SEB components, near-surface wind fields, and cloud properties is the Modèle Atmosphérique Régionale (MAR) regional climate model [*Gallée and Schayes*, 1994]. MAR is a coupled atmosphere-land surface model that has been developed and widely utilized for polar climate studies. It includes a 1-D model, the Soil Ice Snow Vegetation Atmosphere Transfer (SISVAT) scheme [*De Ridder and Gallée*, 1998], to calculate mass and energy fluxes between the land surface, snow surface, and atmosphere. SISVAT incorporates a multilayer snowpack model (CROCUS) capable of simulating detailed processes including meltwater refreezing and snow metamorphism affecting surface albedo [*Brun et al*., 1992; *Fettweis et al*., 2013a]. MAR version 3.9.6, forced with ERA-Interim reanalysis data and run at 7.5km spatial resolution and daily temporal resolution over the period 1980–2017, is used in this study.

MAR has been shown through extensive validation efforts to reproduce near-surface temperatures, melt, and SMB values with a high degree of accuracy over the Greenland and Antarctic ice sheets [*Rae et al*. 2012; *Fettweis et al*., 2017; *Sutterley et al*., 2018; *Agosta et al*., 2019]. The success of the model in simulating these fields may result from compensating biases, however, as some MAR versions have been found to overestimate downwelling shortwave radiation and underestimate downwelling longwave radiation over Greenland due to underestimation of cloudiness [*Franco et al*., 2013; *Fettweis et al*., 2017]. Net shortwave radiation simulated by the model may also be affected by inaccuracies in albedo, particularly in the low-elevation bare ice zone where the lower limit of albedo is fixed at 0.4 in the model but has been observed to be as low as 0.2 in reality [*Alexander et al*., 2014; *Tedesco et al*., 2016a; *Fettweis et al*., 2017].

Turbulent fluxes of sensible and latent heat from MAR have not been examined as thoroughly as radiative SEB components. Validation of turbulent fluxes is difficult because the single-level "bulk" method used to calculate them from both model output and from station observations likely results in underestimation of their magnitude, particularly during intense melt events in the ablation zone [*Fausto et al*., 2016b; *Hermann et al*., 2018]. MAR uses a sophisticated scheme — incorporating surface snow/ice density, snow depth, snow erosion, and sastrugi — to determine the roughness length for momentum for turbulent flux calculations [*Alexander et al*., 2019], while turbulent flux calculations from observations typically use simplified roughness length values for snow or ice surfaces [*Van As et al*., 2012; *Fausto et al*., 2016b].

3.2.1b Programme for monitoring of the Greenland Ice Sheet (PROMICE) observations and derived fluxes

Daily observations from Programme for Monitoring of the Greenland Ice Sheet (PROMICE) stations [*Van As et al*., 2011b] are used to analyze near-surface atmospheric conditions over the GrIS and for comparison with MAR, reanalysis, and satellite data. PROMICE provides observations of standard meteorological variables such as temperature and wind speed, as well as measured radiative fluxes (downwelling and upwelling shortwave and longwave radiation) and derived turbulent fluxes (sensible and latent heat flux) calculated using a SEB model described by *Van As* [2011a]. This model assumes a roughness length of 1 mm at all PROMICE station sites and uses the observed surface temperature to calculate near-surface atmospheric gradients, rather than the surface temperature for which all SEB components are in balance [*Van As*, personal communication]. Both of these factors introduce uncertainty into the turbulent flux calculations.

This study focuses on conditions in the western and northeastern sectors of the GrIS during AR events, and thus data from 11 PROMICE stations located in the Nuuk (NUK), Kangerlussuaq (KAN), Upernavik (UPE), Thule (THU), and Kronprins Christian Land (KPC) regions of the GrIS (Figure 3.1) are utilized. Most stations are located in either the lower ablation zone or in the upper ablation zone near the equilibrium line, with elevations ranging from 220 m (UPE_L) to 1840 m (KAN_U) above sea level. The chosen stations began recording at various points in the years ranging from 2007–2010 and observations through the summer of 2017 are acquired at all stations, resulting in data for 7–10 summers depending on station.

3.2.1c MERRA-2 and ERA5 reanalysis data

Modern Era Retrospective Analysis for Research and Applications, version 2 (MERRA-2) reanalysis data [*Gelaro et al*., 2017] are used to identify AR events and categorize them based on the intensity of their water vapor transport (see Section 3.2.2a). Following M18, these MERRA-2 data are interpolated to 0.5° lat/lon resolution, with 6-hourly temporal resolution over the period 1980–2017. To generate cross section plots of meteorological variables in the vicinity of the GrIS, ERA5 reanalysis data [*Copernicus Climate Change Service*, 2017] on native model vertical levels are used due to their relatively high spatial (0.28125°) and vertical (137 hybrid sigma/pressure levels) resolution. ERA5 data for model levels 137–79, extending from the surface up to ~250 hPa in a standard atmosphere, are used in this study over the period 2000–2017. Additionally, MERRA-2 data (at native 0.5° lat / 0.625° lon resolution) and ERA5 data are used for comparisons of SEB terms and cloud properties with MAR output and PROMICE data.

3.2.1d Hybrid RACMO-satellite cloud data

In order to evaluate the accuracy of MAR, ERA5, and MERRA-2 cloud liquid water path (LWP) and ice water path data (IWP) across the GrIS, a hybrid regional climate model-satellite dataset developed by *Van Tricht et al*. [2016] is employed. This "hybrid RACMO-satellite" dataset combines highly accurate, but temporally limited, active lidar and radar satellite cloud observations with the hourly resolution (but less accurate) LWP and IWP output from version 2.3 of the RACMO regional climate model. The satellite LWP and IWP values are derived by combining backscattered energy measurements from the Cloud-Aerosol Lidar with Orthogonal Polarization (CALIOP) and Cloud Profiling Radar (CPR) sensors aboard the CALIPSO and CloudSat satellites, respectively. MODIS radiances are used to fill gaps in the data when the retrieval algorithms of these two active sensors fail to converge.

To combine the RACMO and satellite data, the satellite observations are first aggregated into 2° × 2° grid cells and the RACMO data are regridded to this same 2° grid. A correction factor is then calculated based on the difference between 3-day moving averages of the satellite and model data at each hourly model timestep, and this correction factor is used to rescale the RACMO LWP and IWP values toward the satellite data. The correction factor is exponentially weighted to avoid adding excessive LWP and IWP to the output when no cloud is present in the model. Further details on this data are provided by *Van Tricht et al*. [2016], who find that the hybrid RACMO-satellite dataset agrees significantly better with ground-based LWP retrievals from Summit Station during July–December 2010 (see below) than the raw RACMO output, although the hybrid data still slightly underestimate LWP. The hybrid RACMO-satellite dataset encompasses the period 2007–2010, with 3-hourly temporal resolution that is resampled to daily means in the present study.

3.2.1e Summit Station cloud liquid water path retrievals

To provide an additional check on the model and reanalysis cloud data, ground-based LWP retrievals from Summit Station, located in the high-elevation dry snow zone of the central GrIS [*Shupe et al*., 2013] (see Figure 3.1), are utilized. LWP values are estimated by applying a physical microwave retrieval algorithm to radiances measured by a pair of microwave radiometers at two low-frequency channels (23.84 and 31.40 GHz) and one high-frequency channel (90.0 GHz) [*Turner et al*., 2007; *Pettersen et al*., 2016; *Miller et al*., 2017]. The addition of the high-frequency channel helps constrain LWP when little cloud liquid is present, reducing mean LWP uncertainty to ~5 g m^{-2} [*Pettersen et al*., 2018; *Miller et al*., 2017]. LWP retrievals from July 2010 through August 2017 are resampled to daily mean temporal resolution in this study.

3.2.1f CERES SYN1DEG radiative fluxes and cloud properties

A final data source used for comparison of surface radiative fluxes and cloud properties with MAR and PROMICE data is the Clouds and the Earth's Radiant Energy System Synoptic 1-degree resolution dataset (CERES SYN1deg), version 3 [*Wielicki et al*., 1996]. Daily mean surface shortwave and radiative fluxes, cloud area fraction, cloud liquid water path, and cloud ice water path data provided by CERES SYN1deg at 1° resolution over the period 2000–2017 are used. CERES SYN1deg radiative fluxes are calculated using a radiative transfer model that incorporates numerous inputs, including CERES and Moderate Resolution Imaging Spectroradiometer (MODIS) instruments aboard the *Terra* and *Aqua* satellites, cloud properties from MODIS and geostationary satellites, atmospheric profiles from the Goddard Earth Observing System (GEOS) model, and snow and ice cover data from the National Snow and Ice Data Center (NSIDC) and National Oceanic and Atmospheric Administration (NOAA), among other sources [*Rutan et al*., 2015].

3.2.2 Methods

3.2.2a Atmospheric river identification and intensity classification

Following M18, outlines of AR features over the Northern Hemisphere are identified at 6-hourly timesteps using integrated water vapor transport (IVT) fields calculated from MERRA-2 and interpolated to 0.5° lat/lon resolution. IVT is calculated, in units of kg m^{-1} s^{-1}, as the product of specific humidity and vector winds integrated vertically from 1000–200 hPa and divided by gravitational acceleration:

$$IVT = \frac{1}{g}\int_{1000\ hPa}^{200\ hPa} qV\ dp \tag{3.1}$$

where q and V are specific humidity (in kg kg^{-1}) and vector wind (in m s^{-1}) at a given pressure level, dp is the difference between pressure levels, and g is gravitational acceleration (9.80665 m s^{-2}). Intervals between pressure levels (dp) are 50 hPa between 1000 hPa and 500 hPa and 100 hPa between 500 hPa and 200 hPa. The climatological percentile rank of IVT (IVT PR), based on IVT values from 1980–2016 during a 31-day moving window surrounding a given date, is also calculated for input into the AR identification algorithm. ARs are then identified as contiguous regions with IVT $\geq$ 150 kg m^{-1} s^{-1} and IVT PR $\geq$ 85 that also meet size, shape, length, and latitude-dependent transport direction criteria given in Table 3.1. See M18 and Fig. 3.2 for additional details and examples of the AR identification criteria.

To compare atmospheric processes at work during intense AR events to periods with ARs of lesser intensity or no AR present, outlines of the eight major GrIS drainage basins from *Luthcke et al*. [2013] are delineated, and each day in the study period is classified into one of three categories ("no AR", $AR_{<90}$, AR_{90+}) based on basin-scale AR intensity. "No AR" days have no AR present over any part of the given basin at any time on the given day. If an AR outline overlaps with a given basin outline on a given day, that basin is classed as experiencing an AR "landfall". To categorize $AR_{<90}$ and AR_{90+} days for each basin, the distribution of maximum IVT values within the area of overlap between the AR outline and basin outline at times an AR is present is compiled for each season. $AR_{<90}$ days are those with an AR with a maximum IVT value within the given basin outline is less than the 90th percentile of this basin- and season-specific distribution, while AR_{90+} days have a maximum IVT value greater than or equal to the 90th percentile. Except where noted, most analysis in this study focuses on the contrast between AR_{90+} and "no AR" days. The 90th percentile IVT threshold was chosen based on the finding that warm, moist, windy conditions at low-elevation PROMICE stations — similar to the "heat

wave" conditions found to be associated with melt spikes by *Hermann et al*. [2018] — are much more likely to occur during AR events with ≥ 90th percentile IVT (see Appendix A).

3.2.2b Atmospheric composite analyses

To assess the sources of energy contributing to melt during AR events and compare the partitioning of SEB components with non-AR conditions, composite mean net shortwave radiation (SW_{net}), net longwave radiation (LW_{net}), sensible heat flux (SHF), and latent heat flux (LHF) fields on "no AR", $AR_{<90}$, and AR_{90+} days are calculated from MAR output during the summer months (JJA) of 1980–2017. Differences between summed radiative (SW_{net} and LW_{net}) versus non-radiative (SHF and LHF) SEB terms, as well as the total melt energy (SW_{net} + LW_{net} + SHF + LHF), are also compiled. Composite anomalies of all of these quantities are then calculated for each AR category by comparing the daily MAR values to the distribution of all values for the given month during 1980–2017. Rain energy flux and conductive ground heat flux energy sources are not included in this study due to lack of available data on these SEB terms from MAR and PROMICE data. These energy sources are generally small in comparison to radiative and turbulent fluxes [*Charalampidis et al*., 2015], although rain heat flux may be substantial during anomalously heavy rainfall events [*Doyle et al*., 2015; *Fausto et al*., 2016b].

Composites of SEB components are produced for basins 6 and 8 (see Figure 3.1) to examine the physical processes at work during southwest and northwest Greenland AR events. To examine the temporal evolution of the SEB over the course of AR events, composite areal mean values and anomalies of these variables are also compiled over the ablation and accumulation zones of basins 6 and 8 for the ± 5 days surrounding $AR_{<90}$ and AR_{90+} events. Additionally, these composites are produced for basin 2 on basin 8 AR landfall days to examine the special case of melt in the eastern and northeast Greenland ablation zone during AR events

affecting northwest Greenland. The ablation zone is defined as areas where MAR annual mean SMB is less than 0 mmWE, and conversely the accumulation zone includes areas where MAR annual mean SMB is greater than 0 mmWE (see Figure 3.1). For the ± 5 day window calculations, any day with an AR of the given category ($AR_{<90}$ or AR_{90+}) is defined as day 0, and only days surrounding this day with no AR impact of the given intensity are included in the composites. The window is "broken" when another AR of the given intensity occurs; for example, if day 0 is a AR_{90+} day and AR_{90+} events also occur on day -5, day -3, day +3, and day +5, only days -2 through +2 are included in the composite calculations.

Values of radiative and turbulent fluxes output by MAR are compared to the same quantities measured by and derived from PROMICE observations, as well as data from ERA5, MERRA-2, and CERES SYN1deg (radiative fluxes only). MAR, ERA5, MERRA-2, and CERES SYN1deg data for these comparisons are extracted by locating the nearest grid cell to each PROMICE station, with the number of observations available for comparison depending on the record length of each PROMICE station. Comparisons are performed across categories of AR activity for PROMICE stations in basin 6 (KAN_L, KAN_M, KAN_U, NUK_L, NUK_U) and basin 8 (THU_L, THU_U, UPE_L, UPE_U), as well as for two stations located in the eastern part of basin 1 in northeast Greenland (KPC_L, KPC_U). Because the KPC_L and KPC_U stations are near the boundary between basin 1 and basin 2, and the conditions at these stations on basin 8 AR days are likely similar to those experienced in the basin 2 ablation zone, the SEB at these stations is analyzed in relation to AR activity in basin 8.

Composite mean and anomaly maps of cloud properties (cloud cover, liquid water path, and ice water path) from MAR are produced in the same manner as the SEB analysis described above. These cloud properties for each AR activity category are compared to cloud data from

ERA5, MERRA-2, and CERES SYN1deg during the 2000–2017 time period when data are available from all four sources, and to hybrid RACMO-satellite LWP and IWP data during 2007–2010. Cloud LWP data from MAR, ERA5, and MERRA-2 are compared to ground-based retrievals from Summit Station during 2010–2017.

Vertical cross sections of atmospheric variables relevant to cloud formation (specific and relative humidity, vertical velocity) and cloud characteristics (cloud cover, specific cloud ice water content, and specific cloud liquid water content) are compiled across AR activity categories from ERA5 data during 2000–2017. ERA5 data are also utilized to create cross sections of the atmospheric thermal state and wind fields. All cross sections are created with data valid at 1800 UTC to capture the mid-afternoon period when surface melt is typically maximized, and early morning (0600 UTC) cross sections are also compiled for comparison. Finally, synoptic-scale composites of near-surface and mid-tropospheric (500 hPa) pressure, wind, temperature, and moisture conditions across AR activity categories are produced using MERRA-2 data. Due to the large amount of data processing required for the cloud comparison analyses, cross sections, and synoptic composites, in these analyses the sample sizes of the "no AR" and $AR_{<90}$ categories are reduced to match the number of days in the AR_{90+} category through random selection of the equivalent number of "no AR" and $AR_{<90}$ days. A random number generator was used to select "no AR" and $AR_{<90}$ days for inclusion in the composites, with the sample size of "no AR" and $AR_{<90}$ days set equal to the number of AR_{90+} days.

3.3 Results

3.3.1 Surface energy balance during AR events

During AR_{90+} events affecting basin 6 (southwest Greenland), negative SW_{net} anomalies and positive LW_{net} anomalies are modelled by MAR throughout the basin (Figure 3.3). MAR

shows substantial positive latent heat fluxes in the ablation zone and lower accumulation zone, with strong positive sensible heat fluxes in the ablation zone transitioning to weakly positive or weakly negative SHF in the higher elevations of the accumulation zone. Anomalously strong near-surface winds (particularly in the ablation zone) contribute to these turbulent fluxes, with the SHF transition zone corresponding to the area where the difference between 2-m and ice sheet surface temperatures drops to near 0°C (Figure 3.4). The balance of these radiative and turbulent fluxes results in strong positive melt energy anomalies exceeding 50 W m^{-2} in the ablation zone, and lesser but substantial anomalies between 10–50 W m^{-2} in the accumulation zone of basin 6. Notably, the magnitude of the summed turbulent flux terms exceeds net radiation up to 30 W m^{-2} in much of the ablation zone, in agreement with prior studies [e.g. *Braithwaite and Olesen*, 1990; *Fausto et al*., 2016b] finding that the majority of melt energy is contributed by non-radiative fluxes during intense melt events in the southwest Greenland ablation zone.

Analysis of SEB terms averaged over the ablation zone and accumulation zones of basin 6 during the days surrounding AR events (Figure 3.5) shows that positive energy flux anomalies begin 1 day prior to the date of AR_{90+} impact (day -1), with positive anomalies lingering for around 2 additional days (through day +2) on average. In the ablation zone, these anomalies are driven primarily by increased SHF and LHF, accompanied by increased LW_{net} that balances the decrease in SW_{net}. MAR simulates energy flux anomalies of lesser magnitude in the accumulation zone, with similar changes to radiative terms as in the ablation zone and LHF anomalies that are much greater than SHF changes. $AR_{<90}$ events affect the SEB in a qualitatively similar manner, but the magnitude of fluxes associated with $AR_{<90}$ events is much less than AR_{90+} events.

In northwest Greenland, AR_{90+} events affecting basin 8 produce similar changes to the SEB in the immediate vicinity of AR landfall as the corresponding events in basin 6. Decreased SW_{net} is offset by increased LW_{net} throughout basin 8, and strong turbulent fluxes driven by enhanced wind speeds in the ablation zone transition to negative SHF at higher elevations (Figures 3.6 and 3.7). However, basin 8 AR_{90+} events are also accompanied by positive anomalies in melt energy throughout the northern and northeastern GrIS ablation zone that do not appear during basin 6 AR events. These energy fluxes are produced by physical processes that contrast with those at work in the AR landfall area in northwest Greenland. All along the northeastern and eastern margin of the GrIS, positive SW_{net} anomalies, negative LW_{net} anomalies, strong positive SHF anomalies, and negative LHF anomalies occur. Positive wind speed anomalies occur throughout all but a small sliver of the south-central GrIS, with particularly strong winds in the northeast Greenland ablation zone resulting in pronounced dominance of SHF over the summed radiative energy balance terms.

Figure 3.10 examines this region more closely by plotting SEB terms in the basin 2 (northeast Greenland) ablation and accumulation zones over the course of basin 8 AR_{90+} and $AR_{<90}$ events. In the ablation zone, positive SW_{net} anomalies peak on the day of AR_{90+} events (day 0) and the day after (day +1) and SHF peaks on day +1, resulting in the highest energy flux anomalies on the day after AR_{90+} events. These anomalies linger longer than in basin 8 itself, with energy fluxes slowly returning to pre-event values by day +5. In the accumulation zone, small SHF anomalies result in relatively small amounts of enhanced energy flux, with values returning to normal within 3 days. Less intense $AR_{<90}$ events in northwest Greenland result in small increases in SW_{net} and SHF in the northeast Greenland ablation zone, but this effect

appears to be counterbalanced by negative LW_{net} anomalies and their overall impact on the SEB is negligible.

Tables 3.2 and 3.3 show that MAR tends to underestimate SW_{net} when compared to PROMICE data, particularly at sites in the ablation zone where MAR bare ice albedo may be fixed at higher values than reality [*Fettweis et al*., 2017]. MAR also exhibits a negative LW_{net} bias. The mean differences between MAR and PROMICE SHF are relatively low (Table 3.3), but the standard deviations of these differences are quite high relative to their mean values. Table 3.2 shows that the magnitude and sign of differences between mean MAR and PROMICE SHF fluctuates from station to station and, in a few cases, across AR conditions at the same station. For example, the mean MAR SHF value at NUK_L is much higher than the corresponding PROMICE value on AR_{90+} days, but MAR simulates less SHF than PROMICE at NUK_L on "no AR" and $AR_{<90}$ days. Mean LHF values from MAR are higher than PROMICE LHF values for all stations and AR conditions, with positive LHF biases especially pronounced during AR_{90+} conditions. These positive LHF biases likely compensate at least partially for the negative SW_{net} and LW_{net} biases in the ablation zone and allow MAR to simulate surface melt accurately [*Fettweis et al*., 2017; *Sutterley et al*., 2018].

These discrepancies in turbulent fluxes between MAR and PROMICE are perhaps not surprising given the uncertainties involved in their calculation (see Section 3.2.1), and it must be noted again that PROMICE SHF and LHF values are derived using a 1-D SEB model with significant uncertainties, particularly relating to the fixed roughness length of 1 mm at all stations. PROMICE turbulent fluxes thus do not represent "true" values, and it is likely that the single-level "bulk" flux calculation method used in both the PROMICE and MAR turbulent flux derivations underestimates the magnitude of heat transfer to the surface by turbulent fluxes,

especially during periods of intense warm air advection and melt [*Fausto et al*., 2016b; *Hermann et al*., 2018]. MAR near-surface wind speeds exhibit only a small positive bias at most PROMICE stations (Table 3.4) and thus differences in wind speed are likely not the primary source of the turbulent flux disparities between MAR and PROMICE.

In comparison to ERA5, MERRA-2, and CERES SYN1deg, MAR shows the best overall performance in reproducing SEB terms from PROMICE (Table 3.3). MAR has the lowest bias in LW_{net} and SHF, with LHF biases of comparable magnitude (but opposite sign) to MERRA-2 and ERA5. MERRA-2 appears to match PROMICE observations of SW_{net} more closely than the other datasets. Although the values of each SEB term vary considerably between data sources, all four sources agree on the sign and spatial patterns of the changes in each term across categories of AR conditions (Figures 3.9–3.12).

3.3.2 Cloud properties during AR events

Having described the SEB changes that occur during basin 6 and basin 8 AR_{90+} events, we now analyze the atmospheric processes that produce these anomalous energy fluxes. We begin by examining the impact of clouds on shortwave and longwave radiative fluxes. On AR_{90+} days in basin 6, MAR simulates extensive cloud cover throughout the basin and surrounding areas, with up to 30–40% more cloud cover on average compared to "no AR" days (Fig. 3.13). Except over the lower ablation zone, these simulated MAR clouds appear to contain very little liquid water over the GrIS. LWP values in the 10–40 g m^{-2} range have been shown to maximize positive cloud radiative effects by enhancing downward longwave radiation while allowing some shortwave radiation to filter through [*Bennartz et al*., 2013; *Van Tricht et al*., 2016; *Nicolas et al*., 2017]. MAR produces these LWP values over only a narrow band of the lower accumulation zone during AR_{90+} events, instead simulating very high IWP values over much of the western

GrIS. These extensive ice clouds force the decreases in SW_{net} and increases in LW_{net} during AR_{90+} events described in the previous section.

In agreement with MAR, ERA5 and MERRA-2 show large increases in cloud cover over basin 6 on AR_{90+} days compared to "no AR" days, with ERA5 in particular showing 90–100% mean cloud cover over most of the basin (Figure 3.14). Their depiction of cloud liquid and ice water differs substantially from MAR, however. Both ERA5 and MERRA-2 show LWP > 10 g m^{-2} over all but the eastern interior GrIS on AR_{90+} days, and LWP > 40 g m^{-2} extending well into the higher elevations of the accumulation zone in basin 6. ERA5 depicts modest IWP values of 30–90 g m^{-2} over most of basin 6, while MERRA-2 depicts higher IWP values in the 100–200 g m^{-2} range over the basin, which are nevertheless much lower than the > 250 g m^{-2} values simulated by MAR.

Comparison of the MAR, ERA5, and MERRA-2 LWP and IWP data with the hybrid RACMO-satellite data (Figure 3.14) and Summit Station LWP retrievals (Table 3.5) suggests that the ERA5 and MERRA-2 LWP and IWP values are much more realistic than the MAR output. The spatial patterns of LWP and IWP in the hybrid RACMO-satellite data are reproduced well by ERA5 and MERRA-2, with higher amounts of LWP and IWP across the western GrIS during AR_{90+} events compared to "no AR" conditions. LWP appears to still be underestimated by ERA5 and MERRA-2 on AR_{90+} days, with LWP > 40 g m^{-2} extending to higher elevations of the western GrIS accumulation zone in the hybrid RACMO-satellite data compared to ERA5 and MERRA-2. This is confirmed by the Summit Station retrievals, as mean ERA5 and MERRA-2 LWP at Summit Station is within the range of the observational uncertainty on "no AR" days but 15–20 g m^{-2} lower than the ground-based retrievals on AR_{90+} days (Table 3.5). Compared to the hybrid RACMO-satellite IWP data, ERA5 appears to slightly underestimate IWP in most areas

during both “no AR” and AR_{90+} conditions, while MERRA-2 reproduces the magnitude and spatial pattern of IWP quite well (Figure 3.14). These discrepancies between MAR and ERA5 / MERRA-2 are also evident for AR_{90+} events impacting basin 8 (Figures 3.15 and 3.16, Table 3.6), with the zone of enhanced cloudiness shifting to northwest Greenland.

A vertical cross section of mean afternoon (1800 UTC) cloud properties from ERA5 over the K-transect region of basin 6 (Figure 3.17) suggests that cloud liquid water is concentrated in the lower troposphere, 50–100 hPa above the ice sheet surface, on AR_{90+} days. Extensive ice clouds are located in a broad swath of the upper troposphere centered around ~400 hPa, with a mixture of cloud liquid and ice between these regions. Overall cloud cover is much more extensive throughout the troposphere on AR_{90+} days compared to “no AR” days. During basin 8 AR_{90+} events, cloud cover increases throughout the troposphere over basin 8 itself (Figure 3.18), resembling the enhanced cloud cover observed over the K-transect on basin 6 AR_{90+} days. East of the ice divide, however, there is a sharp gradient in cloud cover, with very little cloudiness shown by ERA5 along the eastern half of the cross section in northeast Greenland. Clouds are especially sparse over the northeast Greenland ablation zone on AR_{90+} days, resulting in the positive SW_{net} anomalies and negative LW_{net} anomalies described in the previous section.

3.3.3 Atmospheric forcing of surface energy balance and cloud properties during AR events

On AR_{90+} days in basin 6 (southwest Greenland), the synoptic-scale atmospheric circulation in the lower troposphere features an anomalous area of low pressure over the Labrador Sea, Davis Strait, and Baffin Island (Figure 3.19; see Figure 1.1 for reference map of these locations). Off the southeast coast of Greenland, the seasonally weak Icelandic Low appears as a broad closed MSLP contour on basin 6 “no AR” days, but is replaced by an anomalous anticyclone on AR_{90+} days. The combination of low pressure to the west of

Greenland and high pressure to the east generates southerly advection of anomalously warm, moist air from the Atlantic over southwest and western Greenland on basin 6 AR_{90+} days. In the middle troposphere (Figure 3.20), a trough of low pressure is centered over northern Baffin Bay and Baffin Island on basin 6 AR_{90+} days, with an anomalous ridge of high pressure centered off the southeast coast of Greenland and extending across the southern and eastern two-thirds of Greenland. This trough-ridge couplet is accompanied by a northward deviation of the jet stream from its climatological position over the North Atlantic, with 500 hPa wind speeds maximized over southwest Greenland. During basin 8 AR_{90+} events (Figures 3.21 and 3.22) these lower- and middle-tropospheric features are qualitatively similar but displaced to the northwest, with anomalous middle-tropospheric ridging extending over virtually all of Greenland.

Vertical cross sections of wind fields and thermal variables over the K-transect region (Figures 3.23 and 3.24) and across northern Greenland (Figures 3.25 and 3.26) provide further insight into the surface-atmosphere interactions that result in enhanced turbulent heat fluxes on AR_{90+} days. Climatologically, the wind field over the GrIS is katabatic, with negatively buoyant downslope flow forced by cooling of the near-surface atmosphere over the ice sheet and maximized in the vicinity of steeply sloping terrain [*van den Broeke et al*., 1994; *Parish and Bromwich*, 1989]. The katabatic wind is typically weakest on summer afternoons, as the ice sheet surface temperature is warmer than in other seasons (and fixed at 0°C during surface melt), reducing the thermal gradient between the near-surface katabatic layer and the free atmosphere during synoptically quiescent conditions [*van Angelen et al*., 2011; *Moore et al*., 2013]. The relative weakness of climatological summer katabatic winds can be seen in our 1800 UTC "no AR" wind values cross section over the K-transect (Figure 3.23; compare to stronger morning katabatic winds in Figure 3.27).

On AR_{90+} days, in contrast, warm air advection results in above-freezing temperatures just above the ice sheet surface that extend much further inland to higher elevations compared to "no AR" conditions (Figure 3.24). This increases the local-scale temperature deficit of near-surface air over the ice sheet relative to the surrounding atmosphere, resulting in enhanced thermal wind forcing that is maximized in areas of steeply sloped terrain. Further, there is a substantial synoptic-scale pressure gradient that contributes to the wind forcing on AR_{90+} days. This can be clearly seen in the large-scale MSLP and 500 hPa height maps (Figures 3.19 and 3.20), and more subtly appears in the sloping of potential temperature and geopotential height contours from the ridge over Greenland to the trough over Baffin Bay in the AR_{90+} cross section (Figure 3.24). This large-scale pressure gradient generates what previous authors have termed a "barrier jet" or "Greenland plateau jet" in the free atmosphere perpendicular to the terrain gradient of the western GrIS, which is coupled to the near-surface katabatic layer through the positive vertical wind shear above the boundary layer [*van den Broeke and Gallée*, 1996; *Moore et al*., 2013]. The coupling of these locally- and synoptically-forced winds results in mixing of warm air downward into the boundary layer and strong downward fluxes of sensible heat toward the ice sheet surface, as has been noted by previous studies in the presence of strong synoptic forcing [*Meesters*, 1994; *van den Broeke and Gallée*, 1996; *Heinemann and Falk*, 2002]. Although we focus on late afternoon (1800 UTC) conditions to capture the time of maximum melt, it is worth noting that early morning (0600 UTC) wind speeds are higher (Figure 3.27) on AR_{90+} days compared to "no AR" days and the strength of the early morning inversion is substantially reduced (Figure 3.28), which indicates strong turbulent heat fluxes on AR_{90+} days even during the time of day with little to no incoming solar radiation.

During basin 8 AR_{90+} events, the afternoon wind and thermal cross sections (Figure 3.25 and 3.26) resemble the K-transect cross sections in the AR landfall area of northwest Greenland, although katabatic winds are stronger than over the K-transect on "no AR" days due to the greater slope angle. Over northeast Greenland, the thermal cross sections (Figure 3.26) show above-freezing temperatures extending to much higher altitudes over the ice sheet on AR_{90+} compared to "no AR" afternoons, and the closely packed potential temperature contours indicate a strengthening of the temperature inversion on basin 8 AR_{90+} days. These features are produced by downslope flow and adiabatic warming above the near-surface katabatic layer, which increases the temperature deficit of the katabatic layer and strengthens the wind speed, particularly in the area immediately upslope from the steepest topography (Figure 3.25). There is some evidence of connection between the katabatic wind and the middle- to upper-tropospheric jet, but the synoptic pressure gradient is weaker than in northwest Greenland, and the vertical distance between the core of the upper-level jet and the near-surface katabatic wind maximum is much greater than in northwest Greenland. Thus the local-scale katabatic and thermal forcing likely plays the dominant role in driving enhanced speeds in northeast Greenland during northwest Greenland AR events. This enhanced katabatic wind entrains adiabatically warmed air from just above the katabatic layer and mixes it toward the surface, leading to the enhanced SHF described in Section 3.3.1.

Additional insight into the drivers of anomalous radiative and turbulent energy fluxes during AR_{90+} events is provided by cross sections of moisture and vertical velocity fields (Figures 3.29 and 3.30). Over the K-transect region, ERA5 shows specific humidity values that are on the order of 5–20 g kg^{-1} higher throughout the lower and middle troposphere on AR_{90+} compared to "no AR" days (Figure 3.29). This anomalous atmospheric moisture content, along

with widespread upward motion above the boundary layer, results in extensive cloud formation in the vicinity of AR landfall (see Figures 3.13, 3.14, 3.17, and 3.18) that produces negative SW_{net} and positive LW_{net} anomalies in this region. Combined with the strong wind speeds detailed above, the high atmospheric water vapor content also results in increased latent heat flux. Over northeast Greenland during basin 8 AR_{90+} events, downward vertical motion extends through a deeper layer of the troposphere than normal, with especially intense downslope flow along the steepest slopes near the ice sheet edge (Figure 3.30). The strong downsloping warms the air above the boundary layer and water vapor content decreases as air passes over the GrIS terrain barrier, resulting in very low relative humidity throughout the troposphere over the northeast GrIS ablation zone. This combination of drying, warming, enhanced downward motion, and increased katabatic wind speeds explains the positive SW_{net} and negative LW_{net} anomalies (due to decreased cloud cover), positive SHF anomalies, and negative LHF anomalies over the northeastern GrIS ablation zone on AR_{90+} days.

3.4 Summary and Conclusions

Through analysis of the surface energy balance, cloud properties, and synoptic- to local-scale atmospheric conditions during AR events, we have elucidated the atmospheric forcing and surface-atmosphere interactions that generate enhanced GrIS surface melt when a strong AR affects western Greenland during summer. In the immediate vicinity of the AR landfall (the GrIS drainage basin which directly overlaps with the outline of an AR feature), AR_{90+} days are characterized by cloudy, moist, warm, and windy atmospheric conditions over the ice sheet. The presence of clouds — which are produced by enhanced lower- and middle-tropospheric vertical motion acting on anomalous amounts of water vapor — decreases SW_{net} and increases LW_{net}. As these radiative anomalies tend to cancel one another, turbulent fluxes of sensible and latent heat

become the dominant terms of the SEB across the lower elevations of the GrIS where enhanced wind speeds occur. This anomalously strong barrier wind is driven by a combination of an increased synoptic-scale pressure gradient and the intensified local-scale thermal contrast between the cool near-ice atmospheric layer and the surrounding atmosphere as it is heated through warm air advection.

In contrast to the processes producing melt in the vicinity of AR landfall, during strong AR events affecting northwest Greenland, enhanced melt energy is also produced in the northeast GrIS ablation zone in dry, clear, and windy conditions due to downsloping. Anomalously clear skies resulting from downward motion and drying lead to enhanced SW_{net} over this area, while adiabatic warming above the near-ice layer leads to increased katabatic wind speeds and SHF. Our finding of melt forced by downsloping in northeast Greenland during northwest Greenland ARs agrees with the results of *Cullather and Nowicki* [2018], who found a relationship between anomalously clear conditions and melt area in basin 2 through linear regression. Together our results suggest that downsloping regimes are responsible for the largest melt events in this region.

We find that all model, reanalysis, satellite, and observational data sources employed in this study agree on the qualitative changes in SEB terms, cloud properties, and atmospheric conditions that occur during strong summer AR events. However, there is considerable disagreement among these datasets regarding the values of SEB terms as well as cloud liquid and ice water quantities during AR events. MAR generally performs better than ERA5 and MERRA-2 in reproducing SEB terms, using measured radiative fluxes and derived turbulent fluxes from PROMICE stations as reference data. However, it still exhibits a negative SW_{net} bias and positive LHF bias in the western Greenland ablation zone, particularly during AR_{90+} events. Additionally,

based on the results of previous studies [*Fausto et al*., 2016b; *Hermann et al*., 2018 — see Section 3.3.1], it is possible that SHF in the ablation zone during AR_{90+} events is substantially greater than either the values simulated by MAR or those derived from PROMICE observations. MAR appears to severely underestimate cloud liquid amounts and overestimate cloud ice over the GrIS regardless of AR conditions. ERA5 and MERRA-2 perform much better than MAR when compared to hybrid RACMO-satellite cloud data and Summit Station LWP retrievals, but these reanalyses still have too little cloud liquid on average over most of the GrIS (including Summit Station) during AR_{90+} events.

Our results may provide a pathway toward reconciling contrasting perspectives on the role of clouds in GrIS melt. A number of studies [e.g. *Bennartz et al*., 2013; *Van Tricht et al*., 2016; *Gallagher et al*., 2018] have found that clouds act to warm the GrIS surface. In contrast, *Hofer et al*. [2017] found a decreasing trend in summer cloud cover over much of Greenland during 1995–2009, and calculated that decreased cloud cover drove the increasing GrIS melt trend over this time period through enhanced SW_{net} and melt-albedo feedback. In this study, we show that intense GrIS melt occurs under cloudy conditions in the vicinity of AR landfall, but melt also occurs under anomalously clear skies in eastern Greenland during strong northwest Greenland AR events. Moreover, ARs often occur along the upstream flank of a blocking anticyclone [*Liu and Barnes*, 2015; *Baggett et al*., 2016; *Mundhenk et al*., 2016; *Bozkurt et al*., 2018], and in many cases latent heat release in the rising warm conveyer belt associated with an AR helps to amplify the blocking anticyclone [*McLeod and Mote*, 2015; *Pfahl et al*., 2015; *Grams and Archambault*, 2016]. Greenland blocking events often last for several days or even weeks [*Davini et al*., 2012; *Wang et al*., 2019], lingering for a much longer period of time than a typical AR event.

Therefore we propose a conceptual model whereby a strong AR produces an intense initial melt surge — often through simultaneous cloudy and clear melt regimes, varying spatially across the GrIS — and forces a decrease in GrIS albedo. If the AR event is accompanied and/or followed in subsequent days by Greenland blocking conditions and decreased cloud cover, melt-albedo feedback triggered by the AR will contribute to enhanced melt through absorption of solar radiation. We note that a few ephemeral strong AR events interspersed with longer-lived blocking conditions during a given summer could manifest as an overall anomalously low amount of seasonally averaged cloud cover, and that the decreasing cloud cover trend found by *Hofer et al*. [2017] overlaps temporally with an increasing trend in the magnitude of seasonally-summed summer moisture transport to western Greenland [*Mattingly et al*., 2016; M18]. We hypothesize that both cloudy and clear atmospheric regimes synergistically combine to force anomalous GrIS melt during at least some summers, as also suggested by *Oltmanns et al*. [2019]. Future studies should investigate this hypothesis in more detail by examining the evolution of GrIS albedo and SEB prior to, during, and after strong AR and blocking events during individual summers. It is also possible that AR landfalls in other areas of Greenland may force melt in remote regions through downsloping, and this possibility should be investigated further. For example, a series of ARs affected eastern Greenland during April and May 2019, at the same time as unusual early season melt was observed in the western GrIS ablation zone. Finally, the effects of ARs on GrIS SEB should be analyzed during other seasons to determine similarities and differences between the effects of summer and non-summer AR events, including possible preconditioning of warm season melt by non-summer ARs.

Table 3.1. Summary of AR identification criteria.

	Criterion applied to potential AR objects	Purpose / other notes
Raw IVT	> 150 kg m^{-1} s^{-1}	Relatively low threshold accounts for lesser magnitude of moisture transport in higher latitudes
IVT percentile rank (IVT PR)	$>$ 85th %-ile	
Minimum size	$>$ 150 reanalysis grid points ($0.5° \times 0.5°$)	First pass which reduces number of objects processed by algorithm in subsequent tests
Location	Some part of object located poleward of 10°N	
Length	$>$ 1500 km	Great circle distance between the two most distant perimeter points of object
Length-to-width ratio	> 1.5	"Effective Earth surface width": the object length divided by object Earth surface area
Zonal transport component	u-wind > 2 m s^{-1} (from west) if object centroid is south of 35°N	Filters out zonal tropical moisture plumes with east-to-west moisture transport
Meridional transport component	v-wind > 0 m s^{-1} (from south) if object centroid is south of 70°N	Ensures that ARs transport moisture poleward, but allows for high-latitude ARs approaching Greenland from the Arctic

Table 3.2. Comparison of mean surface energy balance terms from MAR to PROMICE measured (SW_{net}, LW_{net}) and derived (SHF, LHF) surface energy balance terms at selected stations across AR regimes ("no AR", $AR_{<90}$, AR_{90+}). The "n"' column denotes the sample size of "no AR", $AR_{<90}$, and AR_{90+} days at each PROMICE station. For basin 6 and 8 stations, AR conditions are defined based on the presence of AR events in the same basin, while for the KPC_L and KPC_U stations in basin 1, "no AR", $AR_{<90}$, and AR_{90+} days days are defined based on conditions in basin 8 to analyze the influence of northwest Greenland AR conditions on the surface energy balance in northeast Greenland. All units are W m^{-2}.

					SW_{net}			LW_{net}			SHF			LHF		
Basin	Station	n (rad. terms)	n (turb. terms)	Data source	No AR	$AR_{<90}$	AR_{90+}	No AR	$AR_{<90}$	AR_{90+}	No AR	$AR_{<90}$	AR_{90+}	No AR	$AR_{<90}$	AR_{90+}
6	KAN_L	683; 193; 17	581; 183; 10	PROMICE	134.14	113.06	93.12	-43.44	-25.76	-3.40	27.96	52.06	64.15	-8.13	-1.76	17.00
				MAR	126.39	109.25	92.34	-52.58	-35.01	-12.67	41.93	71.07	93.10	-1.89	5.66	39.57
	KAN_M	571; 176; 17	382; 109; 14	PROMICE	125.99	112.79	117.65	-53.07	-35.03	-11.06	11.74	22.51	38.39	-12.30	-8.67	10.71
				MAR	100.92	90.54	84.83	-59.86	-42.54	-19.39	16.90	29.12	61.11	-1.82	0.91	24.89
	KAN_U	618; 193; 17	491; 137; 14	PROMICE	72.79	62.48	68.92	-53.06	-38.40	-17.95	8.55	17.55	35.79	-18.17	-18.83	-0.34
				MAR	71.84	65.39	64.39	-63.19	-49.25	-24.35	4.55	10.35	30.32	-1.86	-0.89	16.01
	NUK_L	575; 186; 18	475; 143; 17	PROMICE	157.75	111.32	65.03	-34.24	-12.04	16.96	35.60	52.67	66.46	-5.37	2.48	23.99
				MAR	119.70	86.07	36.95	-64.07	-35.82	-1.07	13.65	38.93	94.04	-5.13	4.86	43.91
	NUK_U	490; 152; 16	395; 107; 15	PROMICE	102.93	75.37	53.84	-42.67	-18.52	9.13	22.25	34.91	58.17	-13.95	-7.72	14.93
				MAR	96.67	73.82	30.26	-52.85	-27.04	8.72	28.82	47.19	93.76	-5.10	4.88	54.17
8	THU_L	374; 100; 16	331; 84; 13	PROMICE	117.27	89.08	71.34	-42.42	-20.33	-9.02	25.54	46.18	54.32	-16.36	-2.62	4.13
				MAR	88.98	77.90	61.24	-64.37	-43.79	-32.89	3.00	19.77	27.56	-4.08	2.08	9.84
	THU_U	481; 131; 26	386; 92; 16	PROMICE	85.18	62.13	44.77	-44.94	-19.87	-6.91	24.70	38.50	35.53	-12.15	-1.17	3.64
				MAR	72.15	58.78	45.82	-53.77	-31.88	-19.74	18.03	21.01	14.37	0.63	6.70	9.63
	UPE_L	567; 153; 30	551; 151; 28	PROMICE	101.79	94.62	66.38	-30.56	-17.86	-0.06	27.62	51.05	117.83	-3.16	-1.07	1.33
				MAR	114.61	102.73	67.67	-59.35	-43.48	-18.80	-2.32	23.86	93.36	-1.72	0.54	3.19
	UPE_U	566; 152; 30	469; 135; 28	PROMICE	112.25	110.54	80.96	-47.30	-35.39	-15.91	24.17	39.40	68.70	-14.49	-11.92	-13.00
				MAR	92.31	88.20	58.72	-51.34	-38.87	-17.22	28.07	44.48	95.28	-5.18	-2.48	2.50
1	KPC_L	496; 116; 22	313; 84; 19	PROMICE	106.69	130.76	131.42	-45.36	-49.54	-49.87	38.44	58.00	64.19	-21.65	-20.24	-21.72
				MAR	94.28	105.82	113.91	-62.59	-65.29	-70.60	14.15	21.65	30.68	-5.58	-5.08	-11.76
	KPC_U	670; 160; 32	581; 132; 30	PROMICE	78.42	88.02	92.04	-50.63	-57.00	-57.18	13.16	19.00	21.84	-16.60	-17.46	-16.84
				MAR	70.35	79.93	84.59	-57.40	-63.02	-64.77	11.47	17.59	23.83	-1.86	-2.61	-4.32

Table 3.3. MAR, ERA5, MERRA-2, and CERES SYN1deg error statistics (bias, standard deviation of bias [σ_{bias}], and root mean square difference [RMSD]) compared to PROMICE measured (SW_{net}, LW_{net}) and derived (SHF, LHF) surface energy balance terms. Error statistics are calculated by determining the difference between each PROMICE value and the corresponding MAR / ERA5 / MERRA-2 / CERES SYN1deg value at the nearest grid cell, then generating the distribution of these differences across all 11 PROMICE stations from Table 3.2. The "n" column denotes the sample size of difference values for the given AR regime. Note that CERES SYN1deg only provides radiative fluxes so the SHF and LHF rows are left blank. All units are W m^{-2}.

			MAR			**ERA5**			**MERRA-2**			**CERES SYN1deg**		
		n	bias	σ_{bias}	RMSD	bias	σ_{bias}	RMSD	bias	σ_{bias}	RMSD	bias	σ_{bias}	RMSD
	No AR	836	-14.98	32.19	35.51	-24.37	55.33	60.46	3.93	36.87	37.08	27.87	61.43	67.45
SW_{net}	$AR_{<90}$	497	-7.03	33.25	33.99	-21.62	51.39	55.75	6.09	38.64	39.12	45.78	72.18	85.47
	AR_{90+}	241	-12.11	24.57	27.39	-30.00	42.74	52.22	-1.98	30.60	30.67	48.29	75.99	90.04
	no AR	836	-14.38	19.88	24.53	-15.25	21.32	26.21	-18.32	17.11	25.06	16.02	31.78	35.59
LW_{net}	$AR_{<90}$	497	-14.59	16.83	22.27	-17.48	20.25	26.75	-21.42	16.05	26.77	-0.42	33.35	33.35
	AR_{90+}	241	-11.43	12.87	17.21	-14.18	16.14	21.48	-17.44	12.00	21.17	-10.01	33.72	35.17
	no AR	777	-8.29	23.30	24.73	-30.75	37.46	48.46	-27.00	25.83	37.37			
SHF	$AR_{<90}$	459	-1.60	27.41	27.46	-39.18	44.12	59.00	-34.29	32.10	46.97			
	AR_{90+}	219	2.98	36.86	36.99	-39.39	45.38	60.09	-36.26	37.55	52.20			
	no AR	777	8.07	10.60	13.32	-8.09	24.20	25.52	-7.63	20.95	22.30			
LHF	$AR_{<90}$	459	7.73	12.99	15.12	-12.77	25.78	28.77	-10.98	22.63	25.16			
	AR_{90+}	219	13.95	16.77	21.81	-14.84	26.66	30.51	-13.99	22.50	26.50			

Table 3.4. As in Table 3.2, but MAR wind speed is compared to PROMICE observations (in units of m s^{-1}).

				Wind Speed		
Basin	Station	n	Data source	No AR	$AR_{<90}$	AR_{90+}
6	KAN_L	617; 193; 17	PROMICE	3.65	4.82	5.11
			MAR	5.20	6.80	7.71
	KAN_M	571; 176; 17	PROMICE	3.99	5.44	5.51
			MAR	4.41	5.86	6.90
	KAN_U	617; 192; 17	PROMICE	4.61	6.26	7.16
			MAR	3.99	5.54	6.73
	NUK_L	607; 174; 17	PROMICE	3.18	3.79	4.16
			MAR	5.07	6.03	7.86
	NUK_U	440; 122; 15	PROMICE	3.87	4.57	4.91
			MAR	5.01	6.06	8.25
8	THU_L	372; 100; 16	PROMICE	5.36	9.72	12.61
			MAR	4.78	9.41	12.11
	THU_U	491; 134; 27	PROMICE	5.48	9.29	12.19
			MAR	5.42	8.64	11.46
	UPE_L	567; 153; 30	PROMICE	2.74	3.77	6.02
			MAR	3.00	4.81	7.00
	UPE_U	564; 152; 30	PROMICE	4.15	5.02	7.18
			MAR	4.68	5.97	8.48
1	KPC_L	499; 118; 22	PROMICE	5.60	6.23	5.98
			MAR	5.20	5.45	5.74
	KPC_U	672; 162; 32	PROMICE	4.23	4.55	4.29
			MAR	4.37	4.62	4.49

Table 3.5. Comparison of daily mean liquid water path (g m^{-2}) retrievals from Summit Station with MAR, ERA5, and MERRA-2 data across categories of AR activity in basin 6. The "n" column denotes the sample size of "no AR", $AR_{<90}$, and AR_{90+} days during the 2010–2017 period of overlapping data. The mean uncertainty value for each AR category is also included for the Summit LWP data.

	n	Summit LWP (mean)	Summit LWP (mean uncertainty)	MAR LWP	ERA5 LWP	MERRA-2 LWP
No AR	383	12.85	4.50	0.23	9.26	14.66
$AR_{<90}$	127	21.23	4.51	0.20	11.50	17.84
AR_{90+}	16	35.66	4.53	0.55	18.99	21.85

Table 3.6. As in Table 3.5, but for categories of AR activity in basin 8.

	n	Summit LWP (mean)	Summit LWP (mean uncertainty)	MAR LWP	ERA5 LWP	MERRA-2 LWP
No AR	390	14.36	4.51	0.15	9.66	15.52
$AR_{<90}$	115	18.21	4.48	0.42	14.87	16.33
AR_{90+}	21	23.65	4.53	0.72	11.74	14.31

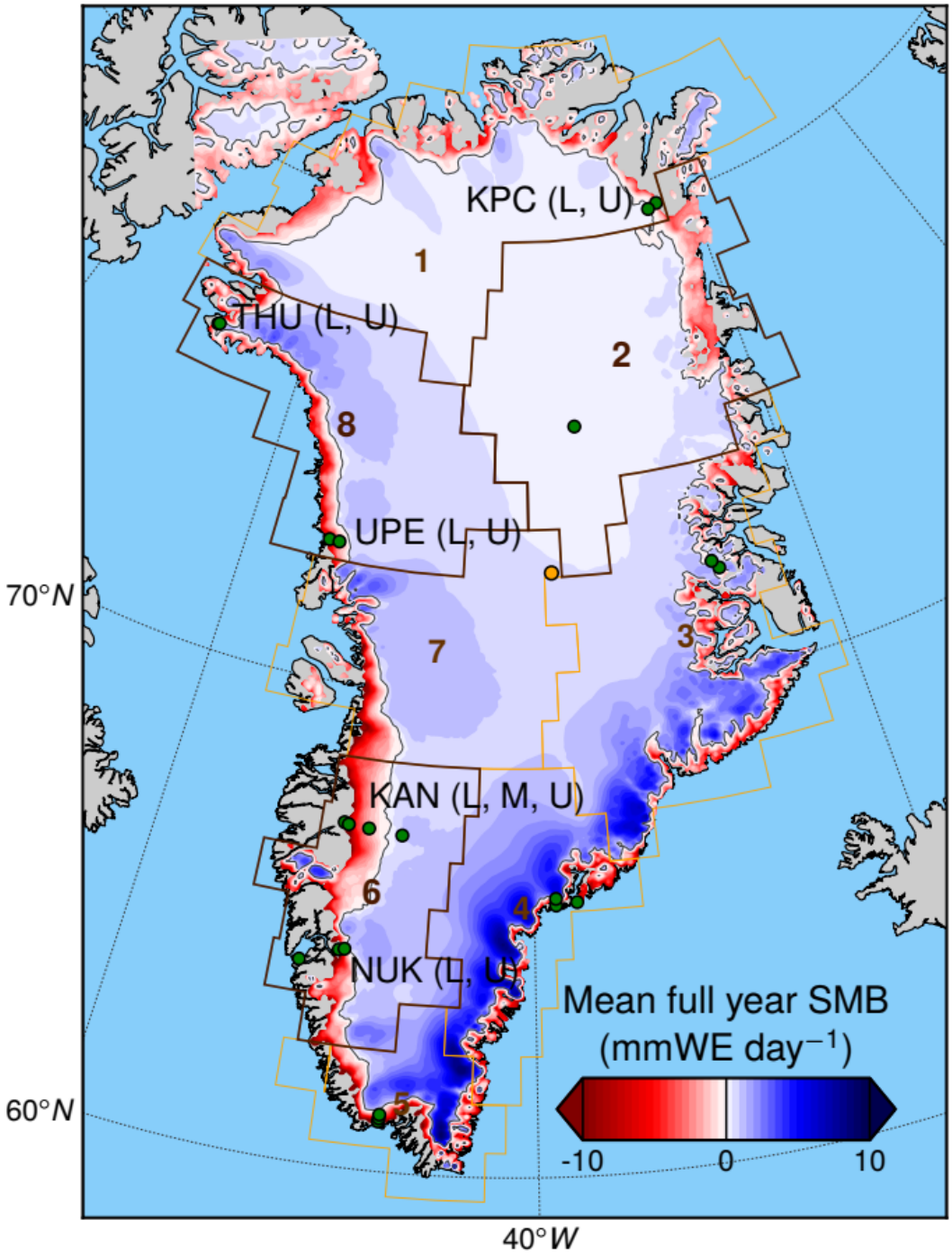

Figure 3.1. Annual mean surface mass balance modelled by MAR (1980–2017), locations of all active PROMICE stations (green dots), and location of Summit Station (orange dot). PROMICE stations utilized in this chapter are labeled, with stations labeled "L" and "U" the lower and upper station at each site (as well as the middle-elevation station labeled "M" in the Kangerlussuaq region). Outlines of the eight major GrIS drainage basins are also drawn on the map, with basins 2, 6, and 8 emphasized in this study.

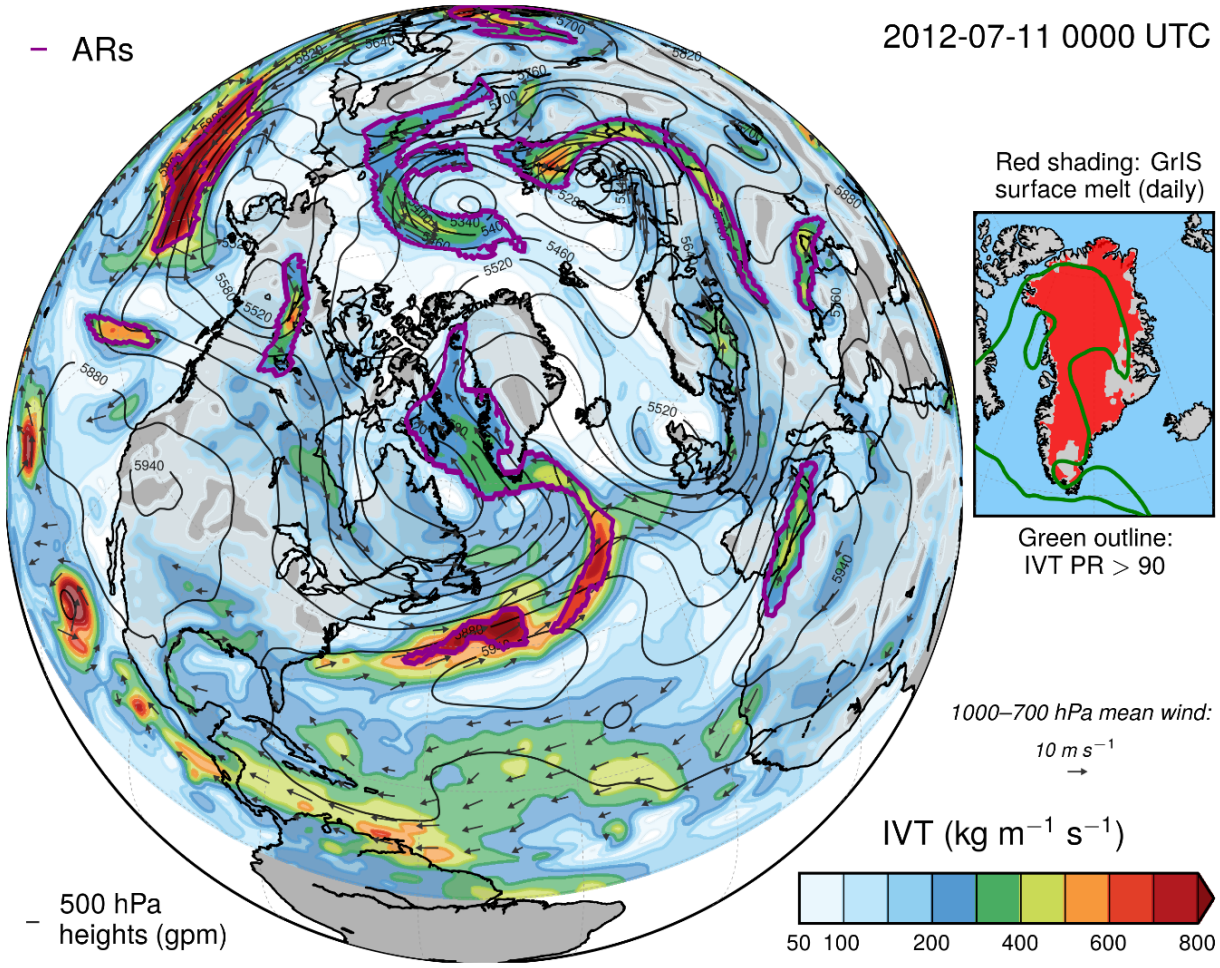

Figure 3.2. MERRA-2 IVT, 500 hPa height, 1000–700 hPa mean wind, and outlines of AR features during extreme West Greenland AR / melt event on 11 July 2012. Inset panel shows extent of GrIS surface melt detected by passive microwave satellite observations and outline of area where IVT percentile rank (PR) exceeded the 90th climatological percentile.

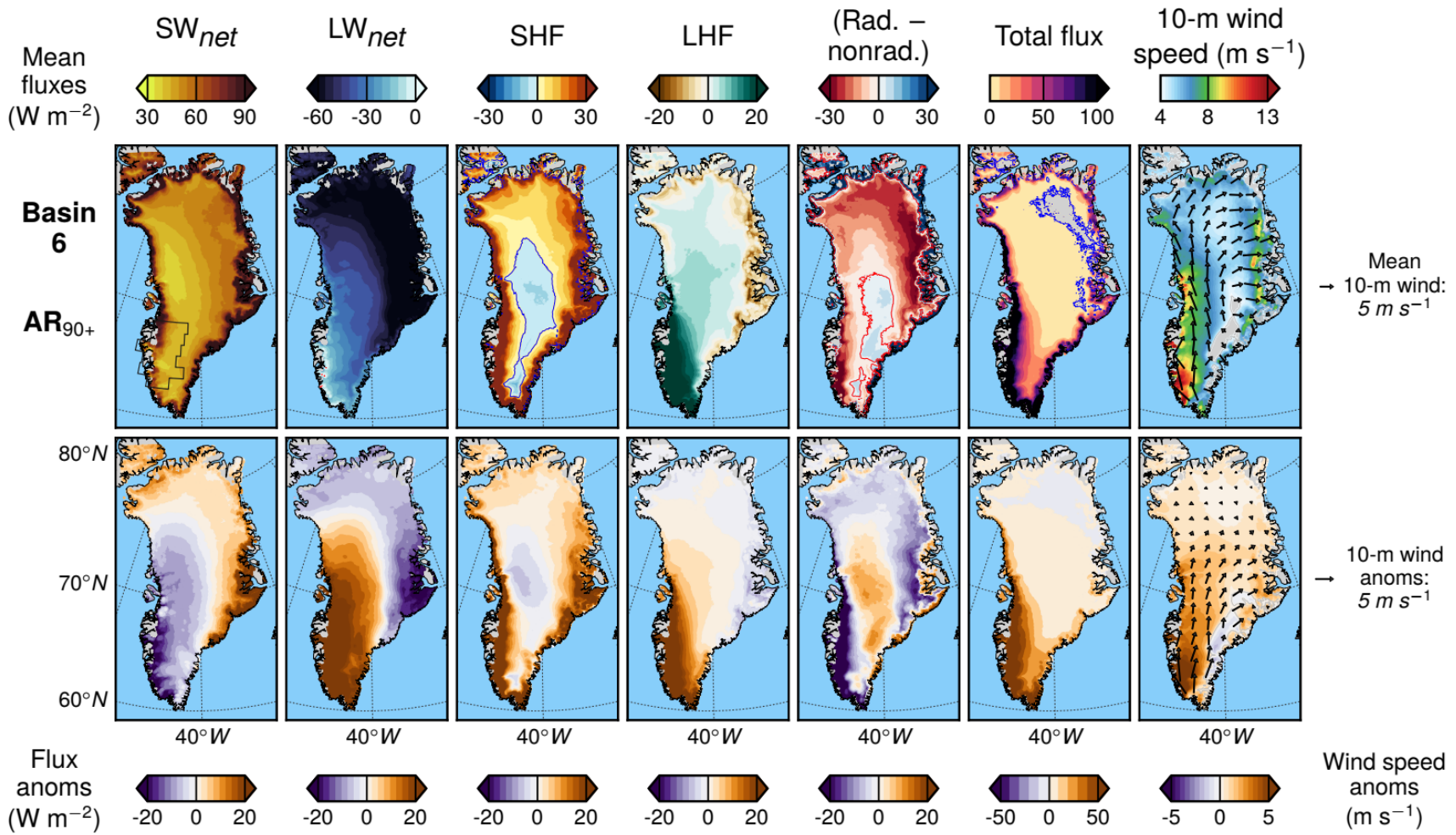

Figure 3.3. Surface energy balance terms from MAR: composite means (top row) and anomalies (bottom row) on AR$_{90+}$ days in basin 6. Also included are composite mean and anomalies of the difference between summed radiative and non-radiative flux terms (rad. – nonrad.), the sum of all terms (total flux), and maps of 10-m wind speed and direction.

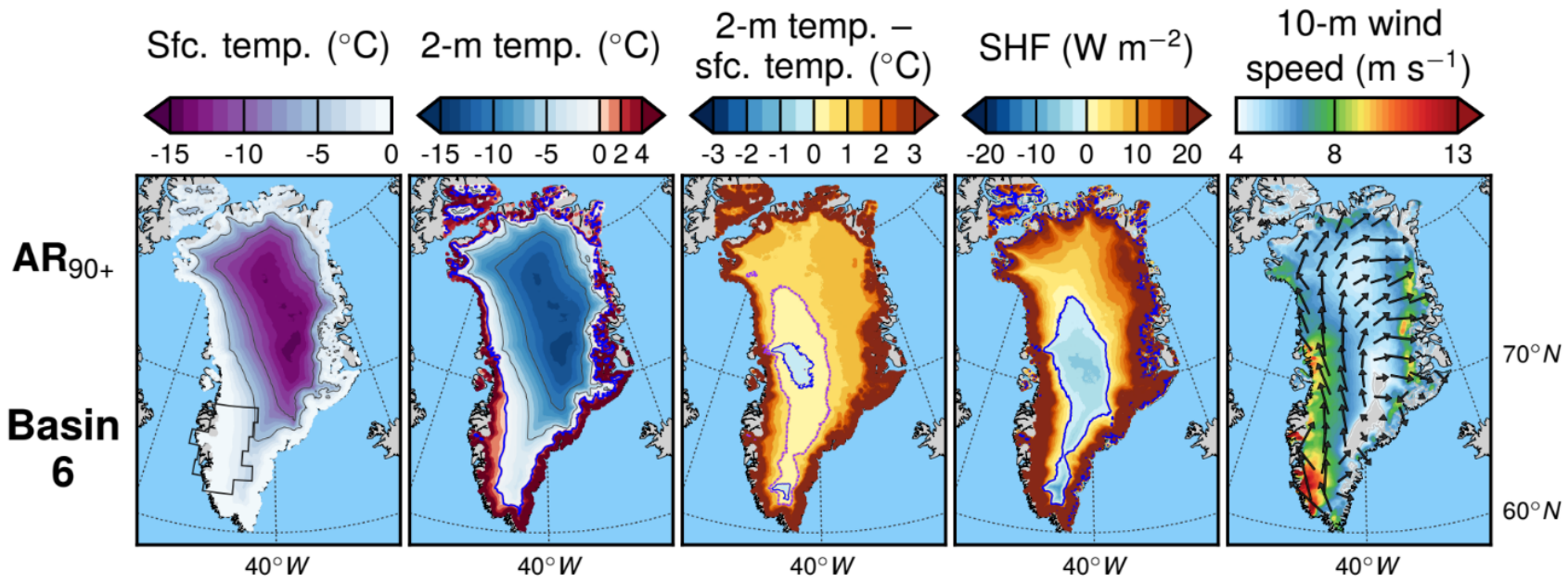

Figure 3.4. Maps explaining the spatial patterns of positive and negative SHF simulated by MAR over the GrIS during AR_{90+} events in basin 6: ice sheet surface temperature, 2-m temperature, the difference between 2-m temperature and ice sheet surface temperature (with differences < 0.5°C outlined in purple), SHF, and 10-m wind speed.

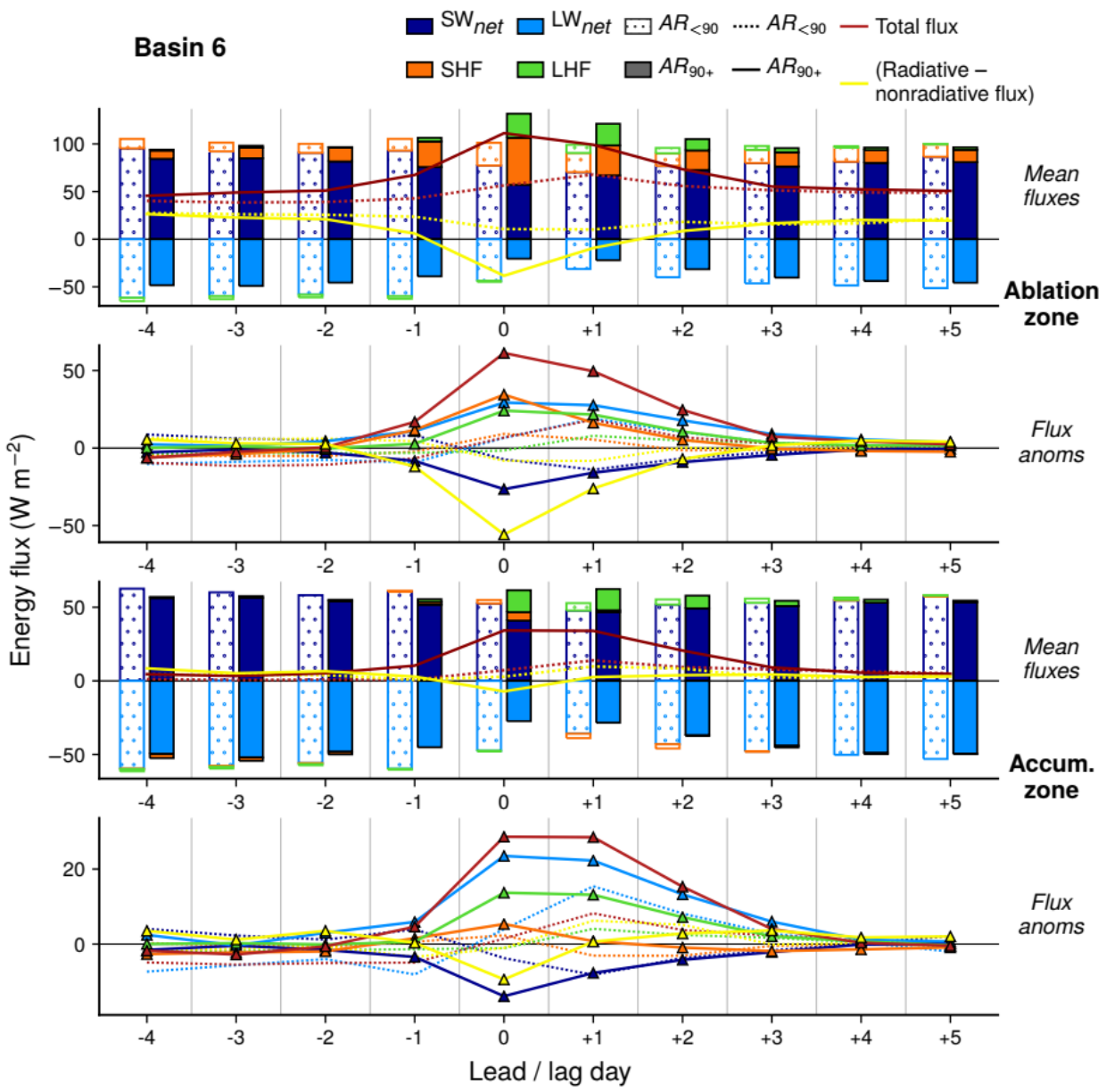

Figure 3.5. Composite mean and anomalies of MAR surface energy balance terms averaged over the ablation zone and accumulation zone of basin 6 for the days surrounding $AR_{<90}$ and AR_{90+} events. Also plotted is the difference between summed radiative and non-radiative flux terms (yellow lines) and the sum of all terms (red lines).

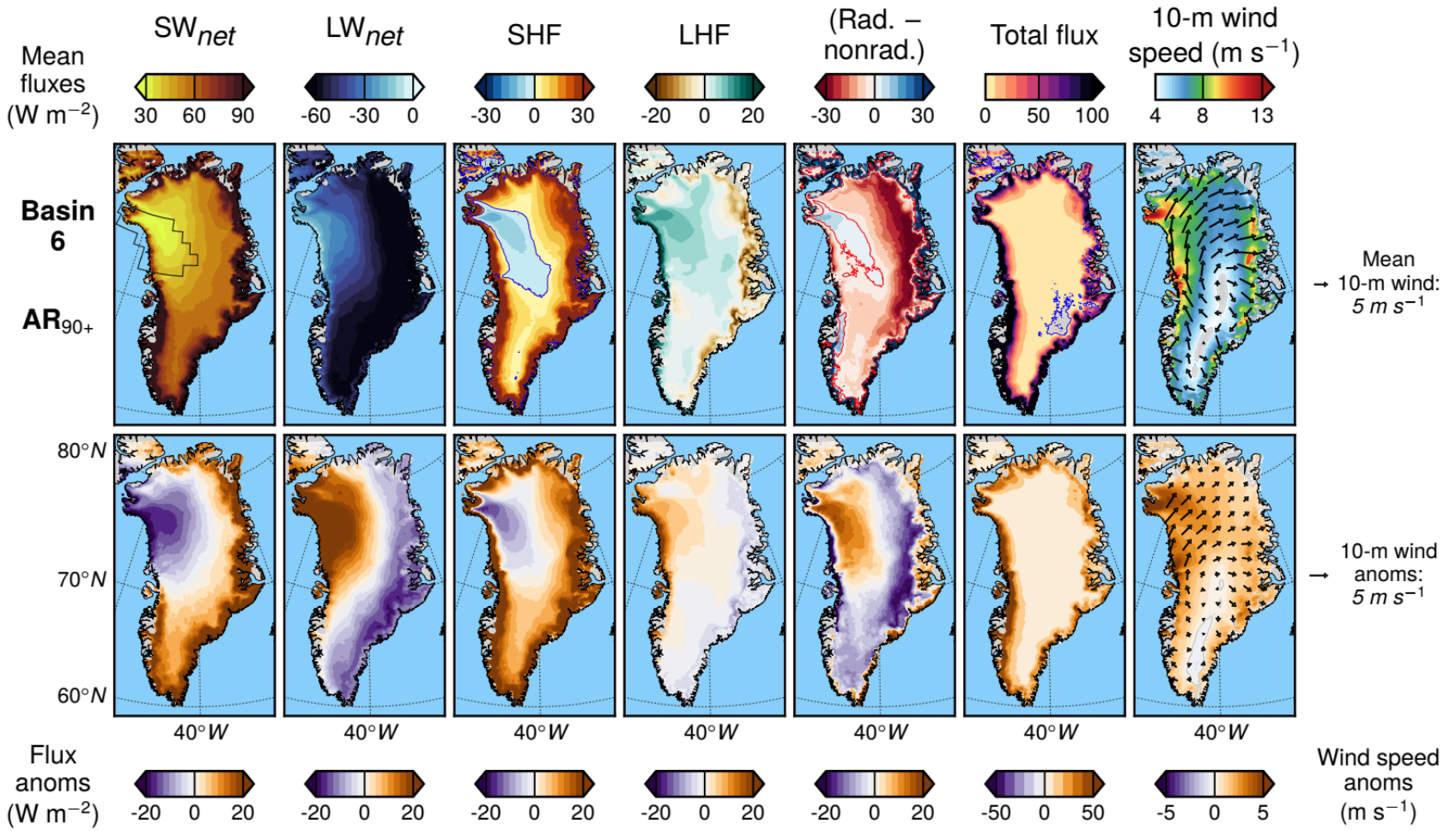

Figure 3.6. As in Figure 3.3 but for basin 8 AR$_{90+}$ days.

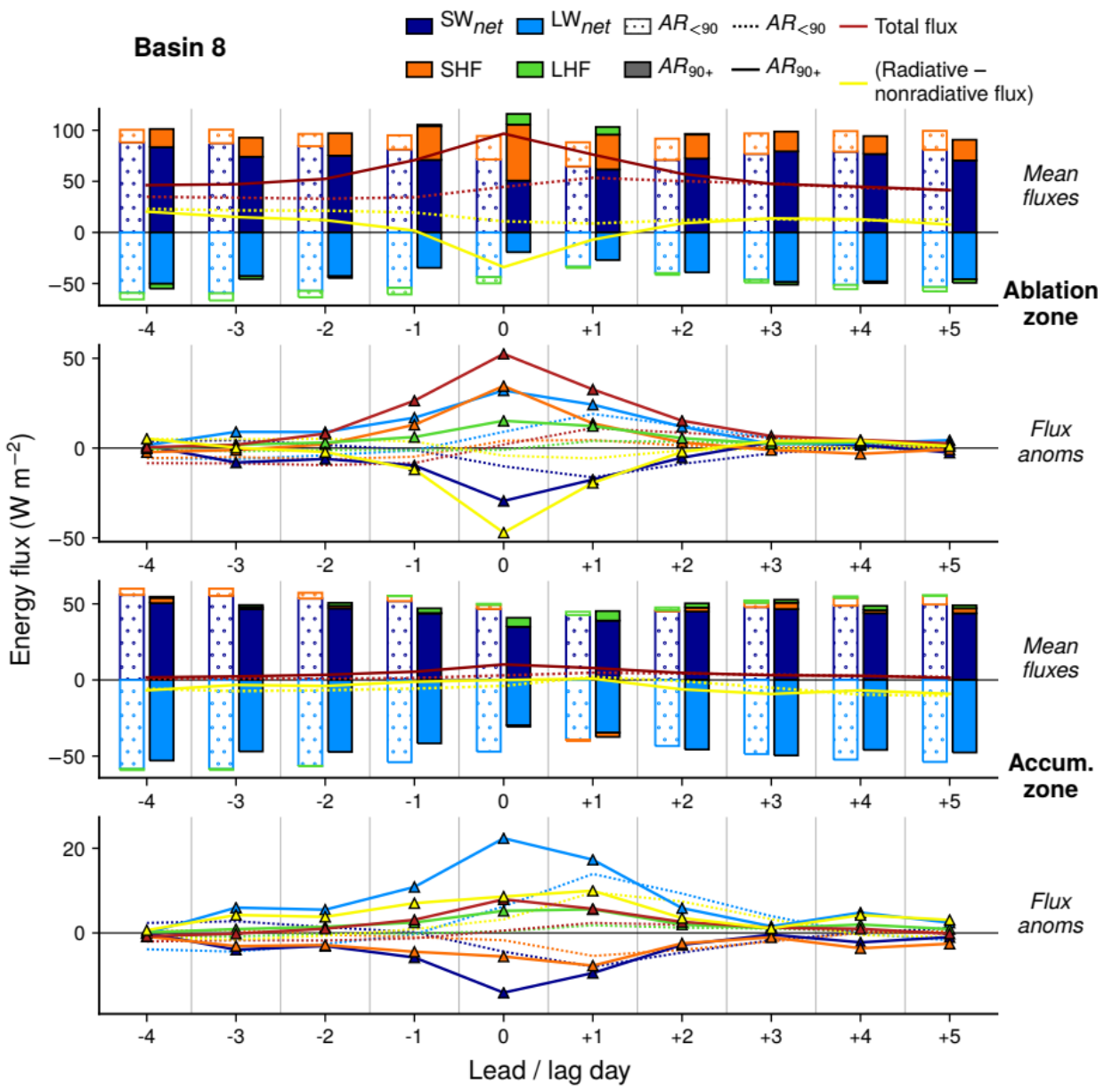

Figure 3.7. Composite mean and anomalies of MAR surface energy balance terms averaged over the ablation zone and accumulation zone of basin 8 for the days surrounding $AR_{<90}$ and AR_{90+} events. Also plotted is the difference between summed radiative and non-radiative flux terms (yellow lines) and the sum of all terms (red lines).

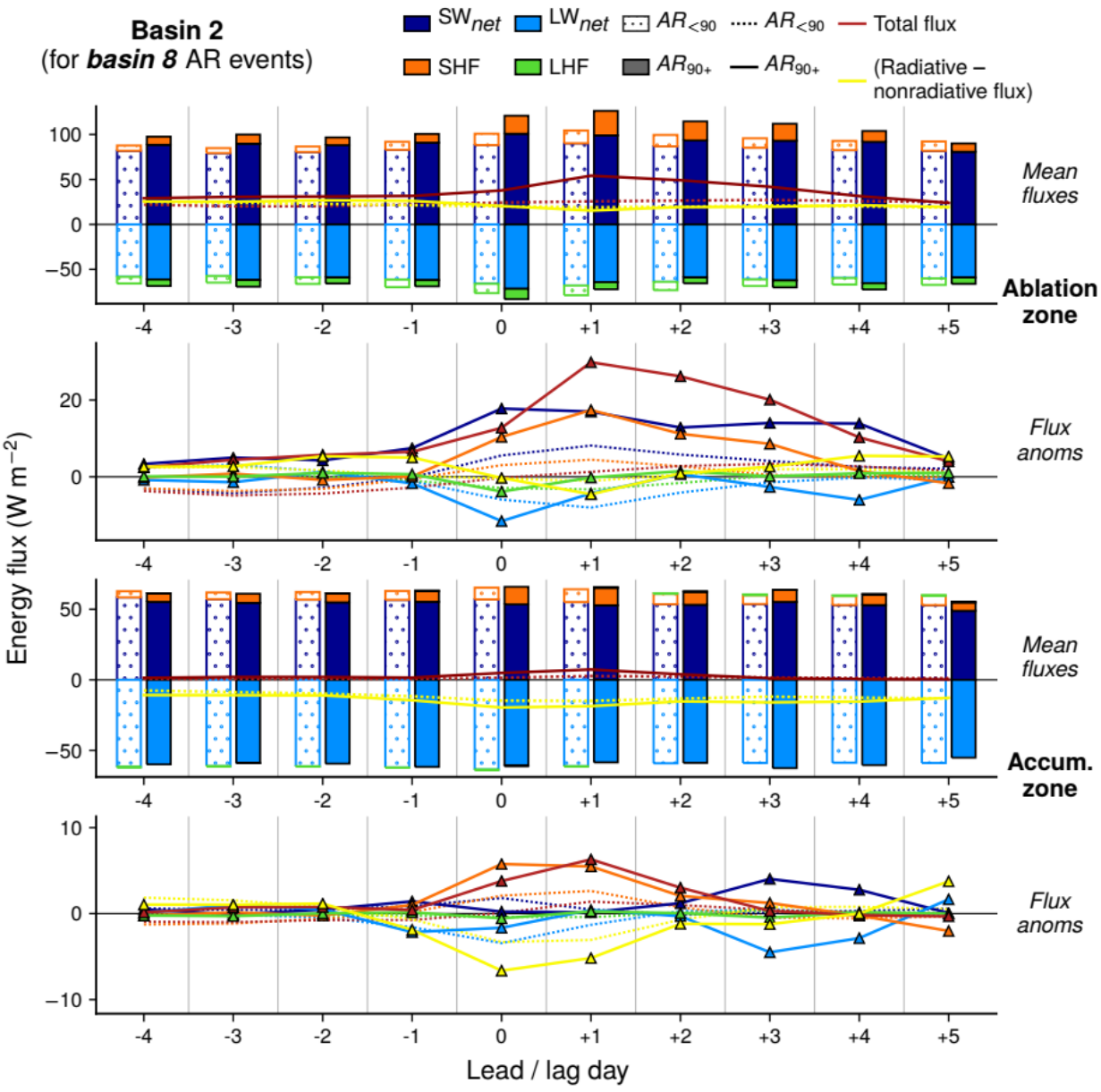

Figure 3.8. As in Figure 3.7, except quantities plotted are averaged over the ablation and accumulation zones of basin 2 in relation to AR events over basin 8.

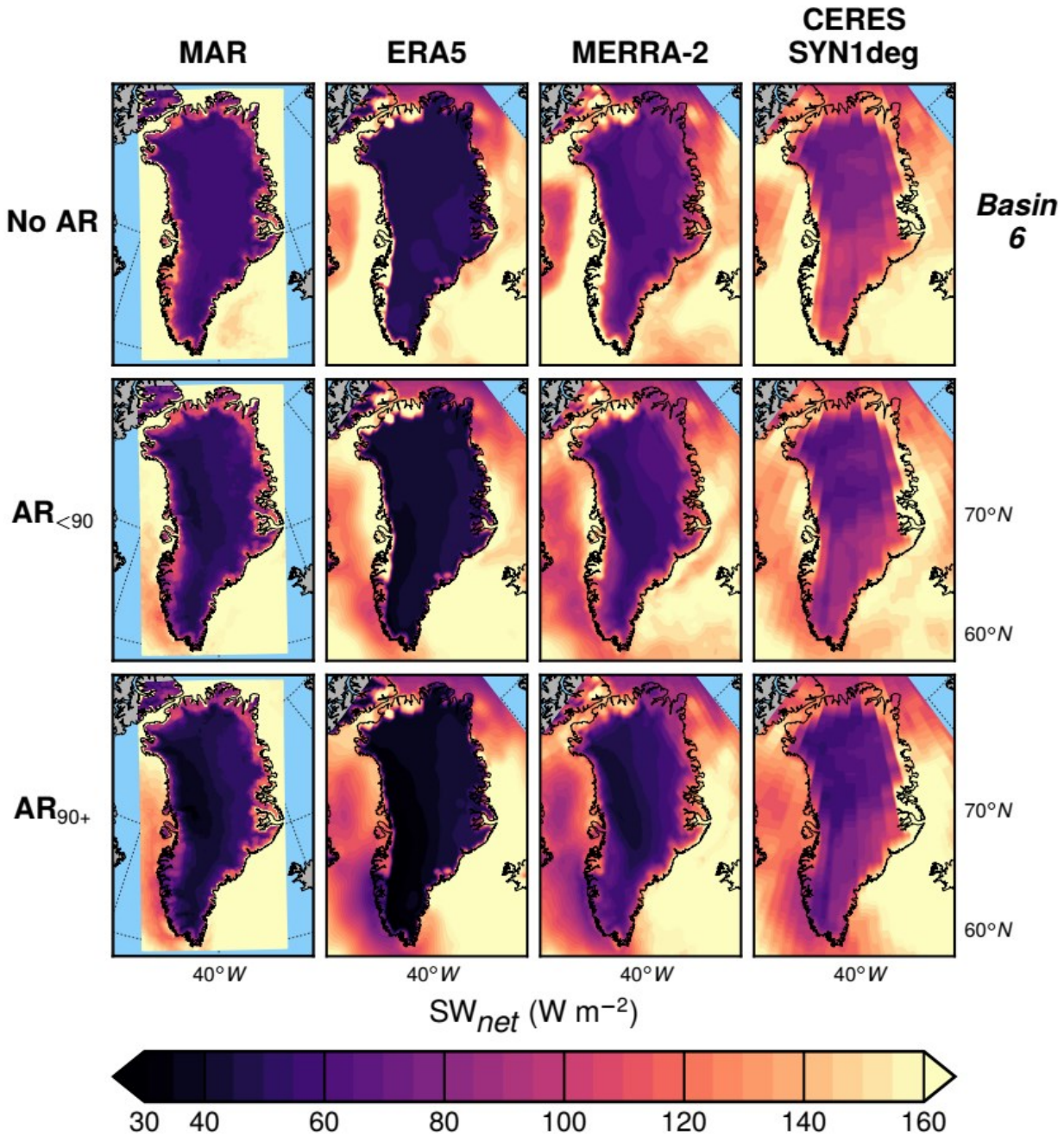

Figure 3.9. Comparison of mean SW_{net} from MAR, ERA5, MERRA-2, and CERES SYN1deg across categories of AR activity in basin 6.

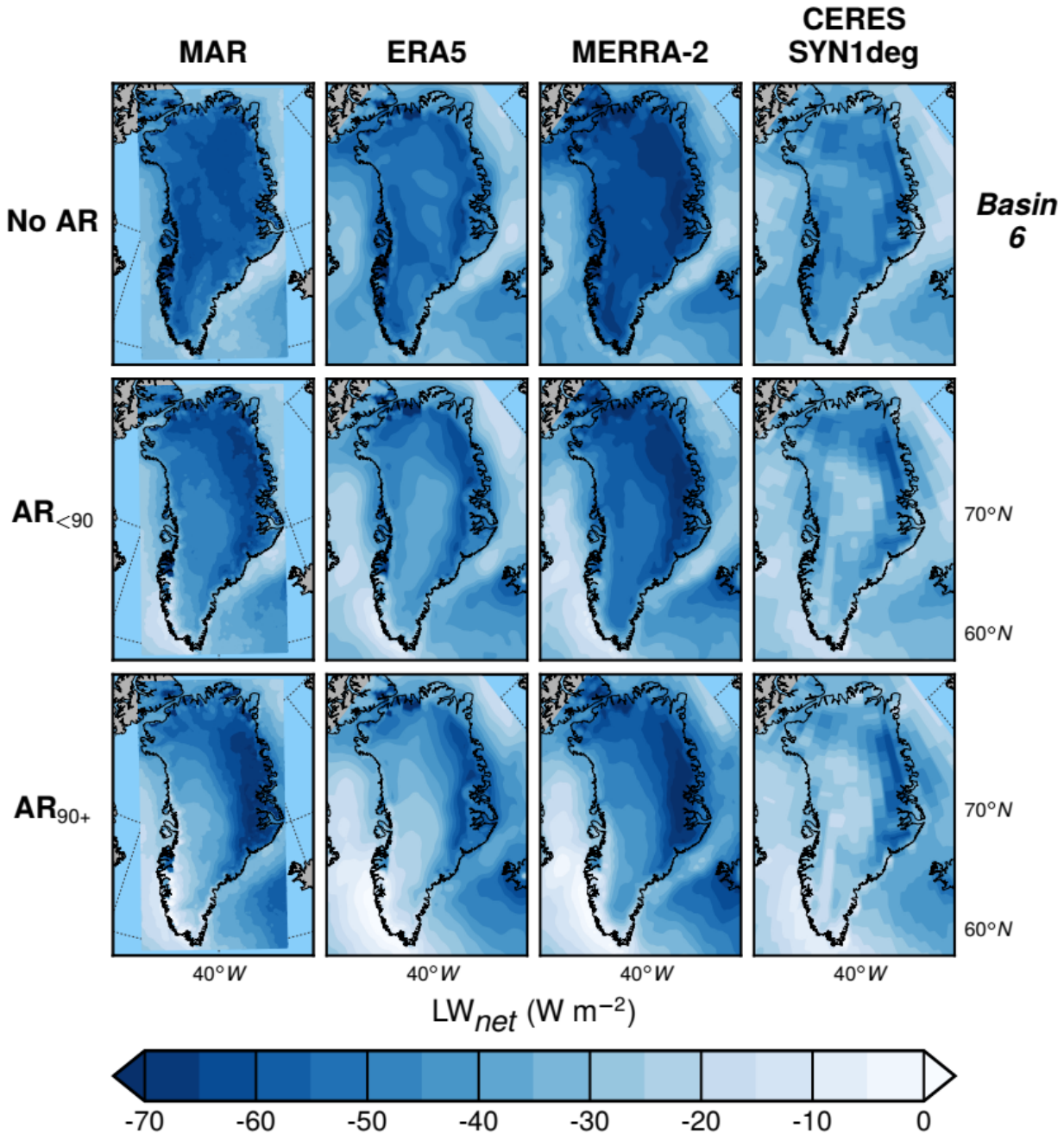

Figure 3.10. Comparison of mean LW_{net} from MAR, ERA5, MERRA-2, and CERES SYN1deg across categories of AR activity in basin 6.

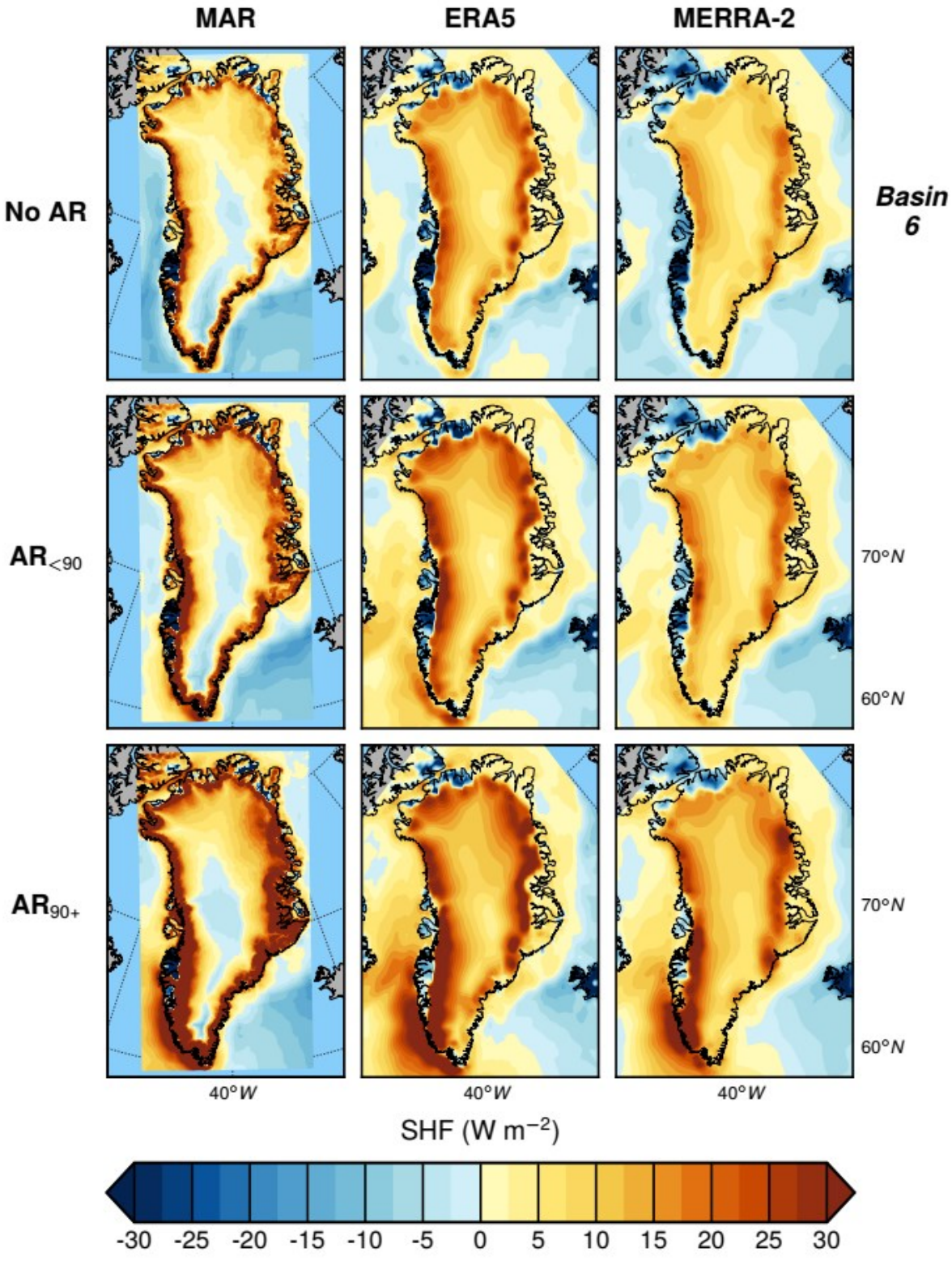

Figure 3.11. Comparison of mean SHF from MAR, ERA5, and MERRA-2 across categories of AR activity in basin 6.

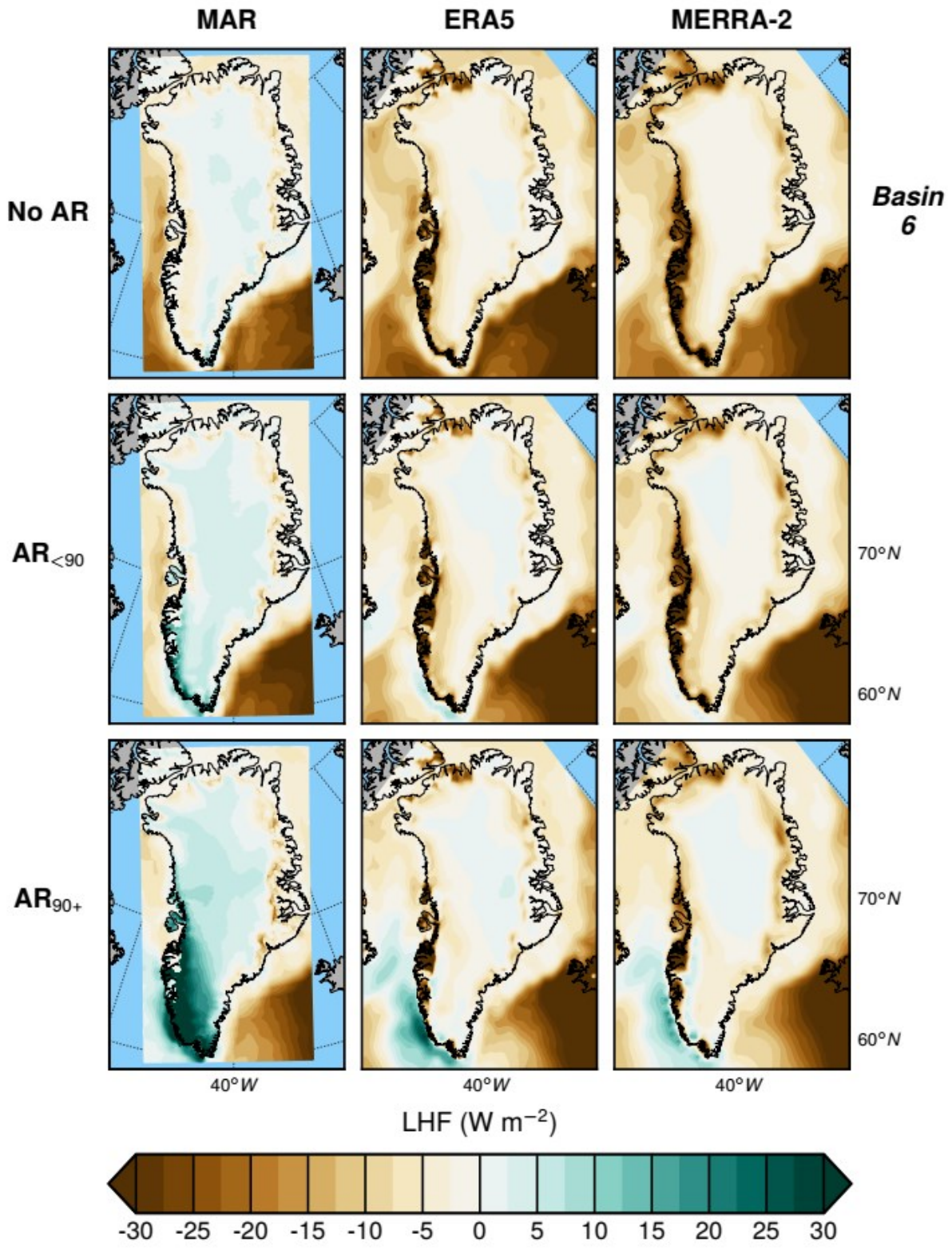

Figure 3.12. Comparison of mean LHF from MAR, ERA5, and MERRA-2 across categories of AR activity in basin 6.

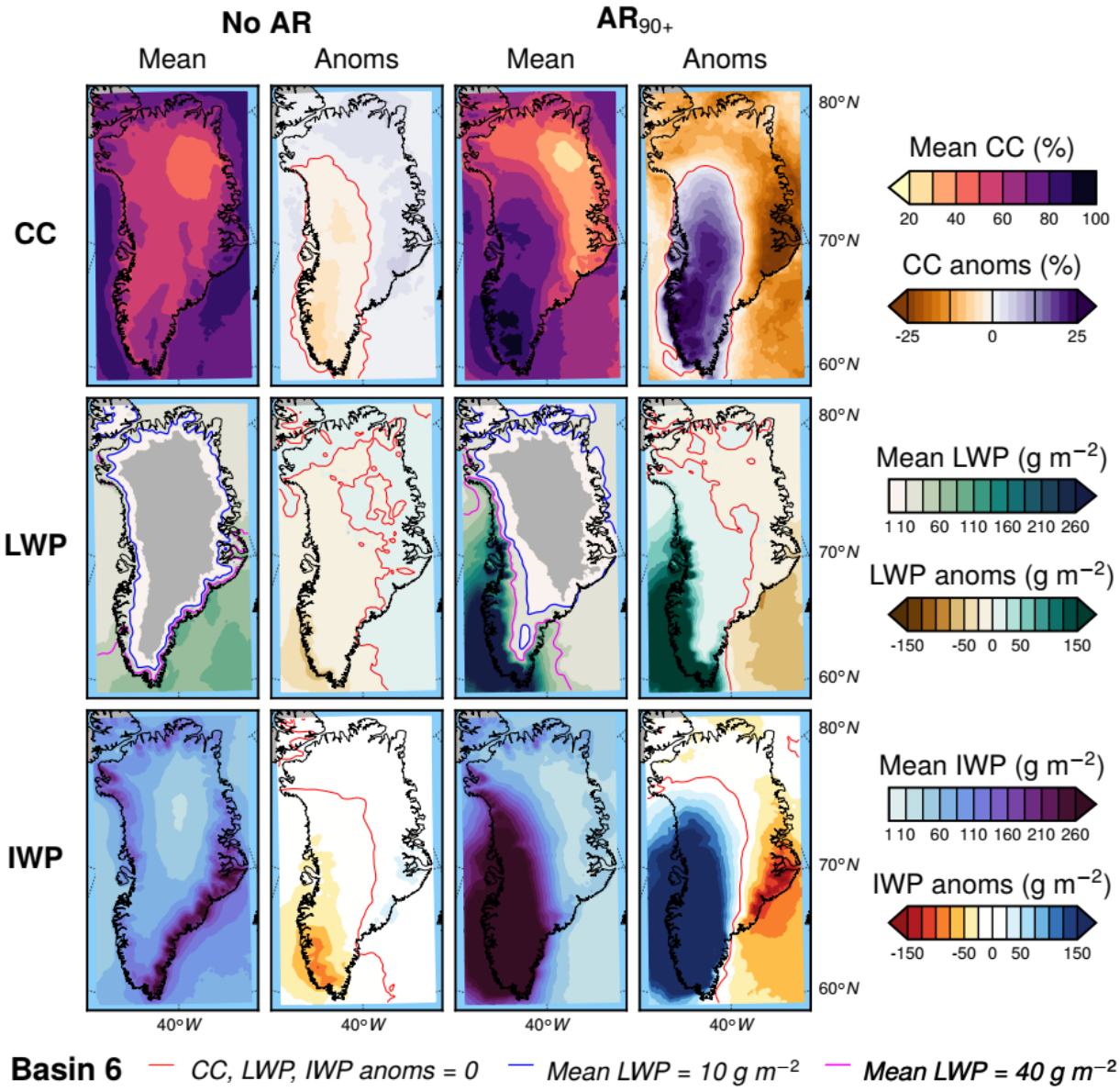

Figure 3.13. Composite mean and anomaly maps of MAR cloud cover (CC), cloud liquid water path (LWP), and cloud ice water path (IWP) from MAR for "no AR" days (left 2 columns) and AR_{90+} days (right 2 columns) over basin 6. Contours of 10 g m^{-2} and 40 g m^{-2} values are also plotted on the LWP maps, as previous studies [e.g. *Bennartz et al*., 2013] have found that these LWP values are associated with "radiatively opaque" clouds and a positive cloud radiative effect.

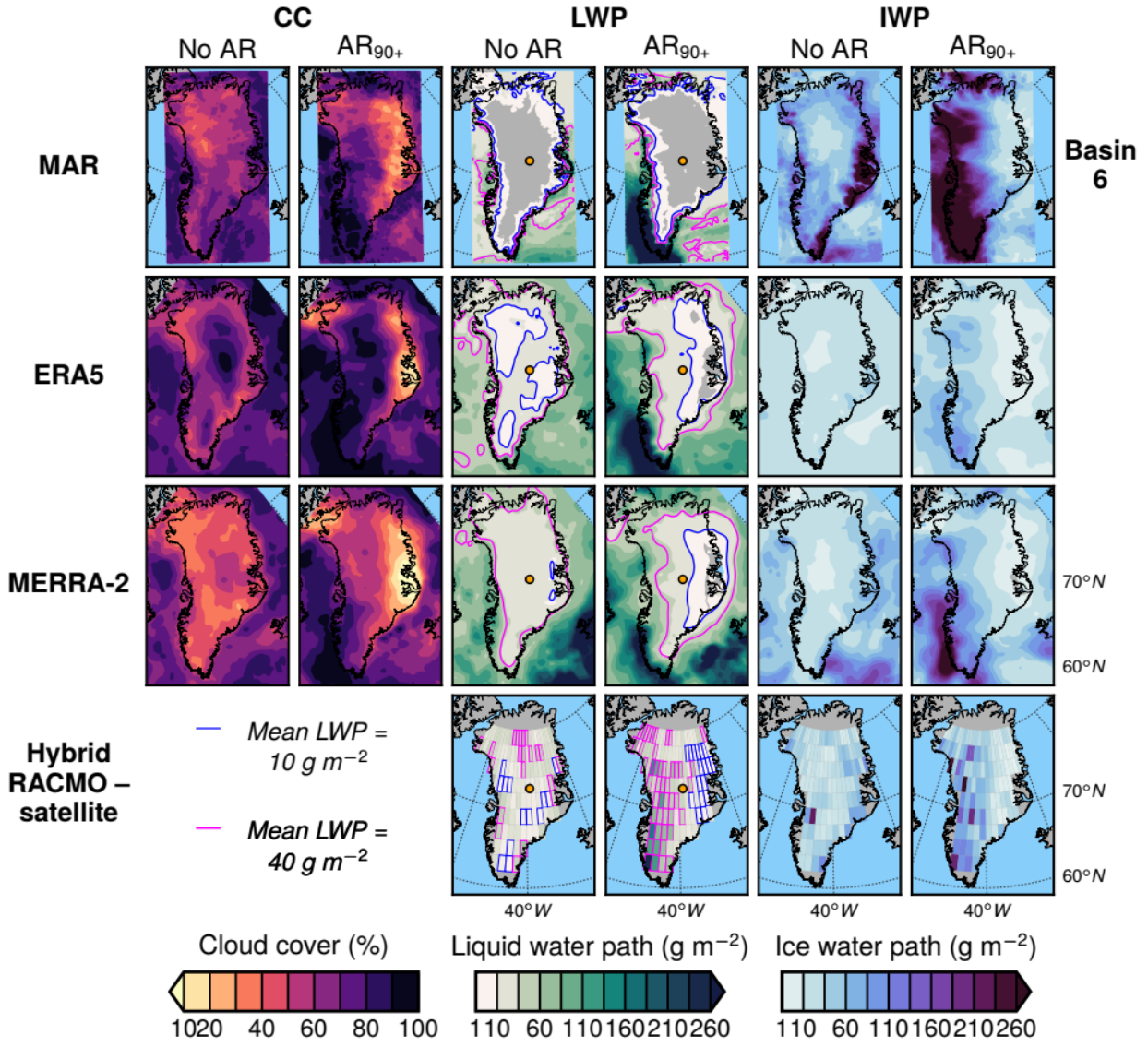

Figure 3.14. Comparison of mean cloud cover (CC), cloud liquid water path (LWP), and cloud ice water path (IWP) from MAR, ERA5, MERRA-2, and hybrid RACMO-satellite data on "no AR" and AR_{90+} days in basin 6 during 2010–2017. As in Figure 3.13, contours of 10 g m^{-2} and 40 g m^{-2} values are plotted on the LWP maps in blue and pink, respectively (on hybrid RACMO-satellite maps, grid cells with < 10 g m^{-2} LWP are outlined in blue and > 40 g m^{-2} LWP in pink). The location of Summit Station is plotted with an orange dot on LWP maps.

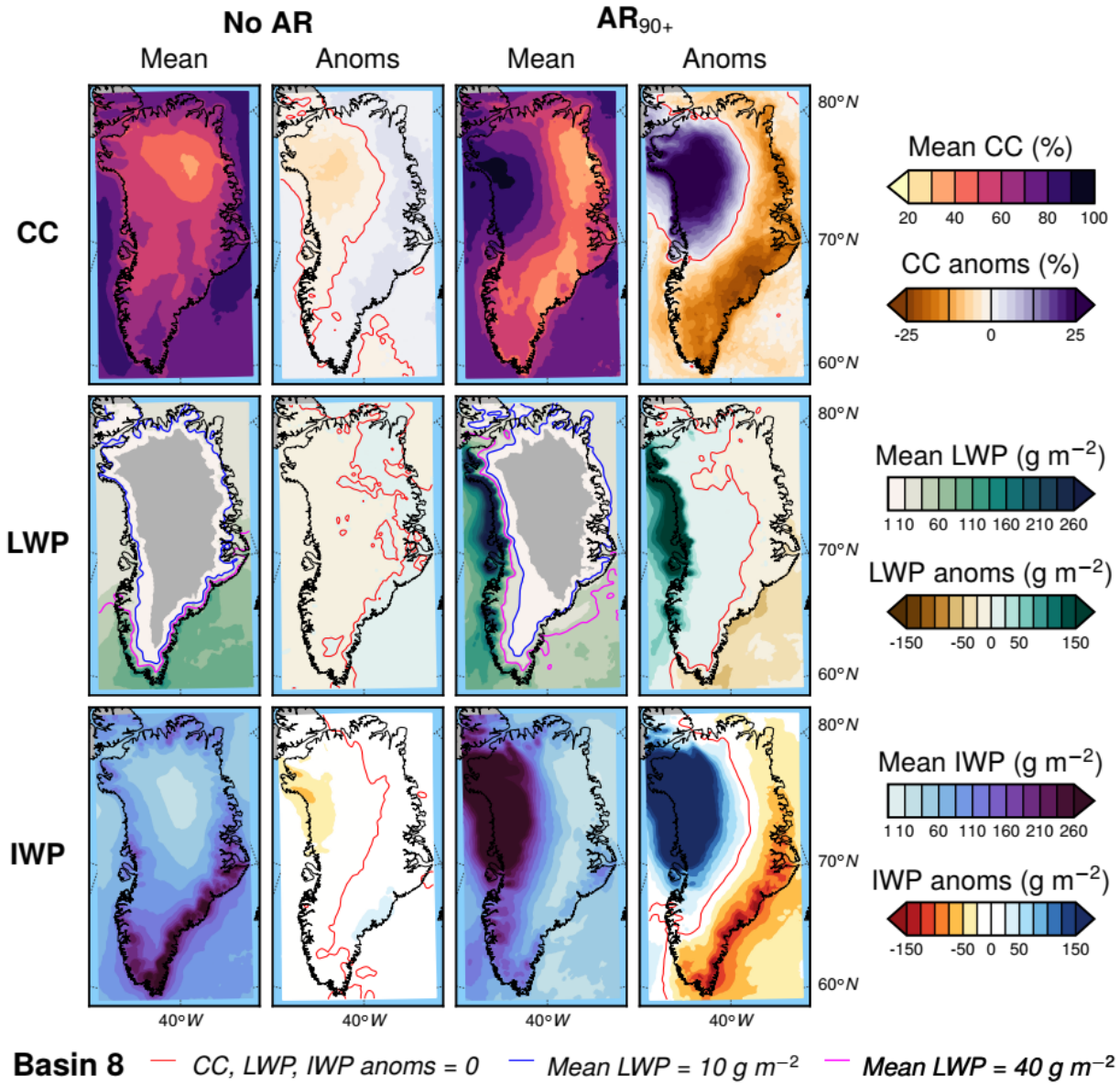

Figure 3.15. Composite mean and anomaly maps of MAR cloud cover (CC), cloud liquid water path (LWP), and cloud ice water path (IWP) from MAR for "no AR" days (left 2 columns) and AR_{90+} days (right 2 columns) over basin 8. Contours of 10 g m^{-2} and 40 g m^{-2} values are also plotted on the LWP maps.

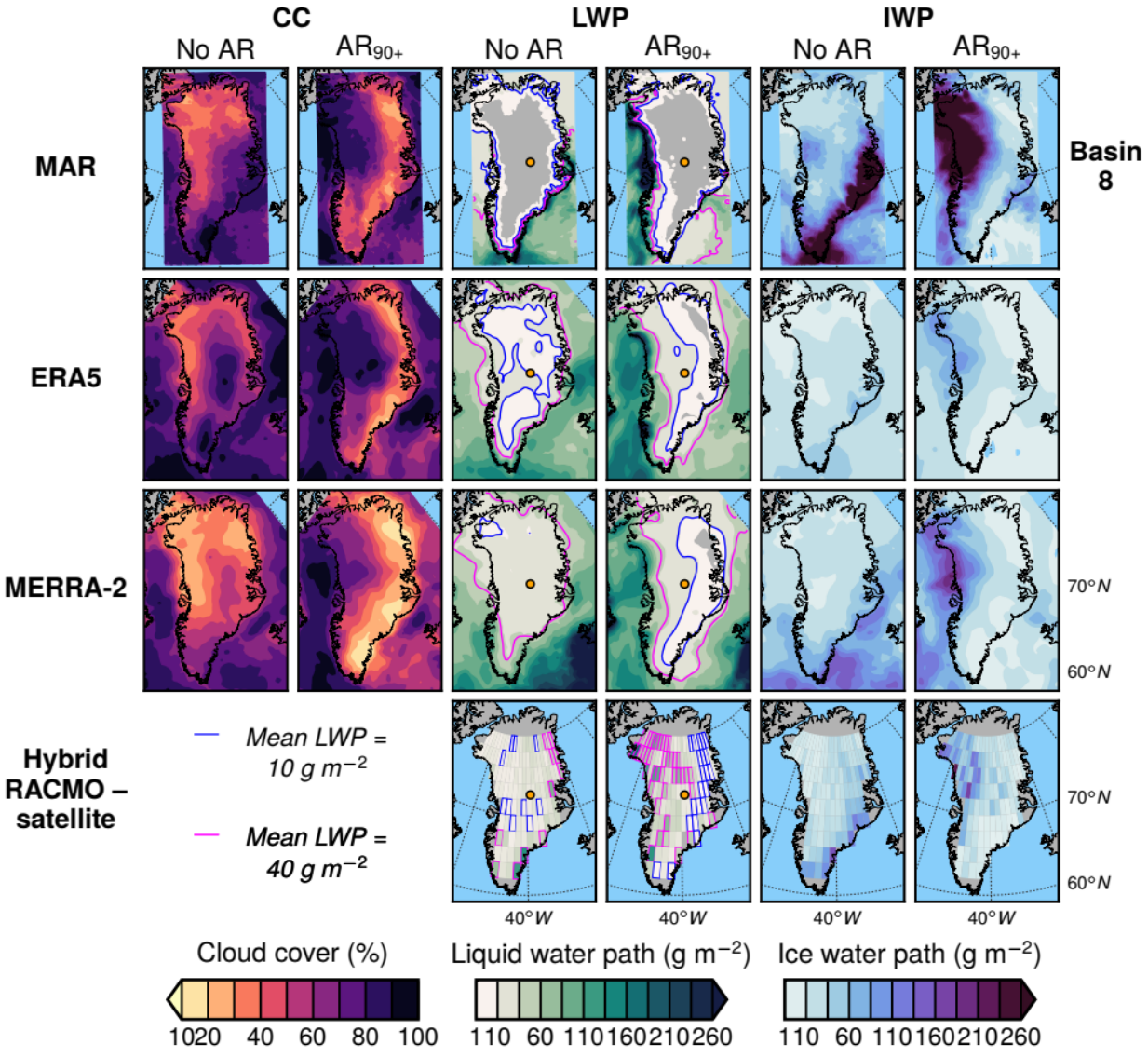

Figure 3.16. Comparison of mean cloud cover (CC), cloud liquid water path (LWP), and cloud ice water path (IWP) from MAR, ERA5, MERRA-2, and hybrid RACMO-satellite data on "no AR" and AR_{90+} days in basin 8 during 2010–2017. As in Figure 3.15, contours of 10 g m^{-2} and 40 g m^{-2} values are plotted on the LWP maps in blue and pink, respectively (on hybrid RACMO-satellite maps, grid cells with < 10 g m^{-2} LWP are outlined in blue and > 40 g m^{-2} LWP in pink). The location of Summit Station is plotted with an orange dot on LWP maps.

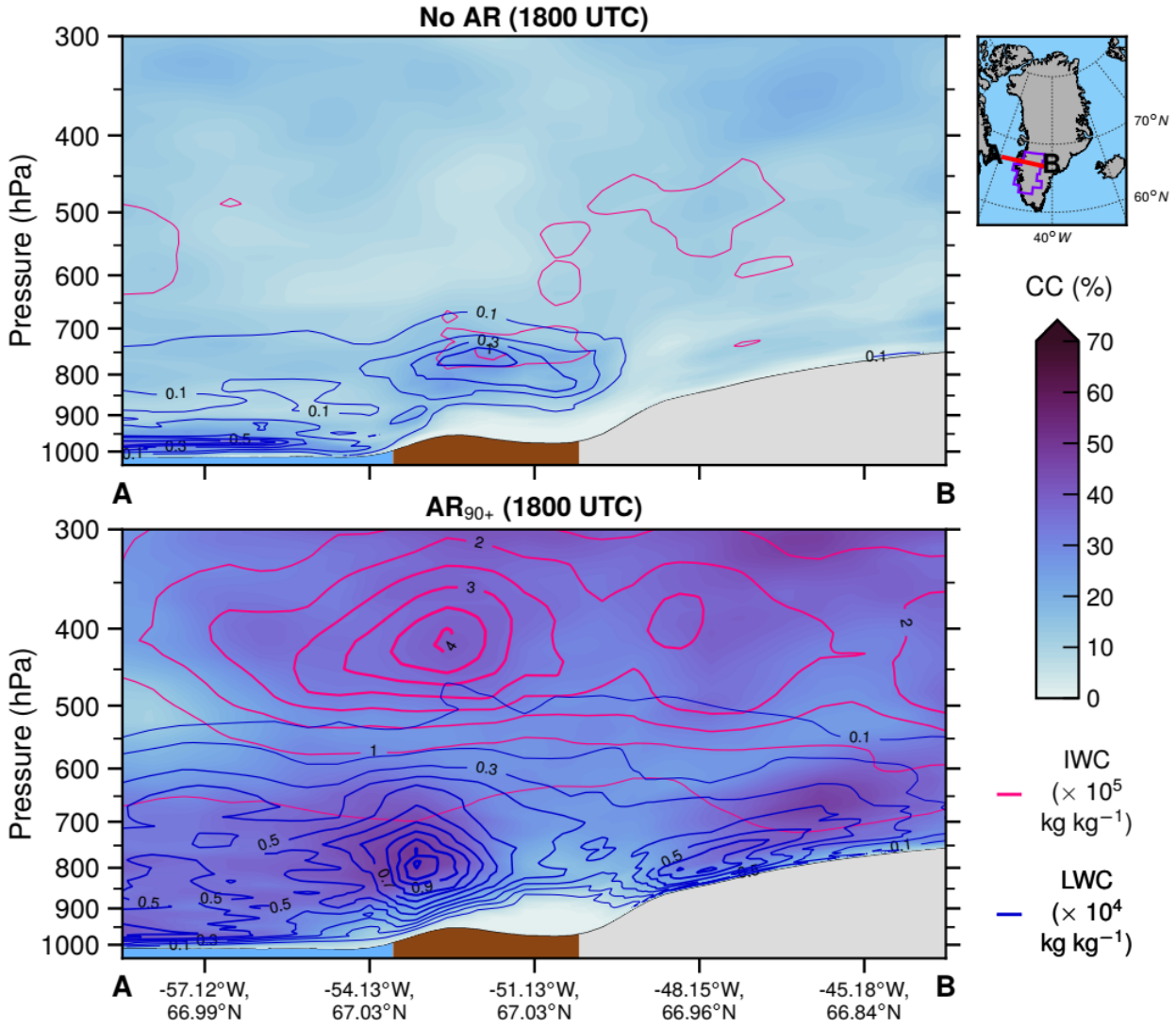

Figure 3.17. Vertical cross sections of ERA5 cloud cover (CC), cloud specific ice water content (IWC), and cloud specific liquid water content (LWC) along a transect extending from Davis Strait inland through the K-transect region of basin 6. Cross sections are composites of conditions at 1800 UTC on "no AR" days (top) and AR_{90+} days (bottom). Inset map shows location of transect from point A to point B. Below-surface areas are filled according to surface type: ocean (blue), ice-free land (brown), and ice sheet (light gray).

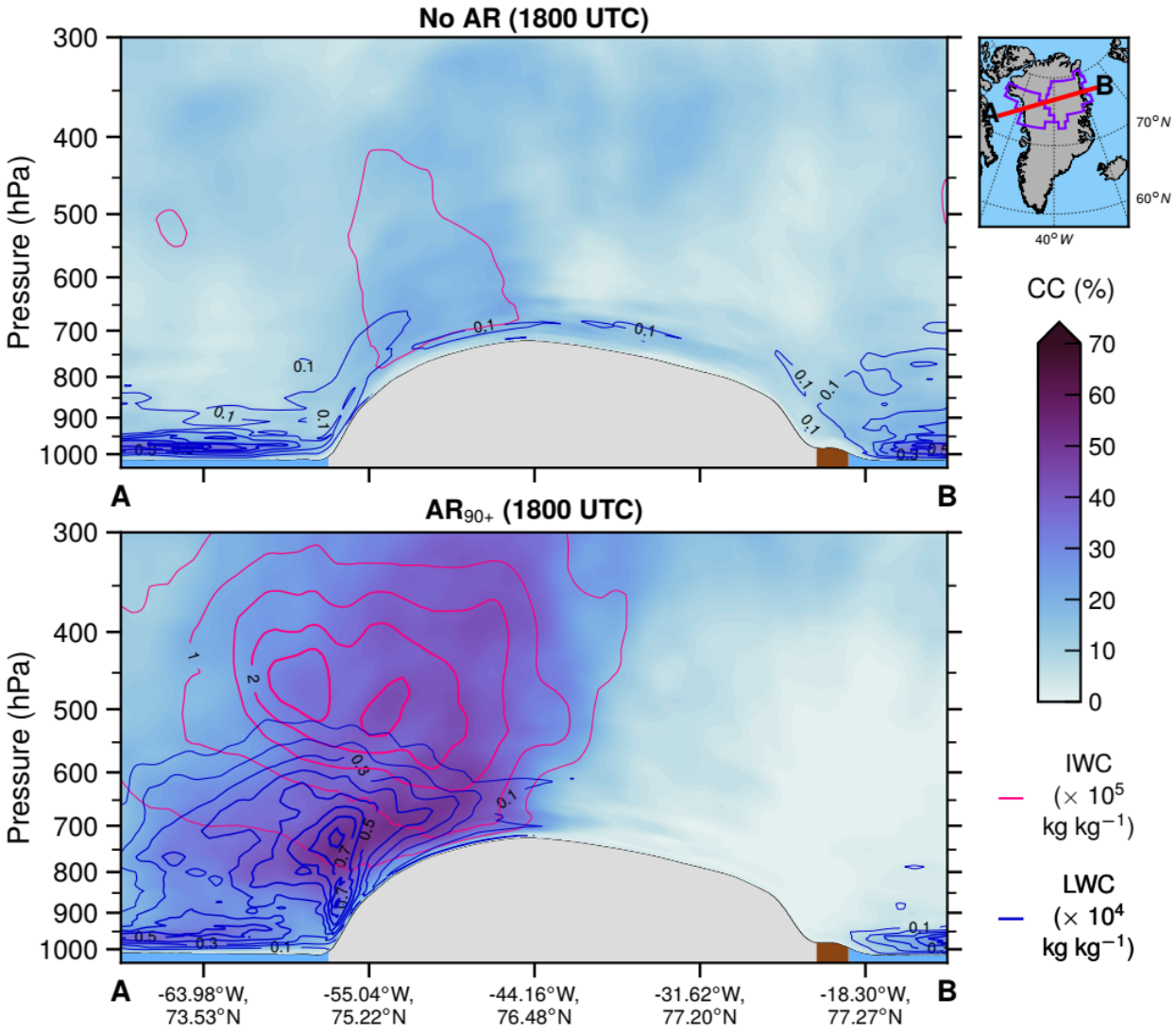

Figure 3.18. As in Figure 3.17, but for basin 8 "no AR" and AR_{90+} days. Cross sections are extended across Greenland from basin 8 through basin 2 to show conditions in northeast Greenland during AR events affecting northwest Greenland.

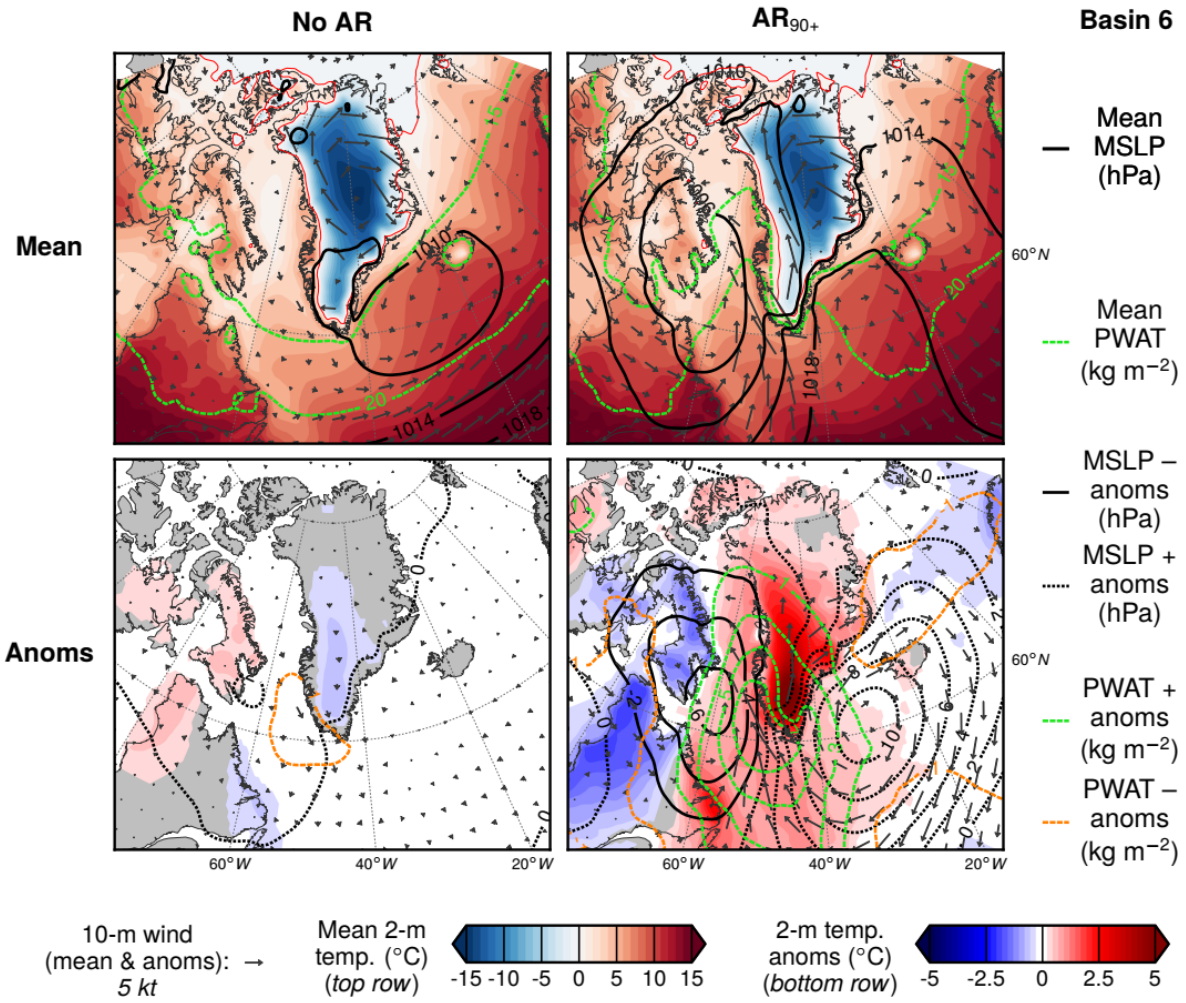

Figure 3.19. Synoptic composite mean and anomaly maps of near-surface conditions from MERRA-2 on "no AR" and AR_{90+} days in basin 6. Variables mapped are mean sea level pressure (MSLP), 10-m wind, 2-m temperature, and precipitable water (PWAT).

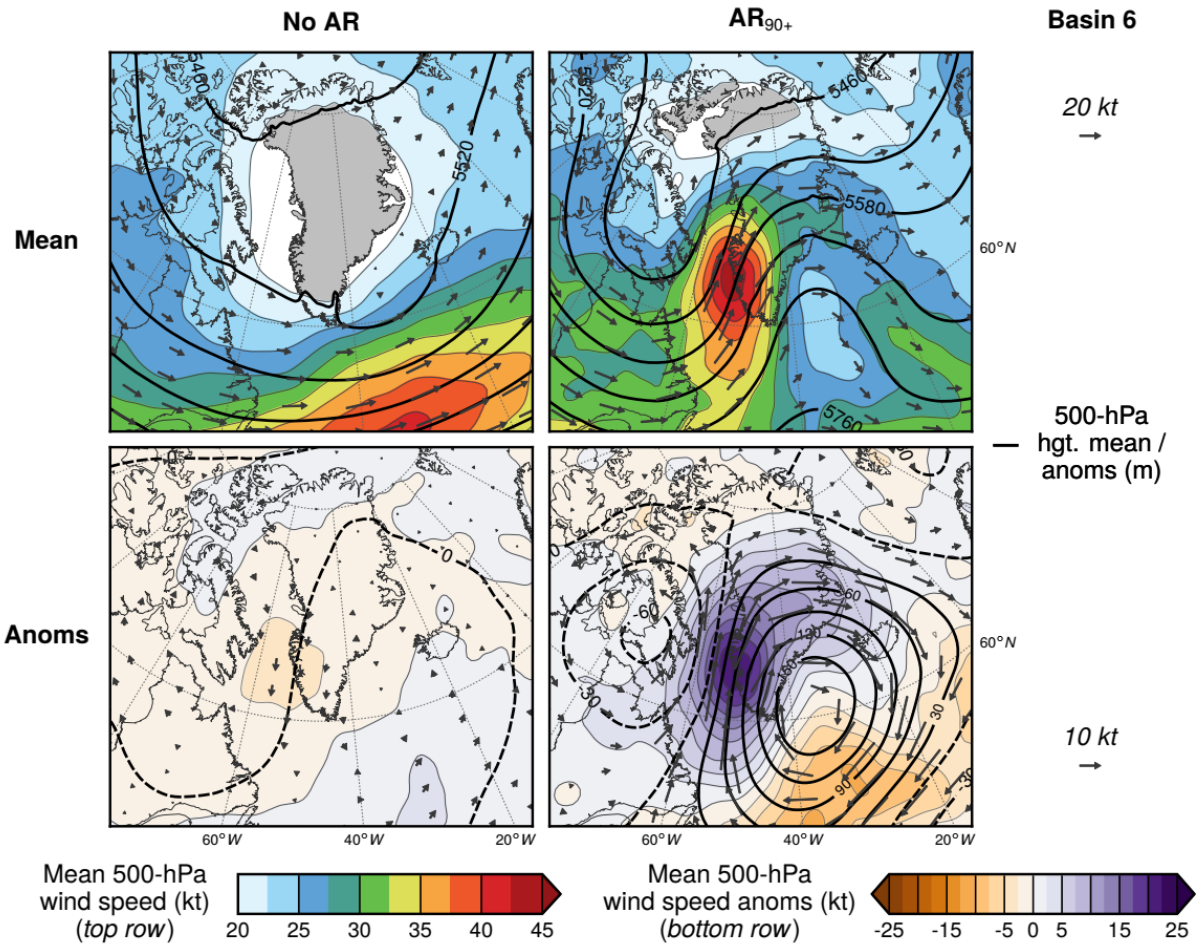

Figure 3.20. As in Fig. 3.19 but for mid-tropospheric (500 hPa) variables: geopotential height and wind speed.

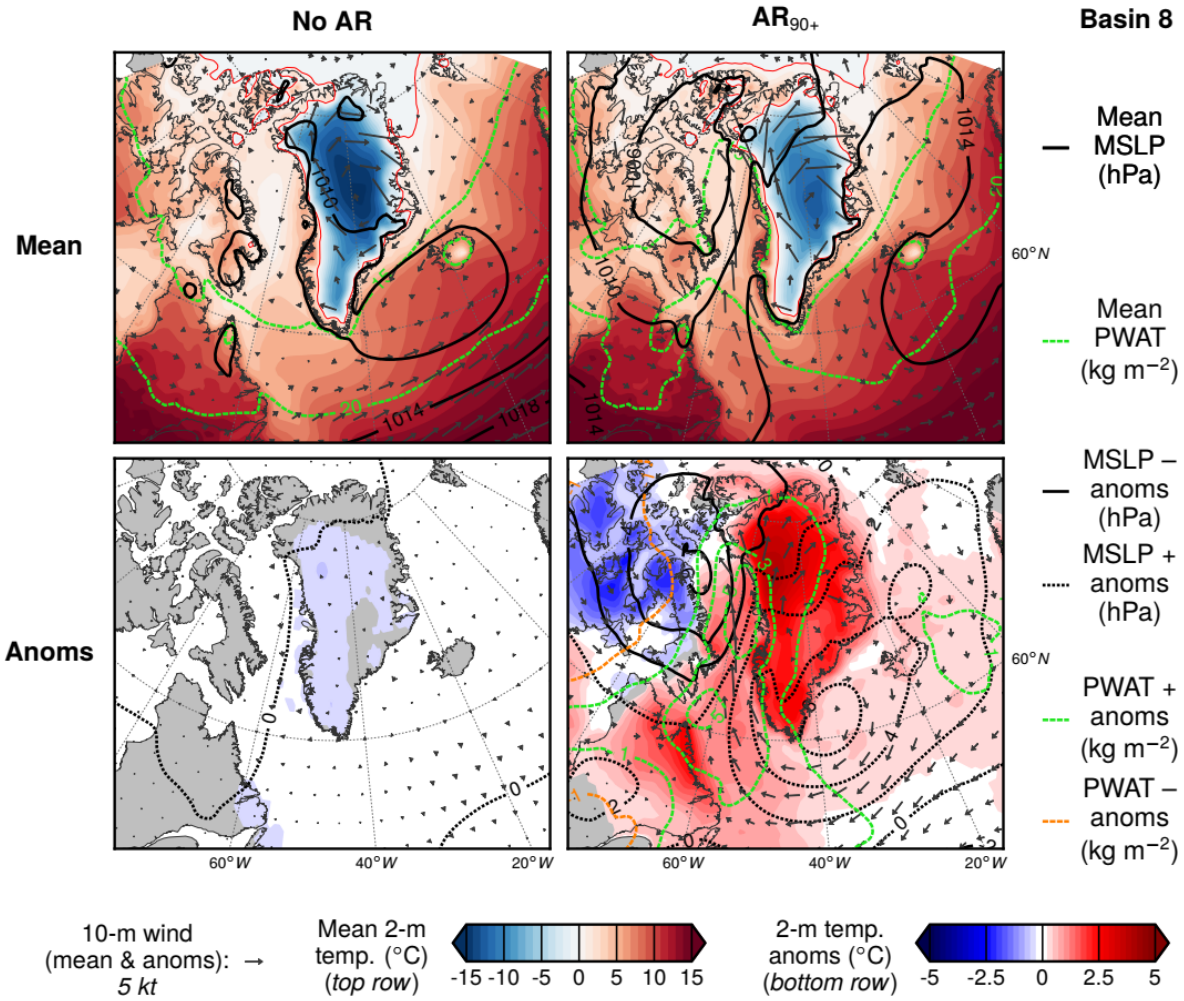

Figure 3.21. Synoptic composite mean and anomaly maps of near-surface conditions from MERRA-2 on "no AR" and AR_{90+} days in basin 8. Variables mapped are mean sea level pressure (MSLP), 10-m wind, 2-m temperature, and precipitable water (PWAT).

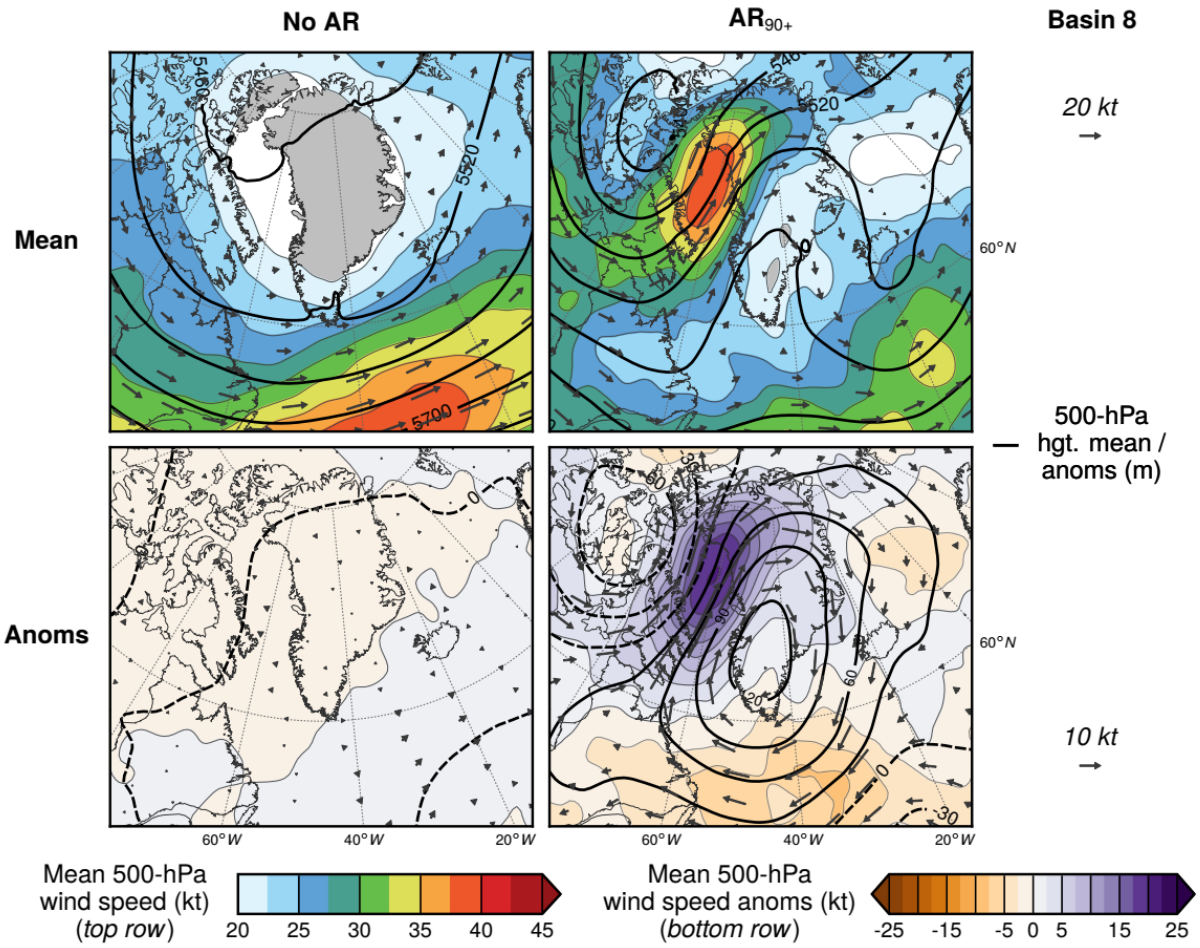

Figure 3.22. As in Figure 3.21 but for mid-tropospheric (500 hPa) variables: geopotential height and wind speed.

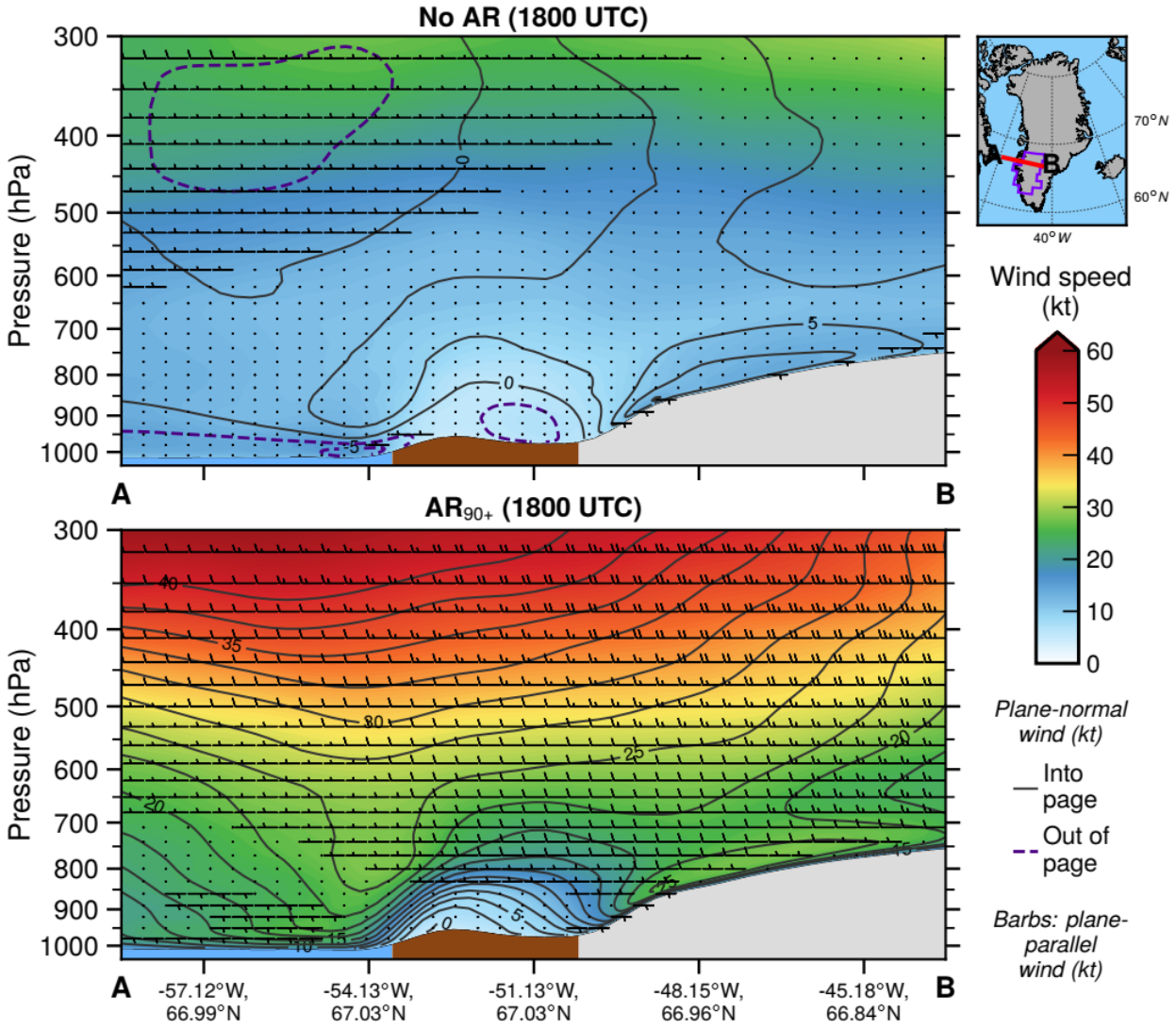

Figure 3.23. As in Figure 3.17, but cross section shows wind fields (wind speed, magnitude of the wind component into and out of the cross section [solid and dashed contours], and magnitude of plane-parallel wind component [barbs]) in the K-transect region.

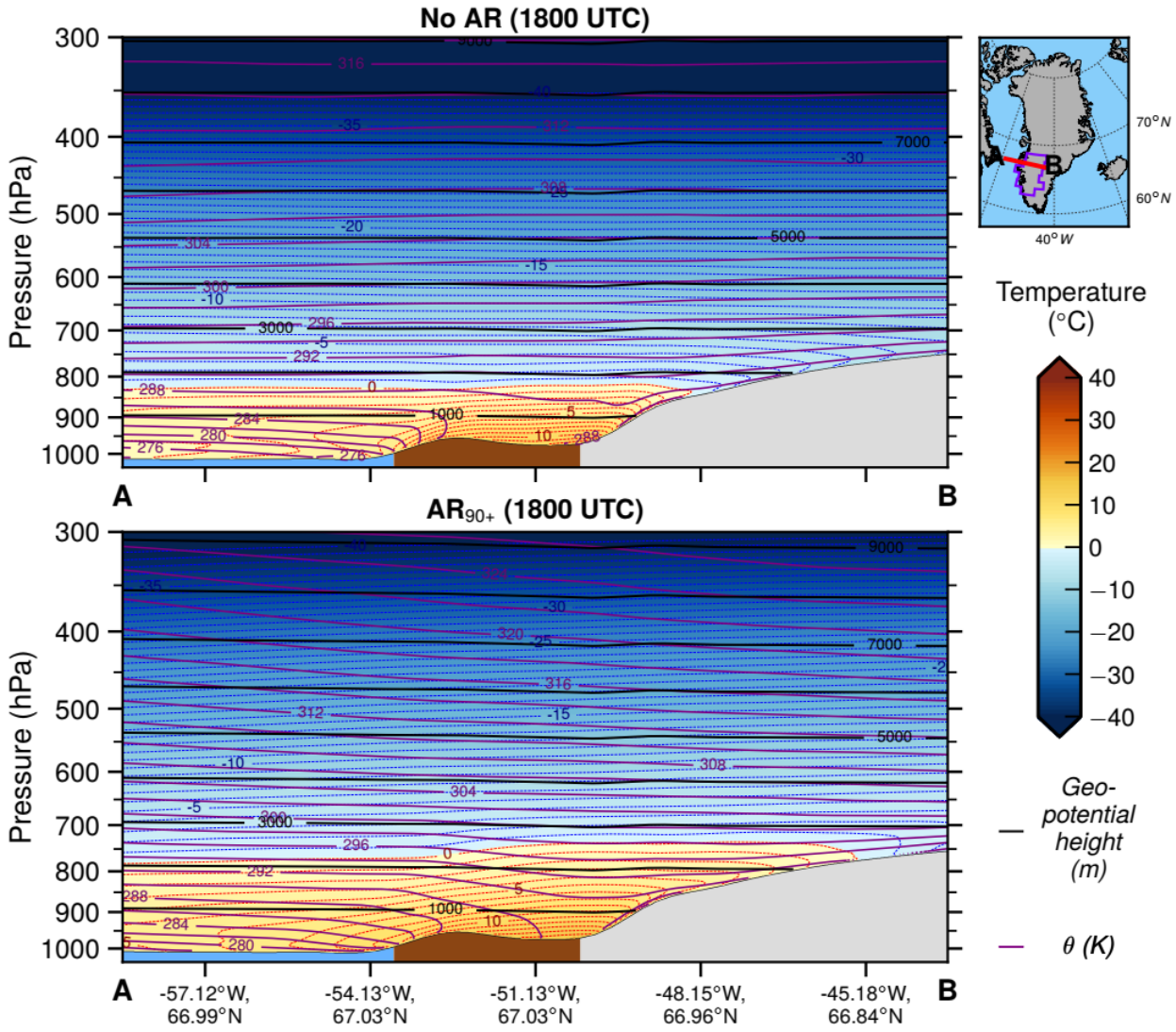

Figure 3.24. As in Figures 3.17 and 3.23, but cross section shows thermal fields (temperature, potential temperature [θ], and geopotential height) in the K-transect region.

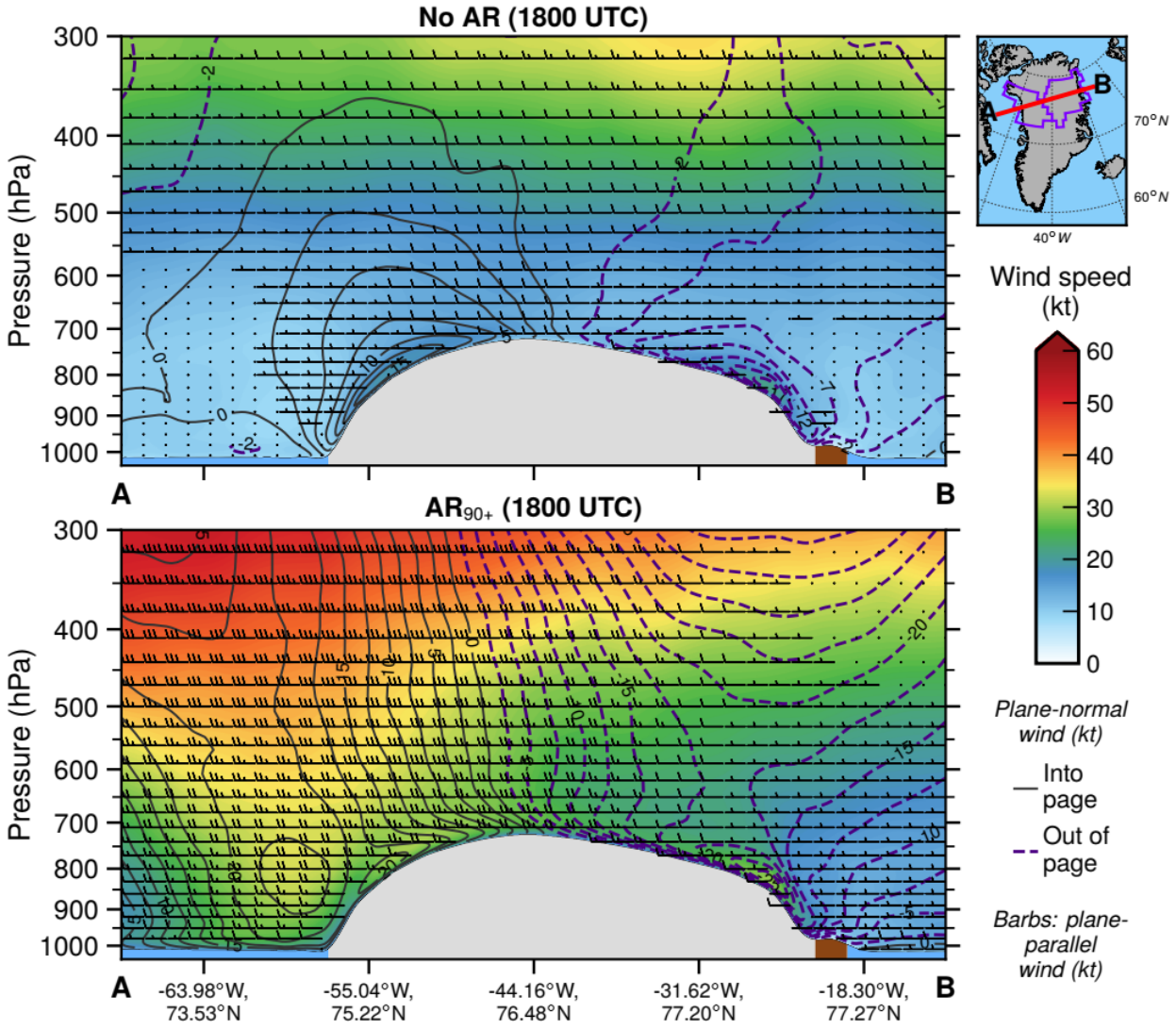

Figure 3.25. As in Figure 3.23, but cross section extends across Greenland from basin 8 through basin 2 for basin 8 "no AR" and AR_{90+} days.

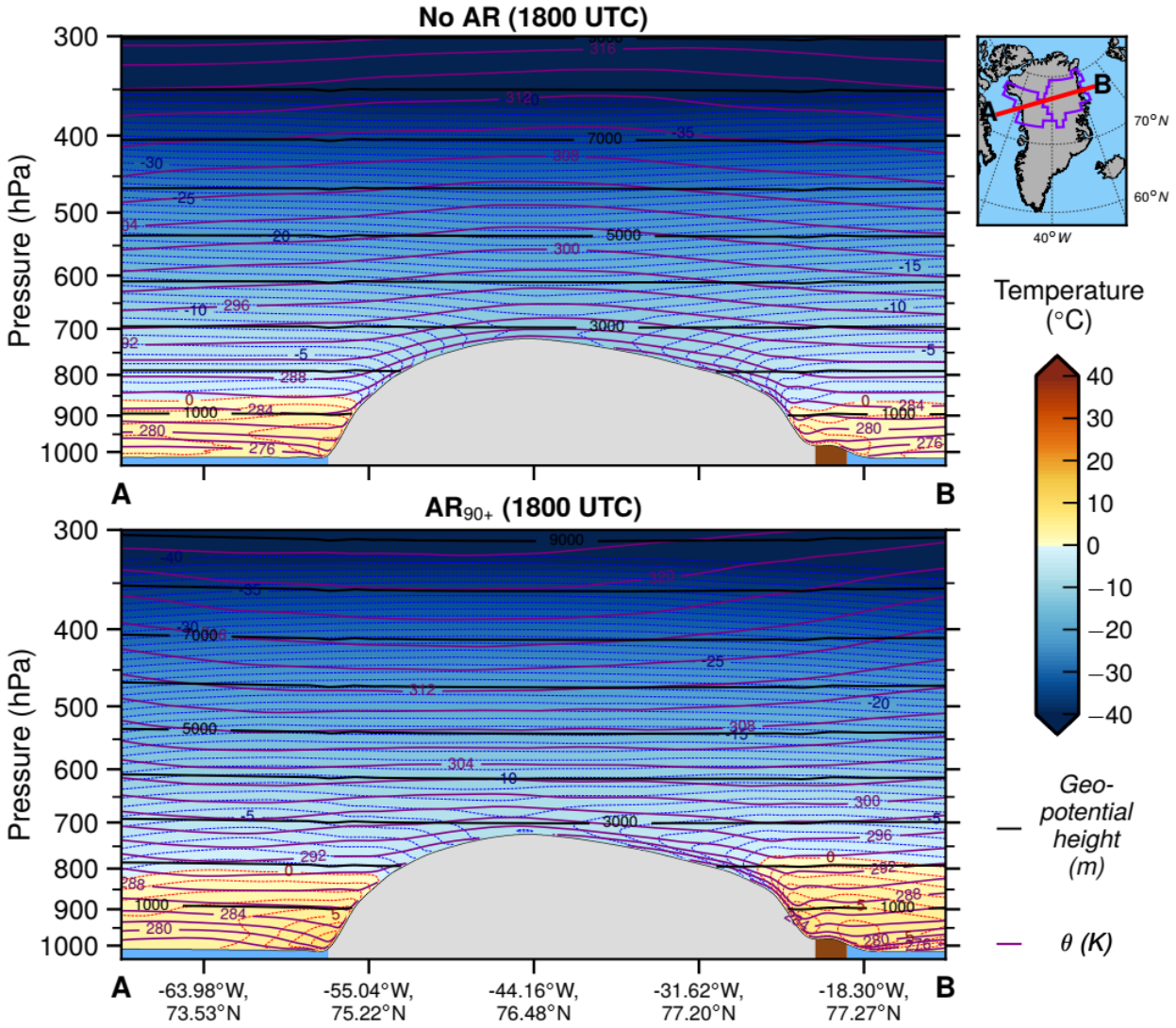

Figure 3.26. As in Figure 3.24, but cross section extends across Greenland from basin 8 through basin 2 for basin 8 "no AR" and AR_{90+} days.

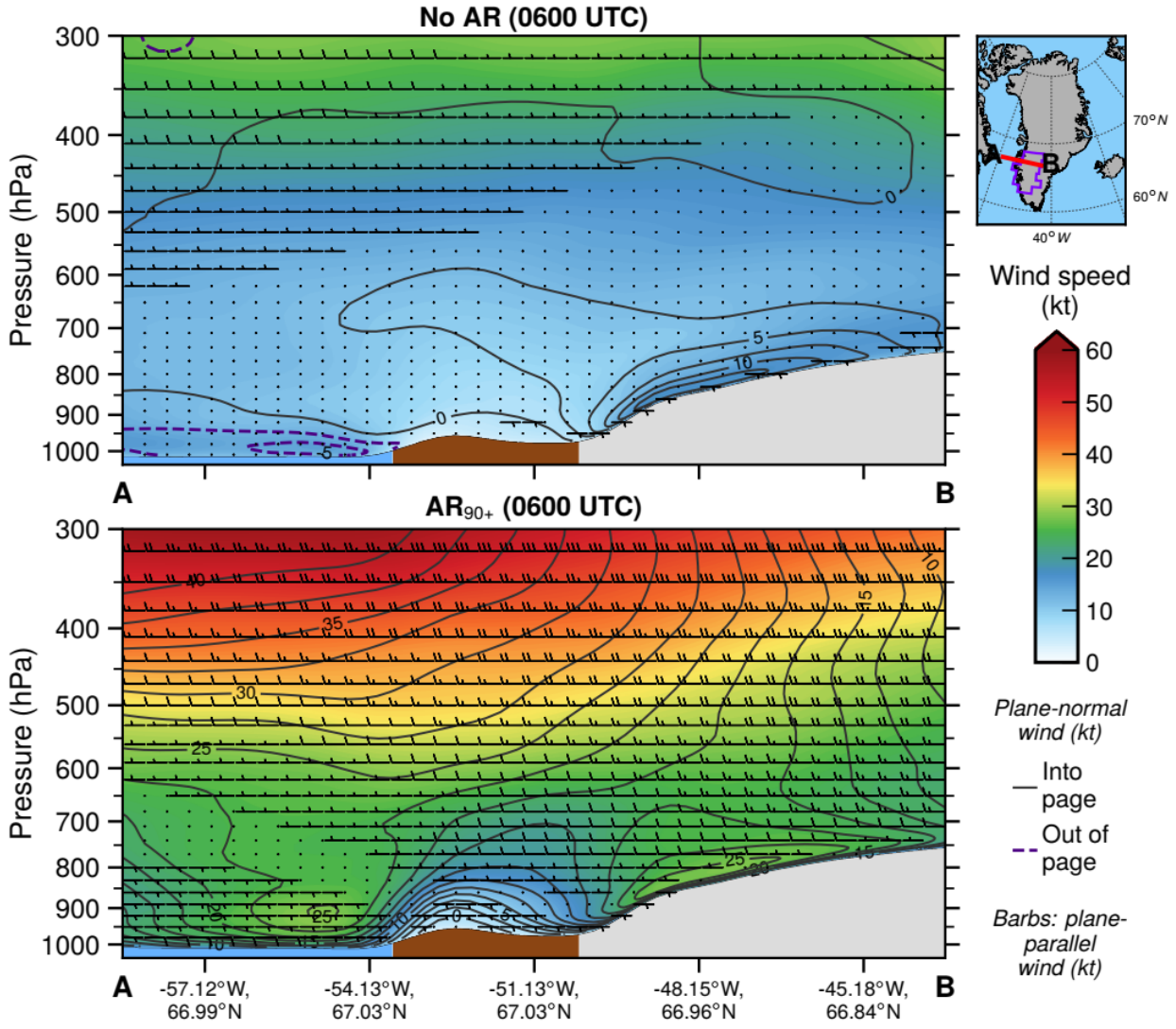

Figure 3.27. Vertical cross sections of ERA5 wind fields (wind speed, magnitude of the wind component into and out of the cross section [solid and dashed contours], and magnitude of plane-parallel wind component [barbs]) along a transect extending from Davis Strait inland through the K-transect region of basin 6. Cross sections are composites of conditions at 0600 UTC on "no AR" days (top) and AR_{90+} days (bottom). Inset map shows location of transect from point A to point B. Below-surface areas are filled according to surface type: ocean (blue), ice-free land (brown), and ice sheet (light gray).

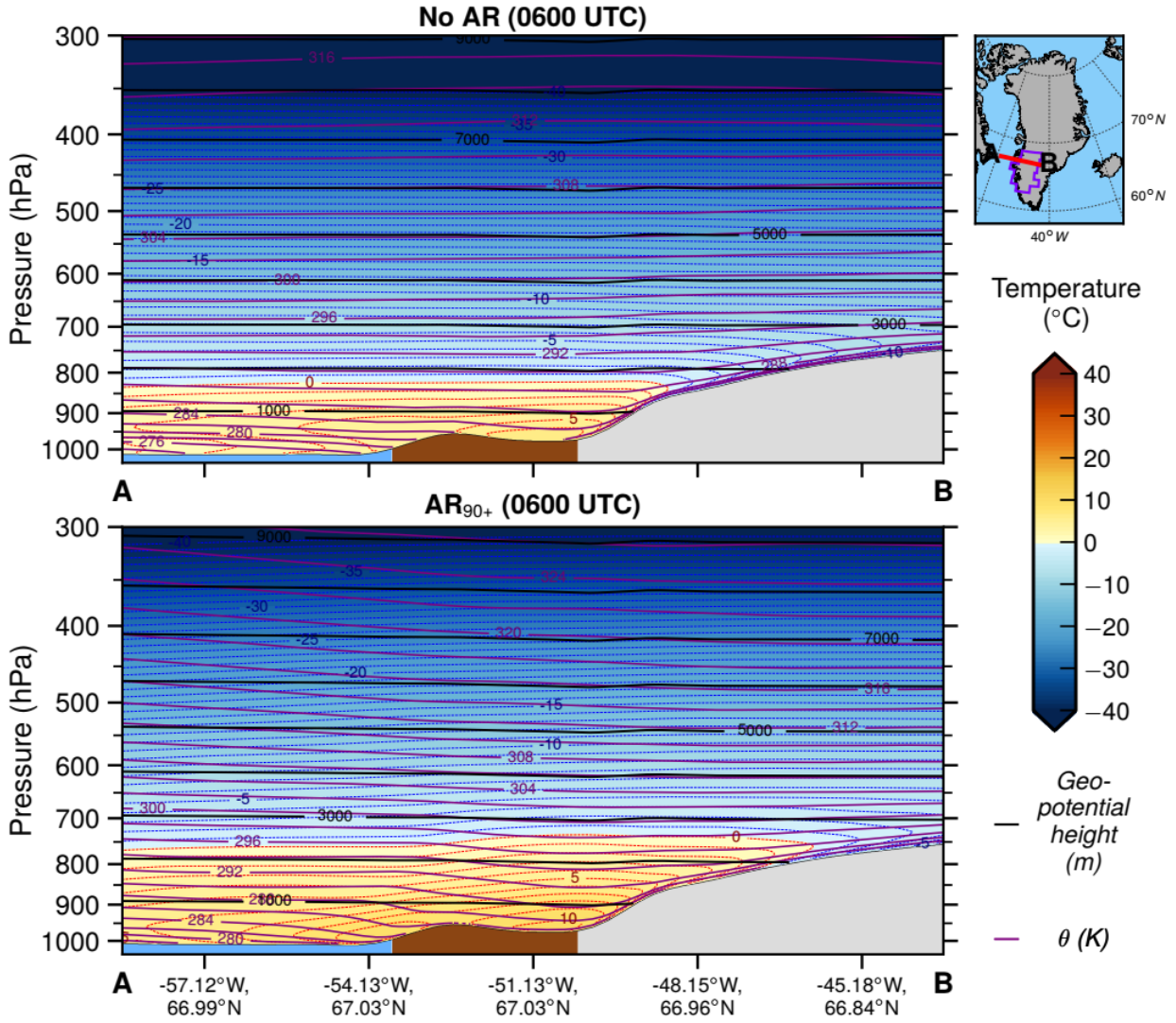

Figure 3.28. As in Figure 3.27, but cross section shows thermal fields (temperature, potential temperature [θ], and geopotential height) in the K-transect region.

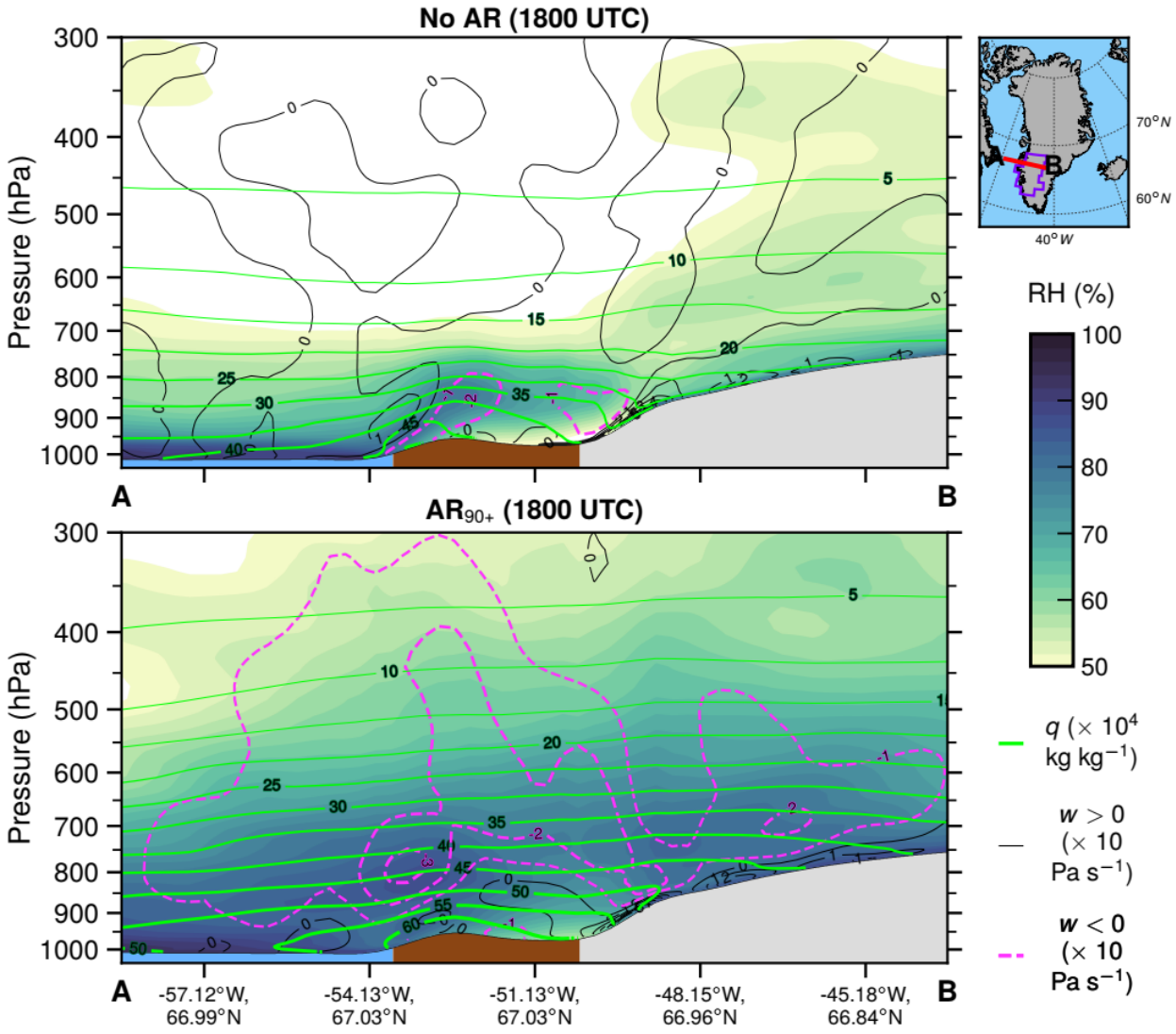

Figure 3.29. As in Figures 3.17, 3.23, and 3.24, but cross section shows moisture fields (specific humidity [q] and relative humidity [RH]) along with upward and downward vertical velocity ($w < 0$ and $w > 0$, respectively) in the K-transect region.

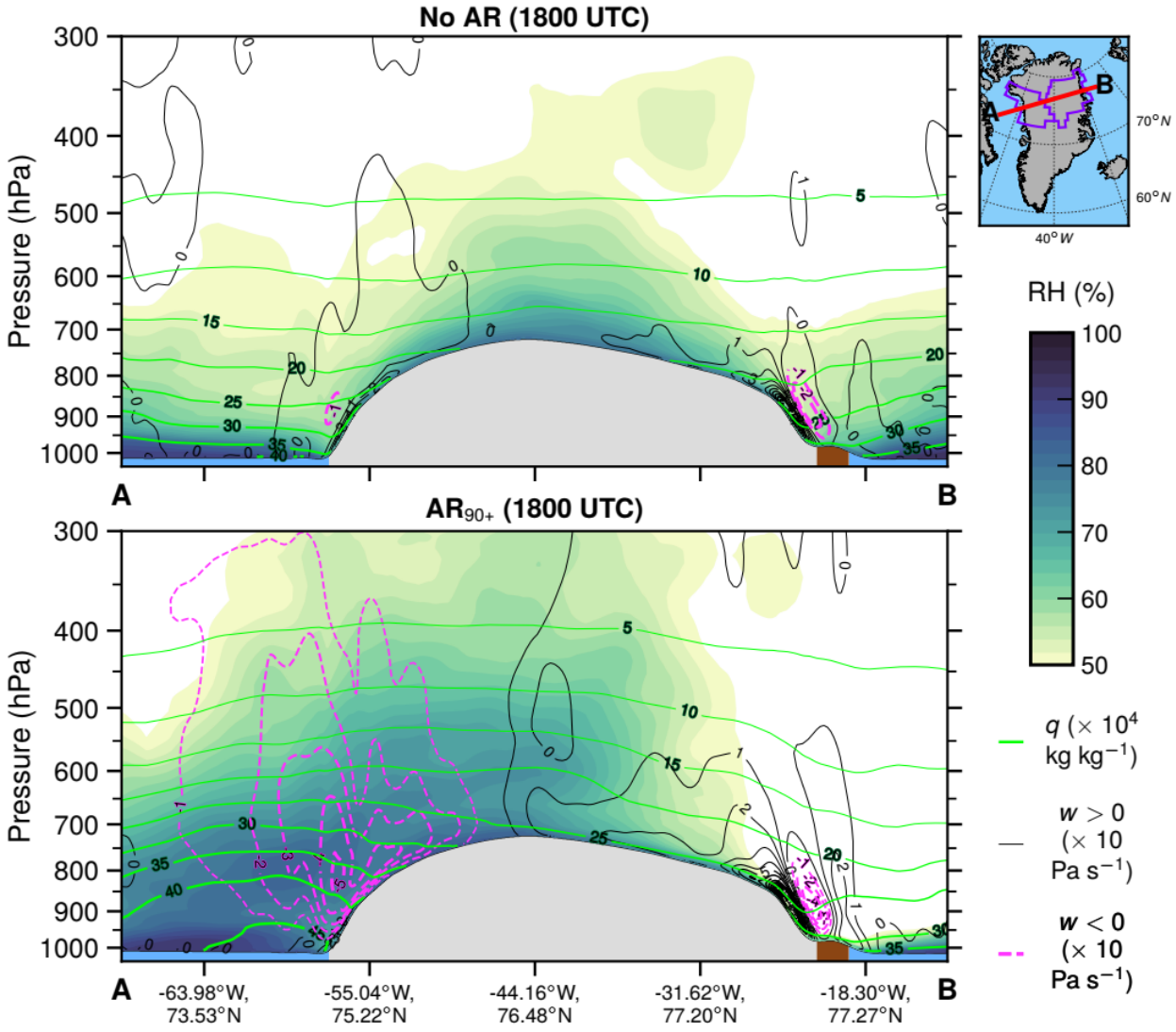

Figure 3.30. As in Figure 3.29, but cross section extends across Greenland from basin 8 through basin 2 for basin 8 "no AR" and AR_{90+} days.

CHAPTER 4

EVAPORATIVE MOISTURE SOURCES CONTRIBUTING TO ATMOSPHERIC RIVER EVENTS IN WESTERN GREENLAND[3]

[3] Mattingly, K. S. and T. L. Mote (2019), Evaporative moisture sources contributing to atmospheric river events in western Greenland. To be submitted to *Journal of Geophysical Research: Atmospheres*.

Abstract

Greenland Ice Sheet (GrIS) melt is partially controlled by variability in the large-scale atmospheric circulation through its influence on the surface energy balance. Episodes of synoptic-scale water vapor transport in narrow plumes called atmospheric rivers (ARs) have been shown to force GrIS melt through modification of radiative and turbulent energy fluxes. In this study, the dynamical processes by which ARs link distant regions within the global hydrological cycle are investigated through analyses of the evaporative water vapor source regions for ARs impacting western Greenland. Conditions preceding ARs are first examined from a Eulerian perspective by comparing reanalysis evaporation fields and related variables during the 10 days prior to AR landfall to AR-free conditions. Moisture uptake by air parcels arriving over western Greenland is then analyzed from a Lagrangian perspective by tracking humidity changes along modelled parcel trajectories. Results show that evaporative sources of water vapor reaching western Greenland shift equatorward during ARs, with enhanced moisture uptake occurring over a broad swath of the Atlantic Ocean during winter and summer, and parts of eastern North America during summer. Although air parcels gain water vapor from areas of anomalous evaporation identified by the Eulerian analysis, moisture uptake also occurs over areas of below-normal evaporation south of Greenland, likely due to convergence within the warm conveyer belts of extratropical cyclones. Thus ARs affecting western Greenland draw moisture from a mixture of distant, low-latitude sources and more proximate areas of the subpolar North Atlantic Ocean that contribute water vapor as air parcels approach Greenland.

4.1 Introduction

Poleward energy transport in the atmosphere and oceans plays a critical role in the global climate system, as it acts to offset the net meridional imbalance in top of atmosphere net radiation [*Oort*, 1971; *Stone*, 1978]. In the atmosphere, poleward energy fluxes occur through transport of dry static energy and moisture (latent heat) fluxes, with the moisture flux contribution to atmospheric energy transport nearly equivalent to that of dry static energy in the mid-latitudes [*Pierrehumbert*, 2002; *Trenberth and Stepaniak*, 2003; *Frierson et al*., 2007]. Poleward moisture transport in the mid- and high-latitudes is often organized into narrow bands known as "atmospheric rivers" (ARs), which have been found to be responsible for a major proportion of total water vapor transport despite their limited geographical extent [*Zhu and Newell*, 1998; *Liu and Barnes*, 2015]. AR are often responsible for flooding and contribute to water supplies in mid-latitude regions such as the U.S. west coast and western Europe [*Ralph et al.*, 2006; *Neiman et al*., 2008; *Azad and Sorteberg*, 2017]. In polar regions, ARs have been linked to intense snow accumulation in East Antarctica [*Gorodetskaya et al*., 2014], extreme warm events in the Antarctic peninsula [*Bozkurt et al*., 2017], and impeded growth of Arctic sea ice extent during the freeze season [*Hegyi and Taylor*, 2018].

ARs can be readily identified as long, coherent bands of enhanced moisture transport and cloud cover in synoptic-scale maps of meteorological data and satellite imagery, giving the impression that ARs directly transport moisture from evaporative sources at their upstream origins to sinks at their downstream ends. The direct flow of water vapor from the tropics and subtropics to the extratropics implied by this Eulerian perspective of ARs, however, has been called into question by several studies. *Bao et al*. [2006] and *Knippertz et al*. [2013] found that some, but not all, AR events along the west coast of North America are associated with direct

export of moisture from tropical sources to extratropical latitudes. *Newman et al*. [2012] showed that moisture within ARs originates from a combination of water vapor evaporated locally from the ocean along the AR path as well as moisture exported from subtropical regions (see also Figure 11e in *Cordeira et al*. [2013]). *Dacre et al*. [2015, 2019] argued that AR features are the footprints of saturated air formed by moisture convergence around poleward-moving extratropical cyclones, and that much of the water vapor within this convergence zone is supplied by evaporation along and downstream from the cyclone path rather than remote sources. Moisture is continually lost through precipitation and replenished through evaporation from the local environment, such that the fraction of water vapor contributed from earlier evaporation diminishes as the cyclone and its attendant moist air stream propagates poleward. Although the evaporative sources of water vapor within ARs thus are more complex than Eulerian analysis of total moisture flux would suggest, a number of analyses employing Lagrangian air parcel tracing methods have nevertheless found that AR events in the middle- and high-latitude Northern Hemisphere bring water vapor from unusually low-latitude sources. Studies of AR-induced heavy precipitation events in Norway [*Stohl et al*., 2008; *Sodemann and Stohl*, 2013], throughout western Europe [*Ramos et al*., 2016], and in the northern Alps [*Piaget et al*., 2015] have found that much of the water vapor contributing to these events evaporated in distant tropical and subtropical areas of the Atlantic Ocean.

One important aspect of moisture transport by ARs in the Northern Hemisphere is its effects on the Greenland Ice Sheet (GrIS). The GrIS contains enough ice to cause ~7.4 m of global mean sea level rise if fully melted and has been losing mass at an enhanced rate since the late 20th Century [*Bamber et al*., 2018; *Bevis et al*., 2019]. This multi-decadal increasing trend in GrIS mass loss coincided temporally with a period of anomalous moisture transport over western

Greenland by ARs [*Mattingly et al*., 2016]. Strong ARs have been shown to force intense surface melt at daily time scales during the summer, particularly when the AR-induced moisture transport is focused (i.e. makes landfall) over western Greenland [*Mattingly et al*., 2018]. The physical processes by which ARs force GrIS surface melt are complex and spatially variable. Melt typically occurs under conditions of anomalous cloud cover, longwave radiation, and turbulent (sensible and latent heat) fluxes in the vicinity of AR landfall, while melt is simultaneously often produced by clear-sky downsloping conditions in areas separated from the AR landfall by the topographic barrier of the ice sheet [*Mattingly et al*., 2019].

Although AR-induced moisture transport and its impacts on the GrIS have intensified in recent years, the evaporative moisture sources and moisture transport pathways involved in these events have only been examined in a few case studies. *Bonne et al*. [2015] found that the AR associated with the extreme July 2012 GrIS melt event transported moisture evaporated from the subtropics and mid-latitudes to the NEEM site in northwest Greenland, with particularly strong water vapor uptake over the western Atlantic Ocean and northeastern United States. (Refer to Figure 1.1 for the location of NEEM and all other geographic features discussed in this chapter). *Neff et al*. [2014] similarly found that the air mass arriving at Summit Station in central Greenland during this event originated over northeastern North America and the western Atlantic before being advected poleward over the ice sheet. A few other studies have examined the general moisture sources for the GrIS without analyzing AR events specifically. Using a Lagrangian moisture source identification method during 30 selected winter seasons from 1958–2002, *Sodemann et al*. [2008] found that GrIS moisture sources exhibit pronounced variability across NAO phases, with moisture originating mostly from the high-latitude Atlantic Ocean and Nordic Seas during positive NAO phases and water vapor uptake shifting to mid-latitude and

subtropical sources during negative NAO phases. *Bonne et al*. [2014] and *Steen-Larsen et al*. [2015] also identified distinct Arctic and lower-latitude North Atlantic moisture sources from water vapor stable isotope observations at Ivittuut in southern Greenland. *Ahlstrøm et al*. [2017], while not directly quantifying moisture uptake, used Lagrangian air parcel back trajectory modelling to show that air masses of southerly origin became more common at Tasersiaq lake in southwest Greenland during 2003–2014 compared to 1975–2002.

In a warming climate, poleward water vapor transport is projected to intensify by both model simulations and theoretical arguments [*Held and Soden*, 2006; *Kattsov et al*., 2007; *Hwang and Frierson*, 2010; *Lavers et al*., 2015]. To understand the implications of these projections for the future mass balance of the GrIS, the dynamics of present-day poleward moisture transport must be understood, including the processes by which ARs link distant regions within the global hydrological cycle. Investigating the dominant present-day evaporative source regions for water vapor transported to the GrIS will help identify areas where changes in evaporative conditions may remotely influence its future evolution. Determining the moisture source regions for ice sheet accumulation is also important for interpreting the paleoclimate signals contained in ice cores [*Sime et al*., 2013; *Steen-Larsen et al*., 2017].

In this study, we analyze the synoptic to hemispheric-scale hydrologic processes that produce enhanced moisture transport over Greenland during strong AR events, and compare the conditions at work during strong ARs to periods with no AR. *Mattingly et al.* [2018, 2019] found that ARs making landfall in western Greenland cause the most intense GrIS surface melt events, and thus we focus our analysis on GrIS drainage basin 6 in southwest Greenland (see Figure 4.1). We first examine the conditions producing western Greenland ARs from a Eulerian perspective, focusing on differences in time-mean evaporation and moisture transport across the Northern

Hemisphere during 10-day periods preceding strong ARs to periods with no AR impacts in Greenland. We then trace the evaporative moisture sources of water vapor reaching western Greenland during AR events from a Lagrangian perspective, calculating moisture uptake and precipitation along air parcel trajectories that terminate in the lower troposphere over western Greenland. Previous studies [*Bonne et al*., 2014; *Pfahl et al*. 2014] have shown contrasting evaporative and moisture source conditions over the Northern Hemisphere during boreal summer (JJA) and winter (DJF), with longer atmospheric water vapor residence times, greater moisture transport distances, and much higher amounts of continental evapotranspiration during JJA compared to DJF. Spring and fall generally exhibit a mixture of these characteristics. Therefore, we focus on the end-member seasons of JJA and DJF in this study.

4.2 Data and Methodology

4.2.1 Atmospheric river identification and intensity classification

As in *Mattingly et al.* [2018], MERRA-2 reanalysis data [*Gelaro et al*., 2017] are used to identify AR outlines over the Northern Hemisphere. U- and v-wind components and specific humidity (q) are first obtained at native MERRA-2 resolution (0.5° latitude × 0.625° longitude) every 6 hours during 1980–2017 at pressure levels from 1000 hPa to 200 hPa. Increments between pressure levels are 50 hPa between 1000 and 500 hPa, and 100 hPa between 500 hPa and 200 hPa. These pressure-level data are used to calculated integrated water vapor transport (IVT):

$$IVT = \frac{1}{g}\int_{1000\ hPa}^{200\ hPa} qV\ dp \tag{4.1}$$

where g is the gravitational acceleration (9.80665 m s^{-2}), q is the specific humidity (kg kg^{-1}) at the given pressure level, V is the vector wind (m s^{-1}) at the given pressure level, and dp is the difference between consecutive pressure levels. The climatological percentile rank of IVT (IVT

PR) is calculated by comparing each 6-hourly IVT value to the distribution of all 6-hourly IVT values within ± 15 days of the given day during all years from 1980–2017. IVT and IVT PR are interpolated to 0.5° × 0.5° latitude / longitude resolution, and ARs are identified as contiguous areas with IVT ≥ 150 kg m^{-1} s^{-1} and IVT PR ≥ 85 that meet size, shape, location, and moisture transport direction criteria detailed by *Mattingly et al*. [2018].

The analyses of large-scale evaporative conditions and moisture uptake sources in the following sections focus on the contrast between intense AR events and periods with no AR activity. To demarcate these atmospheric regimes, all JJA and DJF days are classified into "no AR", $AR_{<90}$, and AR_{90+} categories according to the maximum daily IVT PR within the area of overlap between any AR outline and each GrIS drainage basin (see Figure 4.1), following the method of *Mattingly et al*. [2019]. This 90th percentile threshold was chosen based on the finding that the odds of anomalously warm, moist, windy conditions at low-elevation PROMICE observing stations [*van As et al.*, 2011] increase dramatically when IVT PR exceeds this value. As this study concerns intense AR events in western Greenland, analyses are performed for summer and winter "no AR" and AR_{90+} conditions over GrIS basin 6 (Figure 4.1), and $AR_{<90}$ events are not examined.

4.2.2 Evaporative conditions preceding "no AR" and AR_{90+} days

ERA-Interim reanalysis data [*Dee et al.*, 2011] are used to examine a number of large-scale oceanic and atmospheric fields during 10-day periods preceding "no AR" and AR_{90+} days in basin 6. Humidity fields from this dataset correspond well to observations over the oceans [*Pfahl and Niedermann*, 2011], and it has been widely used to study oceanic evaporation patterns and trace evaporative sources of water vapor [e.g. *Knippertz et al*, 2013; *Pfahl et al*., 2014; *Aemisegger and Papritz*, 2018; *Vázquez et al*., 2019]. Evaporation, 10-m u- and v-wind

components, and sea surface temperature (SST) are acquired at native ~0.7° spatial resolution for each 6-hourly timestep during 1980–2017. In the same manner as the MERRA-2 data (Section 2.1), u- and v-wind components and q are obtained at constant pressure levels from 1000 hPa to 200 hPa and used to calculate IVT over the same period. Finally, q is also obtained at the lowermost ERA-Interim hybrid sigma-pressure model level (~10 m above the surface) to examine the spatial variability of the near-surface ocean-atmosphere specific humidity gradient that, along with near-surface wind speed and stability, determines the oceanic evaporation rate in ERA-Interim [*Aemisegger and Papritz*, 2018]. To calculate the specific humidity gradient, the saturation vapor pressure (e_w) is first calculated from SST according to the *Bolton* [1980] approximation:

$$e_w \approx 6.112(e^{\frac{17.67T}{T+243.5}}) \tag{4.2}$$

where T is the SST (°C). The saturation specific humidity of the sea surface (q_s; g kg^{-1}) is then calculated as:

$$q_s \approx 0.622(\frac{e_w}{P}) \tag{4.3}$$

where P is the surface pressure (hPa). The specific humidity gradient (Δq) between the atmosphere and ocean is the difference between q at the lowest model level (q_a) and q_s:

$$\Delta q = q_a - q_s \tag{4.4}$$

Composite mean and anomaly maps of the aforementioned ERA-Interim variables are produced by averaging data over 10-day periods preceding "no AR" and AR_{90+} sample dates, with anomalies calculated relative to the 1980–2017 monthly mean of the given variable. The 10 day length of the pre-event window is chosen to correspond with the temporal span of HYSPLIT back trajectories initiated in basin 6 (see Section 2.3) and the approximate residence time of water vapor in the atmosphere [*Trenberth*, 1998; *Yang et al*., 2019]. No double-counting of dates

in composites is allowed. For AR_{90+} composites, sample dates are identified by iterating backward in time from the end of the study period. When an AR_{90+} date over basin 6 is found, the 10 prior days are excluded from consideration (irrespective of whether another AR_{90+} day occurs in this window), and the search resumes at day -11. Because there are many more "no AR" than AR_{90+} days, "no AR" days are randomly selected with an equivalent sample size to the AR_{90+} category for the given season (JJA or DJF). Additionally, there must be no AR_{90+} or $AR_{<90}$ days over basin 6 during the 10 days preceding a "no AR" day for it to be considered for random sampling.

Evaporation data from three other sources — MERRA-2, Objectively Analyzed Air-Sea Fluxes for the Global Oceans (OAFlux) version 3, and the Global Land Evaporation Amsterdam Model (GLEAM) version 3.3a — are used to provide a check on the ERA-Interim data and highlight additional characteristics of large-scale evaporation. OAFlux uses an optimal blending of active and passive satellite retrievals with three reanalysis datasets (NCEP/NCAR Reanalysis 1, NCEP/DOE reanalysis 2, and ERA-40) to provide evaporation and turbulent flux at 1° latitude / longitude resolution over the global oceans, with daily data available beginning in 1985 [*Yu et al*., 2008]. GLEAM v3.3a provides estimates of land surface evapotranspiration at 0.25° latitude / longitude resolution from 1980 to present, using a model that ingests active and passive satellite retrievals of precipitation, vegetation optical depth, root-zone soil moisture, and snow water equivalent, along with gauge-based precipitation and ERA5 reanalysis net radiation and air temperature [*Martens et al*., 2017]. Evaporation comparisons from these datasets are performed over the common data period of 1985–2017.

4.2.3 Air parcel back trajectories and moisture uptake analysis

NOAA's Hybrid Single-Particle Lagrangian Integrated Trajectory model (HYSPLIT) model [*Stein et al*., 2015], in conjunction with the PySPLIT Python library [*Warner*, 2018], is used to simulate three-dimensional 10-day (-240 hour) back trajectories of air parcels reaching GrIS basin 6. The model is forced with 1° resolution NCEP Global Data Assimilation System data during 2005–2017, as NOAA's Air Resources Laboratory provides archived GDAS data in a format pre-packaged for HYSPLIT input during this period. For these simulations, all JJA and DJF AR_{90+} dates in basin 6 during 2005–2017 are sampled, even if another AR_{90+} event occurred within 10 days. As with the synoptic composite analyses (Section 2.2), "no AR" days are randomly selected to match the AR_{90+} sample size during JJA and DJF. However, there is no requirement for the 10 days prior to a "no AR" sample date to be free of AR events, as the Lagrangian analysis is performed on individual trajectories arriving on specific days and thus does not blend AR and non-AR dates in basin 6. On each "no AR" and AR_{90+} sample date, back trajectories are initiated at 1200 UTC for three vertical levels (10 m, 100 m, and 500 m above ground level [AGL]) over 52 points spaced at 0.5° latitude / 1° longitude intervals over the central area of basin 6 (see Figure 4.1). These levels correspond to the vertical layer over which previous studies have released air parcels for identification of moisture sources in Greenland [*Bonne et al*., 2014, 2015; *Steen-Larsen et al*., 2015]. In the subsequent analyses, all of these 152 trajectories launched on each sample date are grouped to represent the history of air parcels with pathways terminating in the lower troposphere over basin 6. The position of the parcel is output by HYSPLIT 1-hourly intervals along each trajectory.

Using PySPLIT algorithms, each trajectory is post-processed to calculate a number of derived quantities related to the hydrologic cycle along its path. The moisture_uptake PySPLIT

function calculates the location and magnitude of water vapor addition to the parcel from changes in q (Δq) along the path, under the assumption that increases in q ($\Delta q > 0$) result from evaporation into the parcel and decreases in q ($\Delta q < 0$) represent precipitation [*Dirmeyer and Brubaker*, 1999; *Stohl and James*, 2004]. Following prior studies [*Sodemann et al*, 2008; *Molina and Allen*, 2019], 6-hourly timesteps when $|\Delta q| > 0.2$ g kg^{-1} were taken to represent evaporation or precipitation, as Δq of smaller magnitude and on shorter time scales may result from spurious numerical noise in the model. If a trajectory experiences multiple instances of moisture uptake and precipitation along its path, more recent moisture uptakes (i.e. closer to hour 0) are weighted more heavily than earlier uptakes to account for their increased importance [*Sodemann et al.*, 2008]. Additionally, moisture uptakes were classified as occurring in either the boundary layer or the free troposphere, with moisture uptakes occurring while the air parcel was below 900 hPa assumed to occur in the well-mixed planetary boundary layer. This boundary layer threshold is the PySPLIT default value and has been employed in previous studies [*Baldini et al.*, 2010; *Krklec and Domínguez-Villar*, 2014; *Warner*, 2018]; other studies [e.g. *Pfahl and Wernli*, 2008; *Pfahl et al*., 2014; *Molina and Allen*, 2019] have employed a variable threshold that utilizes the estimated boundary layer height from reanalysis datasets.

The other trajectory-derived quantities are moisture flux vectors, calculated as the product of instantaneous parcel motion and specific humidity using the calculate_vector and calculate_moistureflux PySPLIT functions, and evaporation minus precipitation (E – P), which was calculated as the change in specific humidity for all trajectory points where $|\Delta q| > 0.2$ g kg^{-1}. Moisture flux vectors are calculated at each 1-hourly trajectory output timestep excluding the first and last trajectory points, while E – P is output by the moisture_uptake PySPLIT function at

6-hourly intervals. Unlike the moisture uptake diagnostics, E–P does not account for earlier precipitation along a trajectory's path.

Trajectory-derived quantities were interpolated to a 1° latitude / longitude resolution grid over the Northern Hemisphere to map moisture source diagnostics and the density of trajectories. Trajectory density maps are 2-D histograms of all 1-hourly trajectory points, displaying the probability density of these points (the count of points in each grid cell divided by the total number of trajectory points). Moisture flux maps include all 1-hourly trajectory data except the first and last point of each trajectory. The number of trajectory points sampled for each of the moisture uptake and E – P maps varies because a given 6-hourly trajectory point is only included for interpolation to the 1° output grid if the given moisture uptake / E – P criteria are met at that point. For example, a trajectory point only contributes to the "moisture uptake in the boundary layer" maps if its specific humidity increased by > 0.2 g kg^{-1} during the previous 6 hours and its pressure is > 900 hPa. Some grid cells through which one or more sample trajectories passed may nevertheless appear as contributing no moisture if none of these trajectories met the moisture uptake criteria over that grid cell. Moisture uptake values are normalized across all grid cells contributing moisture to a given trajectory, such that they represent the mean contribution to moisture arriving at the trajectory end point by the given grid cell. E – P maps display all grid cells where trajectories exceeded the $|\Delta q| > 0.2$ g kg^{-1} threshold and are not normalized by trajectory frequency.

4.3 Results

4.3.1 Synoptic-scale evaporative conditions preceding active and inactive AR periods in western Greenland

During summer, the spatial pattern of evaporation over the Atlantic basin is characterized by strong evaporation over the tropical and subtropical Atlantic Ocean, Caribbean Sea, and Gulf of Mexico, with a northward extension of enhanced evaporation along the Gulf Stream offshore of the east coast of the United States (Figure 4.2). Significant evapotranspiration also occurs over the North American land mass and most of Europe, with particularly high amounts of water vapor (up to 5 mm day^{-1}) transferred to the atmosphere over the eastern United States. The large-scale pattern of IVT resembles a large anticyclonic gyre over the Atlantic basin, with easterly IVT up to 400 kg m^{-1} s^{-1} in the tropics and westerly moisture transport of approximately the same magnitude north of 30°N.

The contrast in water vapor transport around Greenland between the 10 days preceding "no AR" conditions and AR_{90+} events in basin 6 is evident in the mean composite maps. A clear Icelandic Low signature can be seen in the cyclonic curvature of IVT vectors southeast of Greenland in the "no AR" composites (top left panel of Figure 4.2), which results in weak northerly moisture transport over the southern half of Greenland. In contrast, the AR_{90+} composite (bottom left panel of Figure 4.2) shows southerly moisture transport of up to ~100 kg m^{-1} s^{-1} along the west coast of Greenland and over Baffin Bay, and the continuity of southerly flow with westerly vectors and considerable evaporation over Canada suggests that moisture is transported from North America to Greenland.

A somewhat different picture emerges from the anomaly maps. The "no AR" anomalies (top right panel of Figure 4.2) are largely consistent with the mean maps, with a cyclonic IVT

anomaly over an area of enhanced evaporation southeast of Greenland, and anomalous northerly moisture transport collocated with slightly above normal evaporation in Baffin Bay and the Labrador Sea. However, the AR_{90+} anomaly map shows a large area of anomalously strong evaporation in the eastern Atlantic off the western coast of Europe, and the IVT vector anomalies suggest direct transport of moisture from this anomalous evaporative source to southern Greenland around an anomalous anticyclonic circulation off Greenland's southeast coast. Enhanced evaporation also occurs over most of Europe and the northern half of North America, with moisture transport from northeast Canada to western Greenland again implied by westerly IVT vector anomalies over this area. A separate area of enhanced evaporation occurs in the western Atlantic off the east coast of the United States; IVT vector anomalies are weak over this area, but the strong mean southwesterly IVT vectors in this region suggest that water vapor may be transported poleward from this region. In the northwest Atlantic and Labrador Sea, evaporation is strongly reduced in the area of most intense poleward moisture transport.

During winter (Figure 4.3), oceanic evaporation is concentrated most strongly over the Gulf Stream, and the mean evaporation values in this area (exceeding 10 mm day^{-1} prior to AR_{90+} events) are higher than at any continental or oceanic location during summer. Land surface evapotranspiration effectively shuts down over most subtropical and mid-latitude continental areas. Moisture transport is stronger in the mid-latitudes than the subtropics, with a sharp contrast in moisture transport between "no AR" and AR_{90+} periods that again stands out in the mean IVT composites. During the period preceding "no AR" days in basin 6, zonal flow over the Atlantic transports moisture into western Europe and moisture transport around Greenland is minimal, in a pattern resembling positive NAO conditions. During the 10 days preceding AR_{90+} events, in contrast, IVT vectors suggest strong meridional moisture transport from the Gulf

Stream to southern Greenland. The AR_{90+} anomaly map (bottom right panel of Figure 4.3) shows a contiguous belt of enhanced evaporation extending from the Gulf of Mexico northeastward across the length of the Atlantic to the west coast of Europe and the western Mediterranean Sea, with especially intense evaporation over the Gulf Stream off the southeast coast of the United States. As in the summer composites, the AR_{90+} anomaly map shows easterly IVT anomalies along the southern fringe of an anticyclonic anomaly southeast of Greenland, with this easterly IVT signature passing over a belt of enhanced evaporation off the west coast of Europe before turning poleward south of Greenland.

To ensure that the spatial patterns and magnitude of evaporation calculated by ERA-Interim are realistic, we compare the ERA-Interim evaporation maps with data from MERRA-2, OAFlux, and GLEAM (see Section 4.2.2). All four datasets show similar large-scale patterns of evaporation across most seasonal and AR condition subsets, with generally only subtle differences in the spatial structure and magnitude of evaporation over oceans and land surfaces (Figures 4.4 and 4.5). The datasets appear to be in closer agreement over the oceans, particularly in winter when the spatial structure of evaporation over the Atlantic poleward of 20°N is remarkably similar between ERA-Interim, MERRA-2, and OAFlux (Figure 4.5).

Evaporation from the ocean surface in ERA-Interim is controlled by the near-surface (10-m) wind speed and the gradient in specific humidity between the atmosphere and ocean surface (Δq), along with a stability-dependent mass transfer coefficient [*Aemisegger and Papritz*, 2018]. To evaluate spatial variability in conditions contributing to evaporation prior to "no AR" and AR_{90+} sample days in basin 6, as well as the relationships between sea surface temperature (SST) and these controls on evaporation, 10-m wind and Δq are plotted along with SST in Figures 4.6

and 4.7. A negative difference in q between the atmosphere and ocean ($-\Delta q$) favors evaporation according to the sign convention of these maps.

Over the subtropical Atlantic, Gulf of Mexico, and Gulf Stream during summer, the strong evaporation shown in Figure 4.2 is produced by near-surface winds of up to 10 m s^{-1} blowing across a broad zone of highly negative Δq and warm SSTs (Figure 4.6, left panels). During the 10 days preceding "no AR" sample days, the anomalous area of evaporation in the subpolar North Atlantic shown in Figure 4.2 occurs as northerly wind anomalies flow over a zone of negative Δq that extends across both positive and negative SST anomalies (Figure 4.6, right panels). This region of evaporation occurs in the cold sector behind the anomalously strong Icelandic Low, as cool air flowing from the north produces a negative ocean-atmosphere specific humidity gradient in the presence of anomalously strong winds that favor evaporation. South of this area, a belt of anomalously positive Δq extends across the Atlantic where advection of warm, moist air can be inferred from southwesterly 10-m wind anomalies, leading to decreased evaporation despite anomalously strong winds and positive SST anomalies.

Prior to JJA AR_{90+} days, a prominent area of positive SST anomalies exists over the subpolar North Atlantic, Labrador Sea, and Baffin Bay. Over the western half of this positive SST anomaly zone in the Labrador Sea and Baffin Bay, positive Δq anomalies exist in the presence of warm air advection, leading to decreased evaporation despite higher than normal SSTs. The pattern of warm SST anomalies in this region closely resembles the SST anomalies found by *McLeod and Mote* [2015] (their Figure 8) during extreme Greenland blocking events associated with precursor cyclones, suggesting a link between cyclones and ARs affecting western Greenland, Greenland blocking, and subpolar North Atlantic SSTs. Contrasting conditions occur over the eastern half of this warm SST zone, where cold air advection along the

eastern flank of an anomalous anticyclone southeast of Greenland flows over the warm SSTs, promoting evaporation in concert with stronger wind speeds than normal.

Over the Gulf Stream off the east coast of the United States, strongly negative Δq values overlap with weakly positive SST anomalies prior to JJA AR_{90+} days, resulting in the evaporation anomalies seen in Figure 4.2. The cause of this enhanced ocean-atmosphere humidity gradient is not readily apparent. One possibility, suggested by the slight northerly component to the vector wind anomalies in this area, is that advection of relatively cool, dry air originating from the cooler ocean waters near the northeast United States coast produces this atmosphere-ocean humidity gradient. Wind speed anomalies do not appear as important as the humidity gradient for anomalous evaporation over the Gulf Stream, in agreement with the results of *Pfahl et al*. [2014].

During winter, the spatial patterns of 10-m wind speed and Δq anomalies producing evaporation (Figure 4.7) are generally similar to summer, with a few noticeable differences. Negative SST anomalies extend across a broad swath of the mid-latitude Atlantic prior to "no AR" sample days, with a marked contrast between positive SST anomalies in the marginal seas surrounding Greenland and cooler than normal SSTs to the south of this zone. During the periods preceding AR_{90+} days, a concentrated zone of strongly positive SST anomalies exists to the south of Greenland and extending into the Labrador Sea and Baffin Bay as well as the Denmark Strait. These anomalously warm SSTs combine with southerly flow along the western flank of an anomalous anticyclone to the southeast of Greenland to produce strongly positive Δq values and the negative evaporation anomalies shown in Figure 4.3. South of this zone, a belt of negative Δq anomalies extends from the Gulf of Mexico northeastward across the Atlantic to western Europe, promoting evaporation in a zone displaced slightly to the south of its JJA position (Figure 4.6).

4.3.2 Source regions of water vapor arriving in western Greenland during active and inactive AR periods

Having evaluated evaporation and moisture transport conditions preceding basin 6 "no AR" and AR_{90+} sample days in a Eulerian frame of reference, we now analyze the movement and water cycle history of air parcels reaching southwest Greenland from a Lagrangian perspective. We first examine the overall density of 10-day HYSPLIT back trajectories arriving in basin 6 on JJA and DJF "no AR" and AR_{90+} sample days and the differences in trajectory density between active and inactive periods. We then describe the water cycle history of these trajectories using calculations of moisture uptake in the boundary layer and free troposphere, E – P, and moisture flux derived from changes in specific humidity and wind velocity along each trajectory path, as described in Section 4.2.3.

Air parcels arriving in basin 6 on "no AR" sample days during JJA generally traverse paths that are limited to the southern GrIS and surrounding seas (top left panel of Figure 4.8). Trajectory density is especially high over the Davis Strait – Baffin Bay – Labrador Sea oceanic region to the west of Greenland, as well as the Denmark Strait and Greenland Sea to the southeast and east of Greenland. On AR_{90+} JJA sample days (top right panel of Figure 4.9), there is a pronounced southward shift in trajectory density relative to "no AR" days. A large fraction of air parcels bound for southwest Greenland pass over northeastern North America and over adjacent waters of the Gulf of St. Lawrence, northwest Atlantic Ocean, and Labrador Sea, with particularly high trajectory density extending from the lower St. Lawrence River valley northeastward into the Gulf of St. Lawrence. High trajectory density also is found from the central Atlantic Ocean northward to the subpolar North Atlantic south of Greenland, and a substantial number of trajectories also pass through a broad region of the northeast Atlantic

offshore of western Europe. A relatively small, but non-negligible, fraction of trajectories originates at subtropical latitudes as low as 25–30°N over the western and central Atlantic Ocean and the coastal southeast United States. The southward shift in parcel trajectories arriving on AR_{90+} days relative to "no AR" days is especially illustrated by the trajectory density difference map (bottom right panel of Figure 4.8), showing the more polar air mass sources for basin 6 on "no AR" days compared to AR_{90+} days.

The contrast in trajectory density between "no AR" and AR_{90+} events during winter (Figure 4.9) is generally similar to the summer patterns, with more southerly air mass origins again found for AR_{90+} days. Due to the stronger westerly flow in the boreal winter, winter trajectories show a tendency to traverse longer paths than summer trajectories, with substantial trajectory densities extending further away from Greenland compared to summer. On "no AR" winter days (top left panel of Figure 9) there is evidence of frequent transport of air from the Barents-Kara and Greenland Seas to basin 6, as well as less frequent long-range air parcel transport from eastern Europe and northern Canada. On AR_{90+} days (top right panel of Figure 9), a substantial fraction of air parcels originate from as far away as the northeast Pacific Ocean, with frequent trajectory passage over northern and northeastern North America. Another area of high trajectory density is located in the northeast Atlantic, similar to the summer maps (Figure 4.8). Air mass transport from the Barents-Kara Seas is much reduced on winter AR_{90+} days compared to "no AR" conditions. Notably, long-range transport from the western subtropical Atlantic Ocean during AR_{90+} events appears rare during winter.

During summer, moisture uptake in the boundary layer by air parcels arriving in basin 6 on "no AR" sample days is most concentrated over the Davis Strait, Baffin Bay, and the Labrador Sea (Figure 4.10). Substantial boundary layer moisture uptake also occurs along the

southeast coast of Greenland and, to a lesser extent, in the Nordic Seas and in southern Hudson Bay. Free troposphere moisture uptake occurs in roughly the same areas, although comparatively little free troposphere moisture uptake occurs over the Davis Strait and Baffin Bay, and more moisture is taken up in the free troposphere than in the boundary layer to the southeast coast of Greenland. High amounts of free troposphere moisture uptake over the southern GrIS are likely the signature of air being lifted above 900 hPa over the elevated topography in this region. The poleward limit of boundary layer and free troposphere moisture uptake appears to correspond to the sea ice edge over the Arctic Ocean, shown as monthly means for July and January during 1979–2017 in Figure 4.12. There appears to be a small amount of boundary layer moisture uptake over sea ice in the Pacific, although this may reflect the retreat of the sea ice edge during the 2002–2017 period of back trajectory analysis compared to the 1979–2017 sea ice climatology.

Moisture uptake by air parcels arriving in basin 6 on JJA AR_{90+} days exhibits a pronounced equatorward shift in comparison to "no AR" days (bottom row of Figure 4.10). In the boundary layer, moisture uptake is concentrated in a fan-shaped area radiating to the southwest, south, and southeast of Greenland, with a separate region of significant boundary layer moisture uptake in the vicinity of Iceland. The corridor of moisture uptake to the southwest of Greenland extends to quite low latitudes, with substantial moisture uptake contributions as far equatorward as the southeast coast of the United States. A concentrated zone of moisture uptake is located over Maine, New Brunswick, and the Gulf of St. Lawrence, extending northeastward along the boundary between the Labrador Sea and open Atlantic to southern Greenland. Strong boundary layer moisture uptake also occurs south of Greenland in the North Atlantic, roughly between 45°N and 60°N. Scattered boundary layer moisture uptake also occurs in the subtropical

central Atlantic Ocean, although this uptake is not as concentrated as the low-latitude uptake along the United States coastline.

Patterns of moisture uptake in the free troposphere on JJA AR_{90+} days are generally similar to boundary layer uptake, although little free troposphere moisture uptake is indicated in the aforementioned coastal United States region, and a region of substantial free troposphere uptake appears over the east-central subtropical Atlantic. The most concentrated areas of free troposphere moisture uptake appear in the subpolar North Atlantic south of Greenland and over the northeastern tip of North America. In the subpolar North Atlantic, this free troposphere moisture uptake is likely forced by ascent within warm conveyer belts associated with the ARs affecting basin 6. Over northeastern North America, it is probable that much of this "free troposphere" moisture uptake actually represents boundary layer evapotranspiration from elevated, forested land areas in New England, eastern Quebec, and Newfoundland and Labrador. Future studies should reproduce this analysis using the estimated boundary layer height from reanalysis datasets (see Section 4.2.3), rather than the 900 hPa boundary layer threshold employed in this study, to determine if this is the case. The identification of this region of northeast North America as a significant summer moisture source for southwest Greenland is supported by the results of *Bonne et al*. [2014] and *Steen-Larsen et al*. [2015]; the latter study found a pronounced signature of low deuterium excess values in moisture originating from this region using water vapor stable isotope observations from Ivittuut.

Examination of the E – P and moisture transport maps in Figure 4.10 provides additional insight into the sources and transport of moisture to basin 6 during JJA AR_{90+} events. Evaporation dominates over precipitation throughout the outer fringes of the region through which air parcels pass on their path to southwest Greenland. E – P values are especially high

over the Gulf Stream waters off the southeast United States coast and in the eastern Atlantic off the coasts of western Europe and northwest Africa. The contribution of these distant sources to moisture in basin 6 calculated through the moisture uptake analysis is not as high as the strong evaporation values might suggest, likely due to the relatively infrequent passage of trajectories over these regions (Figure 4.8) as well as rainout at later times along the trajectory path. It is also notable that southwesterly poleward moisture transport is quite intense in air parcels moving off the United States east coast and bound for basin 6 during AR_{90+} events. Although the relatively infrequent trajectory passage through this area is again indicated by the light coloration of the moisture flux vectors, this area of strong moisture transport, in combination with the E – P maps, suggests that the southern Gulf Stream can serve as a significant moisture source for southwest Greenland AR events in some cases.

Finally, the main features of the winter moisture uptake maps (Figure 4.11) are generally similar to summer, with moisture uptake mostly limited to polar regions for "no AR" sample days and extended further equatorward for AR_{90+} sample days. There is a notable tendency for more moisture uptake to occur over the Nordic Seas for winter "no AR" days in comparison to summer. Boundary layer and free troposphere moisture uptake is prevented by sea ice coverage in the interior Arctic Ocean, Davis Strait, and most of Hudson Bay (see Figure 4.12). As suggested by the trajectory density analysis, moisture uptake contributing to AR_{90+} events occurs in more poleward locations in winter compared to summer, with uptake concentrated in the Labrador Sea, subpolar North Atlantic, and northeast Atlantic. Substantial boundary layer moisture uptake also occurs in the vicinity of the St. Lawrence River valley and Gulf of St. Lawrence, and there is also a small, concentrated area of boundary layer moisture uptake over the English Channel. The narrow band of negative E – P values extending southeastward from

the southern tip of Greenland suggests convergence and uplift of air streams flowing from western and eastern Atlantic moisture sources in this area. A few areas of modest boundary layer and free troposphere moisture uptake are found over the northeast Pacific for AR_{90+} events, but the strongly negative E – P values along the Alaska and western Canada coastlines associated with these trajectories shows that rainout along their paths prevents the Pacific from serving as a significant moisture source for winter AR_{90+} events.

4. Discussion and Conclusions

Combining Eulerian analysis of the mean large-scale hydrological cycle with Lagrangian tracing of air parcel transport pathways and water cycle histories, our analyses reveal the large-scale evaporative conditions preceding active and inactive AR days in southwest Greenland, and shows how air parcels bound for Greenland are affected by moisture uptake and precipitation along their paths. Importantly, the Lagrangian trajectory analysis reveals evaporative source regions and transport pathways for water vapor reaching Greenland that cannot be inferred from time-mean evaporation and IVT maps alone and shows that areas of enhanced or suppressed evaporation preceding AR events do not necessarily correspond to moisture source or sink areas for air parcels en route to Greenland.

Comparison of the JJA evaporation and moisture transport anomaly maps in Figure 4.2 with the moisture uptake analyses in Figure 4.10 illustrates this point and demonstrates how the Eulerian and Lagrangian analyses can complement one another. During the 10 days preceding JJA AR_{90+} sample days in basin 6, anomalous evaporation occurs over northern North America, the western subtropical Atlantic Ocean off the east coast of the United States, and in the eastern Atlantic to the west of Europe (Figure 4.2). The Lagrangian back trajectory analysis shows that only some of this enhanced evaporation typically contributes moisture to AR events in

Greenland. In the vicinity of North America, boundary layer moisture uptake occurs over the eastern portion of the land surface evaporative anomalies in eastern Canada and the northeast United States, while only the western fringe of the subtropical Atlantic area of anomalous evaporation (along the southeast United States coast) contributes appreciable amounts of moisture to the western Greenland ARs. Boundary layer moisture uptake in the mid-latitude eastern Atlantic corresponds closely to the area of evaporative anomalies in this region for AR_{90+} events, demonstrating a location where the time-mean evaporation and back trajectory analyses provide similar conclusions. In contrast, the area of strongly negative evaporative anomalies in the Labrador Sea and subpolar North Atlantic to the south of Greenland is collocated with intense boundary layer and free troposphere moisture uptake identified by the trajectory analysis. This is likely an area where both strong depletion of water vapor through precipitation and replenishment through evaporation occurs within the warm conveyer belts of extratropical cyclones, resulting in a local along-path AR moisture source of the type described by *Dacre et al*. [2015].

In interpreting the Lagrangian moisture source results, it is important to note that this study only examined back trajectories terminating in the near-surface atmospheric layer (10 m – 500 m AGL) over western Greenland. Previous studies [e.g *Knippertz et al*., 2013; *Sodemann and Stohl*, 2013] have shown that parcel trajectories associated with long-range moisture transport from subtropical to extratropical latitudes tend to rise into the middle and upper troposphere upon reaching the downstream terminus of warm conveyer belts. Therefore, it is possible that our methodological design does not appropriately represent the influence of distant moisture sources that may contribute water vapor which typically rises to high altitudes upon reaching Greenland. Given the importance of liquid, mixed-phase, and ice clouds to the surface

energy balance of the GrIS during AR events [*Bennartz et al*., 2013; *van Tricht et al*., 2016; *Mattingly et al*., 2019] — many of which are likely located higher in the atmosphere than 500 m AGL [*Shupe et al*., 2013; *Miller et al*., 2017] — future studies should investigate the moisture source regions and transport characteristics of air parcels arriving in a deeper vertical layer of the lower and middle troposphere above the GrIS. Remotely-sourced moisture that rises into the middle and upper troposphere near Greenland also likely plays an important role in the development and maintenance of Greenland blocking anticyclones through latent heat release [*Pfahl et al*., 2015; *Grams and Archambault*, 2016]. In addition to the direct effects of Greenland blocks on the GrIS surface energy balance (higher near-surface temperatures, increased shortwave radiation), if accompanied by low pressure to the west of Greenland, these blocking anticyclones will result in a strengthened pressure gradient and accompanying barrier winds that intensify sensible heat flux along the western GrIS margin [*van den Broeke and Gallée*, 1996; *Mattingly et al*., 2019].

In addition to sampling a broader depth of the troposphere, future studies should also extend the record length of the Lagrangian trajectory analyses to match the time span of the Eulerian analyses, using a long-term reanalysis dataset such as ERA-Interim or MERRA-2 to drive the HYSPLIT model. This will provide for a longer-term assessment of moisture sources for ARs affecting the GrIS and will allow moisture sources earlier in the record to be compared to recent years to determine if GrIS moisture sources have shifted equatorward in concert with the recent decreasing GrIS mass trend. Moisture sources may also be compared for conditions of above- and below-normal Arctic sea ice extent to investigate whether variability in sea ice helps to control the export of moisture from the Arctic Ocean to Greenland. This may be particularly relevant for areas of the GrIS located at higher latitudes than basin 6, and future studies should

therefore also investigate the evaporative moisture sources for a variety of locations throughout the GrIS.

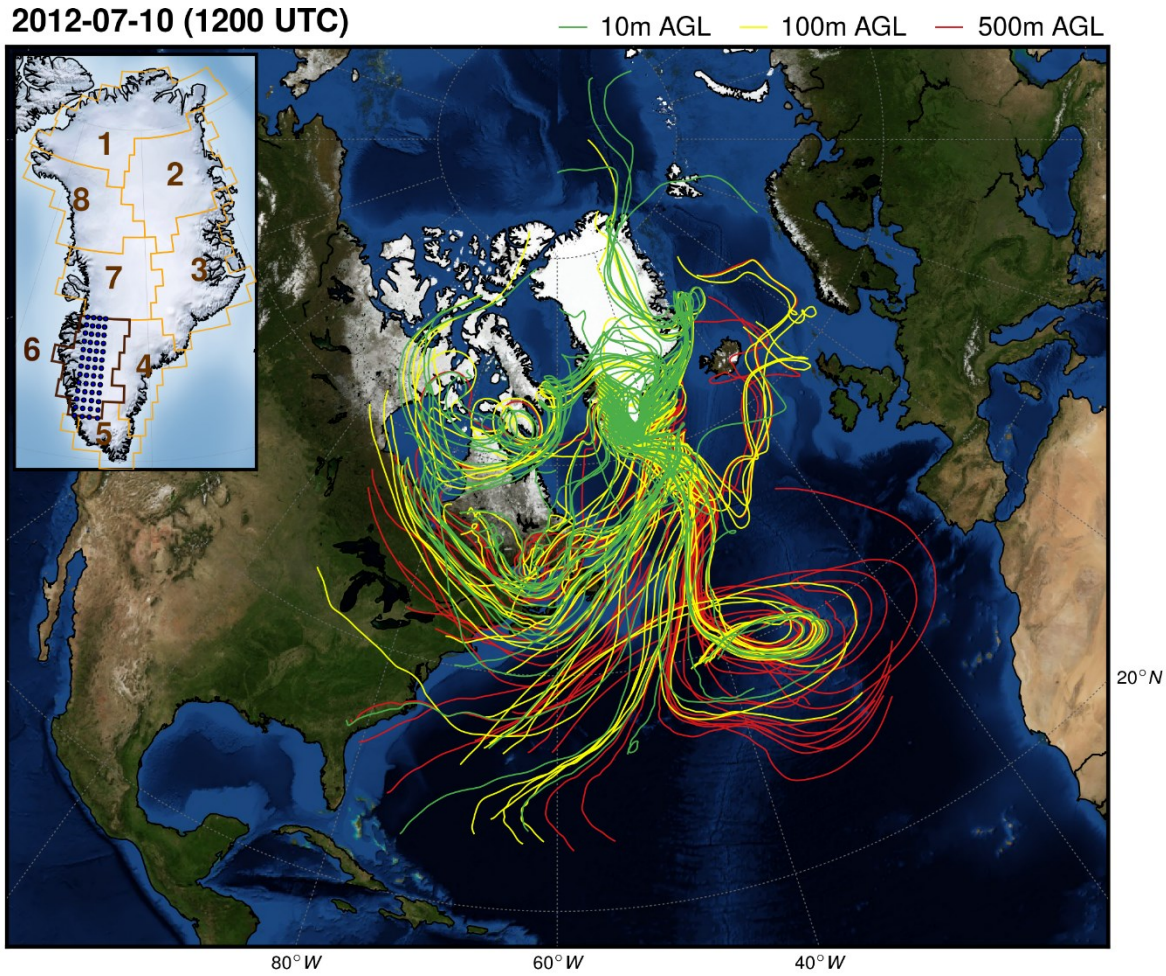

Figure 4.1. Examples of 10-day HYSPLIT back trajectories initiated over basin 6 during an AR_{90+} event at 1200 UTC 10 July 2012. Green lines show path of back trajectories ending at 10 m AGL, yellow lines show trajectories ending at 100 m AGL, and red lines show trajectories ending at 500 m AGL. Inset map shows outlines of all eight GrIS drainage basins and the locations of 52 points (spaced at 0.5° latitude / 1° longitude) from which back trajectories are launched at 1200 UTC on each sample date.

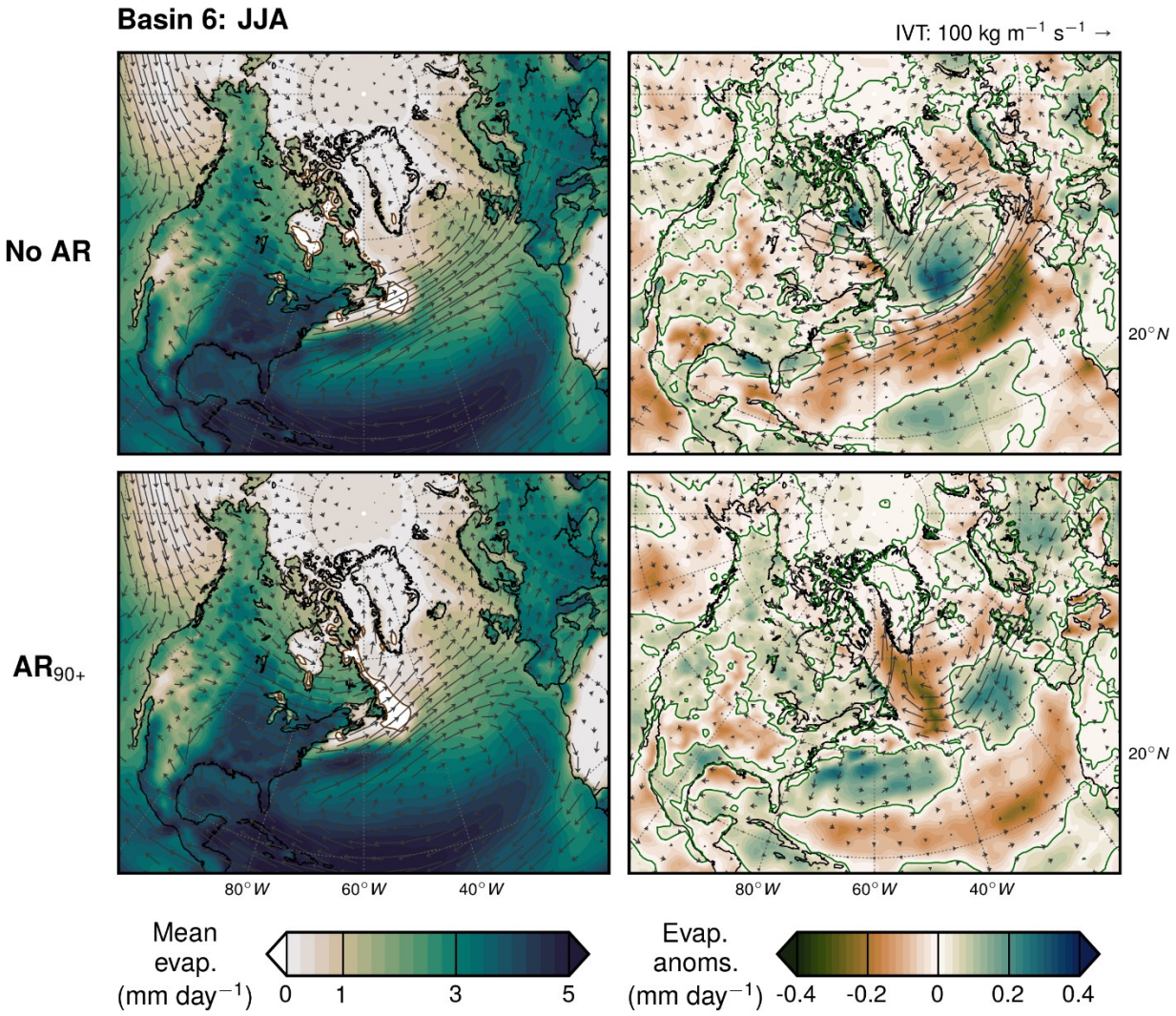

Figure 4.2. Left column: mean ERA-Interim evaporation (fill) and integrated water vapor transport (IVT; arrows) during the 10 days preceding "no AR" (top row) and AR$_{90+}$ sample dates (bottom row) during JJA. Right column: evaporation and IVT anomalies (departure from the 1980–2017 monthly mean) during the 10 days preceding "no AR" (top row) and AR$_{90+}$ (bottom row) sample dates during JJA.

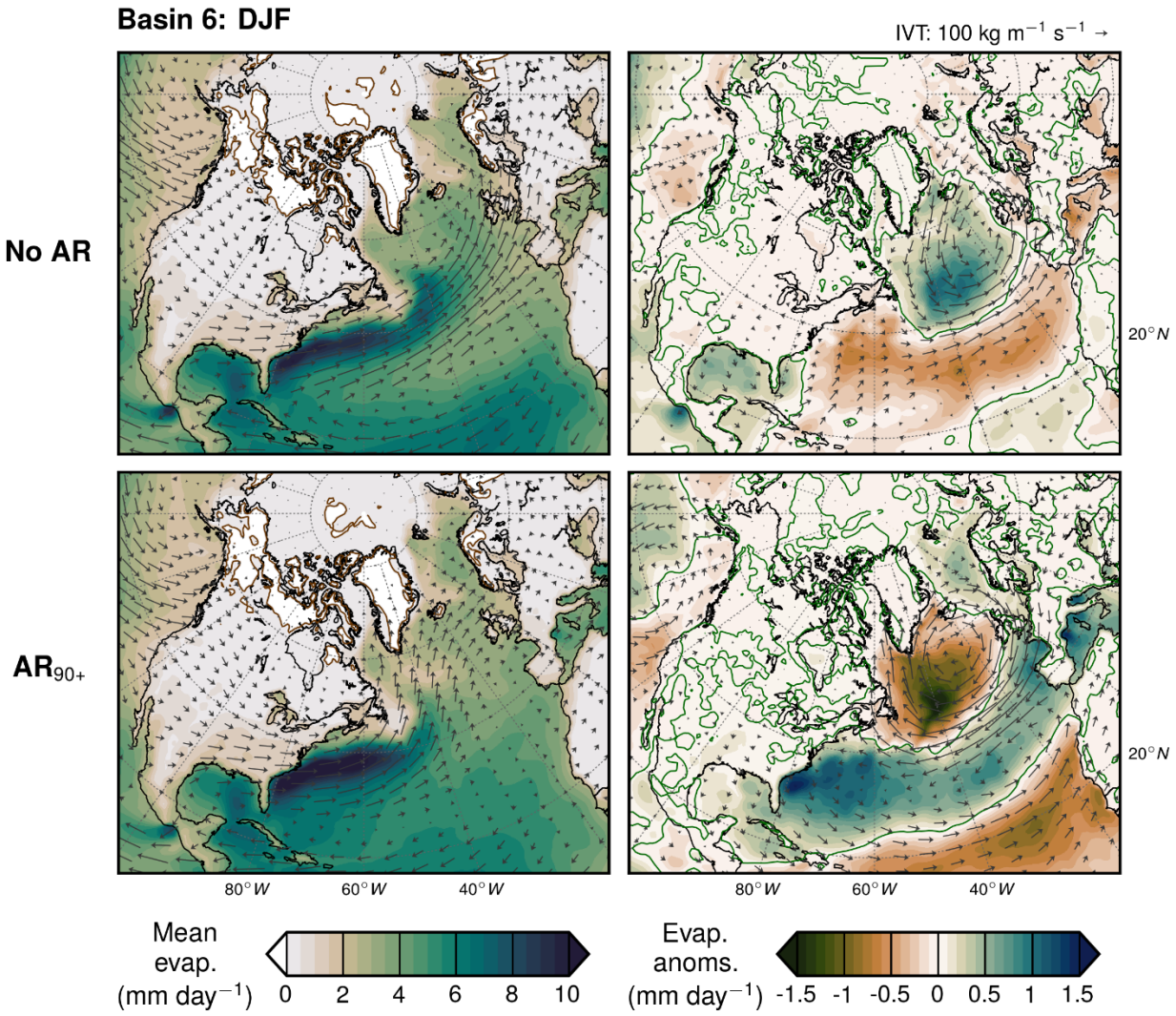

Figure 4.3. As in Figure 4.2, but for DJF "no AR" and AR$_{90+}$ sample dates.

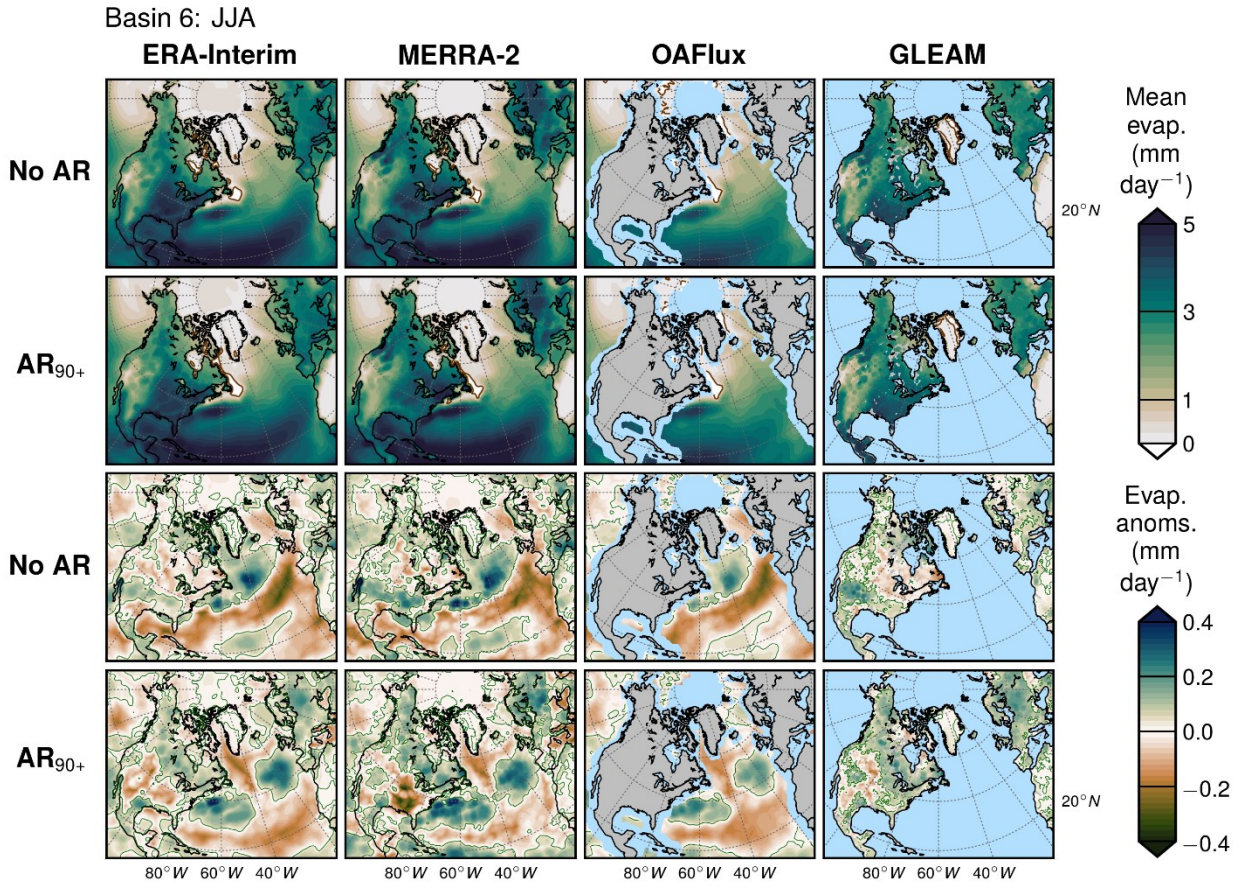

Figure 4.4. Comparison of mean evaporation and evaporation anomalies from ERA-Interim, MERRA-2, OAFlux, and GLEAM during the 10 days preceding "no AR" and AR_{90+} sample dates in JJA. Top two rows show mean evaporation and bottom two rows show evaporation anomalies, with "no AR" composites in rows 1 and 3 and AR_{90+} composites in rows 2 and 4. The four different data sources are shown in the four columns of the grid.

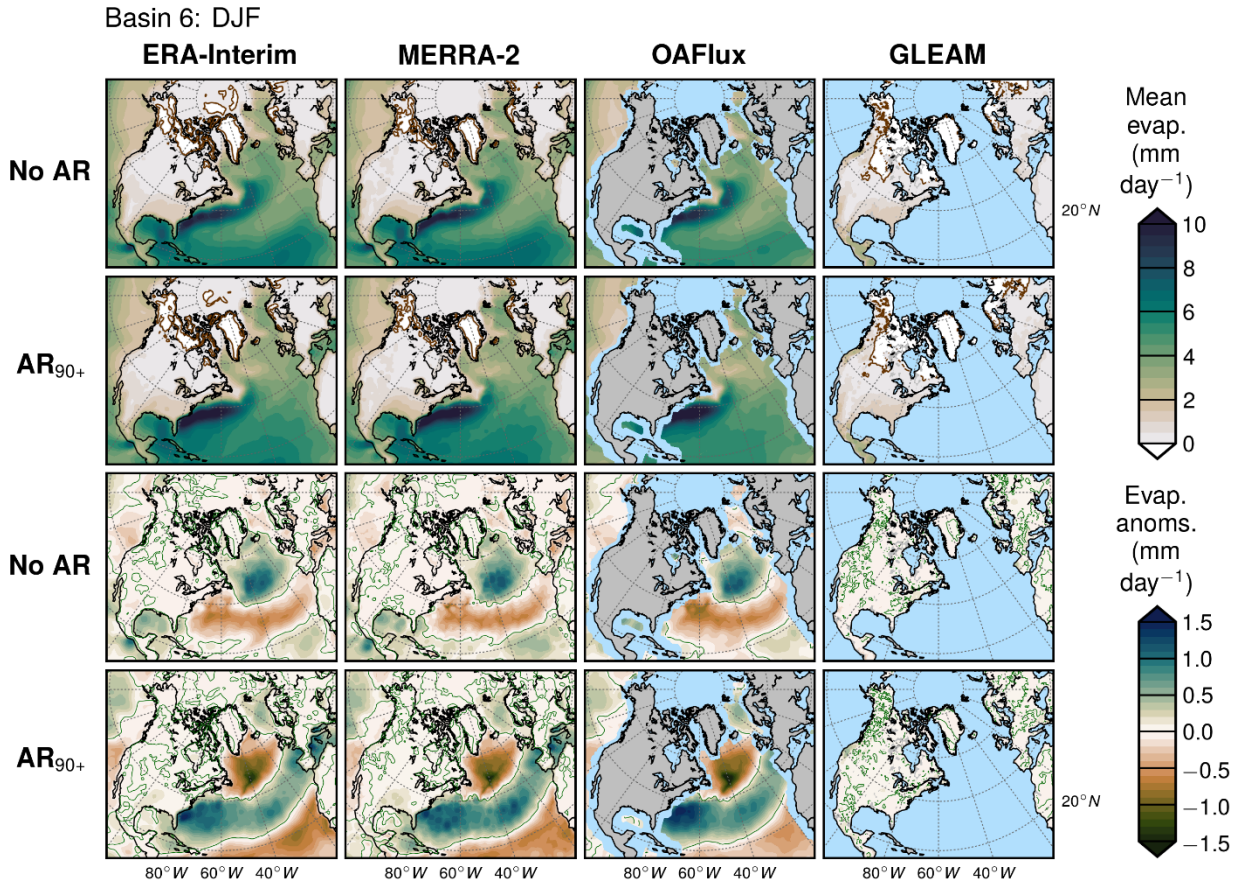

Figure 4.5. As in Figure 4.4, but during DJF.

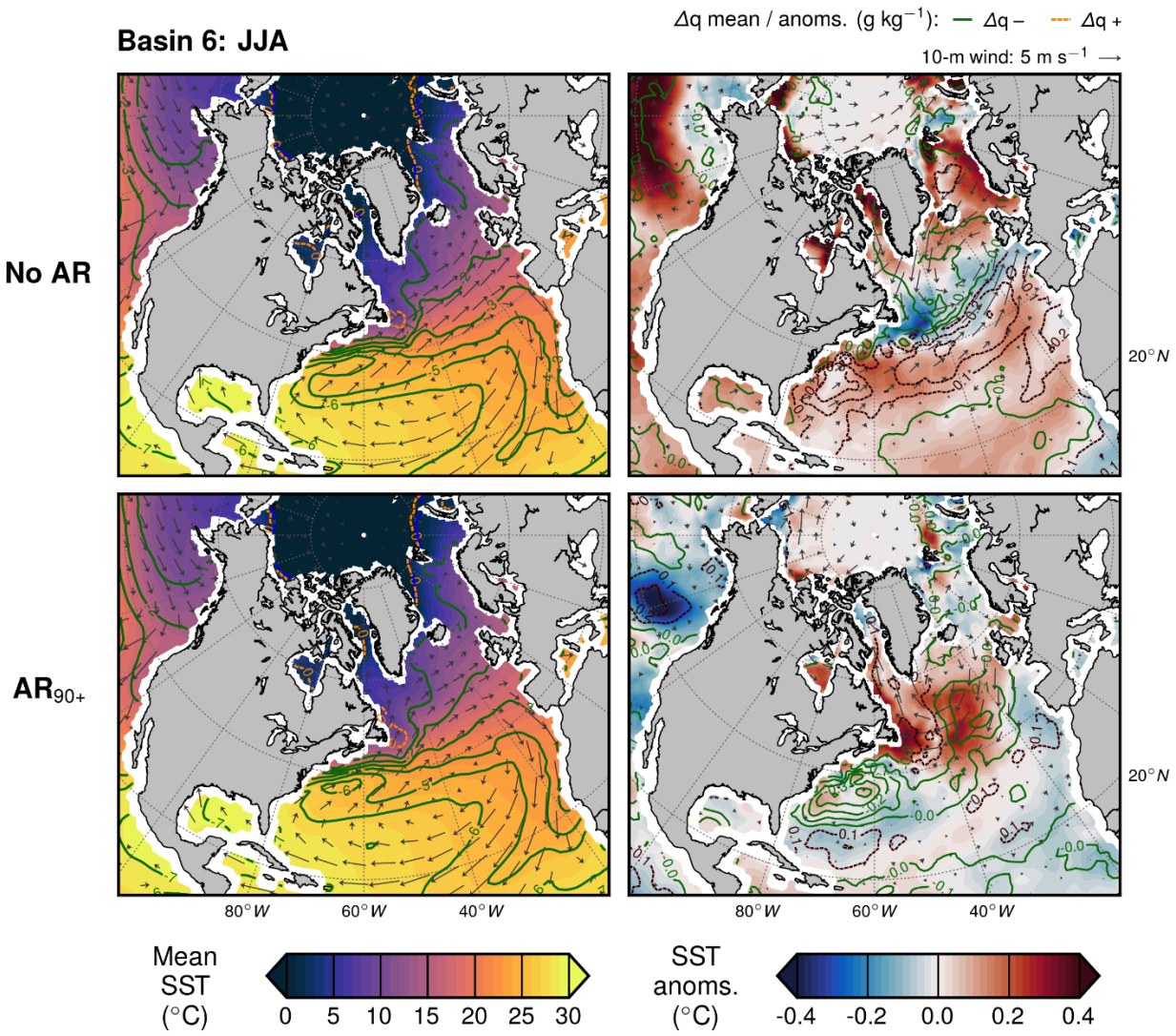

Figure 4.6. Comparison of large-scale oceanic evaporative conditions during the 10 days preceding "no AR" (top row) and AR90+ sample dates (bottom row) during JJA. Left column shows mean sea surface temperature (SST), 10-m wind vectors, and ocean-atmosphere specific humidity gradient (Δq). Right column shows anomalies of these quantities.

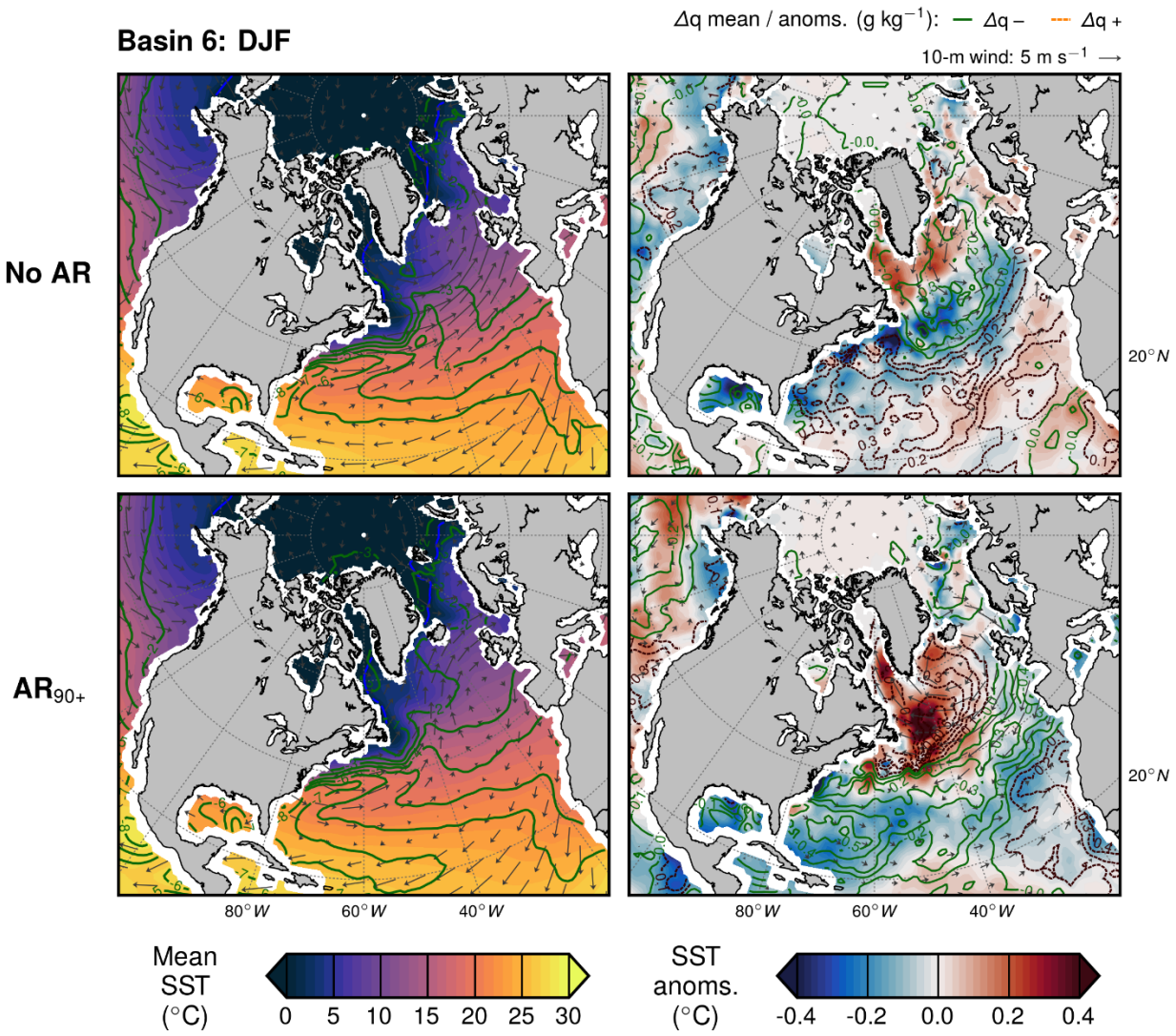

Figure 4.7. As in Figure 4.6, but during DJF.

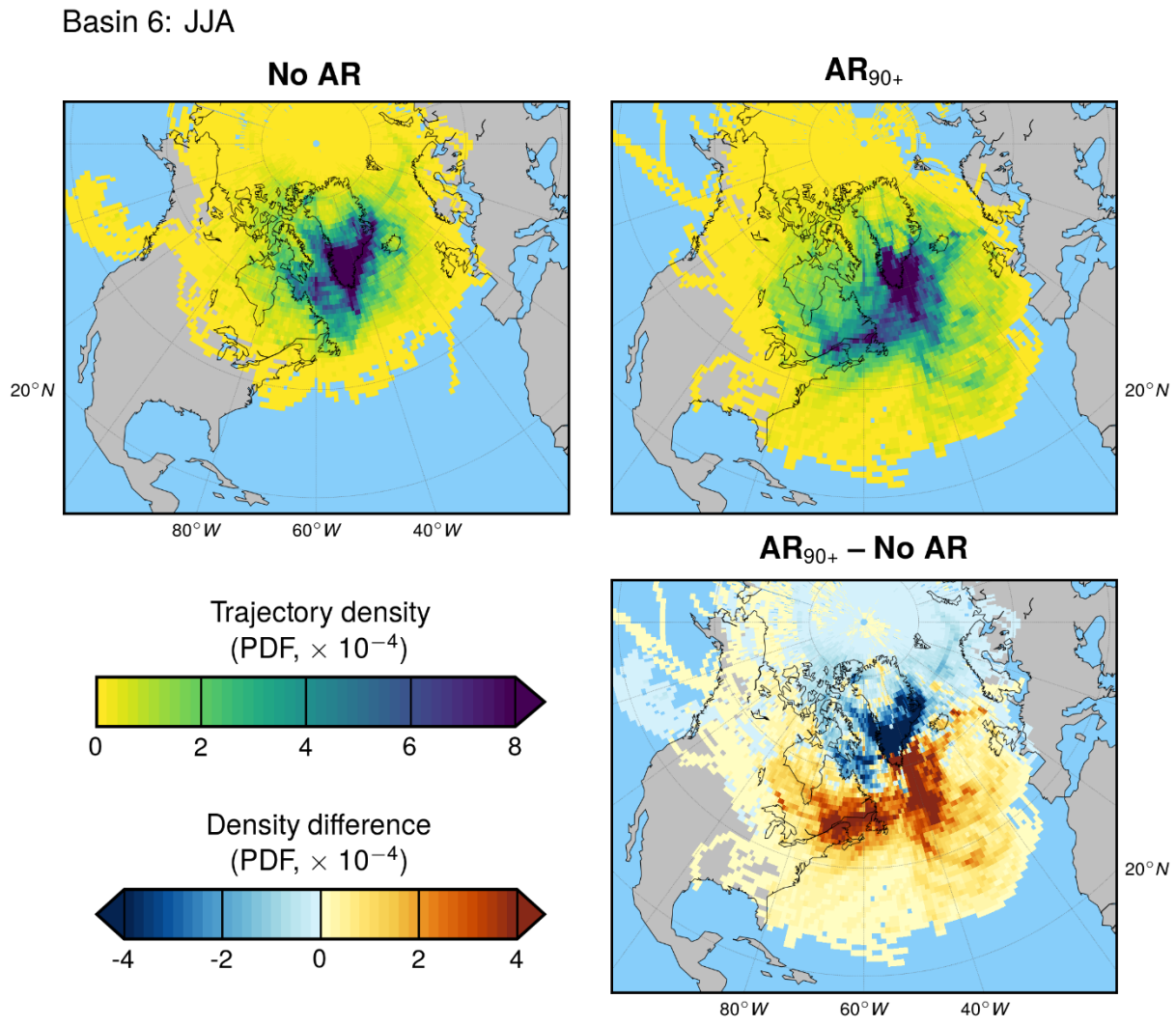

Figure 4.8. Top row: mean HYSPLIT trajectory density for 10-day back trajectories initiated on "no AR" sample dates (left) and AR_{90+} sample dates (right) during JJA. Bottom right shows the difference in trajectory density between AR_{90+} and "no AR" sample periods.

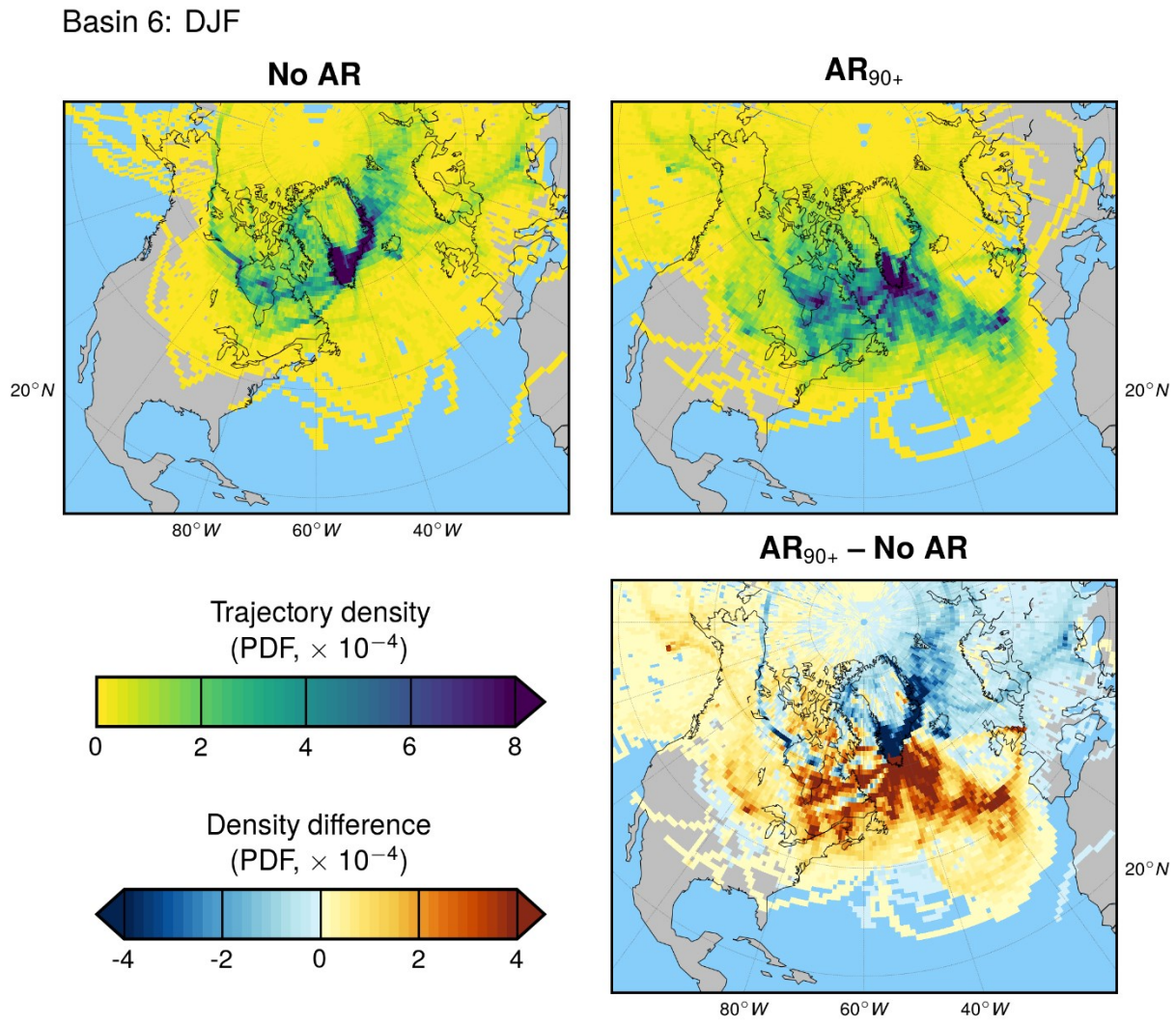

Figure 4.9. As in Figure 4.8, but for DJF "no AR" and AR_{90+} sample dates.

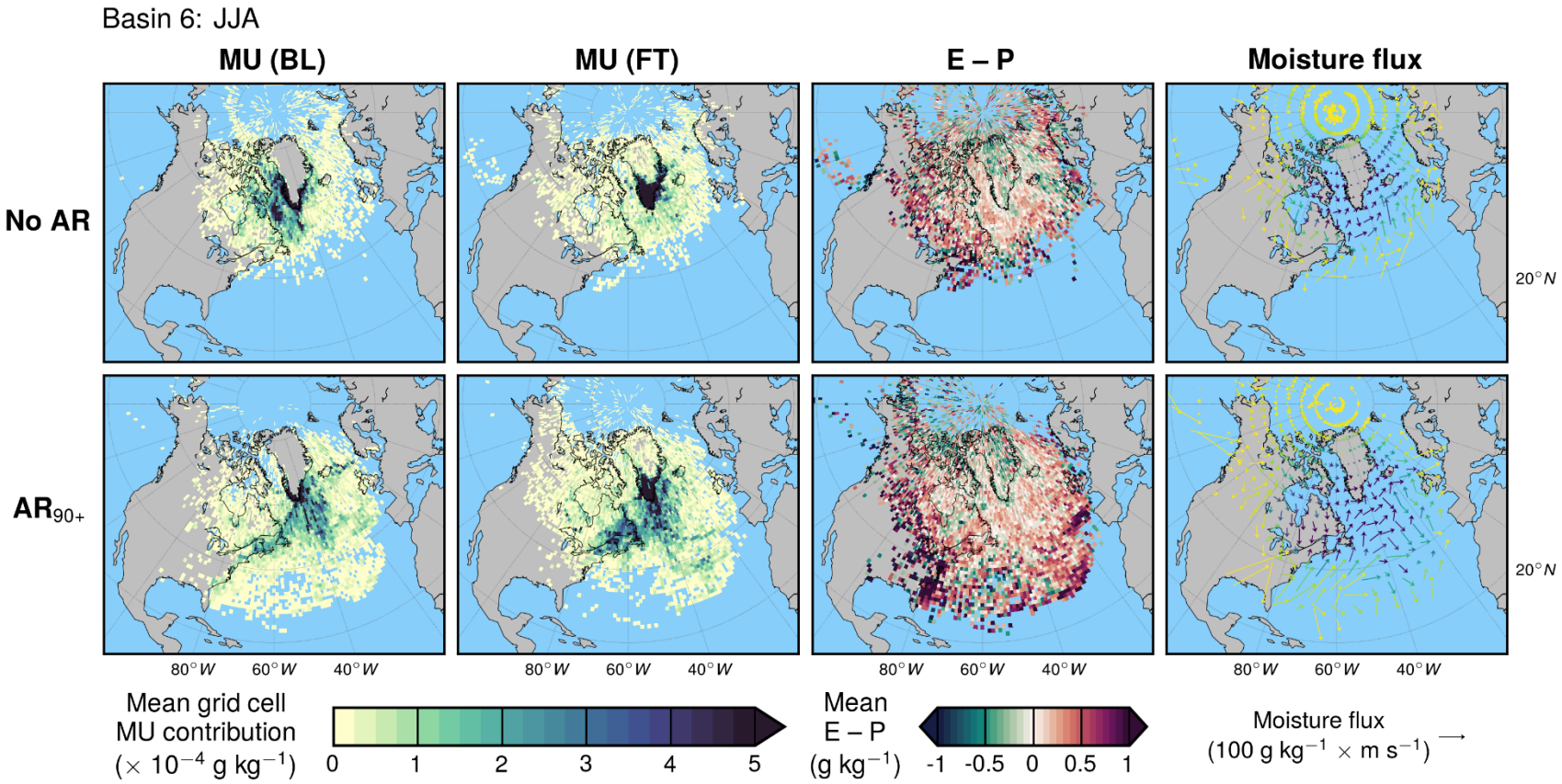

Figure 4.10. Moisture source diagnostics for HYSPLIT trajectories initiated on "no AR" sample dates (top row) and AR_{90+} sample dates (bottom row) during JJA. Left two columns show trajectory frequency-weighted moisture uptake in the boundary layer and free troposphere (MU BL and MU FT, respectively). Middle right column shows mean evaporation – precipitation (E–P). Right column shows mean moisture flux vectors along parcel trajectories for all 1° × 1° grid cells through which at least one trajectory passed during the given season and AR condition. Length of moisture flux vector arrows indicates the mean intensity of moisture transport, and color of arrows indicates how frequently trajectories passed through the area (light yellow / green = low trajectory density; dark blue = high trajectory density).

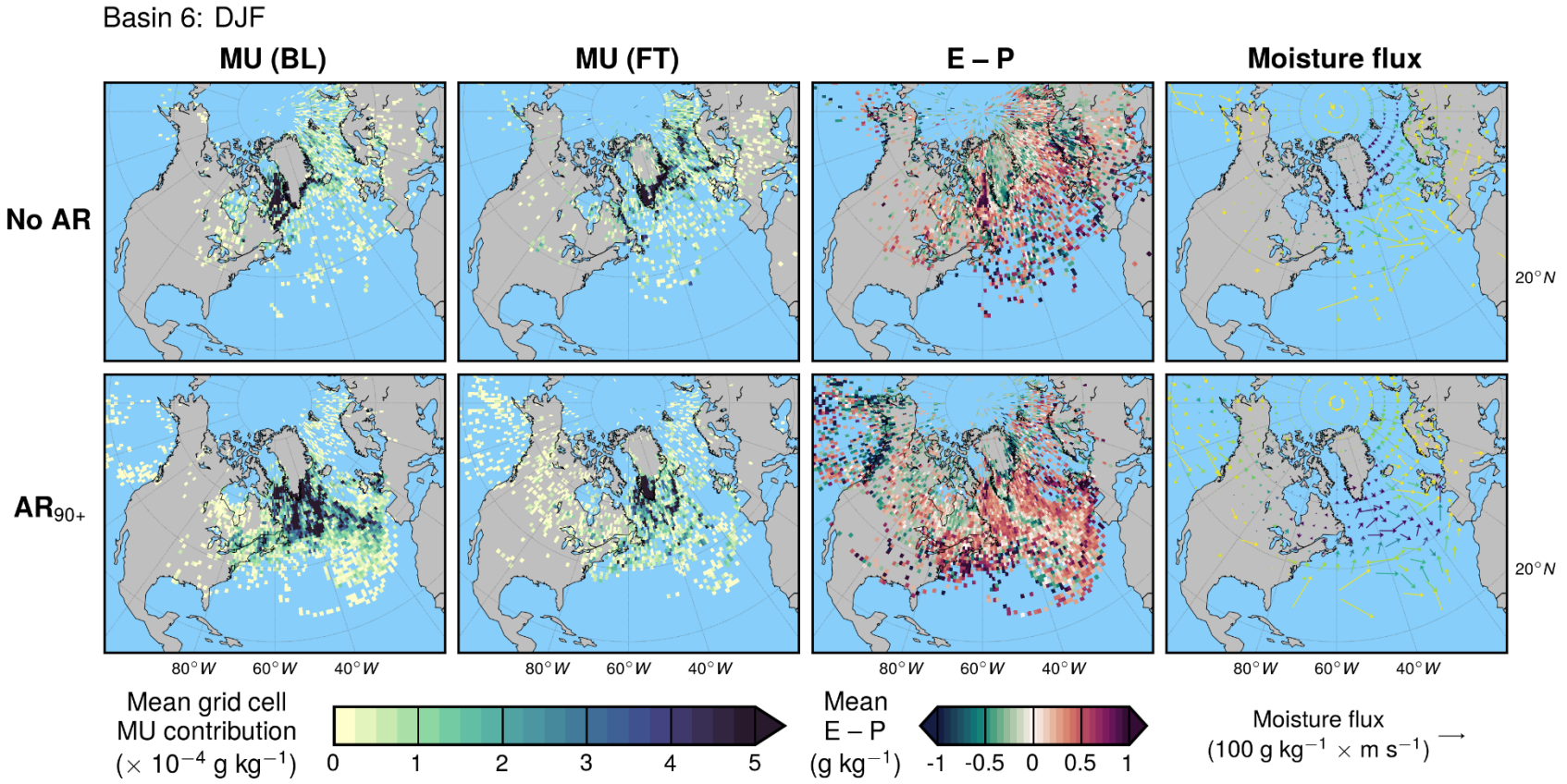

Figure 4.11. As in Figure 4.10, but for DJF "no AR" and AR_{90+} trajectories.

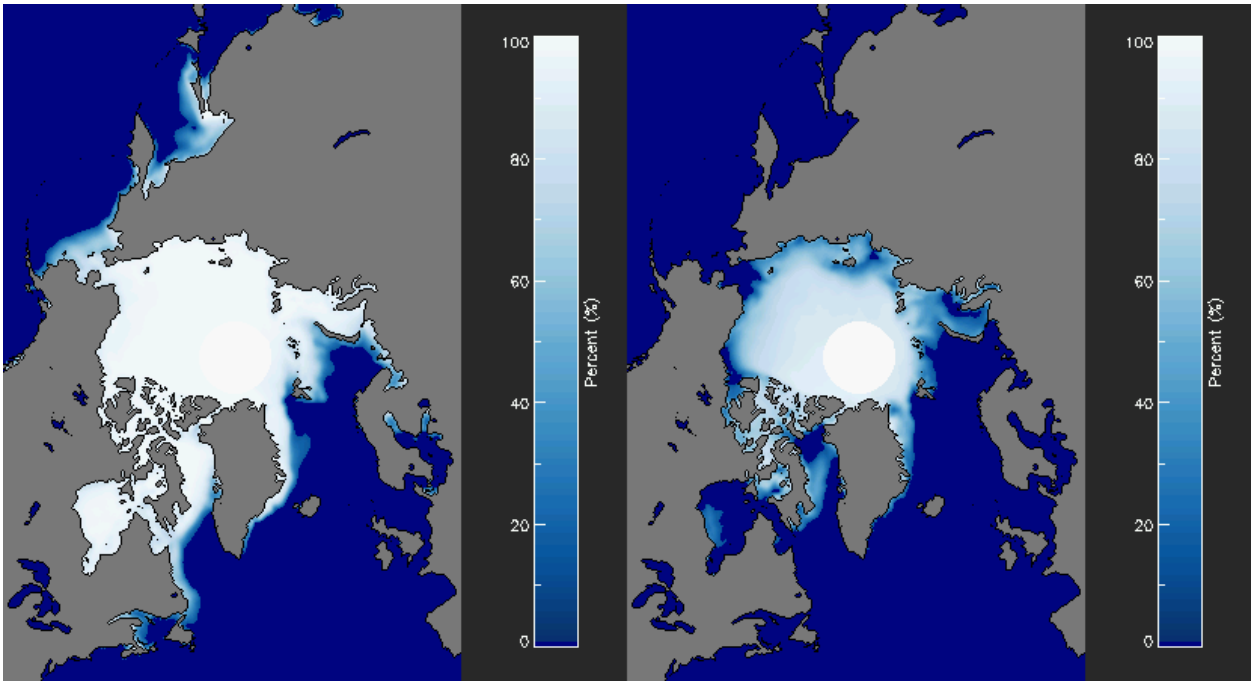

Figure 4.12. Mean Arctic sea ice concentration during January (left) and July (right), 1979–2017. Figures reproduced from the National Snow and Ice Data Center [*Stroeve and Meier*, 2018].

CHAPTER 5

CONCLUSION

In this dissertation, the impacts of poleward moisture transport by atmospheric rivers (ARs) on the Greenland Ice Sheet (GrIS) have been analyzed from a multi-scale perspective, contextualizing ice sheet mass changes that are local and regional in scope within the synoptic- to global-scale flows of energy and mass that drive the Earth's climate system. It has been shown that the decreasing GrIS mass trend that began in the late 1990s is connected with increasing poleward moisture transport by ARs to western Greenland over the same period, among other key findings. This research demonstrates that the characteristics of short-lived, intense moisture transport to Greenland by ARs must be reproduced by global climate models (GCMs) in order for projections of GrIS mass evolution to be accurate. Through its contributions to scientific understanding of the ocean-atmosphere-cryosphere interactions that control the mass balance of the GrIS and identification of specific features that must be captured in model simulations, this dissertation will contribute to refined projections of future global mean sea level rise.

The first of the three manuscripts comprising this dissertation (Chapter 2) provided clear evidence of the critical role that enhanced AR activity has played in the recent acceleration of GrIS mass loss. From 2000–2012, a nearly continuous string of years with anomalously strong water vapor transport to western Greenland by ARs coincided with the extensively documented increasing GrIS mass loss trend. This period of enhanced AR activity culminated in the extreme AR and GrIS mass loss conditions July 2012, as nearly the entire ice sheet experienced surface melt for the first time since the 19th Century at the same time as one of the most intense AR

events on record passed over the ice sheet. Through a long-term (1980–2016) analysis of AR events, it was found that this event, while extreme, was consistent with the typical effects of strong summer ARs, as there is a clear signal for intense SMB losses during strong AR events across the historical record. It was also shown that ARs bring enhanced snow accumulation (SMB gains) to the GrIS during winter and at higher elevations during summer, but the scale of potential mass gains from AR-induced snowfall is much less than the mass losses for which they are responsible during the summer.

Chapter 3 built on the results of Chapter 2 by analyzing the physical mechanisms by which strong summer ARs induce GrIS melt when they make landfall in western Greenland. Through analysis of the relationship between the surface energy balance and cloud properties during strong AR events, along with the synoptic- to local-scale atmospheric conditions and surface-atmosphere interactions driving these surface energy balance and cloud changes, the complex set of processes by which ARs force melt was revealed. In immediate vicinity of AR landfall, days with an AR exceeding the 90th IVT percentile (AR_{90+} days) typically are characterized by cloudy, moist, warm, and windy conditions over the ice sheet. The cloudy conditions produce compensating negative net shortwave radiation anomalies and positive net longwave radiation anomalies, while the enhanced wind speeds drive strong turbulent fluxes of sensible and latent heat into the surface, particularly in the low-elevation GrIS ablation zone. These “barrier winds” are in turn driven by a combination of synoptic- and local-scale forcing. The large-scale pressure gradient between high pressure over the ice sheet and low pressure over Baffin Bay combines with an increased local thermal contrast between the cool near-ice atmospheric layer and the advectively warmed free troposphere to produce anomalously high wind speeds. During strong summer AR events that make landfall in northwest Greenland, a

distinct set of physical mechanisms produces melt along the eastern margin of the GrIS. Wind flow downslope produces clear skies and positive net shortwave radiation anomalies in this region, and adiabatically-warmed air is entrained into the boundary layer from above to increase sensible heat flux.

The third and final manuscript (Chapter 4) analyzed whether present-day AR events link melting in Greenland with conditions in distant lower-latitude regions through an examination of the evaporative moisture sources for water vapor arriving in southwest Greenland. Both Eulerian and Lagrangian analyses of the hydrological cycle were employed to provide complementary information on large-scale patterns of evaporation and their contributions to water vapor during strong AR events compared to "no AR" days. The Eulerian method consisted of time-mean composites of evaporative conditions during the 10 days preceding strong AR events and "no AR" days, while the Lagrangian method involved the calculation of moisture uptake along air parcel trajectories tracked backward from southwest Greenland for 10 days. Results demonstrated a clear shift toward lower-latitude moisture sources during strong AR events in comparison to "no AR" days during both summer and winter. Moisture arriving in southwest Greenland on "no AR" days is primarily drawn from the surrounding seas in relatively close proximity to Greenland, with substantial contribution from the Barents-Kara Seas as well. During strong AR events, moisture uptake occurs in several preferred regions of the Atlantic Ocean and northeastern North America before air parcels arrive in Greenland. The largest moisture source for strong AR events is the subpolar North Atlantic to the south of Greenland, but substantial evaporative moisture sources are found as far as the Gulf Stream off the southeastern United States coastline and the subtropical Atlantic Ocean off the northwest coast of Africa during the summer. The St. Lawrence Valley region of northeastern North America

serves as a particularly important moisture source for strong summer AR events. During winter, evaporative moisture sources for ARs shift poleward and oceanic moisture uptake is preferred over land surface evapotranspiration.

Adding to the body of literature on local and remote mechanisms contributing to Arctic Amplification discussed in Chapter 1, this dissertation provides clear evidence that lower-latitude forcing is key to anomalous GrIS melt episodes during the summer. The strong AR events that are shown to force intense SMB losses on daily time scales in Chapter 2 involve moisture transport across hundreds to thousands of kilometers from mid-latitude and, in some cases, subtropical sources to the GrIS, as shown in Chapter 4. In this respect, the results of this dissertation align with the burgeoning literature, reviewed in Chapter 1, that links poleward moisture transport from lower-latitude sources to enhanced melt and impeded freeze-up of Arctic sea ice. However, the local-scale physical mechanisms through which ARs force GrIS melt are found in Chapter 3 to differ from the processes by which poleward moisture intrusions affect sea ice. While enhanced downwelling longwave radiation under cloudy conditions has been found to be the main energy source for sea ice melt, Chapter 3 finds a more complex, spatially varying mixture of cloudy and clear energetic regimes supporting GrIS melt during strong summer AR events, and a barrier wind unique to the GrIS helps drive enhanced turbulent heat fluxes in the vicinity of AR landfall.

The intensity of moisture transport within these AR events has increased alongside increasing GrIS melt since the late 20th Century, as shown in Chapter 2. This trend is consistent with theoretical and model-based projections of increasing poleward moisture transport reviewed in Chapter 1, suggesting that this anticipated effect of climate change has already transitioned from prediction into reality. The near-total melting of the GrIS surface in July 2012 — for the

first time in over a century — provides further evidence that Greenland's climate has departed the bounds of natural variability. However, these events have occurred during unusually favorable states of the NAO and AMO for Greenland warmth, and the degree to which these internal modes of climate variability are modified by background warming is not clear. The future evolution of the GrIS will undoubtedly be determined by internal climate variability in concert with anthropogenic climate change. Therefore, building on this dissertation, future research should further investigate the large-scale dynamical drivers of Greenland AR activity and assess the ability of GCMs to simulate these dynamical drivers and AR events, applying this knowledge to GCM projections with the goal of improving predictions of the future evolution of the GrIS.

REFERENCES

Aemisegger, F., and L. Papritz (2018), A climatology of strong large-scale ocean evaporation events. Part I: identification, global distribution, and associated climate conditions, *Journal of Climate*, *31*(18), 7287–7312, doi:10.1175/JCLI-D-17-0591.1.

Agosta, C., C. Amory, C. Kittel, A. Orsi, V. Favier, H. Gallée, M. R. van den Broeke, J. T. M. Lenaerts, J. M. van Wessem, W. J. van de Berg, and X. Fettweis (2019), Estimation of the Antarctic surface mass balance using the regional climate model MAR (1979–2015) and identification of dominant processes, *The Cryosphere*, *13*(1), 281–296, doi:10.5194/tc-13-281-2019.

Ahlstrøm, A. P., D. Petersen, P. L. Langen, M. Citterio, and J. E. Box (2017), Abrupt shift in the observed runoff from the southwestern Greenland ice sheet, *Science Advances*, *3*(12), e1701169, doi:10.1126/sciadv.1701169.

Alexander, P., M. Tedesco, X. Fettweis, R. van de Wal, C. Smeets, and M. van den Broeke (2014), Assessing spatio-temporal variability and trends in modelled and measured Greenland Ice Sheet albedo (2000–2013), *The Cryosphere*, *8*(6), 2293–2312, doi:10.5194/tc-8-2293-2014.

Alexander, P. M., A. N. LeGrande, E. Fischer, M. Tedesco, X. Fettweis, M. Kelley, S. M. J. Nowicki, and G. A. Schmidt (2019), Simulated Greenland surface mass balance in the GISS ModelE2 GCM: Role of the ice sheet surface, *Journal of Geophysical Research: Earth Surface*, *124*(3), 750–765, doi:10.1029/2018JF004772.

Alexeev, V. A., and C. H. Jackson (2013), Polar amplification: is atmospheric heat transport important?, *Climate Dynamics*, *41*(2), 533–547, doi:10.1007/s00382-012-1601-z.

Alexeev, V. A., J. E. Walsh, V. V. Ivanov, V. A. Semenov, and A. V. Smirnov (2017), Warming in the Nordic Seas, North Atlantic storms and thinning Arctic sea ice, *Environmental Research Letters*, *12*(8), 084011, doi:10.1088/1748-9326/aa7a1d.

Alley, R. B., J. T. Andrews, J. Brigham-Grette, G. K. C. Clarke, K. M. Cuffey, J. J. Fitzpatrick, S. Funder, S. J. Marshall, G. H. Miller, J. X. Mitrovica, D. R. Muhs, B. L. Otto-Bliesner, L. Polyak, and J. W. C. White (2010), History of the Greenland Ice Sheet: paleoclimatic insights, *Quaternary Science Reviews*, *29*(15), 1728–1756, doi:10.1016/j.quascirev.2010.02.007.

American Meteorological Society (AMS) (2017), Atmospheric river, accessed 10 Dec 2017 at http://glossary.ametsoc.org/wiki/Atmospheric_river.

Van Angelen, J. H., M. Van den Broeke, and W. Van de Berg (2011), Momentum budget of the atmospheric boundary layer over the Greenland ice sheet and its surrounding seas, *Journal of Geophysical Research: Atmospheres*, *116*(D10), D10101, doi:10.1029/2010JD015485.

Van As, D. (2011a), Warming, glacier melt and surface energy budget from weather station observations in the Melville Bay region of northwest Greenland, *Journal of Glaciology*, *57*(202), 208–220, doi:10.3189/002214311796405898.

Van As, D., R. S. Fausto, A. P Ahlstrøm, S. B. Andersen, M. L. Andersen, M. Citterio, K. Edelvang, P. Gravesen, H. Machguth, F. M. Nick, S. Nielsen, and A. Weidick (2011b), Programme for Monitoring of the Greenland Ice Sheet (PROMICE): first temperature and ablation records, *Geological Survey of Denmark and Greenland Bulletin*, 23, 73–76.

Van As, D., A. L. Hubbard, B. Hasholt, A. B. Mikkelsen, M. R. van den Broeke, and R. S. Fausto (2012), Large surface meltwater discharge from the Kangerlussuaq sector of the Greenland ice sheet during the record-warm year 2010 explained by detailed energy balance observations, *The Cryosphere*, *6*(1), 199–209, doi:10.5194/tc-6-199-2012.

Van As, D., M. Langer Andersen, D. Petersen, X. Fettweis, J. H. van Angelen, J. T. M. Lenaerts, M. R. van den Broeke, J. M. Lea, C. E. Bøggild, A. P. Ahlstrøm, and K. Steffen (2014), Increasing meltwater discharge from the Nuuk region of the Greenland ice sheet and implications for mass balance (1960–2012), *Journal of Glaciology*, *60*(220), 314–322, doi:10.3189/2014JoG13J065.

Auger, J. D., S. D. Birkel, K. A. Maasch, P. A. Mayewski, and K. C. Schuenemann (2017), Examination of precipitation variability in southern Greenland, *Journal of Geophysical Research: Atmospheres*, *122*(12), 6202–6216, doi:10.1002/2016JD026377.

Azad, R., and A. Sorteberg (2017), Extreme daily precipitation in coastal western Norway and the link to atmospheric rivers, *Journal of Geophysical Research: Atmospheres*, *122*(4), 2080–2095, doi:10.1002/2016JD025615.

Backes, T. M., M. L. Kaplan, R. Schumer, and J. F. Mejia (2015), A climatology of the vertical structure of water vapor transport to the Sierra Nevada in cool season atmospheric river precipitation events, *Journal of Hydrometeorology*, *16*(3), 1029–1047, doi:10.1175/JHM-D-14-0077.1.

Baggett, C., and S. Lee (2015), Arctic warming induced by tropically forced tapping of available potential energy and the role of the planetary-scale waves, *Journal of the Atmospheric Sciences*, *72*(4), 1562–1568, doi:10.1175/JAS-D-14-0334.1.

Baggett, C., S. Lee, and S. Feldstein (2016), An investigation of the presence of atmospheric rivers over the North Pacific during planetary-scale wave life cycles and their role in Arctic warming, *Journal of the Atmospheric Sciences*, *73*(11), 4329–4347, doi:10.1175/JAS-D-16-0033.1.

Baldini, L. M., F. McDermott, J. U. Baldini, M. J. Fischer, and M. Möllhoff (2010), An investigation of the controls on Irish precipitation $\delta^{18}O$ values on monthly and event timescales, *Climate Dynamics*, *35*(6), 977–993, doi:10.1007/s00382-010-0774-6.

Bamber, J. L., R. M. Westaway, B. Marzeion, and B. Wouters (2018), The land ice contribution to sea level during the satellite era, *Environmental Research Letters*, *13*(6), 063008, doi:10.1088/1748-9326/aac2f0.

Bao, J., S. Michelson, P. Neiman, F. Ralph, and J. Wilczak (2006), Interpretation of enhanced integrated water vapor bands associated with extratropical cyclones: Their formation and connection to tropical moisture, *Monthly Weather Review*, *134*(4), 1063–1080, doi:10.1175/MWR3123.1.

Barnes, E. A., and D. L. Hartmann (2012), Detection of Rossby wave breaking and its response to shifts of the midlatitude jet with climate change, *Journal of Geophysical Research: Atmospheres*, *117*(D9), D09117, doi:10.1029/2012JD017469.

Barnes, E. A. (2013), Revisiting the evidence linking Arctic amplification to extreme weather in midlatitudes, *Geophysical Research Letters*, *40*(17), 4734–4739, doi:10.1002/grl.50880.

Bendixen, M., L. L. Iversen, and I. Overeem (2017), Greenland: Build an economy on sand, *Science*, *358*(6365), 879, doi: 10.1126/science.aar3388.

Bengtsson, L. (2010), The global atmospheric water cycle, *Environmental Research Letters*, *5*(2), 025202, doi:10.1088/1748-9326/5/2/025202.

Bengtsson, L., K. I. Hodges, S. Koumoutsaris, M. Zahn, and P. Berrisford (2013), The changing energy balance of the polar regions in a warmer climate, *Journal of Climate*, *26*(10), 3112–3129, doi:10.1175/JCLI-D-12-00233.1.

Bennartz, R., M. D. Shupe, D. D. Turner, V. P. Walden, K. Steffen, C. J. Cox, M. S. Kulie, N. B. Miller, and C. Pettersen (2013), July 2012 Greenland melt extent enhanced by low-level liquid clouds., *Nature*, *496*(7443), 83–86, doi:10.1038/nature12002.

Berdahl, M., Å. K. Rennermalm, A. Hammann, J. Mioduszweski, S. Hameed, M. Tedesco, J. Stroeve, T. L. Mote, T. Koyama, and J. R. McConnell (2018), Southeast Greenland winter precipitation strongly linked to the Icelandic Low position, *Journal of Climate*, *31*(11), 4483–4500, doi:10.1175/JCLI-D-17-0622.1.

Bevis, M., C. Harig, S. Khan, A. Brown, F. J. Simons, M. Willis, X. Fettweis, M. R. van den Broeke, F. B. Madsen, E. Kendrick, D. J. Caccamise II, T. van Dam, P. Knudsen, and T. Nylen (2019), Accelerating changes in ice mass within Greenland, and the ice sheet's sensitivity to atmospheric forcing, *Proceedings of the National Academy of Sciences*, *116*(6), 1934–1939, doi:10.1073/pnas.1806562116.

Binder, H., M. Boettcher, C. M. Grams, H. Joos, S. Pfahl, and H. Wernli (2017), Exceptional air mass transport and dynamical drivers of an extreme wintertime Arctic warm event, *Geophysical Research Letters*, *44*(23), 12,028–12,036, doi:10.1002/2017GL075841.

Boisvert, L., and J. Stroeve (2015), The Arctic is becoming warmer and wetter as revealed by the Atmospheric Infrared Sounder, *Geophysical Research Letters*, *42*(11), 4439–4446, doi:10.1002/2015GL063775.

Bolton, D. (1980), The computation of equivalent potential temperature, *Monthly Weather Review*, *108*(7), 1046–1053, doi:10.1175/1520-0493(1980)108<1046:TCOEPT>2.0.CO;2.

Bond, T. C. et al. (2013), Bounding the role of black carbon in the climate system: A scientific assessment, *Journal of Geophysical Research: Atmospheres*, *118*(11), 5380–5552, doi:10.1002/jgrd.50171.

Bonne, J.-L., V. Masson-Delmotte, O. Cattani, M. Delmotte, C. Risi, H. Sodemann, and H. Steen-Larsen (2014), The isotopic composition of water vapour and precipitation in Ivittuut, southern Greenland, *Atmospheric Chemistry and Physics*, *14*(9), 4419–4439, doi:10.5194/acp-14-4419-2014.

Bonne, J.-L., H. C. Steen-Larsen, C. Risi, M. Werner, H. Sodemann, J.-L. Lacour, X. Fettweis, G. Cesana, M. Delmotte, O. Cattani, P. Vallelonga, H. A. Kjær, C. Clerbaux, Á. E. Sveinbjörnsdóttir, and V. Masson-Delmotte (2015), The summer 2012 Greenland heat wave: In situ and remote sensing observations of water vapor isotopic composition during an atmospheric river event, *Journal of Geophysical Research: Atmospheres*, *120*(7), 2970–2989, doi:10.1002/2014JD022602.

Bosilovich, M. G., F. R. Robertson, L. Takacs, A. Molod, and D. Mocko (2017), Atmospheric water balance and variability in the MERRA-2 reanalysis, *Journal of Climate*, *30*(4), 1177–1196, doi:10.1175/JCLI-D-16-0338.1.

Box, J. E., X. Fettweis, J. C. Stroeve, M. Tedesco, D. K. Hall, and K. Steffen (2012), Greenland ice sheet albedo feedback: thermodynamics and atmospheric drivers, *The Cryosphere*, *6*(4), 821–839, doi:10.5194/tc-6-821-2012.

Box, J. E. (2013), Greenland Ice Sheet mass balance reconstruction. Part II: Surface mass balance (1840–2010), *Journal of Climate*, *26*(18), 6974–6989, doi:10.1175/JCLI-D-12-00518.1.

Bozkurt, D., R. Rondanelli, J. C. Marín, and R. Garreaud (2018), Foehn event triggered by an atmospheric river underlies record-setting temperature along continental Antarctica, *Journal of Geophysical Research: Atmospheres*, *123*(8), 3871–3892, doi:10.1002/2017JD027796.

Braithwaite, R. J., and O. B. Olesen (1990), Response of the energy balance on the margin of the Greenland Ice Sheet to temperature changes, *Journal of Glaciology*, *36*(123), 217–221, doi:10.3189/S0022143000009461.

Brands, S., J. Gutiérrez, and D. San-Martín (2016), Twentieth-century atmospheric river activity along the west coasts of Europe and North America: algorithm formulation, reanalysis uncertainty and links to atmospheric circulation patterns, *Climate Dynamics*, *48*(9–10), 2771–2795, doi:10.1007/s00382-016-3095-6.

Van den Broeke, M., P. Duynkerke, and J. Oerlemans (1994), The observed katabatic flow at the edge of the Greenland ice sheet during GIMEX-91, *Global and Planetary Change*, *9*(1–2), 3–15, doi:10.1016/0921-8181(94)90003-5.

Van den Broeke, M. R., and H. Gallée (1996), Observation and simulation of barrier winds at the western margin of the Greenland ice sheet, *Quarterly Journal of the Royal Meteorological Society*, *122*(534), 1365–1383, doi:10.1002/qj.49712253407 .

Van den Broeke, M., E. M. Enderlin, I. M. Howat, P. Kuipers Munneke, B. P. Y. Noël, W. J. van de Berg, E. van Meijgaard, and B. Wouters (2016), On the recent contribution of the Greenland ice sheet to sea level change, *The Cryosphere*, *10*(5), 1933–1946, doi:10.5194/tc-10-1933-2016.

Van den Broeke, M., J. Box, X. Fettweis, E. Hanna, B. Noël, M. Tedesco, D. van As, W. J. van de Berg, L. van Kampenhout (2017), Greenland Ice Sheet surface mass loss: Recent developments in observation and modeling, *Current Climate Change Reports*, *3*(4), 345–356, doi:10.1007/s40641-017-0084-8.

Brun, E., P. David, M. Sudul, and G. Brunot (1992), A numerical model to simulate snow-cover stratigraphy for operational avalanche forecasting, *Journal of Glaciology*, *38*(128), 13–22, doi:10.3189/S0022143000009552.

Budyko, M. I. (1969), The effect of solar radiation variations on the climate of the earth, *Tellus*, *21*(5), 611–619, doi:10.3402/tellusa.v21i5.10109.

Calov, R., S. Beyer, R. Greve, J. Beckmann, M. Willeit, T. Kleiner, M. Rückamp, A. Humbert, and A. Ganopolski (2018), Simulation of the future sea level contribution of Greenland with a new glacial system model, *The Cryosphere*, *12*(10), 3097–3121, doi:10.5194/tc-12-3097-2018.

Cao, Y., S. Liang, X. Chen, T. He, D. Wang, and X. Cheng (2017), Enhanced wintertime greenhouse effect reinforcing Arctic amplification and initial sea-ice melting, *Scientific Reports*, *7*(1), 8462, doi:10.1038/s41598-017-08545-2.

Cassano, J. J., P. Uotila, A. H. Lynch, and E. N. Cassano (2007), Predicted changes in synoptic forcing of net precipitation in large Arctic river basins during the 21st century, *Journal of Geophysical Research: Biogeosciences*, *112*(G4), G04S49, doi:10.1029/2006JG000332.

Castelao, R. M., H. Luo, H. Oliver, Å. K. Rennermalm, M. Tedesco, A. Bracco, P. L. Yager, T. L. Mote, and P. M. Medeiros (2019), Controls on the transport of meltwater from the southern Greenland ice sheet in the Labrador Sea, *Journal of Geophysical Research: Oceans*, In Press, doi:10.1029/2019JC015159.

Cess, R. D. et al. (1991), Interpretation of snow-climate feedback as produced by 17 general circulation models, *Science*, *253*(5022), 888–892, doi:10.1126/science.253.5022.888.

Charalampidis, C., and D. van As (2015), Observed melt-season snowpack evolution on the Greenland ice sheet, *Geological Survey of Denmark and Greenland Bulletin*, (33), 65–68.

Chen, Y., J. R. Miller, J. A. Francis, and G. L. Russell (2011), Projected regime shift in Arctic cloud and water vapor feedbacks, *Environmental Research Letters*, *6*(4), 044007, doi:10.1088/1748-9326/6/4/044007.

Chen, H. W., R. B. Alley, and F. Zhang (2016), Interannual Arctic sea ice variability and associated winter weather patterns: A regional perspective for 1979–2014, *Journal of Geophysical Research: Atmospheres*, *121*(24), 14,433–14,455, doi:10.1002/2016JD024769.

Chen, X., X. Zhang, J. A. Church, C. S. Watson, M. A. King, D. Monselesan, B. Legresy, and C. Harig (2017), The increasing rate of global mean sea-level rise during 1993–2014, *Nature Climate Change*, *7*(7), 492–495, doi:10.1038/nclimate3325.

Clark, P. U., R. B. Alley, and D. Pollard (1999), Northern Hemisphere ice-sheet influences on global climate change, *Science*, *286*(5442), 1104–1111, doi:10.1126/science.286.5442.1104.

Cohen, J. et al. (2014), Recent Arctic amplification and extreme mid-latitude weather, *Nature Geoscience*, *7*(9), 627–637, doi:10.1038/NGEO2234.

Copernicus Climate Change Service (C3S) (2017), ERA5: Fifth generation of ECMWF atmospheric reanalyses of the global climate. Copernicus Climate Change Service Climate Data Store (CDS), accessed 9 May 2019, URL: https://cds.climate.copernicus.eu/cdsapp#!/home.

Cordeira, J. M., F. M. Ralph, and B. J. Moore (2013), The development and evolution of two atmospheric rivers in proximity to western North Pacific tropical cyclones in October 2010, *Monthly Weather Review*, *141*(12), 4234–4255, doi:10.1175/MWR-D-13-00019.1.

Cox, C. J., V. P. Walden, P. M. Rowe, and M. D. Shupe (2015), Humidity trends imply increased sensitivity to clouds in a warming Arctic, *Nature Communications*, *6*, 10117, doi:10.1038/ncomms10117.

Cullather, R. I., and S. M. J. Nowicki (2018), Greenland Ice Sheet surface melt and its relation to daily atmospheric conditions, *Journal of Climate*, *31*(5), 1897–1919, doi:10.1175/JCLI-D-17-0447.1.

Dacre, H. F., P. A. Clark, O. Martinez-Alvarado, M. A. Stringer, and D. A. Lavers (2015), How do atmospheric rivers form?, *Bulletin of the American Meteorological Society*, *96*(8), 1243–1255, doi:10.1175/BAMS-D-14-00031.1.

Dacre, H. F., O. Martinez-Alvarado, and C. O. Mbengue (2019), Linking atmospheric rivers and warm conveyer belt outflows, *Journal of Hydrometeorology*, *20*(6), 1183–1196, doi: 10.1175/JHM-D-18-0175.1.

Davini, P., C. Cagnazzo, S. Gualdi, and A. Navarra (2012), Bidimensional diagnostics, variability, and trends of Northern Hemisphere blocking, *Journal of Climate*, *25*(19), 6496–6509, doi:10.1175/JCLI-D-12-00032.1.

Davini, P., and F. D'Andrea (2016), Northern Hemisphere atmospheric blocking representation in global climate models: Twenty years of improvements?, *Journal of Climate*, *29*(24), 8823–8840, doi:10.1175/JCLI-D-16-0242.1.

Dee, D. P. et al. (2011), The ERA-Interim reanalysis: configuration and performance of the data assimilation system, *Quarterly Journal of the Royal Meteorological Society*, *137*(656), 553–597, doi:10.1002/qj.828.

Delhasse, A., X. Fettweis, C. Kittel, C. Amory, and C. Agosta (2018), Brief communication: Impact of the recent atmospheric circulation change in summer on the future surface mass balance of the Greenland Ice Sheet, *The Cryosphere*, *12*(11), 3409–3418, doi:10.5194/tc-12-3409-2018.

Ding, Q., J. M. Wallace, D. S. Battisti, E. J. Steig, A. J. E. Gallant, H.-J. Kim, and L. Geng (2014), Tropical forcing of the recent rapid Arctic warming in northeastern Canada and Greenland, *Nature*, *509*(7499), 209–212, doi:10.1038/nature13260.

Dirmeyer, P. A., and K. L. Brubaker (1999), Contrasting evaporative moisture sources during the drought of 1988 and the flood of 1993, *Journal of Geophysical Research: Atmospheres*, *104*(D16), 19,383–19,397, doi:10.1029/1999JD900222.

Doyle, S., A. Hubbard, R. S. W. van de Wal, J. Box, D. van As, K. Scharrer, T. Meierbachtol, P. Smeets, J. Harper, E. Johansson, R. Mottram, A. Mikkelsen, F. Wilhelms, H. Patton, P. Christoffersen, and B. Hubbard (2015), Amplified melt and flow of the Greenland ice sheet driven by late-summer cyclonic rainfall, *Nature Geoscience*, *8*(8), 647–653, doi:10.1038/ngeo2482.

Dumont, M., E. Brun, G. Picard, M. Michou, Q. Libois, J. Petit, M. Geyer, S. Morin, and B. Josse (2014), Contribution of light-absorbing impurities in snow to Greenland's darkening since 2009, *Nature Geoscience*, *7*(7), 509–512, doi:10.1038/NGEO2180.

Enderlin, E. M., I. M. Howat, S. Jeong, M.-J. Noh, J. H. Angelen, and M. R. Van den Broeke (2014), An improved mass budget for the Greenland ice sheet, *Geophysical Research Letters*, *41*(3), 866–872, doi:10.1002/2013GL059010.

Fausto, R. S., D. van As, J. E. Box, W. Colgan, and P. L. Langen (2016a), Quantifying the surface energy fluxes in south Greenland during the 2012 high melt episodes using *in-situ* observations, *Frontiers in Earth Science*, *4*, 82, doi:10.3389/feart.2016.00082.

Fausto, R. S., D. van As, J. E. Box, W. Colgan, P. L. Langen, and R. H. Mottram (2016b), The implication of non-radiative energy fluxes dominating Greenland ice sheet exceptional ablation area surface melt in 2012, *Geophysical Research Letters*, *43*(6), 2649–2658, doi:10.1002/2016GL067720.

Feldl, N., S. Bordoni, and T. M. Merlis (2017), Coupled high-latitude climate feedbacks and their impact on atmospheric heat transport, *Journal of Climate*, *30*(1), 189–201, doi:10.1175/JCLI-D-16-0324.1.

Fettweis, X., M. Tedesco, M. van den Broeke, and J. Ettema (2011), Melting trends over the Greenland ice sheet (1958–2009) from spaceborne microwave data and regional climate models, *The Cryosphere*, *5*(2), 359–375, doi:10.5194/tc-5-359-2011.

Fettweis, X., B. Franco, M. Tedesco, J. H. van Angelen, J. T. M. Lenaerts, M. R. van den Broeke, and H. Gallée (2013a), Estimating the Greenland ice sheet surface mass balance contribution to future sea level rise using the regional atmospheric climate model MAR, *The Cryosphere*, *7*(2), 469–489, doi:10.5194/tc-7-469-2013.

Fettweis, X., E. Hanna, C. Lang, A. Belleflamme, M. Erpicum, and H. Gallée (2013b), Important role of the mid-tropospheric atmospheric circulation in the recent surface melt increase over the Greenland ice sheet, *The Cryosphere*, *7*(1), 241–248, doi:10.5194/tc-7-241-2013.

Fettweis, X., J. E. Box, C. Agosta, C. Amory, C. Kittel, C. Lang, D. van As, H. Machguth, and H. Gallée (2017), Reconstructions of the 1900–2015 Greenland ice sheet surface mass balance using the regional climate MAR model, *The Cryosphere*, *11*(2), 1015–1033, doi:10.5194/tc-11-1015-2017.

Flournoy, M. D., S. B. Feldstein, S. Lee, and E. E. Clothiaux (2016), Exploring the tropically excited Arctic warming mechanism with station data: Links between tropical convection and Arctic downward infrared radiation, *Journal of the Atmospheric Sciences*, *73*(3), 1143–1158, doi:10.1175/JAS-D-14-0271.1.

Francis, J. A., and E. Hunter (2007), Changes in the fabric of the Arctic's greenhouse blanket, *Environmental Research Letters*, *2*(4), 045011, doi:10.1088/1748-9326/2/4/045011.

Francis, J. A., and S. J. Vavrus (2012), Evidence linking Arctic amplification to extreme weather in mid-latitudes, *Geophysical Research Letters*, *39*(6), L06801, doi:10.1029/2012GL051000.

Franco, B., X. Fettweis, and M. Erpicum (2013), Future projections of the Greenland ice sheet energy balance driving the surface melt, *The Cryosphere*, *7*(1), 1–18, doi:10.5194/tc-7-1-2013.

Frierson, D. M., I. M. Held, and P. Zurita-Gotor (2007), A gray-radiation aquaplanet moist GCM. Part II: Energy transports in altered climates, *Journal of the Atmospheric Sciences*, *64*(5), 1680–1693, doi:10.1175/JAS3913.1.

Froidevaux, P., and O. Martius (2016), Exceptional integrated vapour transport toward orography: an important precursor to severe floods in Switzerland, *Quarterly Journal of the Royal Meteorological Society*, *142*(698), 1997–2012, doi:10.1002/qj2793.

Gallagher, M. R., M. D. Shupe, and N. B. Miller (2018), Impact of atmospheric circulation on temperature, clouds, and radiation at Summit Station, Greenland, with self-organizing maps, *Journal of Climate*, *31*(21), 8895–8915, doi:10.1175/JCLI-D-17-0893.1.

Gallée, H., and G. Schayes (1994), Development of a three-dimensional meso-γ primitive equation model: katabatic winds simulation in the area of Terra Nova Bay, Antarctica, *Monthly Weather Review*, *122*(4), 671–685, doi:10.1175/15200493(1994)122<0671:DOATDM>2.0.CO;2.

Gao, Y., J. Lu, and R. L. Leung (2016), Uncertainties in projecting future changes in atmospheric rivers and their impacts on heavy precipitation over Europe, *Journal of Climate*, *29*(18), 6711–6726, doi:10.1175/JCLI-D-16-0088.1.

Gautier, A. (2018), Arctic summer 2018: September extent ties for sixth lowest, National Snow and Ice Data Center (NSIDC), accessed 15 July 2019 at https://nsidc.org/arcticseaicenews/2018/10/september-extent-ties-for-sixth-lowest/.

Gelaro, R. et al. (2017), The Modern-Era Retrospective Analysis for Research and Applications, version 2 (MERRA-2), *Journal of Climate*, *30*(14), 5419–5454, doi:10.1175/JCLI-D-16-0758.1.

Gimeno, L., M. Vázquez, R. Nieto, and R. Trigo (2015), Atmospheric moisture transport: the bridge between ocean evaporation and Arctic ice melting, *Earth System Dynamics*, *6*(2), 583–589, doi:doi:10.5194/esd-6-583-2015.

Gimeno, L., M. Vázquez, J. Eiras-Barca, R. Sorí, I. Algarra, and R. Nieto (2019), Atmospheric moisture transport and the decline in Arctic Sea ice, *Wiley Interdisciplinary Reviews: Climate Change*, *10*(4), e588, doi:10.1002/wcc.588.

GISTEMP Team (2019), GISS Surface Temperature Analysis (GISTEMP), NASA Goddard Institute for Space Studies. Dataset accessed 15 July 2019 at data.giss.nasa.gov/gistemp/.

Gong, T., S. Feldstein, and S. Lee (2017), The role of downward infrared radiation in the recent Arctic winter warming trend, *Journal of Climate*, *30*(13), 4937–4949, doi:10.1175/JCLI-D-16-0180.1.

Gorodetskaya, I. V., M. Tsukernik, K. Claes, M. F. Ralph, W. D. Neff, and N. P. Van Lipzig (2014), The role of atmospheric rivers in anomalous snow accumulation in East Antarctica, *Geophysical Research Letters*, *41*(17), 6199–6206, doi:10.1002/2014GL060881.

Grams, C. M., and H. M. Archambault (2016), The key role of diabatic outflow in amplifying the midlatitude flow: A representative case study of weather systems surrounding Western North Pacific extratropical transition, *Monthly Weather Review*, *144*(10), 3847–3869, doi:10.1175/MWR-D-15-0419.1.

Graversen, R. G., T. Mauritsen, M. Tjernström, E. Källén, and G. Svensson (2008), Vertical structure of recent Arctic warming, *Nature*, *451*(7174), 53–56, doi:doi:10.1038/nature06502.

Graversen, R. G., and M. Wang (2009), Polar amplification in a coupled climate model with locked albedo, *Climate Dynamics*, *33*(5), 629–643, doi:10.1007/s00382-009-0535-6.

Graversen, R. G., and M. Burtu (2016), Arctic amplification enhanced by latent energy transport of atmospheric planetary waves, *Quarterly Journal of the Royal Meteorological Society*, *142*(698), 2046–2054, doi:10.1002/qj.2802.

Guan, B., and D. E. Waliser (2015), Detection of atmospheric rivers: Evaluation and application of an algorithm for global studies, *Journal of Geophysical Research: Atmospheres*, *120*(24), 12,514–12,535, doi:10.1002/2015JD024257.

Hahn, L., C. C. Ummenhofer, and Y.-O. Kwon (2018), North Atlantic natural variability modulates emergence of widespread Greenland melt in a warming climate, *Geophysical Research Letters*, *45*(17), 9171–9178, doi:10.1029/2018GL079682.

Hall, D. K., J. C. Comiso, N. E. DiGirolamo, C. A. Shuman, J. E. Box, and L. S. Koenig (2013), Variability in the surface temperature and melt extent of the Greenland ice sheet from MODIS, *Geophysical Research Letters*, *40*(10), 2114–2120, doi:10.1002/grl.50240.

Hanna, E., F. J. Navarro, F. Pattyn, C. M. Domingues, X. Fettweis, E. R. Ivins, R. J. Nicholls, C. Ritz, B. Smith, S. Tulaczyk, P. L. Whitehouse, and H. J. Zwally (2013a), Ice-sheet mass balance and climate change, *Nature*, *498*, 51–59, doi:10.1038/nature12238.

Hanna, E., J. M. Jones, J. Cappelen, S. H. Mernild, L. Wood, K. Steffen, and P. Huybrechts (2013b), The influence of North Atlantic atmospheric and oceanic forcing effects on 1900–2010 Greenland summer climate and ice melt/runoff, *International Journal of Climatology*, *33*(4), 862–880, doi:10.1002/joc.3475.

Hanna, E., X. Fettweis, S. H. Mernild, J. Cappelen, M. H. Ribergaard, C. A. Shuman, K. Steffen, L. Wood, and T. L. Mote (2014), Atmospheric and oceanic climate forcing of the exceptional Greenland ice sheet surface melt in summer 2012, *International Journal of Climatology*, *34*(4), 1022–1037, doi:10.1002/joc.3743.

Hanna, E., T. E. Cropper, R. J. Hall, and J. Cappelen (2016), Greenland Blocking Index 1851–2015: a regional climate change signal, *International Journal of Climatology*, *36*(15), 4847–4861, doi:10.1002/joc.4673.

Hanna, E., R. J. Hall, T. E. Cropper, T. J. Ballinger, L. Wake, T. L. Mote, and J. Cappelen (2018a), Greenland blocking index daily series 1851–2015: Analysis of changes in extremes and links with North Atlantic and UK climate variability and change, *International Journal of Climatology*, *38*(9), 3546–3564, doi:10.1002/joc.5516.

Hanna, E., X. Fettweis, and R. J. Hall (2018b), Brief communication: Recent changes in summer Greenland blocking captured by none of the CMIP5 models, *The Cryosphere*, *12*(10), 3287–3292, doi:10.5194/tc-12-3287-2018.

Hansen, A. M., and R. L. Johnstone (2019), In the Shadow of the Mountain: Assessing early impacts on community development from two mining prospects in South Greenland, *The Extractive Industries and Society*, *6*(2), 480–488, doi:10.1016/j.exis.2019.01.012.

Harman, J. R., and J. A. Winkler (1991), Synoptic climatology: themes, applications, and prospects, *Physical Geography*, *12*(3), 220–230, doi:10.1080/02723646.1991.10642429.

Hegyi, B. M., and P. C. Taylor (2018), The unprecedented 2016–17 Arctic sea ice growth season: The crucial role of atmospheric rivers and longwave fluxes, *Geophysical Research Letters*, *45*(10), 5204–5212, doi:10.1029/2017GL076717.

Heinemann, G., and U. Falk (2002), Surface winds and energy fluxes near the Greenland ice margin under conditions of katabatic winds, *Polarforschung*, *71*(1/2), 15–31.

Held, I. M., and B. J. Soden (2006), Robust responses of the hydrological cycle to global warming, *Journal of Climate*, *19*(21), 5686–5699, doi:10.1175/JCLI3990.1.

Hermann, M., J. E. Box, R. S. Fausto, W. T. Colgan, P. L. Langen, R. Mottram, J. Wuite, B. Noël, M. R. van den Broeke, and D. van As (2018), Application of PROMICE Q-Transect in situ accumulation and ablation measurements (2000–2017) to constrain mass balance at the southern tip of the Greenland ice sheet, *Journal of Geophysical Research: Earth Surface*, *123*(6), 1235–1256, doi:10.1029/2017JF004408.

Hewitson, B., and R. Crane (2002), Self-organizing maps: applications to synoptic climatology, *Climate Research*, *22*(1), 13–26, doi:10.3354/cr022013.

Hofer, S., A. J. Tedstone, X. Fettweis, and J. L. Bamber (2017), Decreasing cloud cover drives the recent mass loss on the Greenland Ice Sheet, *Science Advances*, *3*(6), e1700584, doi:10.1126/sciadv.1700584.

Hu, A., G. A. Meehl, W. Han, and J. Yin (2011), Effect of the potential melting of the Greenland Ice Sheet on the Meridional Overturning Circulation and global climate in the future, *Deep Sea Research Part II: Topical Studies in Oceanography*, *58*(17–18), 1914–1926, doi: 10.1016/j.dsr2.2010.10.069.

Huang, Y., X. Dong, B. Xi, E. K. Dolinar, R. E. Stanfield, and S. Qiu (2017), Quantifying the uncertainties of reanalyzed Arctic cloud and radiation properties using satellite surface observations, *Journal of Climate*, *30*(19), 8007–8029, doi:10.1175/JCLI-D-16-0722.1.

Hwang, Y.-T., and D. M. Frierson (2010), Increasing atmospheric poleward energy transport with global warming, *Geophysical Research Letters*, *37*(24), L24807, doi:10.1029/2010GL045440.

Jakobson, E., T. Vihma, T. Palo, L. Jakobson, H. Keernik, and J. Jaagus (2012), Validation of atmospheric reanalyses over the central Arctic Ocean, *Geophysical Research Letters*, *39*(10), L10802, doi:10.1029/2012GL051591.

Jiang, Z., S. B. Feldstein, and S. Lee (2017), The relationship between the Madden-Julian Oscillation and the North Atlantic Oscillation, *Quarterly Journal of the Royal Meteorological Society*, *143*(702), 240–250, doi:10.1002/qj.2917.

Johansson, E., A. Devasthale, M. Tjernström, A. M. L. Ekman, and T. L'Ecuyer (2017), Response of the lower troposphere to moisture intrusions into the Arctic, *Geophysical Research Letters*, *44*(5), 2527–2536, doi:10.1002/2017GL072687.

Kattsov, V. M., J. E. Walsh, W. L. Chapman, V. A. Govorkova, T. V. Pavlova, and X. Zhang (2007), Simulation and projection of Arctic freshwater budget components by the IPCC AR4 global climate models, *Journal of Hydrometeorology*, *8*(3), 571–589, doi:10.1175/JHM575.1.

Khan, S. A., A. Aschwanden, A. A. Bjørk, J. Wahr, K. K. Kjeldsen, and K. H. Kjær (2015), Greenland ice sheet mass balance: a review, *Reports on Progress in Physics*, *78*(4), 046801, doi:10.1088/00344885/78/4/046801.

Kim, B.-M., J.-Y. Hong, S.-Y. Jun, X. Zhang, H. Kwon, S.-J. Kim, J.-H. Kim, S.-W. Kim, and H.-K. Kim (2017), Major cause of unprecedented Arctic warming in January 2016: Critical role of an Atlantic windstorm, *Scientific Reports*, *7*, 40051, doi:10.1038/srep40051.

Knippertz, P., H. Wernli, and G. Gläser (2013), A global climatology of tropical moisture exports, *Journal of Climate*, *26*(10), 3031–3045, doi:10.1175/JCLI-D-12-00401.1.

Knutti, R., S. Krähenmann, D. J. Frame, and M. R. Allen (2008), Comment on "Heat capacity, time constant, and sensitivity of Earth's climate system" by SE Schwartz, *Journal of Geophysical Research: Atmospheres*, *113*(D15), D15103, doi:10.1029/2007JD009473.

Koeller, P., C. Fuentes-Yaco, T. Platt, S. Sathyendranath, A. Richards, P. Ouellet, D. Orr, U. Skúladóttir, K. Wieland, L. Savard, and M. Aschan (2009), Basin-scale coherence in phenology of shrimps and phytoplankton in the North Atlantic Ocean, *Science*, *324*(5928), 791–793, doi:10.1126/science.1170987.

Koenig, L. S., C. Miège, R. R. Forster, and L. Brucker (2014), Initial in situ measurements of perennial meltwater storage in the Greenland firn aquifer, *Geophysical Research Letters*, *41*(1), 81–85, doi:10.1002/2013GL058083.

Koenig, S. J., R. M. DeConto, and D. Pollard (2014), Impact of reduced Arctic sea ice on Greenland ice sheet variability in a warmer than present climate, *Geophysical Research Letters*, *41*(11), 3933–3942, doi:10.1002/2014GL059770.

Krklec, K., and D. Domínguez-Villar (2014), Quantification of the impact of moisture source regions on the oxygen isotope composition of precipitation over Eagle Cave, central Spain, *Geochimica et Cosmochimica Acta*, *134*, 39–54, doi:10.1016/j.gca.2014.03.011.

Laliberté, F., and P. J. Kushner (2014), Midlatitude moisture contribution to recent Arctic tropospheric summertime variability, *Journal of Climate*, *27*(15), 5693–5707, doi:10.1175/JCLI-D-13-00721.1.

Langen, P. L., R. S. Fausto, B. Vandecrux, R. H. Mottram, and J. E. Box (2016), Liquid water flow and retention on the Greenland Ice Sheet in the regional climate model HIRHAM5: local and large-scale impacts, *Frontiers in Earth Science*, *4*, 110, doi:10.3389/feart.2016.00110.

Lavers, D. A., F. M. Ralph, D. E. Waliser, A. Gershunov, and M. D. Dettinger (2015), Climate change intensification of horizontal water vapor transport in CMIP5, *Geophysical Research Letters*, *42*(13), 5617–5625, doi:10.1002/2015GL064672.

Le clec'h, S., S. Charbit, A. Quiquet, X. Fettweis, C. Dumas, M. Kageyama, C. Wyard, and C. Ritz (2019), Assessment of the Greenland ice sheet–atmosphere feedbacks for the next century with a regional atmospheric model coupled to an ice sheet model, *The Cryosphere*, *13*(1), 373–395, 1–31, doi:10.5194/tc-13-373-2019.

Lee, S., T. Gong, N. Johnson, S. B. Feldstein, and D. Pollard (2011), On the possible link between tropical convection and the Northern Hemisphere Arctic surface air temperature change between 1958 and 2001, *Journal of Climate*, *24*(16), 4350–4367, doi:10.1175/2011JCLI4003.1.

Lee, H. J., M. O. Kwon, S.-W. Yeh, Y.-O. Kwon, W. Park, J.-H. Park, Y. H. Kim, and M. A. Alexander (2017), Impact of poleward moisture transport from the North Pacific on the acceleration of sea ice loss in the Arctic since 2002, *Journal of Climate*, *30*(17), 6757–6769, doi:10.1175/JCLI-D-16-0461.1.

Lee, S., T. Gong, S. B. Feldstein, J. Screen, and I. Simmonds (2017), Revisiting the cause of the 1989–2009 Arctic surface warming using the surface energy budget: downward infrared radiation dominates the surface fluxes, *Geophysical Research Letters*, *44*(20), 10,654–10,661, doi:10.1002/2017GL075375.

Lefebre, F., X. Fettweis, H. Gallée, J.-P. Van Ypersele, P. Marbaix, W. Greuell, and P. Calanca (2005), Evaluation of a high-resolution regional climate simulation over Greenland, *Climate Dynamics*, *25*(1), 99–116, doi:10.1007/s00382-005-0005-8.

Lenssen, N. J. L., G. A. Schmidt, J. E. Hansen, M. J. Menne, A. Persin, R. Ruedy, and D. Zyss (2019), Improvements in the GISTEMP uncertainty model, *Journal of Geophysical Research: Atmospheres*, In Press, doi:10.1029/2018JD029522.

Lim, Y.-K., S. D. Schubert, S. M. Nowicki, J. N. Lee, A. M. Molod, R. I. Cullather, B. Zhao, and I. Velicogna (2016), Atmospheric summer teleconnections and Greenland Ice Sheet surface mass variations: insights from MERRA-2, *Environmental Research Letters*, *11*(2), 024002, doi:10.1088/1748-9326/11/2/024002.

Lindsay, R., M. Wensnahan, A. Schweiger, and J. Zhang (2014), Evaluation of seven different atmospheric reanalysis products in the Arctic, *Journal of Climate*, *27*(7), 2588–2606, doi:10.1175/JCLI-D-13-00014.1.

Lindsey, R. (2017), Greenland Ice Sheet's 2017 weigh-in suggests a small increase in ice mass, accessed 10 Dec 2017 at https://www.climate.gov/news-features/understanding-climate/greenland-ice-sheets-2017-weigh-suggests-small-increase-ice-mass.

Liu, C., and E. A. Barnes (2015), Extreme moisture transport into the Arctic linked to Rossby wave breaking, *Journal of Geophysical Research: Atmospheres*, *120*(9), 3774–3788, doi:10.1002/2014JD022796.

Liu, Y., J. R. Key, Z. Liu, X. Wang, and S. J. Vavrus (2012), A cloudier Arctic expected with diminishing sea ice, *Geophysical Research Letters*, *39*(5), L05705, doi:10.1029/2012GL051251.

Liu, Y., and J. R. Key (2016), Assessment of Arctic cloud cover anomalies in atmospheric reanalysis products using satellite data, *Journal of Climate*, *29*(17), 6065–6083, doi:10.1175/JCLI-D-15-0861.1.

Luo, H., R. M. Castelao, Å. K. Rennermalm, M. Tedesco, A. Bracco, P. L. Yager, and T. L. Mote (2016), Oceanic transport of surface meltwater from the southern Greenland ice sheet, *Nature Geoscience*, *9*, 528–532, doi:10.1038/NGEO2708.

Luthcke, S. B., T. Sabaka, B. Loomis, A. Arendt, J. McCarthy, and J. Camp (2013), Antarctica, Greenland and Gulf of Alaska land-ice evolution from an iterated GRACE global mascon solution, *Journal of Glaciology*, *59*(216), 613–631, doi:10.3189/2013JoG12J147.

MacGregor, J. A., M. A. Fahnestock, G. A. Catania, A. Aschwanden, G. D. Clow, W. T. Colgan, S. Prasad Gogineni, M. Morlighim, S. M. J. Nowicki, J. D. Paden, S. F. Price, and H. Seroussi (2016), A synthesis of the basal thermal state of the Greenland Ice Sheet, *Journal of Geophysical Research: Earth Surface*, *121*(7), 1328–1350, doi:10.1002/2015JF003803.

MacKenzie, B. R., M. R. Payne, J. Boje, J. L. Høyer, and H. Siegstad (2014), A cascade of warming impacts brings bluefin tuna to Greenland waters, *Global Change Biology*, *20*(8), 2484–2491, doi:10.1111/gcb.12597.

Manabe, S., and R. T. Wetherald (1975), The effects of doubling the CO2 concentration on the climate of a general circulation model, *Journal of the Atmospheric Sciences*, *32*(1), 3–15, doi:10.1175/1520-0469(1975)032<0003:TEODTC>2.0.CO;2.

Martens, B., D. Gonzalez Miralles, H. Lievens, R. Van Der Schalie, R. A. De Jeu, D. Fernández-Prieto, H. E. Beck, W. Dorigo, and N. Verhoest (2017), GLEAM v3: Satellite-based land evaporation and root-zone soil moisture, *Geoscientific Model Development*, *10*(5), 1903–1925, doi:10.5194/gmd-10-1903-2017.

Mattingly, K. S., C. A. Ramseyer, J. J. Rosen, T. L. Mote, and R. Muthyala (2016), Increasing water vapor transport to the Greenland Ice Sheet revealed using self-organizing maps, *Geophysical Research Letters*, *43*(17), 9250–9258, doi:10.1002/2016GL070424.

Mattingly, K. S., T. L. Mote, and X. Fettweis (2018), Atmospheric river impacts on Greenland Ice Sheet surface mass balance, *Journal of Geophysical Research: Atmospheres*, *123*(16), 8538–8560, doi:10.1029/2018JD028714.

Mattingly, K. S., T. L. Mote, and X. Fettweis (2019), Strong summer atmospheric rivers trigger Greenland Ice Sheet melt through spatially varying surface energy balance and cloud regimes. *Journal of Climate*, in prep.

McLeod, J. T., and T. L. Mote (2015), Assessing the role of precursor cyclones on the formation of extreme Greenland blocking episodes and their impact on summer melting across the Greenland ice sheet, *Journal of Geophysical Research: Atmospheres*, *120*(24), 12,357–12,377, doi:10.1002/ 2015JD023945.

McLeod, J. T., and T. L. Mote (2016), Linking interannual variability in extreme Greenland blocking episodes to the recent increase in summer melting across the Greenland ice sheet, *International Journal of Climatology*, *36*(3), 1484–1499, doi:10.1002/joc.4440.

McMillan, M., A. Leeson, A. Shepherd, K. Briggs, T. W. K. Armitage, A. Hogg, P. Kuipers Munneke, M. van den Broeke, B. Noël, W. J. van de Berg, S. Ligtenberg, M. Horwath, A. Groh, A. Muir, and L. Gilbert (2016), A high resolution record of Greenland mass balance, *Geophysical Research Letters*, *43*(13), 7002–7010, doi:10.1002/2016GL069666.

Meesters, A. (1994), Dependence of the energy balance of the Greenland ice sheet on climate change: Influence of katabatic wind and tundra, *Quarterly Journal of the Royal Meteorological Society*, *120*(517), 491–517, doi:10.1002/qj.49712051702.

Messori, G., C. Woods, and R. Caballero (2018), On the drivers of wintertime temperature extremes in the high Arctic, *Journal of Climate*, *31*(4), 1597–1618, doi:10.1175/JCLI-D-17-0386.1.

Meyssignac, B., X. Fettweis, R. Chevrier, and G. Spada (2017), Regional sea level changes for the 20th and the 21st century induced by the regional variability in Greenland ice sheet surface mass loss, *Journal of Climate*, 3*0*(6), 2011–2028, doi:10.1175/JCLI-D-16-0337.1.

Miège, C., R. R. Forster, L. Brucker, L. S. Koenig, D. Kip Solomon, J. D. Paden, J. E. Box, E. W. Burgess, J. Z. Miller, L. McNerney, N. Brautigam, R. S. Fausto, and S. Gogineni (2016), Spatial extent and temporal variability of Greenland firn aquifers detected by ground and airborne radars, *Journal of Geophysical Research: Earth Surface*, *121*(12), 2381–2398, doi:10.1002/2016JF003869.

Miller, N. B., M. D. Shupe, C. J. Cox, V. P. Walden, D. D. Turner, and K. Steffen (2015), Cloud radiative forcing at Summit, Greenland, *Journal of Climate*, *28*(15), 6267–6280, doi:10.1175/JCLI-D-15-0076.1.

Miller, N. B., M. D. Shupe, C. J. Cox, D. Noone, P. O. G. Persson, and K. Steffen (2017), Surface energy budget responses to radiative forcing at Summit, Greenland, *The Cryosphere*, *11*(1), 497–516, doi:10.5194/tc-11-497-2017.

Miller, P. W., and T. L. Mote (2018), Characterizing severe weather potential in synoptically weakly forced thunderstorm environments, *Natural Hazards and Earth System Sciences*, *18*(4), 1261–1277, doi:10.5194/nhess-18-1261-2018.

Mioduszewski, J. R., Å. K. Rennermalm, A. Hammann, M. Tedesco, E. U. Noble, J. C. Stroeve, T. L. Mote (2016) Atmospheric drivers of Greenland surface melt revealed by Self Organizing Maps. *Journal of Geophysical Research: Atmospheres*, *21*(10), 5095–5114, doi:10.1002/2015JD024550.

Molina, M. J., and J. T. Allen (2019), On the moisture origins of tornadic thunderstorms, *Journal of Climate*, *32*(14), 4321–4346, doi:10.1175/JCLI-D-18-0784.1.

Moore, G. W. K., I. A. Renfrew, and J. J. Cassano (2013), Greenland plateau jets, *Tellus A: Dynamic Meteorology and Oceanography*, *65*(1), 17468, doi:10.3402/tellusa.v65i0.17468.

Mortin, J., G. Svensson, R. G. Graversen, M.-L. Kapsch, J. C. Stroeve, and L. N. Boisvert (2016), Melt onset over Arctic sea ice controlled by atmospheric moisture transport, *Geophysical Research Letters*, *43*(12), 6636–6642, doi:10.1002/2016GL069330.

Mote, T. L. (1998), Mid-tropospheric circulation and surface melt on the Greenland ice sheet. Part II: synoptic climatology, *International Journal of Climatology*, *18*(2), 131–145, doi:10.1002/(SICI)1097-0088(199802)18:2<131::AID-JOC228>3.0.CO;2-S.

Mote, T. L. (2014) *MEaSUREs Greenland Surface Melt Daily 25km EASE-Grid 2.0, Version 1*. Boulder, Colorado USA. NASA National Snow and Ice Data Center Distributed Active Archive Center, accessed 19 June 2016 at http://dx.doi.org/10.5067/MEASURES/CRYOSPHERE/nsidc-0533.001.

Mouginot, J., E. Rignot, A. A. Bjørk, M. van den Broeke, R. Millan, M. Morlighem, B. Noël, B. Scheuchl, and M. Wood (2019), Forty-six years of Greenland Ice Sheet mass balance from 1972 to 2018, *Proceedings of the National Academy of Sciences*, *116*(19), 9239–9244, doi:10.1073/pnas.1904242116.

Mundhenk, B. D., E. A. Barnes, and E. D. Maloney (2016), All-Season climatology and variability of atmospheric river frequencies over the North Pacific, *Journal of Climate*, *29*(13), 4885–4903, doi:10.1175/JCLI-D-15-0655.1.

Murphy, D., S. Solomon, R. Portmann, K. Rosenlof, P. Forster, and T. Wong (2009), An observationally based energy balance for the Earth since 1950, *Journal of Geophysical Research: Atmospheres*, *114*(D17), D17107, doi:10.1029/2009JD012105.

National Snow and Ice Data Center (NSIDC) (2015), 2015 melt season in review, accessed 10 Dec 2017 at http://nsidc.org/greenland-today/2015/11/.

National Snow and Ice Data Center (NSIDC) (2016), 2016 melt season in review, accessed 10 Dec 2017 at http://nsidc.org/greenland-today/2016/10/.

National Snow and Ice Data Center (NSIDC) (2019), SOTC: Sea Ice, accessed 15 July 2019 at https://nsidc.org/cryosphere/sotc/sea_ice.html/.

Nayak, M. A., G. Villarini, and A. A. Bradley (2016), Atmospheric rivers and rainfall during NASA's Iowa Flood Studies (IFloodS) campaign, *Journal of Hydrometeorology*, *17*(1), 257–271, doi:10.1175/JHM-D-14-0185.1.

Neff, W., G. P. Compo, F. Martin Ralph, and M. D. Shupe (2014), Continental heat anomalies and the extreme melting of the Greenland ice surface in 2012 and 1889, *Journal of Geophysical Research: Atmospheres*, *119*(11), 6520–6536, doi:10.1002/2014JD021470.

Neiman, P. J., F. M. Ralph, G. A. Wick, J. D. Lundquist, and M. D. Dettinger (2008), Meteorological characteristics and overland precipitation impacts of atmospheric rivers affecting the West Coast of North America based on eight years of SSM/I satellite observations, *Journal of Hydrometeorology*, *9*(1), 22–47, doi:10.1175/2007JHM855.1.

Newman, M., G. N. Kiladis, K. M. Weickmann, F. M. Ralph, and P. D. Sardeshmukh (2012), Relative contributions of synoptic and low-frequency eddies to time-mean atmospheric moisture transport, including the role of atmospheric rivers, *Journal of Climate*, *25*(21), 7341–7361, doi:10.1175/JCLI-D-11-00665.1.

Nghiem, S., D. Hall, T. Mote, M. Tedesco, M. Albert, K. Keegan, C. Shuman, N. DiGirolamo, and G. Neumann (2012), The extreme melt across the Greenland ice sheet in 2012, *Geophysical Research Letters*, *39*(20), L20502, doi:10.1029/2012GL053611.

Nicolas, J. P. et al. (2017), January 2016 extensive summer melt in West Antarctica favoured by strong El Niño, *Nature Communications*, *8*, 15799, doi:10.1038/ncomms15799.

Nilsson, J., P. Vallelonga, S. B. Simonsen, L. Sandberg Sørensen, R. Forsberg, D. Dahl-Jensen, M. Hirabayashi, K. Goto-Azuma, C. S. Hvidberg, H. A. Kjær, and K. Satow (2015), Greenland 2012 melt event effects on CryoSat-2 radar altimetry, *Geophysical Research Letters*, *42*(10), 3919–3926, doi:10.1002/2015GL063296.

Noël, B., X. Fettweis, W. Van de Berg, M. Van den Broeke, and M. Erpicum (2014), Sensitivity of Greenland Ice Sheet surface mass balance to perturbations in sea surface temperature and sea ice cover: a study with the regional climate model MAR, *The Cryosphere*, *8*(5), 1871–1883, doi:10.5194/tc-8-1871-2014.

Noël, B., W. van de Berg, S. Lhermitte, B. Wouters, H. Machguth, I. Howat, M. Citterio, G. Moholdt, J. Lenaerts, and M. van den Broeke (2017), A tipping point in refreezing accelerates mass loss of Greenland's glaciers and ice caps, *Nature Communications*, *8*(14730), 1, doi:10.1038/ncomms14730.

O'Reilly, C. H., S. Minobe, and A. Kuwano-Yoshida (2016), The influence of the Gulf Stream on wintertime European blocking, *Climate Dynamics*, *47*(5), 1545–1567, doi:10.1007/s00382-015-2919-0.

Oliver, H., H. Luo, R. M. Castelao, G. L. van Dijken, K. S. Mattingly, J. J. Rosen, T. L. Mote, K. R. Arrigo, Å. K. Rennermalm, M. Tedesco, and P. L. Yager (2018), Exploring the potential impact of Greenland meltwater on stratification, photosynthetically active radiation, and primary production in the Labrador Sea, *Journal of Geophysical Research: Oceans*, *123*(4), 2570–2591, doi:10.1002/2018JC013802.

Oltmanns, M., F. Straneo, and M. Tedesco (2019), Increased Greenland melt triggered by large-scale, year-round cyclonic moisture intrusions, *The Cryosphere*, *13*(3), 815–825, doi:10.5194/tc-13-815-2019.

Oort, A. H. (1971), The observed annual cycle in the meridional transport of atmospheric energy, *Journal of the Atmospheric Sciences*, *28*(3), 325–339, doi:10.1175/1520-0469(1971)028<0325:TOACIT>2.0.CO;2.

Oort, A. H., and J. P. Peixóto (1983), Global angular momentum and energy balance requirements from observations, in *Advances in Geophysics*, vol. 25, pp. 355–490, Elsevier.

Overland, J. E., P. Turet, and A. H. Oort (1996), Regional variations of moist static energy flux into the Arctic, *Journal of Climate*, *9*(1), 54–65, doi:10.1175/1520-0442(1996)009<0054:RVOMSE>2.0.CO;2.

Overland, J. E., M. Wang, J. E. Walsh, and J. C. Stroeve (2014), Future Arctic climate changes: Adaptation and mitigation time scales, *Earth's Future*, *2*(2), 68–74, doi:10.1002/2013EF000162.

Overland, J., J. A. Francis, R. Hall, E. Hanna, S.-J. Kim, and T. Vihma (2015), The melting Arctic and midlatitude weather patterns: are they connected?, *Journal of Climate*, *28*(20), 7917–7932, doi:10.1175/JCLI-D-14-00822.1.

Parish, T. R., and D. H. Bromwich (1989), Instrumented Aircraft Observations of the Katabatic Wind Regime Near Terra Nova Bay, *Monthly Weather Review*, *117*(7), 1570–1585, doi:10.1175/1520-0493(1989)117<1570:IAOOTK>2.0.CO;2.

Park, D.-S. R., S. Lee, and S. B. Feldstein (2015), Attribution of the recent winter sea ice decline over the Atlantic sector of the Arctic Ocean, *Journal of Climate*, *28*(10), 4027–4033, doi:10.1175/JCLI-D-15-0042.1.

Park, H.-S., S. Lee, S.-W. Son, S. B. Feldstein, and Y. Kosaka (2015a), The impact of poleward moisture and sensible heat flux on Arctic winter sea ice variability, *Journal of Climate*, *28*(13), 5030–5040, doi:10.1175/JCLI-D-15-0074.1.

Park, H.-S., S. Lee, Y. Kosaka, S.-W. Son, and S.-W. Kim (2015b), The impact of Arctic winter infrared radiation on early summer sea ice, *Journal of Climate*, *28*(15), 6281–6296, doi:10.1175/JCLI-D-14-00773.1.

Payne, A. E., and G. Magnusdottir (2015), An evaluation of atmospheric rivers over the North Pacific in CMIP5 and their response to warming under RCP 8.5, *Journal of Geophysical Research: Atmospheres*, *120*(11), 11,173–11,190, doi:10.1002/2015JD023586.

De la Peña, S., I. Howat, P. Nienow, M. van den Broeke, E. Mosley-Thompson, S. Price, D. Mair, B. Noël, and A. Sole (2015), Changes in the firn structure of the western Greenland Ice Sheet caused by recent warming, *The Cryosphere*, *9*(3), 1203–1211, doi:10.5194/tc-9-1203-2015.

Petersen, G. N., J. E. Kristjánsson, and H. Ólafsson (2004), Numerical simulations of Greenland's impact on the Northern Hemisphere winter circulation, *Tellus A*, 56(2), 102–111, doi:10.1111/j.1600-0870.2004.00047.x.

Pettersen, C., R. Bennartz, M. S. Kulie, A. J. Merrelli, M. D. Shupe, and D. D. Turner (2016), Microwave signatures of ice hydrometeors from ground-based observations above Summit, Greenland, *Atmospheric Chemistry and Physics*, *16*(7), 4743–4756, doi:10.5194/acp-16-4743-2016.

Pettersen, C., R. Bennartz, A. J. Merrelli, M. D. Shupe, D. D. Turner, and V. P. Walden (2018), Precipitation regimes over central Greenland inferred from 5 years of ICECAPS observations., *Atmospheric Chemistry & Physics*, *18*(7), 4715–4735, doi:10.5194/acp-18-4715-2018.

Pfahl, S., and H. Wernli (2008), Air parcel trajectory analysis of stable isotopes in water vapor in the eastern Mediterranean, *Journal of Geophysical Research: Atmospheres*, *113*(D20), D20104, doi:10.1029/2008JD009839.

Pfahl, S., E. Madonna, M. Boettcher, H. Joos, and H. Wernli (2014), Warm conveyor belts in the ERA-Interim dataset (1979–2010). Part II: Moisture origin and relevance for precipitation, *Journal of Climate*, *27*(1), 27–40, doi:10.1175/JCLI-D-13-00223.1.

Pfahl, S., and N. Niedermann (2011), Daily covariations in near-surface relative humidity and temperature over the ocean, *Journal of Geophysical Research: Atmospheres*, *116*(D19), D19104, doi:10.1029/2011JD015792.

Pfahl, S., C. Schwierz, M. Croci-Maspoli, C. Grams, and H. Wernli (2015), Importance of latent heat release in ascending air streams for atmospheric blocking, *Nature Geoscience*, *8*(8), 610–614, doi:10.1038/ngeo2487.

Piaget, N., P. Froidevaux, P. Giannakaki, F. Gierth, O. Martius, M. Riemer, G. Wolf, and C. M. Grams (2015), Dynamics of a local Alpine flooding event in October 2011: moisture source and large-scale circulation, *Quarterly Journal of the Royal Meteorological Society*, *141*(690), 1922–1937, doi:10.1002/qj.2496.

Pierrehumbert, R. T. (2002), The hydrologic cycle in deep-time climate problems, *Nature*, *419*(6903), 191–198, doi:10.1038/nature01088.

Pithan, F., and T. Mauritsen (2014), Arctic amplification dominated by temperature feedbacks in contemporary climate models, *Nature Geoscience*, *7*(3), 181–184, doi:10.1038/NGEO2071.

Pithan, F., T. G. Shepherd, G. Zappa, and I. Sandu (2016), Missing orographic drag leads to climate model biases in jet streams, blocking and storm tracks, *Geophysical Research Letters*, *43*(13), 7231–7240, doi:10.1002/2016GL069551.

Poinar, K., I. Joughin, S. B. Das, M. D. Behn, J. Lenaerts, and M. R. Broeke (2015), Limits to future expansion of surface-melt-enhanced ice flow into the interior of western Greenland, *Geophysical Research Letters*, *42*(6), 1800–1807, doi:10.1002/2015GL063192.

Polar Portal (2017), End of the SMB Season summary 2017, accessed 10 Dec 2017 at http://polarportal.dk/en/nyheder/arkiv/nyheder/end-of-the-smb-season-summary-2017/.

Quinn, P. et al. (2008), Short-lived pollutants in the Arctic: their climate impact and possible mitigation strategies, *Atmospheric Chemistry and Physics*, *8*(6), 1723–1735, doi:10.5194/acp-8-1723-2008.

Radić, V., A. J. Cannon, B. Menounos, and N. Gi (2015), Future changes in autumn atmospheric river events in British Columbia, Canada, as projected by CMIP5 global climate models, *Journal of Geophysical Research: Atmospheres*, *120*(18), 9279–9302, doi:10.1002/2015JD023279.

Rae, J. G. L. et al. (2012), Greenland ice sheet surface mass balance: evaluating simulations and making projections with regional climate models, *The Cryosphere*, *6*(6), 1275–1294, doi:10.5194/tc-6-1275-2012.

Rajewicz, J., and S. J. Marshall (2014), Variability and trends in anticyclonic circulation over the Greenland ice sheet, 1948–2013, *Geophysical Research Letters*, *41*(8), 2842–2850, doi:10.1002/2014GL059255.

Ralph, F. M., P. J. Neiman, and G. A. Wick (2004), Satellite and CALJET aircraft observations of atmospheric rivers over the eastern North Pacific Ocean during the winter of 1997/98, *Monthly Weather Review*, *132*(7), 1721–1745, doi:10.1175/1520-0493%282004%29132<1721%3ASACAOO>2.0.CO%3B2.

Ralph, F. M., P. J. Neiman, G. A. Wick, S. I. Gutman, M. D. Dettinger, D. R. Cayan, and A. B. White (2006), Flooding on California's Russian River: Role of atmospheric rivers, *Geophysical Research Letters*, *33*(13), L13801, doi:10.1029/2006GL026689.

Ramos, A. M., R. Nieto, R. Tomé, L. Gimeno, R. M. Trigo, M. L. Liberato, and D. A. Lavers (2016), Atmospheric rivers moisture sources from a Lagrangian perspective, *Earth System Dynamics*, *7*(2), 371–384, doi:10.5194/esd-7-371-2016.

Reeves Eyre, J. E. J., and X. Zeng (2017), Evaluation of Greenland near surface air temperature datasets, *The Cryosphere*, *11*(4), 1591–1605, doi:10.5194/tc-11-1591-2017.

Rhines, P., S. Häkkinen, and S. A. Josey (2008), Is oceanic heat transport significant in the climate system?, in *Arctic-Subarctic Ocean Fluxes: Defining the Role of the Northern Seas in*, edited by Dickson, Robert R, pp. 87–109, Springer.

De Ridder, K., and H. Gallée (1998), Land surface-induced regional climate change in southern Israel, *Journal of Applied Meteorology*, *37*(11), 1470–1485, doi:10.1175/1520-0450(1998)037<1470:LSIRCC>2.0.CO;2.

Rienecker, M. M. et al. (2011), MERRA: NASA's Modern-Era Retrospective analysis for Research and Applications, *Journal of Climate*, *24*(14), 3624–3648, doi:10.1175/JCLI-D-11-00015.1.

Rimbu, N., G. Lohmann, M. Werner, and M. Ionita (2017), Links between central Greenland stable isotopes, blocking and extreme climate variability over Europe at decadal to multidecadal time scales, *Climate Dynamics*, *49*(1–2), 649–663, doi:10.1007/s00382-016-3365-3.

Rinke, A., C. Melsheimer, K. Dethloff, and G. Heygster (2009), Arctic total water vapor: Comparison of regional climate simulations with observations, and simulated decadal trends, *Journal of Hydrometeorology*, *10*(1), 113–129, doi:10.1175/2008JHM970.1.

Rivera, E. R., F. Dominguez, and C. L. Castro (2014), Atmospheric rivers and cool season extreme precipitation events in the Verde River basin of Arizona, *Journal of Hydrometeorology*, *15*(2), 813–829, doi:10.1175/JHM-D-12-0189.1.

Rosen, J. (2016), Cold truths at the top of the world, *Nature*, *532*(7599), 296–299, doi:10.1038/532296a.

Rückamp, M., U. Falk, S. Lange, K. Frieler, and A. Humbert (2018), The effect of overshooting 1.5°C global warming on the mass loss of the Greenland ice sheet, *Earth System Dynamics*, *9*(4), 1169–1189, doi:10.5194/esd-9-1169-2018.

Ruixin, H. (2005), Contribution of oceanic circulation to the poleward heat flux, *Journal of Ocean University of China*, *4*(4), 277–287, doi:10.1007/s11802-005-0048-9.

Rutan, D. A., S. Kato, D. R. Doelling, F. G. Rose, L. T. Nguyen, T. E. Caldwell, and N. G. Loeb (2015), CERES synoptic product: Methodology and validation of surface radiant flux, *Journal of Atmospheric and Oceanic Technology*, *32*(6), 1121–1143, doi:10.1175/JTECH-D-14-00165.1.

Rutz, J. J., W. J. Steenburgh, and F. M. Ralph (2014), Climatological characteristics of atmospheric rivers and their inland penetration over the western United States, *Monthly Weather Review*, *142*(2), 905–921, doi:10.1175/MWR-D-13-00168.1.

Saha, S. et al. (2010), The NCEP Climate Forecast System Reanalysis, *Bulletin of the American Meteorological Society*, *91*(8), 1015–1057, doi:10.1175/2010BAMS3001.1.

Scaife, A. A., D. Copsey, C. Gordon, C. Harris, T. Hinton, S. Keeley, A. O'Neill, M. Roberts, and K. Williams (2011), Improved Atlantic winter blocking in a climate model, *Geophysical Research Letters*, *38*(23), doi:10.1029/2011GL049573.

Schuenemann, K. C., and J. J. Cassano (2009), Changes in synoptic weather patterns and Greenland precipitation in the 20th and 21st centuries: 1. Evaluation of late 20th century simulations from IPCC models, *Journal of Geophysical Research: Atmospheres*, *114*(D20), D20113, doi:10.1029/2009JD011705.

Schuenemann, K. C., J. J. Cassano, and J. Finnis (2009), Synoptic forcing of precipitation over Greenland: Climatology for 1961–99, *Journal of Hydrometeorology*, *10*(1), 60–78, doi:10.1175/2008JHM1014.1.

Schuenemann, K. C., and J. J. Cassano (2010), Changes in synoptic weather patterns and Greenland precipitation in the 20th and 21st centuries: 2. Analysis of 21st century atmospheric changes using self-organizing maps, *Journal of Geophysical Research: Atmospheres*, *115*(D5), D05108, doi:10.1029/2009JD011706.

Screen, J. A., and I. Simmonds (2014), Amplified mid-latitude planetary waves favour particular regional weather extremes, *Nature Climate Change*, *4*(8), 704, doi:10.1038/NCLIMATE2271.

Screen, J. A., C. Deser, D. M. Smith, X. Zhang, R. Blackport, P. J. Kushner, T. Oudar, K. E. McCusker, and L. Sun (2018), Consistency and discrepancy in the atmospheric response to Arctic sea-ice loss across climate models, *Nature Geoscience*, *11*(3), 155, doi:10.1038/s41561-018-0059-y.

Serreze, M., A. Barrett, J. Stroeve, D. Kindig, and M. Holland (2009), The emergence of surface-based Arctic amplification, *The Cryosphere*, *3*(1), 11–19, doi:10.5194/tc-3-11-2009.

Serreze, M. C., and R. G. Barry (2011), Processes and impacts of Arctic amplification: A research synthesis, *Global and Planetary Change*, *77*(1), 85–96, doi:10.1016/j.gloplacha.2011.03.004.

Serreze, M. C., A. P. Barrett, and J. Stroeve (2012), Recent changes in tropospheric water vapor over the Arctic as assessed from radiosondes and atmospheric reanalyses, *Journal of Geophysical Research: Atmospheres*, *117*(D10), D10104, doi:10.1029/2011JD017421.

Shupe, M. D., and J. M. Intrieri (2004), Cloud radiative forcing of the Arctic surface: The influence of cloud properties, surface albedo, and solar zenith angle, *Journal of Climate*, *17*(3), 616–628, doi:10.1175/1520-0442(2004)017<0616:CRFOTA>2.0.CO;2.

Shupe, M. D. et al. (2013), High and dry: New observations of tropospheric and cloud properties above the Greenland Ice Sheet, *Bulletin of the American Meteorological Society*, *94*(2), 169–186, doi:10.1175/BAMS-D-11-00249.1.

Sime, L. C., C. Risi, J. C. Tindall, J. Sjolte, E. W. Wolff, V. Masson-Delmotte, and E. Capron (2013), Warm climate isotopic simulations: what do we learn about interglacial signals in Greenland ice cores?, *Quaternary Science Reviews*, *67*, 59–80, doi:10.1016/j.quascirev.2013.01.009.

Singh, H. K. A., C. M. Bitz, A. Donohoe, and P. J. Rasch (2017), A source–receptor perspective on the polar hydrologic cycle: sources, seasonality, and Arctic–Antarctic parity in the hydrologic cycle response to CO2 doubling , *Journal of Climate*, *30*(24), 9999–10017, doi:10.1175/JCLI-D-16-0917.1.

Skific, N., J. A. Francis, and J. J. Cassano (2009), Attribution of projected changes in atmospheric moisture transport in the Arctic: A self-organizing map perspective, *Journal of Climate*, *22*(15), 4135–4153, doi:10.1175/2009JCLI2645.1.

Skific, N., and J. A. Francis (2012), Self-organizing maps: A powerful tool for the atmospheric sciences. In: Johnsson, M. (Ed.), Applications of Self-Organizing Maps, INTECH Open Access Publisher. Available from http://www.intechopen.com/books/applications-of-self-organizing-maps/self-organizing-maps-a-powerful-tool-for-the-atmospheric-sciences.

Skific, N., and J. A. Francis (2013), Drivers of projected change in arctic moist static energy transport, *Journal of Geophysical Research: Atmospheres*, *118*(7), 2748–2761, doi:10.1002/jgrd.50292.

Sodemann, H., C. Schwierz, and H. Wernli (2008), Interannual variability of Greenland winter precipitation sources: Lagrangian moisture diagnostic and North Atlantic Oscillation influence, *Journal of Geophysical Research: Atmospheres*, *113*(D3), D03107, doi:10.1029/2007JD008503.

Sodemann, H., and A. Stohl (2013), Moisture origin and meridional transport in atmospheric rivers and their association with multiple cyclones, *Monthly Weather Review*, *141*(8), 2850–2868, doi:10.1175/MWR-D-12-00256.1.

Solomon, A. (2006), Impact of latent heat release on polar climate, *Geophysical Research Letters*, *33*(7), L07716, doi:10.1029/2005GL025607.

Solomon, A., M. D. Shupe, and N. B. Miller (2017), Cloud–atmospheric boundary layer–surface interactions on the Greenland ice sheet during the July 2012 extreme melt event, *Journal of Climate*, *30*(9), 3237–3252, doi:10.1175/JCLI-D-16-0071.1.

Steen-Larsen, H. C., A. Sveinbjörnsdottir, T. Jonsson, F. Ritter, J.-L. Bonne, V. Masson-Delmotte, H. Sodemann, T. Blunier, D. Dahl-Jensen, and B. Vinther (2015), Moisture sources and synoptic to seasonal variability of North Atlantic water vapor isotopic composition, *Journal of Geophysical Research: Atmospheres*, *120*(12), 5757–5774, doi:10.1002/2015JD023234.

Steen-Larsen, H. C., C. Risi, M. Werner, K. Yoshimura, and V. Masson-Delmotte (2017) Evaluating the skills of isotope-enabled general circulation models against in situ atmospheric water vapor isotope observations, *Journal of Geophysical Research: Atmospheres*, *122*(1), 246–263, doi:10.1002/2016JD025443.

Steger, C. R., C. H. Reijmer, M. R. van den Broeke, N. Wever, R. R. Forster, L. S. Koenig, P. Kuipers Munneke, M. Lehning, S. Lhermitte, S. R. M. Ligtenberg, C. Miège, and B. P. Y. Noël (2017), Firn meltwater retention on the Greenland Ice Sheet: A model comparison, *Frontiers in Earth Science*, *5*, 3, doi:10.3389/feart.2017.00003.

Stein, A., R. R. Draxler, G. D. Rolph, B. J. Stunder, M. Cohen, and F. Ngan (2015), NOAA's HYSPLIT atmospheric transport and dispersion modeling system, *Bulletin of the American Meteorological Society*, *96*(12), 2059–2077, doi:10.1175/BAMS-D-14-00110.1.

Stohl, A., and P. James (2004), A Lagrangian analysis of the atmospheric branch of the global water cycle. Part I: Method description, validation, and demonstration for the August 2002 flooding in central Europe, *Journal of Hydrometeorology*, *5*(4), 656–678, doi:10.1175/1525-7541(2004)005<0656:ALAOTA>2.0.CO;2.

Stohl, A., C. Forster, and H. Sodemann (2008), Remote sources of water vapor forming precipitation on the Norwegian west coast at 60 N—A tale of hurricanes and an atmospheric river, *Journal of Geophysical Research: Atmospheres*, *113*(D5), D05102, doi:10.1029/2007JD009006.

Stone, P. H. (1978), Constraints on dynamical transports of energy on a spherical planet, *Dynamics of Atmospheres and Oceans*, *2*(2), 123–139, doi:10.1016/0377-0265(78)90006-4.

Stouffer, R. J. (2004), Time scales of climate response, *Journal of Climate*, *17*(1), 209–217, doi:10.1175/1520-0442(2004)017<0209:TSOCR>2.0.CO;2.

Stroeve, J., and W. N. Meier (2018) Sea ice trends and climatologies from SMMR and SSM/I-SSMIS, Version 3, Monthly Climatology. Boulder, Colorado, USA, NASA National Snow and Ice Data Center Distributed Active Archive Center, doi: https://doi.org/10.5067/IJ0T7HFHB9Y6. Accessed 6 July 2019.

Sutterley, T. C., I. Velicogna, X. Fettweis, E. Rignot, B. Noël, and M. van den Broeke (2018), Evaluation of reconstructions of snow/ice melt in Greenland by regional atmospheric climate models using laser altimetry data, *Geophysical Research Letters*, *45*(16), 8324–8333, doi:10.1029/2018GL078645.

Swales, D., M. Alexander, and M. Hughes (2016), Examining moisture pathways and extreme precipitation in the US Intermountain West using self organizing maps, *Geophysical Research Letters*, *43*(4), 1727–1735, doi:10.1002/2015GL067478.

Tachibana, Y., K. K. Komatsu, V. A. Alexeev, L. Cai, and Y. Ando (2019), Warm hole in Pacific Arctic sea ice cover forced mid-latitude Northern Hemisphere cooling during winter 2017–18, *Scientific Reports*, *9*(1), 5567, doi:10.1038/s41598-019-41682-4.

Tedesco, M., X. Fettweis, T. Mote, J. Wahr, P. Alexander, J. Box, and B. Wouters (2013), Evidence and analysis of 2012 Greenland records from spaceborne observations, a regional climate model and reanalysis data, *The Cryosphere*, *7*(2), 615–630, doi:10.5194/tc-7-615-2013.

Tedesco, M., S. Doherty, X. Fettweis, P. Alexander, J. Jeyaratnam, and J. Stroeve (2016a), The darkening of the Greenland ice sheet: trends, drivers, and projections (1981–2100), *The Cryosphere*, *10*(2), 477–496, doi:10.5194/tc-10-477-2016.

Tedesco, M., T. Mote, X. Fettweis, E. Hanna, J. Jeyaratnam, J. Booth, R. Datta, and K. Briggs (2016b), Arctic cut-off high drives the poleward shift of a new Greenland melting record, *Nature Communications*, *7*, 11723, doi:10.1038/ncomms11723.

Tedesco, M., J. E. Box, J. Cappelen, R. S. Fausto, X. Fettweis, K. Hansen, T. Mote, I. Sasgen, C. J. P. P. Smeets, D. van As, R. S. W. van de Wal, and I. Velicogna (2017a), Greenland Ice Sheet. In Arctic Report Card: Update for 2017, accessed 10 Dec 2017 at http://www.arctic.noaa.gov/Report-Card/Report-Card-2017/ArtMID/7798/ArticleID/697/Greenland-Ice-Sheet.

Tedstone, A. J., J. L. Bamber, J. M. Cook, C. J. Williamson, X. Fettweis, A. J. Hodson, and M. Tranter (2017b), Dark ice dynamics of the south-west Greenland Ice Sheet, *The Cryosphere*, *11*(6), 2491–2506, doi:10.5194/tc-11-2491-2017.

Thomas, R. H. (2001), Program for Arctic Regional Climate Assessment (PARCA): Goals, key findings, and future directions, *Journal of Geophysical Research: Atmospheres*, *106*(D24), 33,691–33,705, doi:10.1029/2001JD900042.

Trenberth, K. E., and A. Solomon (1994), The global heat balance: Heat transports in the atmosphere and ocean, *Climate Dynamics*, *10*(3), 107–134, doi:10.1007/BF00210625.

Trenberth, K. E. (1998), Atmospheric moisture residence times and cycling: Implications for rainfall rates and climate change, *Climatic Change*, *39*(4), 667–694, doi:10.1023/A:1005319109110.

Trenberth, K. E., and J. M. Caron (2001), Estimates of meridional atmosphere and ocean heat transports, *Journal of Climate*, *14*(16), 3433–3443, doi:10.1175/1520-0442(2001)014<3433:EOMAAO>2.0.CO;2.

Trenberth, K. E., and D. P. Stepaniak (2003), Seamless poleward atmospheric energy transports and implications for the Hadley circulation, *Journal of Climate*, *16*(22), 3706–3722, doi:10.1175/1520-0442(2003)016<3706:SPAETA>2.0.CO;2.

Trenberth, K. E., and D. P. Stepaniak (2004), The flow of energy through the Earth's climate system, *Quarterly Journal of the Royal Meteorological Society*, *130*(603), 2677–2701, doi:10.1256/qj.04.83.

Trenberth, K. E., and J. T. Fasullo (2017), Atlantic meridional heat transports computed from balancing Earth's energy locally, *Geophysical Research Letters*, *44*(4), 1919–1927, doi:10.1002/2016GL072475.

Van Tricht, K., S. Lhermitte, J. Lenaerts, I. V. Gorodetskaya, T. S. L'Ecuyer, B. Noël, M. R. Van den Broeke, D. D. Turner, and N. P. Van Lipzig (2016), Clouds enhance Greenland ice sheet meltwater runoff, *Nature Communications*, *7*, 10266, doi:10.1038/ncomms10266.

Turner, D. D., S. A. Clough, J. C. Liljegren, E. E. Clothiaux, K. E. Cady-Pereira, and K. L. Gaustad (2007), Retrieving liquid water path and precipitable water vapor from the Atmospheric Radiation Measurement (ARM) microwave radiometers, *IEEE Transactions on Geoscience and Remote Sensing*, *45*(11), 3680–3690, doi:10.1109/TGRS.2007.903703.

Vázquez, M., I. Algarra, J. Eiras-Barca, A. M. Ramos, R. Nieto, and L. Gimeno (2019), Atmospheric rivers over the Arctic: Lagrangian characterisation of their moisture sources, *Water*, *11*(1), 41, doi:10.3390/w11010041.

Wallace, J. M., I. M. Held, D. W. Thompson, K. E. Trenberth, and J. E. Walsh (2014), Global warming and winter weather, *Science*, *343*(6172), 729–730, doi:10.1126/science.343.6172.729.

Wang, S., D. Nath, W. Chen, and L. Wang (2019), Recent strengthening of Greenland blocking drives summertime surface warming over northern Canada and eastern Siberia, *Journal of Climate*, *32*(11), 3263–3278, doi:10.1175/JCLI-D-18-0410.1.

Wang, W., C. S. Zender, and D. van As (2018), Temporal characteristics of cloud radiative effects on the Greenland Ice Sheet: Discoveries from multiyear automatic weather station measurements, *Journal of Geophysical Research: Atmospheres*, *123*(20), 11,348–11,361, doi:10.1029/2018JD028540.

Warner, M. S. (2018), Introduction to PySPLIT: A Python toolkit for NOAA ARL's HYSPLIT model, *Computing in Science & Engineering*, *20*(5), 47–62, doi:10.1109/MCSE.2017.3301549.

Wernli, H., and L. Papritz (2018), Role of polar anticyclones and mid-latitude cyclones for Arctic summertime sea-ice melting, *Nature Geoscience*, *11*(2), 108–113, doi:10.1038/s41561-017-0041-0.

Wielicki, B. A., B. R. Barkstrom, E. F. Harrison, R. B. Lee III, G. Louis Smith, and J. E. Cooper (1996), Clouds and the Earth's Radiant Energy System (CERES): An earth observing system experiment, *Bulletin of the American Meteorological Society*, *77*(5), 853–868, doi:10.1175/1520-0477(1996)077<0853:CATERE>2.0.CO;2.

Wilton, D. J., A. Jowett, E. B. G. R. Hanna, M. R. Van den Broeke, X. Fettweis, and P. Huybrechts (2017), High resolution (1 km) positive degree-day modelling of Greenland ice sheet surface mass balance, 1870–2012 using reanalysis data, *Journal of Glaciology*, *63*(237), 176–193, doi:10.1017/jog.2016.133.

Winton, M. (2006), Amplified Arctic climate change: What does surface albedo feedback have to do with it?, *Geophysical Research Letters*, *33*(3), L03701, doi:10.1029/2005GL025244.

Woods, C., R. Caballero, and G. Svensson (2013), Large-scale circulation associated with moisture intrusions into the Arctic during winter, *Geophysical Research Letters*, *40*(17), 4717–4721, doi:10.1002/grl.50912.

Woods, C., and R. Caballero (2016), The role of moist intrusions in winter Arctic warming and sea ice decline, *Journal of Climate*, *29*(12), 4473–4485, doi:10.1175/JCLI-D-15-0773.1.

Wu, Y., M. Ting, R. Seager, H.-P. Huang, and M. A. Cane (2011), Changes in storm tracks and energy transports in a warmer climate simulated by the GFDL CM2. 1 model, *Climate Dynamics*, *37*(1–2), 53–72, doi:10.1007/s00382-010-0776-4.

Wunsch, C. (2005), The total meridional heat flux and its oceanic and atmospheric partition, *Journal of Climate*, *18*(21), 4374–4380, doi:10.1175/JCLI3539.1.

Yang, H., Q. Li, K. Wang, Y. Sun, and D. Sun (2015), Decomposing the meridional heat transport in the climate system, *Climate Dynamics*, *44*(9–10), 2751–2768, doi:10.1007/s00382-014-2380-5.

Yang, W., and G. Magnusdottir (2017), Springtime extreme moisture transport into the Arctic and its impact on sea ice concentration, *Journal of Geophysical Research: Atmospheres*, *122*(10), 5316–5329, doi:10.1002/2016JD026324.

Yang, X.-Y., J. C. Fyfe, and G. M. Flato (2010), The role of poleward energy transport in Arctic temperature evolution, *Geophysical Research Letters*, *37*(14), L14803, doi:10.1029/2010GL043934.

Yang, Z., W. Huang, X. He, Y. Wang, T. Qiu, J. S. Wright, and B. Wang (2019), Synoptic conditions and moisture sources for extreme snowfall events over east China, *Journal of Geophysical Research: Atmospheres*, *124*(2), 601–623, doi:10.1029/2018JD029280.

Yoo, C., S. Lee, and S. B. Feldstein (2012), Mechanisms of Arctic surface air temperature change in response to the Madden-Julian Oscillation, *Journal of Climate*, *25*(17), 5777–5790, doi:10.1175/JCLI-D-11-00566.1.

Yoo, C., S. B. Feldstein, and S. Lee (2014), The prominence of a tropical convective signal in the wintertime Arctic temperature, *Atmospheric Science Letters*, *15*(1), 7–12, doi:10.1002/asl2.455.

Yoshimori, M., A. Abe-Ouchi, and A. Laîné (2017), The role of atmospheric heat transport and regional feedbacks in the Arctic warming at equilibrium, *Climate Dynamics*, *49*(9), 3457–3472, doi:10.1007/s00382-017-3523-2.

Yu, L., X. Jin, and R. A. Weller (2008), Multidecade global flux datasets from the objectively analyzed air-sea fluxes (OAFlux) project: Latent and sensible heat fluxes, ocean evaporation, and related surface meteorological variables, OAFlux Project Technical Report OA-2008-01, 64 pp., Woods Hole Oceanographic Institution, Woods Hole, Mass.

Zelinka, M. D., and D. L. Hartmann (2012), Climate feedbacks and their implications for poleward energy flux changes in a warming climate, *Journal of Climate*, *25*(2), 608–624, doi:10.1175/JCLI-D-11-00096.1.

Zhong, L., L. Hua, and D. Luo (2018), Local and external moisture sources for the Arctic warming over the Barents-Kara seas, *Journal of Climate*, *31*(5), 1963–1982, doi:10.1175/JCLI-D-17-0203.1.

Zhu, Y., and R. E. Newell (1998), A proposed algorithm for moisture fluxes from atmospheric rivers, *Monthly Weather Review*, *126*(3), 725–735, doi:10.1175/1520-0493(1998)126<0725:APAFMF>2.0.CO;2.

APPENDIX A: ODDS RATIO METHOD FOR CLASSIFYING AR INTENSITY

In order to choose a threshold for discriminating between "normal" and "strong" AR events affecting each GrIS basin, we analyze the frequency of anomalously warm, windy, and moist conditions at the four low-elevation PROMICE stations in basins 6 and 8 (KAN_L, NUK_L, THU_L, and UPE_L) in relation to AR intensity. Using a modified version of the "heat wave" criteria employed by Hermann et al. (2018), we define extreme warm, moist, windy "heat wave" days at KAN_L, NUK_L, and UPE_L as those when any hourly observation contains 2-m temperature and specific humidity values ≥ 5°C and 3 g kg^{-1}, respectively, simultaneous with wind speeds ≥ 8 m s^{-1}. The 2-m temperature threshold is set to 2°C at THU_L due to the infrequency of ≥ 5°C observations at this station, while the specific humidity and wind speed criteria are the same as the other three stations.

We compare the probability of "heat wave" events on days with no AR to days when an AR of any intensity occurred. We then further analyze whether more intense ARs are more likely to result in "heat wave" events by comparing the probability of these events to their probability on "no AR" days across percentiles of basin-scale AR IVT at 1-percentile intervals. These probability comparisons are performed by calculating the odds ratio [*Miller and Mote*, 2018]:

$$OR = \frac{A/C}{B/D} \qquad (A1)$$

where the A / C term in the numerator calculates the ratio of events to non-events when a given condition is met, and B / D in the denominator is the ratio of events to non-events when the condition is not met. In our categorical comparison of "heat wave" events on AR versus "no AR" days, A / C is the ratio of "heat wave" days to non-"heat wave" days when an AR affects the

given basin, and *B / D* is the ratio of "heat wave" days to non-"heat wave" days on days when an AR does not affect the given basin. In calculating the odds ratio across IVT percentile rank thresholds, the condition to be met is that the maximum daily IVT within an AR over the given basin exceeds the given percentile rank of the basin-specific distribution. For example, the odds ratio plotted at the 90th IVT percentile rank in Fig. A1 shows the ratio of "heat wave" days to non-"heat wave" days given the condition that the maximum IVT within any AR over the basin exceeds the 90th percentile of the basin-specific AR IVT distribution, divided by the ratio of "heat wave" days to non-"heat wave" days when there is no AR or an AR with < 90th percentile IVT over the basin.

Fig. A1 shows that the odds of a "heat wave" event are 10–25 times higher on AR days compared to "no AR" days at the four PROMICE stations (gray dashed lines). At each station, the odds ratios remain relatively steady or slowly increase across AR IVT percentiles 0 through 90, then sharply increase around the 90–95th percentiles. Based on this evidence, we chose the 90th percentile of AR IVT as the cutoff point to distinguish between "normal" ARs ($AR_{<90}$) and "strong" ARs (AR_{90+}).

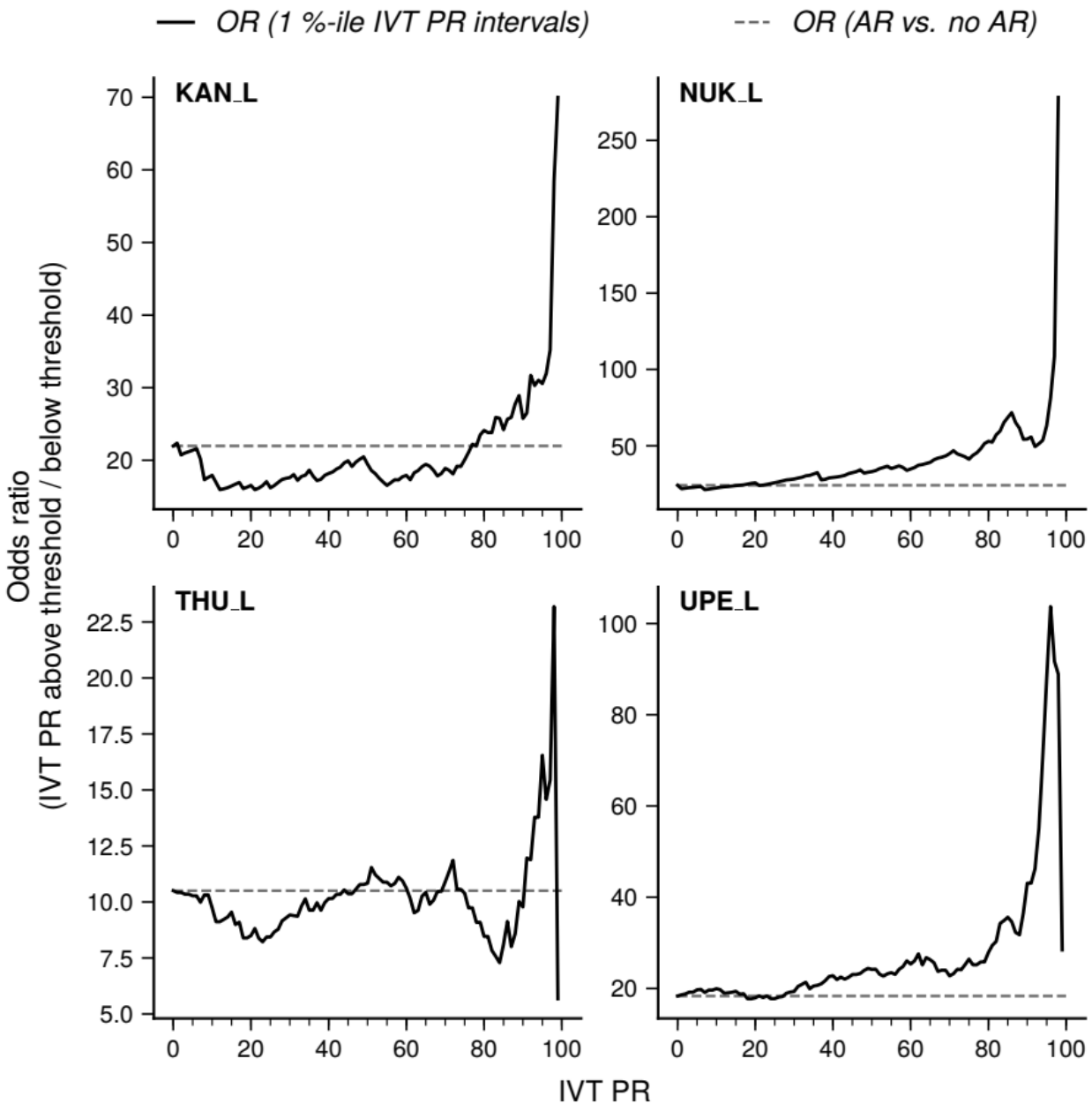

Figure A1. Odds ratio of "heat wave" events across IVT percentiles (solid black lines) at four low-elevation PROMICE stations in basins 6 and 8: KAN_L, NUK_L, THU_L, and UPE_L. Also plotted is the odds ratio of "heat wave" events on days with an AR of any intensity versus "no AR" days (gray dashed lines).